

Towards a high precision measurement of the free neutron lifetime with τ SPECT

Dissertation zur Erlangung des Grades

„Doktor der Naturwissenschaften“

am Fachbereich Physik, Mathematik und Informatik
der Johannes Gutenberg-Universität in Mainz

vorgelegt von

Kim Ulrike Roß

geboren in Heppenheim (Bergstraße)

Mainz, den 21. Juli 2021

Datum der mündlichen Prüfung: 05.11.2021

*Measure what can be measured,
and make measurable what cannot be measured.*

- Galileo Galilei -

Contents

Abstract	vii
Zusammenfassung	ix
Nomenclature	xi
1 Motivation	1
1.1 The discovery of the neutron	1
1.2 Fundamental properties of the neutron	2
1.3 The β decay of the neutron	2
1.3.1 The neutron lifetime and the CKM matrix	4
1.3.2 The neutron lifetime and big bang nucleosynthesis	7
1.4 Summary	10
2 Neutron lifetime experiments	11
2.1 Neutron interactions	11
2.1.1 Weak interaction	11
2.1.2 Strong interaction	11
2.1.3 Gravitational interaction	12
2.1.4 Electromagnetic interaction	12
2.2 Introduction to neutron lifetime experiments	13
2.2.1 Beam experiments	13
2.2.2 Bottle experiments	15
2.2.3 Material wall storage	15
2.2.4 Magnetic storage	17
2.2.5 The neutron lifetime puzzle	17
2.2.6 Neutron lifetime experiments: Current status and prospects	19
3 The lifetime experiment τSPECT	21
3.1 Magnetic storage in τ SPECT	21
3.1.1 Experimental setup	22
3.1.2 The spin flipping unit	26
3.2 Compensation of the octupole field	27
3.2.1 Halbach octupoles	27

3.2.2	The magnetic octupoles in τ SPECT	28
3.2.3	Zero-field points	36
3.3	The spin flipper	39
3.3.1	Birdcage Resonators	39
3.3.2	The birdcage resonator for τ SPECT	40
3.3.3	The magnetic field of the birdcage resonator	44
3.3.4	First experiences with the birdcage resonator and magnetic storage of UCN	46
3.4	The neutron detector	47
3.5	Slow control of the experiment	49
3.6	First operation of τ SPECT after commissioning	51
3.6.1	Position calibration of the translation stages	52
3.6.2	The arrival spectrum	53
3.6.3	The first purely magnetic storage curve	54
3.6.4	Measurement time required for a first neutron lifetime result	59
3.7	Summary	61
4	The theory of spin flip loading in τSPECT	63
4.1	Spin flipping using adiabatic fast passage	63
4.1.1	Adiabatic fast passage spin flipping in longitudinal fields	63
4.1.2	The spin flip efficiency in a Monte Carlo simulation	68
4.2	The energy acceptance of the UCN trap in τ SPECT	73
4.2.1	Derivation of the maximum storable energy (without gravity)	73
4.2.2	The maximum storable energy depending on gravity	75
4.2.3	The storable fraction of the neutron energy spectrum	76
4.2.4	Implications for the birdcage resonator	78
4.3	Summary	79
5	Optimisation of spin flip loading in τSPECT	81
5.1	Spin flipping using a double saddle coil	81
5.1.1	Increasing the UCN density in τ SPECT	82
5.2	Implications for measurements with τ SPECT	91
5.2.1	Improving the compensation of the octupole field	91
5.2.2	Reduction of the current in the main coils	95
5.2.3	Summary of the optimum parameters for τ SPECT	97
5.3	Current status and preparatory studies regarding a lifetime measurement	98
5.3.1	Optimisation of the cleaning process	102
5.3.2	Optimising the data normalisation	106
5.4	Status of the required measurement time for $\Delta\tau_n = 1$ s	109

6	The Double Spin Flip Technique	111
6.1	Energy considerations in the double spin flip technique	111
6.1.1	The energy acceptance in the double spin flip technique	111
6.1.2	The problem with the beam divergence	113
6.1.3	The optimum height for the double spin flip technique	116
6.2	Double spin flipping in practice	117
6.2.1	Position constraints and design of the additional spin flipper	117
6.2.2	Optimisation of the SF1 parameters	119
6.2.3	The filling techniques in comparison	126
6.3	Future optimisation of the double spin flip technique	127
7	Summary and Outlook	131
A	Further contents, procedures and constructions	135
A.1	The UCN source D at the TRIGA reactor	135
A.1.1	The setup of the UCN source	135
A.2	Construction of the compensation octupole	137
A.2.1	The selection of the magnetic segments	137
A.2.2	Construction of the compensation octupole	138
A.2.3	Allan deviation of the Hall probe	142
A.2.4	The orientation of the compensation octupole	143
A.3	The spin flipper	144
A.3.1	The signal phase shift $\Delta\varphi$ for the birdcage resonator	144
A.3.2	Calibration of the pick-up coil for magnetic field measurements	145
A.3.3	The theoretical field shape of birdcage and saddle coil	147
A.4	The neutron detector	148
A.4.1	Neutron event recognition	148
A.4.2	Optimisation of the detector overvoltage	151
A.5	Spin tracking using Monte Carlo simulations	153
A.5.1	Analytic approximation of the magnetic fields in τ SPECT	153
A.5.2	The Monte Carlo simulation	159
A.6	The τ SPECT beamlines	163
A.7	Hardware and electronics	166
A.7.1	The motor control system of the translation stages	166
A.7.2	The shutter interlock system	167
B	Additional figures and tables	169
B.1	Magnetic field measurements	170
B.2	Spin flipper parameter optimisation	175
B.3	Cleaning	177

Abstract

The β decay of the neutron is an interesting quantity both in particle physics as well as in astroparticle physics: A precise determination of the free neutron lifetime τ_n helps understanding Big Bang Nucleosynthesis, during which first light elements were produced. Furthermore, it can be used to calculate the V_{ud} element of the CKM matrix, which is responsible for the mixing of weak eigenstates of quarks.

Currently, two methods to determine the neutron lifetime exist. While beam experiments measure the decay products ('counting the dead'), bottle type experiments store very low energetic neutrons (so-called 'ultracold' neutrons, UCN) in a vessel and count the remaining neutrons after a certain storage time ('counting the survivors'). Both methods yield results with a precision of $\Delta\tau_n/\tau_n = 3 \times 10^{-3}$ or better, but their extracted values for the neutron lifetime differ by 3.9σ . The difficulty with both techniques is to take all systematic effects into account. In bottle type experiments such effects are e.g. interactions of UCN with the walls of the storage vessel. By replacing the material walls by strong magnetic fields, magnetic storage experiments attempt to eliminate this systematic effect and thus allow for measurements of τ_n with higher precision.

The τ SPECT experiment at the TRIGA research reactor in Mainz, Germany, is the first neutron lifetime experiment which employs only magnetic fields for the storage of UCN of energies $E \lesssim 47$ neV. The trap consists of a longitudinal field generated by two cylindrical superconducting coils, as well as a Halbach type octupole made from permanent magnets; the superposition of both creates a low field region, which is surrounded by strong magnetic fields. UCN are filled into the trap by an adiabatic fast passage spin flipper, which generates a rotating magnetic field B_1 and transforms low energetic neutrons in the high-field seeking state to storable low-field seekers. They are stored inside the trap and after varying storage times the surviving neutrons are detected. The neutron lifetime can be extracted from an exponential fit to the counted number of neutrons depending on the storage time.

First storage measurements of UCN in September 2019 were successful but yielded only low statistics, so that the target uncertainty in the neutron lifetime of $\Delta\tau_n = 1.0$ s would have been unachievable in a reasonable amount of measurement time. In this work, the filling process was therefore fully understood, simulated and optimised. The initially used spin flipper (SF) in form of a birdcage resonator was replaced by a double saddle coil, so that due to its high flexibility in finding the appropriate SF-position at different resonance conditions an increase in statistics by a factor of ~ 4 was achieved. Additionally, a modified filling technique involving two double saddle coils was successfully demonstrated as proof of concept.

One of the remaining systematic effects in the experiment is due to marginally trapped neutrons, which poses a loss mechanism additional to β decay. These neutrons have to be

removed ('cleaned') from the spectrum before the storage time begins. First optimisations are presented in this work together with recent storage curve measurements (preliminary results).

Zusammenfassung

Der β -Zerfall des Neutrons spielt sowohl in der Teilchen- als auch in der Astroteilchenphysik eine große Rolle: Eine präzise Bestimmung der Lebensdauer freier Neutronen kann helfen, die primordiale Nukleosynthese in der Zeit kurz nach dem Urknall zu verstehen, während derer die ersten leichten Elemente entstanden. Desweiteren kann sie dazu verwendet werden, das V_{ud} -Element der CKM-Matrix zu berechnen, das für die Mischung schwacher Eigenzustände von Quarks verantwortlich ist.

Zurzeit existieren zwei Methoden zur Bestimmung der Neutronenlebensdauer. Während Strahlexperimente die Zerfallsprodukte messen ("counting the dead"), verwenden Speicherexperimente sehr niederenergetische Neutronen (sogenannte "ultrakalte" Neutronen, UCN) in einem Gefäß und zählen die verbleibenden Neutronen nach einer gewissen Speicherzeit ("counting the survivors"). Beide Methoden erzielen Ergebnisse mit einer Präzision von $\Delta\tau_n/\tau_n = 3 \times 10^{-3}$ oder besser, ihre jeweiligen Werte für die Neutronenlebensdauer liegen allerdings um 3.9σ auseinander. Die Schwierigkeit beider Methoden ist die Berücksichtigung aller systematischen Effekte. Bei Speicherexperimenten sind solche systematischen Effekte beispielsweise Wechselwirkungen von UCN mit den Wänden des Speichergefäßes. Magnetische Speicherexperimente versuchen daher, diesen systematischen Effekt zu beseitigen indem sie die materiellen Wände durch starke Magnetfelder ersetzen, was Messungen von τ_n mit höherer Genauigkeit ermöglicht.

Das τ SPECT Experiment am Forschungsreaktor TRIGA in Mainz, Deutschland, ist das erste Neutronenlebensdauerexperiment, das ausschließlich Magnetfelder zur Speicherung von UCN mit Energien $E \lesssim 47$ neV verwendet. Die Falle besteht aus einem longitudinalen Feld, das von zwei zylindrischen supraleitenden Spulen erzeugt wird, sowie einem Halbach Oktupol aus Permanentmagneten; die Überlagerung der beiden erzeugt einen Bereich mit niedrigem Magnetfeld, der von starken Feldern umgeben ist. UCN werden durch einen "Adiabatic Fast Passage Spin Flipper" in die Falle gefüllt, der ein rotierendes Magnetfeld B_1 erzeugt und niederenergetische Neutronen im Hochfeld-bevorzugenden Spinzustand in speicherbare Niederfeld-bevorzugende Neutronen umwandelt. Diese werden in der Falle gespeichert, nach verschiedenen Speicherzeiten werden die überlebenden Neutronen detektiert. Die Neutronenlebensdauer kann aus einem exponentiellen Fit an die gezählte Anzahl Neutronen in Abhängigkeit von der Speicherzeit extrahiert werden.

Erste Speichermessungen mit UCN wurden im September 2019 erfolgreich durchgeführt, erzielten allerdings nur eine geringe Statistik, sodass die anvisierte Ungenauigkeit in der Bestimmung der Neutronenlebensdauer von $\Delta\tau_n = 1.0$ s in einer angemessenen Messdauer nicht erreichbar gewesen wäre. In dieser Arbeit wurde daher der Füllprozess vollständig verstanden, simuliert und optimiert. Der anfänglich verwendete Spin Flipper (SF) in Form eines "Birdcage Resonators" wurde durch eine Doppel-Sattelspule ersetzt, sodass durch deren hohe Einsatzflexibilität in Bezug auf die passende SF-Position bei verschiedenen

Resonanzbedingungen eine Steigerung der Neutronenstatistik um einen Faktor ~ 4 erreicht werden konnte. Zusätzlich wurde der Einsatz einer modifizierten Füllmethode unter Verwendung zweier Doppel-Sattelspulen in einer Machbarkeitsstudie erfolgreich demonstriert.

Einer der verbleibenden systematischen Effekte im Experiment liegt an marginal gespeicherten Neutronen, die einen Verlustmechanismus zusätzlich zum β -Zerfall darstellen. Diese Neutronen müssen vor dem Beginn der Speicherzeit aus dem Spektrum entfernt werden ('cleaning'). Erste Optimierungen sowie neueste Speicherkurvenmessungen (vorläufige Ergebnisse) werden in dieser Arbeit vorgestellt.

Nomenclature and constants

Acronyms and Abbreviations

ADC	Analog-to-Digital Converter
amu	Atomic Mass Unit
BBN	Big Bang Nucleosynthesis
BSM Physics	Physics Beyond the Standard Model
CAD	Computer Aided Design
CMB	Cosmic Microwave Background
CO	Compensation Octupole
dSF	Double Spin Flip Technique
FEM	Finite Element Method
GUI	Graphical User Interface
HFS	High Field Seeking Neutron
JGU	Johannes Gutenberg University
LFS	Low Field Seeking Neutron
MC simulation	Monte Carlo simulation
MPPC	Multi Pixel Photon Counter
PCB	Printed Circuit Board
PDG	Particle Data Group
PEEK	Polyether ether ketone
PMMA	Polymethyl methacrylate
POM	Polyoxymethylene
PTFE	Polytetrafluoroethylene (Teflon [®])
RF	Radio Frequency
RL	Return Loss
SFU	Spin Flipping Unit
SiPM	Silicon PhotoMultiplier
SM	Standard Model of Particle Physics
SO	Storage Octupole
sSF	Single Spin Flip Technique
SWR	Standing Wave Ratio
TMP	Turbo Molecular Pump

UCN	Ultra Cold Neutron
VCN	Very Cold Neutron
VNA	Vector Network Analyser

Physical constants

e	Elementary charge	$1.602\,176\,634 \times 10^{-19} \text{ C}$
g	Neutron g-factor	$-3.826\,085\,45(90)$
γ	Neutron gyromagnetic ratio	$1.832\,471\,71(43) \times 10^8 \text{ s}^{-1}\text{T}^{-1}$
\hbar	Planck constant (reduced)	$6.582\,119\,569\dots \times 10^{-16} \text{ eVs}$
$G_F/\sqrt{2}$	Fermi coupling constant	$1.166\,378\,7(6) \times 10^{-5} \text{ GeV}^{-2}$
G_N	Newtonian constant of gravitation	$6.674\,30(15) \times 10^{-11} \text{ m}^3\text{kg}^{-1}\text{s}^{-2}$
k_B	Boltzmann constant	$8.617\,333\,262 \times 10^{-5} \text{ eV/K}$
$m_n c^2$	Neutron mass	$939.565\,420\,52(54) \text{ MeV}$
$m_p c^2$	Proton mass	$938.272\,088\,16(29) \text{ MeV}$
μ_0	Vacuum permeability	$1.256\,637\,062\,12(19) \times 10^{-6} \text{ H} \cdot \text{m}^{-1}$
μ_N	Nuclear magneton	$3.152\,451\,258\,44(96) \times 10^{-8} \text{ eV}\text{T}^{-1}$
μ_n	Neutron magnetic moment	$-9.662\,3651(23) \times 10^{-27} \text{ JT}^{-1}$

All constants are the recommended values by the Committee on Data for Science and Technology (CODATA) at the National Institute of Standards and Technology (NIST) [cod19].

Chapter 1

Motivation

Neutrons are neutral spin- $1/2$ particles, which, together with protons, form the atomic nuclei in the elements which make up all matter. Bound in a nucleus, the neutrons are stable, however, as free particles, neutrons undergo β decay. This chapter introduces the discovery of the neutron as well as relevant aspects of the weak interaction that lead to neutron β decay. Afterwards, the importance of the neutron lifetime in modern research is emphasised in two examples, the unitarity test of the CKM matrix, and the understanding of Big Bang nucleosynthesis.

1.1 The discovery of the neutron

In 1920, Ernest Rutherford introduced the idea, that the atomic nucleus has to include a heavy neutral 'particle' [Rut20]. This arose from the observation, that the atomic mass of an element differs from its atomic number, i.e. the number of protons inside the nucleus. He therefore suggested the existence of a neutral bound state consisting of a proton and an electron inside the nucleus.

It was James Chadwick, former student and then co-worker of Rutherford, who discovered the neutron in 1932 by investigating the radiation of α -particle induced decay of ${}^9\text{Be}$ and published a first estimation of the neutron mass between 1.005 and 1.008 amu (atomic mass unit) [Cha32]. In the same year, Dmitri Iwanenko and Werner Heisenberg independently considered the neutron as an individual spin- $1/2$ particle for the first time rather than a bound state [Iwa32, Hei32]. The measured neutron mass did, however, not contradict the value of 1.0078 amu for the sum of masses of proton and electron at that time [Cha32] and therefore the Rutherford picture could not yet be disproved.

A more precise measurement in 1934 by Chadwick and Maurice Goldhaber, in which they used photo dissociation to measure the deuteron binding energy and compared this value to the atomic masses of hydrogen and deuterium from mass spectroscopy, resulted in a value for the neutron mass of 1.0080(5) amu [CG34]. They re-run their experiment with improved mass spectroscopy data in 1935, which resulted in a neutron mass of 1.0087(3) amu [CG35]¹. This value was larger than the proton mass, then estimated as 1.0081 amu, so that the Rutherford picture was disproved. In their publication, Chadwick and Goldhaber also for the first time stated the possibility of free neutron decay into a

¹In [CG35], two values for the neutron mass are stated, 1.0084 amu and 1.0090 amu, which depend on the used value for the deuteron mass. Above, the mean value of these two is calculated.

proton, an electron and an antineutrino, which would not have been possible in the Rutherford picture, because the neutron as a bound state would have had less energy than its individual constituents. For the discovery of the neutron, Chadwick received the Nobel Prize in Physics in 1935.

1.2 Fundamental properties of the neutron

After its discovery, the neutron as well as the proton were considered elementary particles [CG35]. Today all matter (and anti-matter) is described by the Standard Model of Particle Physics (SM), which groups them into leptons (e , μ , τ and their corresponding neutrinos) and quarks. Furthermore, the SM contains the force carriers, which mediate the fundamental interactions (except for gravity): γ (electromagnetic); W^+ , W^- and Z boson (weak); and eight gluons (strong interaction).

In this context, the neutron containing three quarks (one up- and two down-quarks, udd) is classified as a so-called baryon. It is neutral with a current experimental limit of $-2(8) \times 10^{-22} e$ in terms of the elementary charge e [ZBB⁺20] and has a spin of $S = 1/2$, which is directly connected to the magnetic moment [BA13]

$$\vec{\mu} = g\mu_N \frac{\vec{S}}{\hbar} \quad (1.1)$$

with the neutron g-factor g and the nuclear magneton² μ_N . Inserting the constants, the magnetic moment calculates to approximately -60.31 neV/T .

Coming back to the neutron mass, it is today measured as $1.008\,664\,915\,95(49) \text{ amu}$, which translates to the energy equivalent of $939.565\,420\,52(54) \text{ MeV}$ [cod19]³. The neutron is thus $\Delta_m = 1.293\,332\,36(46) \text{ MeV}$ heavier than the proton [cod19]. This mass difference and the similar quark structure between neutrons and protons (protons consist of the quark combination uud) allows the neutron to β decay into a proton by conversion of one down-quark to an up-quark and emission of a W^- boson (see Fig. 1.1). The W^- boson in turn decays into an electron and an electron antineutrino, so that the total decay can be described as

$$n \rightarrow p^+ + e^- + \bar{\nu}_e. \quad (1.2)$$

With three decay particles involved, the decay energy is distributed continuously amongst them, resulting in a proton spectrum with an end-point energy of $E_p = 751 \text{ eV}$ and an electron spectrum with an end-point energy of $E_e = 782 \text{ keV}$ [YCF⁺14]. The average neutron lifetime is currently stated as $\tau_n = 879.4 \pm 0.6 \text{ s}$ by the Particle Data Group (PDG) [ZBB⁺20]. The mentioned properties of the neutron are again summarised in Tab. 1.1.

1.3 The β decay of the neutron

The precision measurement of neutron β decay parameters is a valuable tool for testing theories in particle and astrophysics. The beauty of this decay lies in the neutron being

²All constants and their values are listed on page xii and are only quoted if necessary.

³The precision in the energy conversion decreases due to the relatively poorly known electron charge [ZBB⁺20]

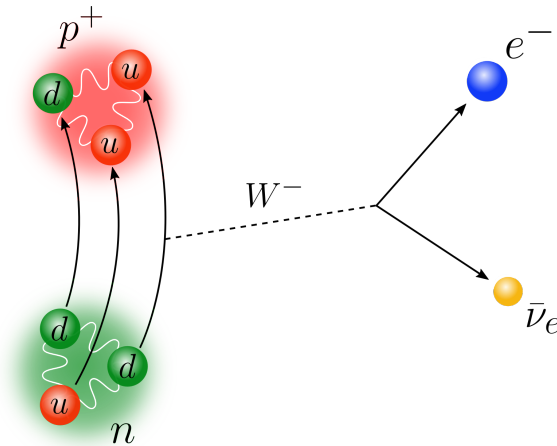


Figure 1.1: β^- decay of the neutron. A down-quark converts to an up-quark by emission of a W^- boson, which in turn decays into an electron and an electron antineutrino.

the prototype of a semileptonic β decaying system without an influence by the structure of a surrounding nucleus, as will be seen further below.

First measurements, showing that neutrons do in fact decay, were done in the late 1940s by A. H. Snell *et al.* [SPM50] and J. M. Robson [Rob50], initially only setting range limits of several minutes on the neutron lifetime. Experiments have become more and more precise since then. Today there exist two different measurement methods, which are consistent amongst each other and yield measurement results on a precision level of 0.1%, but deviate by 4σ [Mum18] (an overview is given in Ch. 2.2). Solving this 'neutron lifetime puzzle' is only one aspect in modern research. Furthermore, precision measurements of the neutron lifetime are used to test theories in particle physics and cosmology, as is shown in the following sections.

Table 1.1: Overview over the neutron properties.

Parameter	Value (rounded)	Source
Mass m_n	939.57 MeV	CODATA [cod19]
$\Delta_m = m_n - m_p$	1.29 MeV	CODATA [cod19]
Charge q	neutral	
Spin \vec{S}	$1/2$	PDG [ZBB ⁺ 20]
Magnetic moment μ_n	-60.31 neV/T	see text
Mean lifetime τ_n	879.4 ± 0.6 s	PDG [ZBB ⁺ 20]

1.3.1 The neutron lifetime and the CKM matrix

In 1963, N. Cabibbo postulated a way to combine strangeness-changing and strangeness-conserving decay processes which are related by the Cabibbo mixing angle θ_C [Cab63]. This concept was included in the later introduced quark model (at that time only the down (d) and strange (s) quark families were known) by differing between quark mass eigenstates and weak eigenstates which are connected by a rotation matrix via

$$\begin{pmatrix} d' \\ s' \end{pmatrix} = \begin{pmatrix} \cos(\theta_C) & \sin(\theta_C) \\ -\sin(\theta_C) & \cos(\theta_C) \end{pmatrix} \begin{pmatrix} d \\ s \end{pmatrix}. \quad (1.3)$$

In 1973, M. Kobayashi and T. Maskawa extended this concept by a third quark family (bottom, b [KM73]), so that mass and weak eigenstates are now linked by the Cabibbo-Kobayashi-Maskawa (CKM) matrix via

$$\begin{pmatrix} d' \\ s' \\ b' \end{pmatrix} = \begin{pmatrix} V_{ud} & V_{us} & V_{ub} \\ V_{cd} & V_{cs} & V_{cb} \\ V_{td} & V_{ts} & V_{tb} \end{pmatrix} \begin{pmatrix} d \\ s \\ b \end{pmatrix}. \quad (1.4)$$

For neutron β decay and its parameters, only the V_{ud} element of this matrix is relevant: its squared value represents the transition probability between a down and an up quark. There exist two different types of transition depending on the initial and final spin states of neutron and proton, respectively, as shown in Fig. 1.2. Both appear with different coupling constants and therefore different strengths.

Vector or Fermi transitions, with coupling constant G_V , occur when e and $\bar{\nu}_e$ couple to a spin state of $S = 0$ (singlet state). With I the nuclear spin of proton and neutron, the transition is therefore allowed only if $\Delta I = 0$ to maintain spin conservation. If the leptons form a triplet state of $S = 1$, the transition allows for $\Delta I = 0, \pm 1$ and is mediated by axial-vector coupling (Gamow-Teller transition, coupling constant G_A) [CGH13]. V_{ud} is directly connected to Fermi transitions by the relation [IPT13]

$$G_V = G_F V_{ud}, \quad (1.5)$$

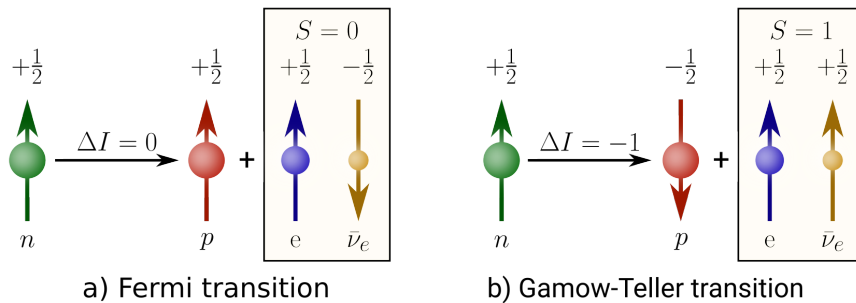


Figure 1.2: Fermi and Gamow-Teller transitions in neutron β decay. a) Fermi (vector) transition with $\Delta I = 0$ resulting in a decay proton of the same spin state as the neutron. If the total angular momentum is maintained, electron and anti-neutrino spin have to combine to a singlet state with $S = 0$. b) The same decay as a Gamow-Teller (axial-vector) transition. Electron and anti-neutrino couple to a triplet spin state with $S = 1$, therefore $\Delta I = 0, \pm 1$ are allowed.

where G_F is the well-known Fermi coupling constant, which is measured in muon decay experiments [WTP⁺11, Gor13]. Determining V_{ud} using the neutron lifetime τ_n requires the ratio between axial-vector and vector coupling constant $\lambda = G_A/G_V$. It can be calculated from the correlation coefficients of β decay asymmetry measurements.

1.3.1.1 Angular correlation coefficients in β decay

The neutron decay rate with respect to the electron energy dE_e and solid angle distributions of electron and anti-neutrino $d\Omega_e$ and $d\Omega_{\bar{\nu}_e}$, can be expressed as (adapted from [JTW57, Sch19])

$$d\Gamma \propto G_F^2 |V_{ud}|^2 dE_e d\Omega_e d\Omega_{\bar{\nu}_e} \times \left(1 + a \frac{\vec{p}_e \vec{p}_{\bar{\nu}_e}}{E_e E_{\bar{\nu}_e}} + A \frac{\vec{\sigma}_n \vec{p}_e}{E_e} + \dots \right) \quad (1.6)$$

with \vec{p}_e , $\vec{p}_{\bar{\nu}_e}$, E_e and $E_{\bar{\nu}_e}$ the electron and antineutrino momentum and energy, m_e the electron mass and $\vec{\sigma}_n$ the neutron spin. Measuring some of these quantities, the correlation coefficients a , A and so on can be calculated⁴ (cf. [MMS⁺19, BAGB⁺20, DBD⁺17, BDA⁺18]). From their results, λ is deduced via [DS11]

$$a = \frac{1 - \lambda^2}{1 + 3\lambda^2} \quad (1.7a)$$

$$A = -2 \frac{\lambda(\lambda + 1)}{1 + 3\lambda^2}. \quad (1.7b)$$

Currently the most precise result comes from the PERKEO III experiment measuring the β asymmetry parameter A [MMS⁺19], which yields

$$|\lambda| = 1.27641(56). \quad (1.8)$$

1.3.1.2 From the neutron lifetime τ_n to V_{ud}

In general, the decay rate of the neutron is given by Fermi's Golden Rule [Mar07]

$$\Gamma = \frac{2\pi}{\hbar} |\mathcal{M}_n|^2 n(E) \quad (1.9)$$

with $n(E)$ the available final density of states and the transition matrix element $|\mathcal{M}_n| \propto G_F V_{ud} / \sqrt{2}$. Including λ and V_{ud} in Γ and integrating over the available energy states, the neutron lifetime $\tau_n = \Gamma^{-1}$ is calculated. According to [ZBB⁺20], the correlation between τ_n , λ and V_{ud} is given by the master formula

$$|V_{ud}|^2 = \frac{5024.7 \text{ s}}{\tau_n (1 + 3\lambda^2) (1 + \Delta_R^V)}, \quad (1.10)$$

in which Δ_R^V accounts for transition-independent radiative corrections which have to be determined separately [MS06, HT15, SGP⁺18].

⁴For simplicity, here only two correlation coefficients are named. [DS11] gives a more detailed overview of the more than 20 correlation coefficients occurring in neutron β decay.

1.3.1.3 V_{ud} and the Standard Model of Particle Physics

The Standard Model of Particle Physics is a well-tested theory, even though it still leaves some open questions unanswered, such as the existence of dark matter or the baryon number violation, which is necessary for an excess of matter compared to anti-matter in the universe [Sak91]. In the search for so-called Physics Beyond the Standard Model (BSM Physics), the SM is tested over and over again. One method here is the unitarity of the CKM matrix.

According to the SM, there exist three quark families causing the 3×3 shape of the CKM matrix (cf. Eq. 1.4). If this theory is correct, the matrix should be unitary, which means that the sum of all transition probabilities for an initial quark state equals 1. For the first row of the CKM matrix this yields [Abe08]

$$|V_{ud}|^2 + |V_{us}|^2 + |V_{ub}|^2 = 1 - \Delta \quad (1.11)$$

with Δ the deviation from unitarity (the SM predicts $\Delta = 0$). Therefore, precise measurements of V_{ud} , V_{us} and V_{ub} are needed: V_{us} is extracted from kaon, hyperon, and tau decays [Mou17, CSW04, ABBH⁺17] and V_{ub} using semileptonic B decays [LAA⁺05, ABB⁺06]. V_{ud} is currently determined with highest precision by so-called superallowed $0^+ \rightarrow 0^+$ β decay between nuclear analog states of spin-parity $J^\pi = 0^+$ [HT18]. The beauty of this decay lies in the pure vector transition depending only on G_V . By measuring the transition strength, which is proportional to the half-life and the energy of the transition, and using Eq. 1.5, V_{ud} is calculated. This includes, however, transition-dependent nuclear and radiative corrections in addition to the transition-independent Δ_R^V . Averaging over the most precise results, [ZBB⁺20] quotes

$$|V_{ud}|^2 = \frac{0.97148(20)}{1 + \Delta_R^V} \quad (1.12)$$

with Δ_R^V the only free parameter. A recent recalculation using a dispersion relation approach resulted in $\Delta_R^V = 0.02467(22)$ [SGP⁺18], which shifted the average of V_{ud} from 0.97420(21) down to [HT15, HT18, ZBB⁺20]

$$|V_{ud}|_{0^+ \rightarrow 0^+} = 0.97370(10)_{\text{exp}}(10)_{\text{RC}}. \quad (1.13)$$

Inserting this value along with the current PDG averages for $V_{us} = 0.2245(8)$ and $V_{ub} = 3.82(24) \times 10^{-3}$ [ZBB⁺20] into Eq. 1.11 results in

$$\Delta_{0^+ \rightarrow 0^+} = 1.49(45) \times 10^{-3}. \quad (1.14)$$

This deviation from unitarity is currently explained by the PDG with a problem in V_{ud} theory, calculations in the determination of V_{us} or new physics [ZBB⁺20].

A promising alternative in the measurement of V_{ud} is thus the β decay of the neutron because it does not require any nuclear corrections [HT18]. From Eq. 1.10 follows, that by measuring τ_n and λ , and inserting Δ_R^V , V_{ud} can be calculated. Using the PDG world average of $\tau_n = 879.4 \pm 0.6$ s in combination with λ (Eq. 1.8) results in

$$|V_{ud}|_{\tau, \lambda} = 0.97339(33)_{\tau}(35)_{\lambda}(10)_{\text{RC}} \quad \text{and} \quad (1.15a)$$

$$\Delta_{\tau, \lambda} = 0.22(10) \times 10^{-2}. \quad (1.15b)$$

A comparison of the results from the superallowed $0^+ \rightarrow 0^+$ decays and neutron decay is shown in Fig. 1.3. The red square and the shaded area mark the total error of V_{ud} added in quadrature. The filled circle depicts the current uncertainty achieved with neutron β decay. As can be seen, high precision measurements of the neutron lifetime with $\Delta\tau_n = 0.1$ s are necessary to reduce the uncertainty in V_{ud} . However only a combination with $\Delta\lambda \leq 1 \times 10^{-4}$ yields a comparable result for the V_{ud} uncertainty inferred from $0^+ \rightarrow 0^+$ decays.

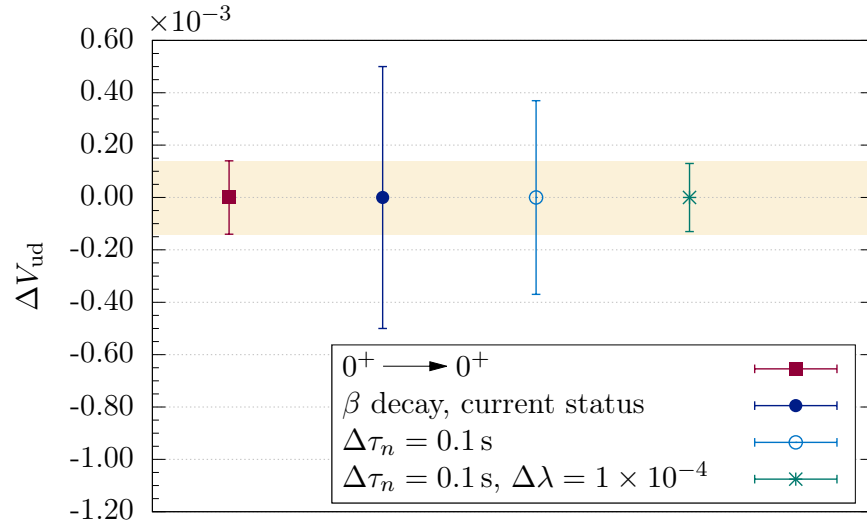


Figure 1.3: Comparison of the V_{ud} uncertainties inferred from superallowed $0^+ \rightarrow 0^+$ decays (red marker and shaded area) and neutron β decay (blue, filled circle) using the PDG average $\tau_n = 879.4(6)$ s [ZBB⁺20] and $|\lambda| = 1.27641(56)$ [MMS⁺19]. So far, neutron β decay cannot compete with the superallowed decays. High precision measurements of τ_n with $\Delta\tau_n = 0.1$ s are necessary (blue, open circle) but only a combination with an improved determination of λ with $\Delta\lambda \leq 1 \times 10^{-4}$ results in a V_{ud} uncertainty comparable to the $0^+ \rightarrow 0^+$ decays (turquoise cross).

1.3.2 The neutron lifetime and big bang nucleosynthesis

The neutron lifetime is not only an important quantity in particle physics but also in cosmology, where it is used to test and improve the theory describing the very early universe: the big bang nucleosynthesis (BBN) model. One feature of this model is the calculation of the primordial abundances of the light nuclei from ^1H up to ^7Li [CFOY16, Gam46, ABG48]⁵.

1.3.2.1 From a hot plasma to primordial nuclei

When the universe was around $20 \mu\text{s}$ old [FKL⁺12], it consisted only of a hot plasma full of particles, such as neutrons, protons, electrons and neutrinos, as well as photons, which

⁵The code called 'Public **A**lgorithm **E**valuating the **N**ucleosynthesis of **P**rimordial **E**lements (PArthENoPE)' is published by the Naples Astroparticle Group and is publicly available under <http://parthenope.na.infn.it/>

were in thermal equilibrium. In fact, the temperature was high enough for reactions like



to occur in both directions and thus keeping the ratio between neutrons and protons constant [BNT99]. In equilibrium, this ratio is given by the Boltzmann factor

$$\frac{n}{p} = \exp\left(\frac{-\Delta_m}{T}\right) \quad (1.17)$$

with Δ_m the neutron-to-proton mass difference (see Tab. 1.1) and T the energy equivalent temperature [MKS05]. However, the universe expanded rapidly and cooled with a rate $\propto T^2$. The weak interaction rate on the other hand decreased much faster ($\propto T^5$) [CFOY16] and therefore weak reactions fell out of thermal equilibrium as soon as the so-called freeze-out condition

$$G_F^2 T^5 \approx \Gamma(T_f) = H(T_f) \approx G_N^{1/2} T^2 \quad (1.18)$$

was met. Here, Γ is the weak interaction rate (cf. Eq. 1.9), H is the Hubble constant, T_f is the freeze-out temperature, and G_F and G_N are the Fermi and Newton's gravitational constant, respectively. According to [CFOY16], T_f calculates to ~ 0.8 MeV and thus, using Eq. 1.17, $n/p \simeq 1/5$. At this point, the only energetically possible weak reaction left was neutron β decay (from left to right in Eq. 1.16c).

However, nucleosynthesis did not begin directly: The binding energy of ${}^2\text{H}$, the first nucleus in the reaction chain, is relatively small ($E_B = 2.2$ MeV) but the photon-to-baryon ratio $\eta^{-1} = n_\gamma/n_B \sim 10^9$ was still so large, that any nucleus was readily destroyed directly after formation [MKS05, CFOY16]. This is also known as the deuterium bottleneck. Only when the temperature was low enough to satisfy $\eta^{-1} \exp(-E_B/T) \sim 1$ did nucleosynthesis begin, which was the case at around 200 s [EMMP99, MKS05]. As this time is on the order of the neutron lifetime, a significant amount of neutrons had already decayed when the deuterium bottleneck broke, so that n/p had by then dropped to $1/7$ [CFOY16].

1.3.2.2 The formation of light elements in BBN

Various processes lead to the formation of ${}^4\text{He}$, one of which is shown in Fig. 1.4 including two ${}^2\text{H}$ nuclei and γ -emission. It is assumed that all deuterium nuclei finally ended up in ${}^4\text{He}$ [EMMP99], so that using $n/p \simeq 1/7$, the theoretical ${}^4\text{He}$ mass fraction (in literature referred to as Y_p) compared to ${}^1\text{H}$ is calculated as

$$Y_p = \frac{2(n/p)}{1 + (n/p)} \approx 0.25 \quad (1.19)$$

by simply counting the number of neutrons and protons needed to form ${}^4\text{He}$ and ${}^1\text{H}$. Other nuclei, such as ${}^3\text{H}$, ${}^3\text{He}$, ${}^6\text{Li}$, ${}^7\text{Li}$ and ${}^7\text{Be}$ were formed in a much smaller fraction (e.g. the ${}^7\text{Li}/{}^1\text{H}$ -ratio is stated as $1.6(3) \times 10^{-10}$ [ZBB⁺20]), of which ${}^3\text{H}$ and ${}^7\text{Be}$ are unstable,

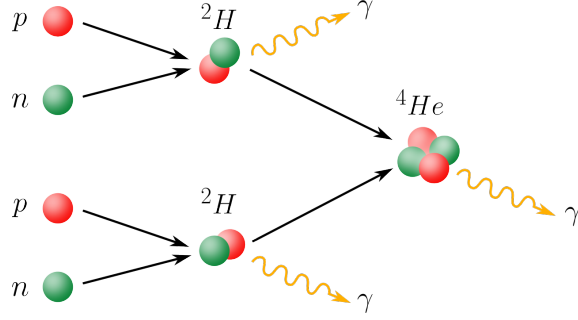


Figure 1.4: An example of ${}^4\text{He}$ synthesis involving two deuterons. A proton and a neutron form a ${}^2\text{H}$ nucleus (deuteron) under emission of a photon γ . Two ${}^2\text{H}$ nuclei then combine to form the ${}^4\text{He}$ nucleus, again under photoemission. Various other processes involving ${}^3\text{H}$ or ${}^3\text{He}$ nuclei do also occur.

so that they decayed with relatively short half-lives⁶ after nucleosynthesis had stopped. Heavier elements were not produced as there exist no stable nuclei with $A = 5$ or $A = 8$ which would be created by $n+{}^4\text{He}$, $p+{}^4\text{He}$ or ${}^4\text{He}+{}^4\text{He}$ reactions [THH⁺18].

The neutron lifetime plays an important role in the BBN model in two ways [LT99]: 1) It scales the weak interaction rate given by Eqs. 1.9 and 1.10 and therefore influences the neutron-to-proton ratio at freeze-out, and 2) due to neutrons decaying during the time of the deuterium bottleneck, the ratio when nucleosynthesis begins depends directly on the neutron lifetime. According to [LT99], the sensitivity of Y_P with respect to the weak reaction rate $\Gamma = 1/\tau_n$ is given as

$$\frac{\delta Y_P}{Y_P} \simeq -0.8 \frac{\delta \Gamma}{\Gamma}. \quad (1.20)$$

From comparisons in [CFOY16] follows, that from all parameters of the BBN model, Y_P is thus mostly sensitive to the neutron lifetime. A prediction on the 0.1% level would require an uncertainty in the neutron lifetime of $\Delta\tau_n = 1$ s or less.

The primordial helium abundance can be determined either experimentally by spectroscopic observations of galactic nebulae, or theoretically from fluctuations in the cosmic microwave background (CMB) in combination with the BBN model. Fig. 1.5 gives an overview over recent measurements [ITG14, AOS15, PPL16, FTD⁺18, VPPS19], the line marks the current status of the BBN model $Y_P = 0.2469(4)$ [AAA⁺20] (Planck collaboration)⁷. Apart from the 2014 result ([VPPS19] suspects unaccounted systematic uncertainties), all results agree with each other within errors. However, the experimental values are currently measured with a precision of $\mathcal{O}(1\%)$ whereas theoretical predictions range down to the 0.1% level already. This should give motivation to experimentalists to increase the precision of their measurements in the future. Nevertheless, because of the high sensitivity to the neutron lifetime, the theoretical prediction of Y_P can be further improved by high precision measurements of τ_n .

⁶Tritium (${}^3\text{H}$) decays with a half-life of $t_{1/2} = 12.32\text{y}$ and ${}^7\text{Be}$ with $t_{1/2} = 53.22\text{d}$ (NuDat 2.8)

⁷The Planck collaboration quotes two results for Y_P which were calculated with different algorithms and are consistent within errors. Here, the mean value was calculated.

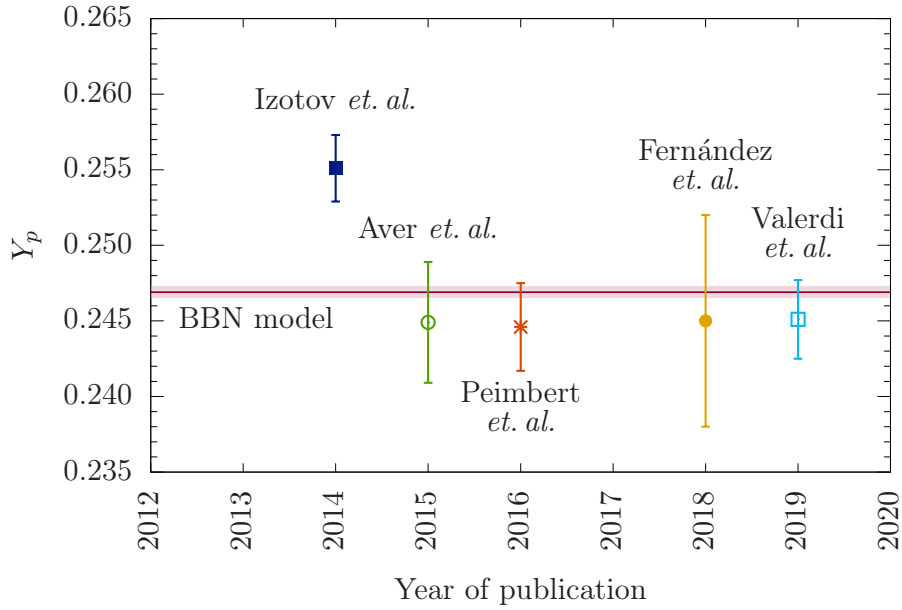


Figure 1.5: Recent experimental determinations of the primordial ${}^4\text{He}$ abundance (markers) and the prediction by the BBN model using parameters obtained by CMB measurements and the neutron lifetime (red line). The predicted value is $Y_P = 0.2469(4)$ as the calculated mean of results in [AAA⁺20]. The experimental results were taken from [ITG14, AOS15, PPL16, FTD⁺18, VPPS19].

1.4 Summary

In this section, the discovery and fundamental properties of the neutron were presented. The importance of the precise measurement of the neutron lifetime was emphasised using two examples from particle and astroparticle physics. The following chapter will give an overview over different experimental methods to measure τ_n with high precision.

Chapter 2

Neutron lifetime experiments

After having seen, why the free neutron lifetime is an important quantity in modern physics, this chapter will take a closer look at the techniques used today to measure the neutron lifetime and how the results improved over the last decades. Before, however, we will have a closer look at how neutrons interact.

2.1 Neutron interactions

The neutron interacts via all four fundamental forces, which is illustrated in Fig. 2.1.

2.1.1 Weak interaction

The weak interaction is responsible for the β decay of free neutrons according to



and has been introduced in Ch. 1 already.

2.1.2 Strong interaction

We consider a material wall with an atomic distance d_a and the neutron as a material wave at wavelength λ_n . If the neutron is slow enough, i.e. $\lambda_n \gg d_a$, the interaction with the wall can be described by an effective potential

$$U = V_F - iW \quad (2.2)$$

similar to a wave scattering on a quantum mechanical wall (a thorough derivation is given in [GRL91]). Here, V_F is the so-called Fermi potential and accounts for reflections on the wall, whereas W is a small absorbing part¹. V_F can further be written as

$$V_F = \frac{2\pi\hbar^2}{m_n} Na \quad (2.3)$$

with m_n the neutron mass, N the number density and a the coherent scattering length of the wall material [GRL91]. So far, the material with the highest Fermi potential known is ^{58}Ni with $V_F = 335 \text{ neV}$ (further values are listed in Tab. B.1).

¹Typical values for the absorption probability $f = W/V_F$ are at $\mathcal{O}(10^{-5})$ [GRL91], which may appear small but are an issue in bottle experiments using material walls

If neutrons impinge on the wall under a small incidence angle ϕ_n , they are reflected in case $E_{\text{kin}} \sin^2(\phi_n) \leq V_F$. If the total kinetic energy is smaller than the Fermi potential, $E_{\text{kin}} \leq V_F$, the neutrons are fully reflected under all incidence angles. They can be stored for long times in suitable storage vessels and are termed *ultracold neutrons* (UCN).

2.1.3 Gravitational interaction

Due to their mass, neutrons interact with Earth's gravitational potential, which means that they are accelerated while flying downwards. Using classical Newton mechanics

$$V_{\text{grav}}(r) = \int_{R_E}^{R_E+h} G_N \frac{M_E m_n}{r^2} \quad (2.4)$$

with Newton's gravitational constant G_N , the neutron mass m_n , and Earth's mass M_E and radius R_E , the kinetic energy gain per meter is calculated as $V_{\text{grav}} = 102.4 \text{ neV/m}$. This means in return, that neutrons lose kinetic energy when flying upwards, and - with V_{grav} on the same order of magnitude as the Fermi potential of many materials - neutrons can be stored using a mixture of material wall and gravitational confinement.

2.1.4 Electromagnetic interaction

The neutron's magnetic moment (cf. Eq. 1.1) interacts with magnetic fields according to

$$V_{\text{magn}} = -\vec{\mu}_n \cdot \vec{B} \approx \pm 60.31 \text{ neV/T} \cdot |\vec{B}| \quad (2.5)$$

with V_{magn} the magnetic potential and \vec{B} the local magnetic flux density (for simplicity, in this work \vec{B} is called the magnetic field²). The Stern-Gerlach force between the neutron and the magnetic field can be written as

$$\vec{F}_{\text{magn}} = -\vec{\nabla} V_{\text{magn}} = \pm |\vec{\mu}_n| \vec{\nabla} |\vec{B}|. \quad (2.6)$$

Both equations are adapted from [GRL91]. With the magnetic moment anti-parallel to the spin ($\vec{\mu} \uparrow \downarrow \vec{S}$) and the spin again being either oriented along or opposite the magnetic field \vec{B} , two cases are distinguished:

1. An anti-parallel orientation of the spin with respect to \vec{B} requires $\vec{\mu}_n \uparrow \uparrow \vec{B}$, which due to the minus sign in Eq. 2.5 leads to a potential minimum at the magnetic field maximum. Consequently, the Stern-Gerlach force (cf. Eq. 2.6) accelerates the neutron into the high magnetic field. Such neutrons are termed *high-field seekers* (HFS).
2. The parallel orientation of the spin to \vec{B} leads to the opposite situation ($\vec{\mu}_n \downarrow \uparrow \vec{B}$), which means that the magnetic field minimum is also the potential minimum and that the Stern-Gerlach force is repulsive at positive field gradients. Hence, being reflected from high magnetic fields, the neutrons are called *low-field seekers* (LFS).

Using this property, surrounding LFS with high magnetic fields, leads to the neutrons being unable to leave if their total kinetic energy is less than V_{magn} .

²The magnetic field, usually called H , is connected to the magnetic flux density B and the material's magnetisation M via $H = \frac{B}{\mu_r \mu_0} - M$.

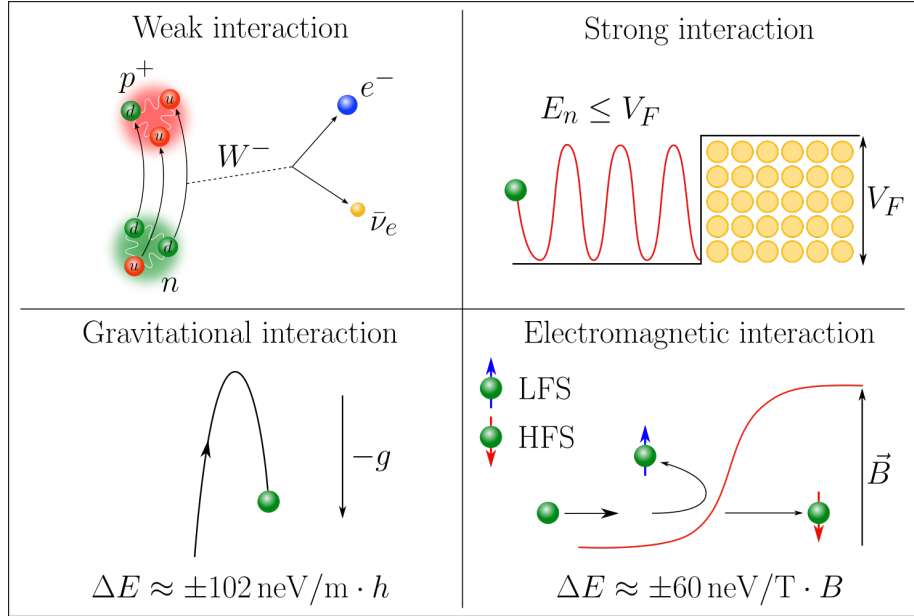


Figure 2.1: Illustration of the four neutron interaction types. Top left: Neutron β decay caused by the weak interaction. Top right: A low energetic neutron is reflected on bulk material, which is regarded as potential step corresponding to its Fermi potential V_F . Bottom left: The neutron is slowed down while flying upwards in Earth's gravitational potential and accelerated afterwards. Bottom right: Depending on the neutron spin orientation, HFS ($\vec{S} \downarrow \uparrow \vec{B}$) are accelerated into high magnetic fields whereas LFS ($\vec{S} \uparrow \uparrow \vec{B}$) are reflected.

2.2 Introduction to neutron lifetime experiments

Experiments for measuring the free neutron lifetime have been done since the 1940s. In the beginning, the only type of measurement was the beam method, because neutron beams from nuclear reactors were available decades before the first UCN sources were built. This section will give a short introduction into beam and bottle type experiments (of which the latter are subdivided into storage using material walls and storage using magnetic fields) along with a brief historical overview over the measurements and techniques developed so far.

2.2.1 Beam experiments

Beam experiments measure the charged decay products emanating from a cold neutron beam in a well-defined volume and relate them to the total number of neutrons in the beam. An exponential decay can be written as

$$\frac{dN}{dt} = -\frac{N}{\tau_n} \quad (2.7)$$

so that identifying dN/dt with the number of charged decay particles (either p or e^-) and N with the total number of neutrons in the beam, the neutron lifetime τ_n can be extracted.

Fig. 2.2 shows a schematic view of a beam lifetime experiment. A cold neutron beam coming from the left traverses a well-known decay volume V_D and finally reaches a neutron

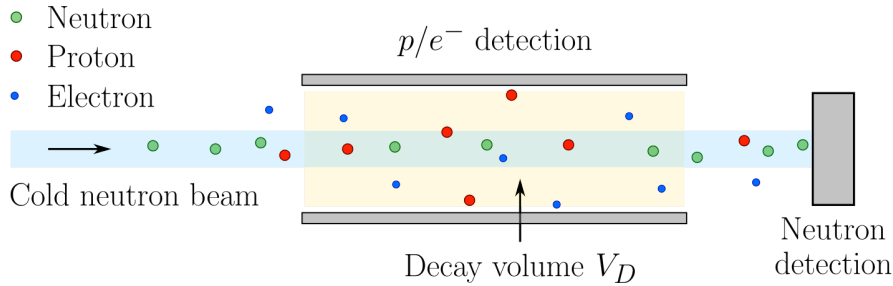


Figure 2.2: Schematic setup of a beam type neutron lifetime experiment. A cold neutron beam (blue area, individual particles in green) traverses a well-known decay volume (yellow area) and reaches a neutron detector. The charged particles (red: protons, blue: electrons) from neutrons that decayed inside the decay volume are measured by a surrounding detector.

detector. Typically, the detector consists of a material with high neutron absorption cross section and a short decay time after neutron capture (commonly used materials are ^3He , ^6Li and ^{10}B). The charged reaction products from this capture are detected by additional sensors afterwards. The measurement of the charged particles from neutron β decay varies between the different experiments, however, a common technique in early experiments was to surround the neutron beam with charged particle detectors [CNB⁺72] or electrostatic fields for charged particle collection [Rob51, BKP⁺78] and thus define the decay volume accordingly.

The charged particles - let's say the protons - and neutrons are detected at a rate R_p and R_n with efficiencies ε_p and ε_n , respectively. Following the calculations in [WG11], the neutron lifetime is then given by

$$\tau_n \propto \left(\frac{R_n}{R_p} \right) \left(\frac{\varepsilon_p}{\varepsilon_n} \right). \quad (2.8)$$

The difficulty with this method lies in the precise determination of 1) the absolute number of decay products, 2) the absolute neutron flux, and 3) the size of the decay volume itself. Furthermore, the production of a continuous neutron beam goes along with a high radiative background.

By storing the decay protons in a quasi-Penning trap and flushing them towards a detector in brief intervals, Byrnes *et. al.* were the first to separate the proton counting from the background ($\tau_n = 889.2 \pm 4.8$ s) [BDS⁺90, BD96]. A similar technique was used in the BL2 experiment at the National Institute of Standards and Technology (NIST) with the additional possibility to alter the length of the Penning trap L and measure R_n/R_p as a function of L . This method could handle two of the three mentioned difficulties, however the absolute measurement of neutrons was and still is one of the main challenges: It requires a precise knowledge of the neutron flux Φ_n , the detector solid angle Ω as well as the areal density of the neutron absorbing deposit of the detector and its absorption cross section σ_n . Especially, the last two parameters are a large contribution to the systematic error of the BL2 result of $\tau_n = 886.6 \pm 1.2(\text{stat}) \pm 3.2(\text{sys})$ s [NDG⁺05]. A re-calibration of the neutron detector with a direct measurement of the detection efficiency ε_n improved the systematic uncertainty to an updated result of $\tau_n = 887.7 \pm 1.2(\text{stat}) \pm 1.9(\text{sys})$ s [YDG⁺13].

2.2.2 Bottle experiments

In contrast to the beam experiments, which are counting the number of neutrons that decayed, the bottle experiments count the surviving neutrons. Ultracold neutrons are confined in a storage vessel for a certain storage time t_s during which they decay, and the remaining neutrons are detected afterwards. Under ideal conditions, the measured number of neutrons $N(t_s)$ depending on the storage time follows an exponential decay law according to

$$N(t_s) = N_0 \cdot \exp(-t_s/\tau) \quad (2.9)$$

with τ corresponding to the neutron lifetime τ_n . Experimentally, at least two different storage times have to be measured, a short t_1 and a longer t_2 on the order of τ_n . Along with the ratio of the remaining neutrons $N(t_1)/N(t_2)$ at these times, the neutron lifetime can be extracted as

$$\tau = \frac{t_2 - t_1}{\ln [N(t_1)/N(t_2)]}. \quad (2.10)$$

Bottle type lifetime experiments have two major advantages over the beam lifetime experiments: $N(t_1)$ and $N(t_2)$ are relative measurements done with the same detector, so that the detection efficiencies ε_n cancel. Furthermore, UCN are produced only at the beginning of each experimental run, which reduces the radiation background to a minimum unlike the beam experiments, where a continuously running cold neutron beam is needed. However, in order to compare the relative measurements, equal initial conditions are required, so that the results have to be normalised.

2.2.3 Material wall storage

The measurement principle is shown schematically by means of Fig. 2.3. Initially, the left and right shutters are open, the bottom shutter is closed. Ultracold neutrons are transported from their source towards the storage vessel, in which they are trapped by closing the right shutter after the filling process has finished. During the subsequent storage time, the neutrons decay. Afterwards, by opening the right and bottom shutters towards the detector (while the left side shutter is closed), the remaining neutrons are counted.

In an ideal storage experiment, the only loss mechanism would be β decay and thus $\tau = \tau_n$. However, using material wall storage, additional loss channels have to be taken into account, which arise from the interaction of the neutrons with the wall material:

1. Absorption or inelastic upscattering by impurities on the surface [Wie18],
2. So-called *thermal upscattering* by phonon interaction between the wall atoms and the neutrons [WG11],
3. Scattering on residual gas (which has to be considered in all neutron lifetime experiments),
4. Gaps and slits in the storage vessel through which the neutrons can escape, and

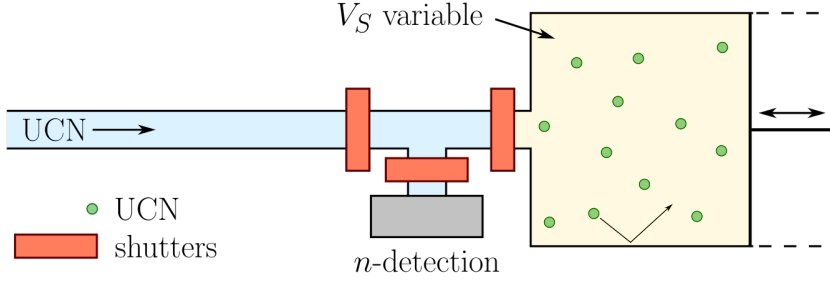


Figure 2.3: Schematic setup of an example bottle type neutron lifetime experiment using wall storage. UCN coming from the left are admitted to a storage vessel with material walls and variable size (yellow area). The shutters in the middle (orange) are used to guide the neutrons to either storage volume or detector (grey), and to close the storage vessel during the storage period.

5. Marginally trapped neutrons with energies higher than the wall potential, but which are reflected under small incident angles. They can be stored for hundreds of seconds but leave the trap sooner or later and have to be removed before the storage time begins (this process is also called 'cleaning').

These loss mechanisms combined with the neutron lifetime result in an effective, experiment dependent storage time

$$\tau_{\text{st}}^{-1} = \tau_n^{-1} + \tau_{\text{abs}}^{-1} + \tau_{\text{up}}^{-1} + \tau_{\text{trap}}^{-1} + \tau_{\text{marg}}^{-1} + \tau_{\text{other}}^{-1}. \quad (2.11)$$

In order to extract τ_n from the measured storage time, the additional decay times have to be corrected for. In turn, the smaller the loss mechanisms, the smaller the corrections, which motivates a proper preparation of the storage vessel: Common techniques are wall coatings with low neutron absorption cross sections and relatively high Fermi potential [MAB⁺89], or cooling the walls to reduce thermal upscattering [MBM⁺93]. As the loss mechanisms are proportional to the number of wall collisions, the size of V_S (and therefore the surface-to-volume ratio of the storage vessel) is often varied. By measuring $\tau_{\text{st}} = \tau_{\text{st}}(V_S)$ and extrapolating to zero wall collisions ($\tau(V_S = \infty)$), the only remaining decay constant is the neutron lifetime τ_n . A good storage vessel is characterised by a storage time constant $\tau_{\text{st}} \sim \tau_n$, which means that loss mechanisms and thus corrections required for the measured result are small.

Since the first bottle lifetime experiments in the 1970s [KKMT80] ($\mathcal{O}(\Delta\tau_n) = 10$ s), corrections and systematic uncertainties have become ever smaller [MAB⁺89, MBM⁺93, PVSG10, ABC⁺15]. The most precise measurements so far, with $\Delta\tau_{n,\text{sys}} < 1$ s, come from the gravitational trap (Gravitrapp) operated by A. Serebrov *et. al.*: It uses a Fomblin[®] oil covered storage vessel ($V_F = 106.5$ neV), which is open at the top, so that here the neutrons are confined by gravity. By tilting the storage vessel, the UCN spectrum is cleaned and marginally trapped neutrons are removed [SVK⁺05] ($\tau_n = 878.5 \pm 0.7_{\text{stat}} \pm 0.3_{\text{sys}}$ s). A larger version of the experiment including a larger storage vessel and a titanium absorber for spectrum cleaning resulted in $\tau_n = 881.5 \pm 0.7_{\text{stat}} \pm 0.6_{\text{sys}}$ s with the systematic error dominated by uncertainties in the wall coatings [SKF⁺18].

2.2.4 Magnetic storage

One way to remove the loss mechanisms associated with wall collisions is using magnetic storage of UCN. The measurement principle is similar to the storage experiments using material walls, only that now the 'walls' of the storage vessel consist of high magnetic fields, trapping neutrons in the low-field seeking spin state (cf. Ch. 2.1.4). The beauty of this technique is that there exist no losses due to neutrons interacting with wall material and therefore no extrapolations with respect to the size of the storage volume have to be made.

However, magnetic storage is not entirely free of neutron loss mechanisms, so that great care has to be taken in the magnetic field design:

1. Non-adiabaticity: Neutrons in a magnetic field precess at the Larmor frequency ω_0 (cf. Eq. 3.1). If the magnetic field changes at a rate on the order of ω_0 or even faster, the neutron spin loses its alignment with the magnetic field. This can result in non-adiabatic spin flips, which transform the neutrons to HFS, so that they will leave the trap. The same is true at zero field points, so that $|\vec{B}| \neq 0$ has to be fulfilled in the entire trap. An introduction into adiabaticity is given in Ch. 4.
2. Marginally trapped neutrons: Similar to the storage using material walls, higher energetic neutrons can be reflected on the magnetic fields under small incident angles. They can therefore fly on stable orbits for long times ($\mathcal{O}(t) = 100$ s) until they eventually escape from the trap. This is a problem, because at short storage times, they are included in the number of surviving neutrons, whereas at long storage times they are not, so that they have to be removed from the trap in advance. Using an asymmetric magnetic field design helps to form chaotic flight trajectories, which increases the probability of large, close to perpendicular incident angles. This leads to a fast decrease in the number of neutrons with ($E > V_{\text{pot}}$), leaving the focus on neutrons with energies close to the trap potential ($E \gtrsim V_{\text{pot}}$). They have to be removed ('cleaned') from the trap actively because otherwise their escape time would still be too long for short storage time measurements. Any cleaning procedure, however, requires chaotic trajectories as well, so that only a combination of asymmetric magnetic field design and active cleaning can sufficiently remove higher energetic neutrons from the trap.

Two experiments using magnetic storage have published their results so far, both using a magneto-gravitational trap. While V. F. Ezhov *et al.* still include a relatively large correction for spin flipped neutrons of 3.7 s (their result is $\tau_n = 878.3 \pm 1.6_{\text{stat}} \pm 1.0_{\text{sys}}$ s [EAB18]), the UCN τ experiment does not require any corrections at all. It stores UCN magnetically by an asymmetrical cup-shaped array of permanent magnets in order to eliminate closed neutron trajectories; towards the top, the UCN are confined by gravity. An additional holding field maintains the spin polarisation during storage [SAB⁺14]. With $\tau_n = 877.75 \pm 0.28_{\text{stat}} (+0.22 / -0.16)_{\text{sys}}$ s, this experiment yields the highest precision in the determination of the neutron lifetime so far [GFCW⁺21].

2.2.5 The neutron lifetime puzzle

After this brief overview over the two lifetime measurement methods (three, if material and magnetic wall storage are counted separately), Fig. 2.4 shows the relevant experimental results since the year 2005 in comparison. The red data points mark beam experiments,

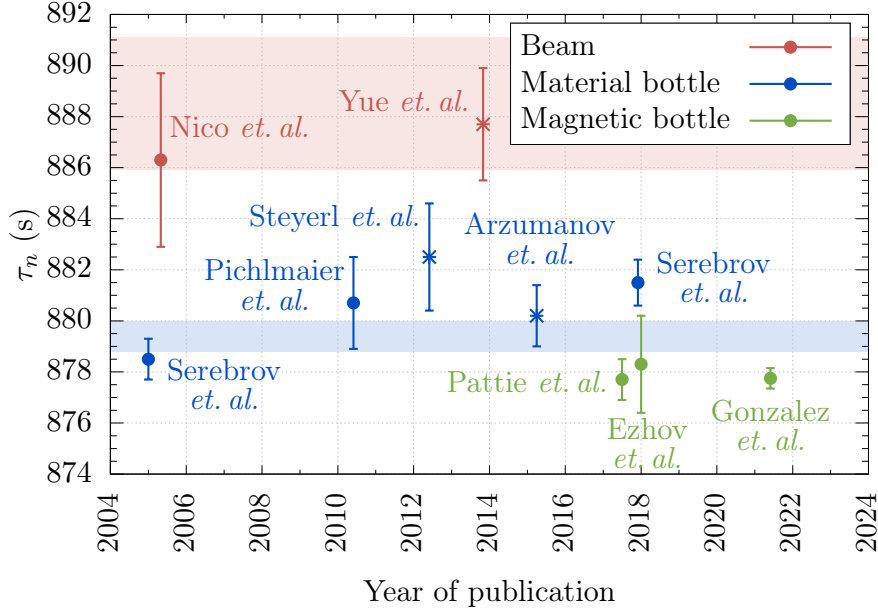


Figure 2.4: Overview of neutron lifetime results obtained with the beam (red data points) and bottle method (blue: material wall storage; green: magnetic storage). The red shaded area marks the weighted average of the [BD96] and [YDG⁺13] result of $\bar{\tau}_{\text{beam}} = 888.0 \pm 2.1$ s. The current PDG average includes all depicted bottle experiments except for the result by Gonzalez *et. al.* and is stated as $\tau_{\text{bottle, PDG}} = 879.4 \pm 0.6$ s [ZBB⁺20] (blue shaded area). The two measurement techniques yield results, which deviate by 3.9σ . Data taken from [SVK⁺05, NDG⁺05, PVSG10, SPK⁺12, YDG⁺13, ABC⁺15, PCCW⁺18, SKF⁺18, EAB18, GFCW⁺21].

stars represent reanalysed results. The red shaded area corresponds to the weighted average of $\bar{\tau}_{\text{beam}} = 888.0 \pm 2.1$ s [YDG⁺13]. All other data points in the plot are the bottle lifetime experiments, which are (except for the result by Gonzalez *et. al.*) currently included in the PDG average of $\tau_{\text{bottle, PDG}} = 879.4 \pm 0.6$ s [ZBB⁺20], with material wall storage in blue and magnetic storage in green. Even though τ_n is measured precisely with both techniques individually (0.3% for the beam and 0.07% for the bottle method), the average results differ by 3.9σ for which there exist no explanations so far and which is therefore also called the ‘neutron lifetime puzzle’ [Pau09].

One possible explanation for this discrepancy could be systematic effects in beam experiments concerning scattering or charge exchange processes between decay protons and residual gas, which were unaccounted for or underestimated so far [BW19, SCK⁺21]. Both could lead to proton losses before they would be detected and thus the measured neutron lifetime would result in a larger value.

Another option could be the neutron decaying by channels still unknown, so that the total neutron lifetime would split into the β and an unknown decay part \mathcal{X} according to

$$\tau_n^{-1} = \tau_\beta^{-1} + \tau_{\mathcal{X}}^{-1}. \quad (2.12)$$

Bottle lifetime experiments measure those neutrons that have not decayed by any channel,

which would then include unknown decays, whereas beam experiments measure the products of β decay only. Again, the neutron lifetime inferred from beam experiments would thus be larger than the result from bottle experiments.

In 2018, a channel was postulated with the neutron decaying into one or more dark particles, such as dark photons [FG18]. The exact realisation of such a decay could, however, be excluded already a short time afterwards [BBGS18, TBB⁺18, KJM⁺19]. Also neutron to mirror-neutron ($n - n'$) oscillations have been proposed, which would result in a smaller measured bottle lifetime [Ber19], but so far only upper limits were measured [BBD⁺07, BBG⁺18, AAB⁺21] to which $n - n'$ oscillations can be excluded.

A further investigation of the neutron lifetime puzzle therefore requires measurements of τ_n with high precision, but also new methods with different systematic effects that in turn have to be well understood [WG11]. Bottle lifetime experiments using magnetic storage are thus a valuable approach, because their systematic effects differ substantially from beam and bottle experiments using wall storage so far.

2.2.6 Neutron lifetime experiments: Current status and prospects

The beam lifetime experiment BL2 is currently taking data to improve the overall uncertainty yielded in [YDG⁺13] to $\Delta\tau = 1$ s [Sau19]. The new experiment BL3 will be used to further investigate systematic effects [WFG⁺16] and aims at $\Delta\tau_{\text{sys}} \sim 0.3$ s [Sau19]. Furthermore, two new beam lifetime experiments are currently commissioned, one at J-PARC with a goal of $\Delta\tau = 1$ s [NHI⁺19], and UCNProBe at Los Alamos National Laboratory, measuring the proton branching ratio in neutron β decay [TCC⁺19] (target precision 0.1 %).

Gravitrap as well as UCN τ are currently taking data to reduce their uncertainties, the experiment by Ezhov is upgraded [Sau19]. In addition, new experiments are planned, such as the Tau2 experiment, which is based on UCN τ , but will replace the array of permanent magnets by superconducting coils to allow for a higher energy acceptance in the trap [SU19].

Chapter 3

The lifetime experiment τ SPECT

After having shown the importance of precision measurements of the neutron lifetime and the advantage of magnetic storage of UCN over storage using bulk material, the magnetic storage lifetime experiment τ SPECT is presented. The first section deals with the storage principle and the experimental setup. Afterwards the development of critical components in the experiment are discussed, which lead to the first purely magnetic storage curve.

3.1 Magnetic storage in τ SPECT

The τ SPECT experiment is located at the pulsed UCN source D at the TRIGA reactor in Mainz [KSB⁺14, KRR⁺17, Kah20] (cf. Ch. A.1). Its key feature is a three-dimensional magnetic trap for spin-polarised UCN in the low-field seeking state, which is defined by the superposition of a longitudinal and a radial magnetic field as shown in Fig. 3.1.

The longitudinal field called B_0 is produced by superconducting coils and was originally used in the a SPECT experiment, measuring the correlation coefficient a in neutron β decay [BAGB⁺20] (cf. Ch. 1.3.1.1). It consists of two magnetic field peaks and a low field region in between - the so-called 'holding field' - to maintain the spin state during storage (cf. Ch. 2.2.4), and is adjusted in magnitude by the current I_{main} flowing through the coils. The radial field is generated by an octupole made from permanent magnets (storage octupole, SO). Its magnetic field increases with r^3 to $B_{\text{oct}} \gtrsim 780 \text{ mT} = B_{\text{oct}}^{\text{min}}$ at the surface of the octupole¹ [Haa16]. The superposition of the two magnetic fields results in a low field region, where LFS can be stored. If I_{main} is set high enough so that at the edge of the magnetic trap $B_0 \geq B_{\text{oct}}^{\text{min}}$, the octupole field limits the trap potential and the maximum storable neutron energy calculates to $E_n^{\text{max}} = V_{\text{pot}} = \mu_n B_{\text{oct}}^{\text{min}} = 47 \text{ neV}$.

This is shown in Fig. 3.2 for $I_{\text{main}} = 33 \text{ A}$. The positions where $B_0(z, I_{\text{main}}) = B_{\text{oct}}^{\text{min}}$ represent the outer edges of the storage volume in longitudinal direction. Given the storage octupole radius $r = 54 \text{ mm}$ (cf. Ch. 3.2.1), the maximum storage volume then calculates to $V_{\text{st}}^{\text{max}} = 10.67 \text{ L}$. However, only neutrons with the highest energies reach the outer edges and thus fill the entire trap. For lower energetic neutrons, the storage volume is reduced depending on the neutron energy and the shape of the magnetic fields, which define the accessible region.

¹The measurements were done by J. Haack on a radius of $r = 51.5 \text{ mm}$, yielding $B_{\text{oct}}^{\text{min}} \simeq 695 \text{ mT}$. This value is extrapolated to $B_{\text{oct}}^{\text{min}}(r = 53.5 \text{ mm}) \simeq 780 \text{ mT}$ close to the octupole surface.

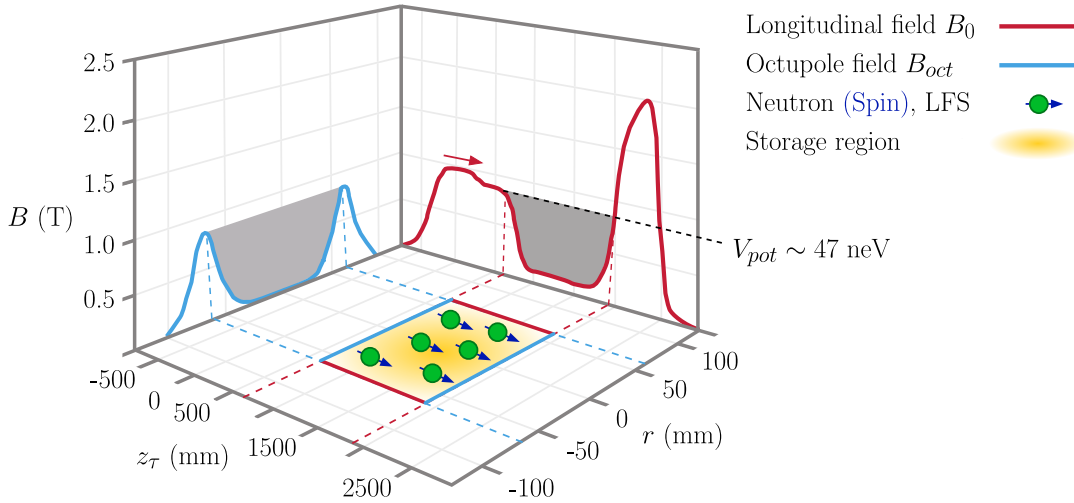


Figure 3.1: Field superposition used for magnetic storage of UCN. An adjustable longitudinal magnetic field (red line, the direction is marked by the red arrow) is produced by superconducting coils, its double-peak shape originates from requirements of the a SPECT experiment. The radial field (blue) is produced by an octupole magnet with $B_{\text{oct}} \gtrsim 780$ mT. The UCN (LFS) are trapped magnetically inside the low field region in the middle of the field superposition (yellow area). Assuming the trap depth limited by the octupole field, the maximum storable neutron energy calculates to $E_n^{\text{max}} = V_{\text{pot}} = 47$ neV. Figure adapted from [Kar17].

Ramping up B_0 to the target current or down to 0 A takes roughly 30 min, so that the trap cannot be filled with UCN or emptied after storage by briefly lowering the magnetic potential. Instead, special filling and emptying processes are required, which are presented in the next section.

3.1.1 Experimental setup

A schematics of the main components in τ SPECT is shown in Fig. 3.3: The experiment is housed inside a cryostat, which is required for cooling the superconducting coils down to below their critical temperature ($T_{C, \text{NbTi}} = 9.2$ K [PKQ⁺19]). Neutrons from the UCN source enter the experiment through a shutter from the left and are transported by a double tube beamline made from stainless steel and quartz glass. As soon as they reach the longitudinal magnetic field, they get spin polarised: High-field seeking UCN are accelerated, whereas LFS are slowed down. If their kinetic energy $E_{\text{kin},0}$ is smaller than the magnetic potential of the first field peak, they are reflected (with $B_0(33 \text{ A}) = 1.020$ T, this corresponds to $V_{\text{pot}} = 61.52$ neV). This means, that only LFS with energies above the first peak potential and HFS reach the trap, which are both unstorable.

Therefore it is necessary to convert the low energetic HFS to the low-field seeking state after they passed the magnetic field peak (cf. Ch. 4.2.1 for the energies involved in this process). This is done by the spin flipping unit (SFU), which consists of a spin flipper (cf. Ch. 3.3.1) and an additional magnetic octupole to reduce the storage octupole field around

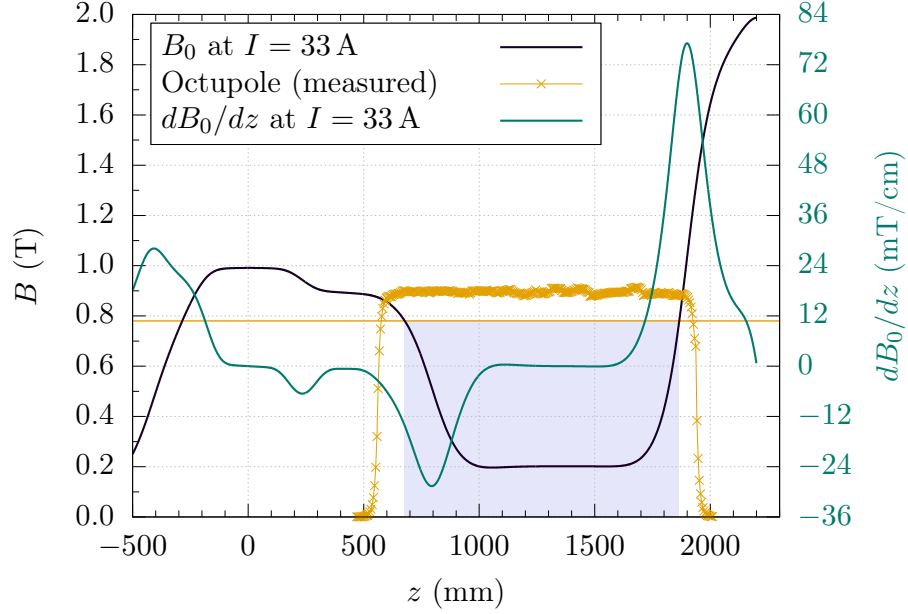


Figure 3.2: Field shape of $B_0(z)$ at $I_{\text{main}} = 33$ A (black solid line) and B_{oct} along the z -axis. The nominal position of the octupole is between $z = 570$ mm and 1950 mm. The original measurement data of the octupole field is re-scaled to $r = 53.5$ mm (yellow markers, only one data set shown), the minimum field $B_{\text{oct},\text{min}} = 780$ mT is indicated by the yellow horizontal line. The right axis refers to the longitudinal field gradient (turquoise line). The positions where $B_0(z, 33 \text{ A}) = B_{\text{oct}}^{\text{min}}$ are the outer confinements of the trap (blueish region) with $V_{\text{st}}^{\text{max}} = 10.67$ L. Stored UCN with energies less than the trap limit occupy a smaller storage volume.

the spin flipper (cf. Ch. 3.2.2).

The theory of the adiabatic fast passage spin flipper is discussed in detail in Ch. 4.1, so that here only the basics are briefly outlined. Neutrons in a magnetic field precess at the Larmor frequency

$$\omega_0 = -\gamma B \quad (3.1)$$

with γ the gyromagnetic ratio of the neutron. In τ SPECT, this frequency is position-dependent. At a position z_{SF} in the decreasing part of the first peak of B_0 , a magnetic field B_1 transversal to the z -axis is irradiated, which oscillates at a frequency $\omega_{\text{SF}} = \omega_0(z_{\text{SF}})$, matching the corresponding Larmor frequency within its centre. In a reference frame rotating at ω_{SF} , the neutrons experience an effective magnetic field consisting of a reduced longitudinal field $-\Delta\omega(z)/\gamma = -(\omega_0(z) - \omega_{\text{SF}})/\gamma$ and B_1 . Due to the negative gradient of B_0 , $\Delta\omega(z) > 0$ if $z < z_{\text{SF}}$ and $\Delta\omega(z) < 0$ if $z > z_{\text{SF}}$. The longitudinal component of the effective field thus changes sign and the neutron spin, following this field adiabatically, is flipped by 180° . Adiabaticity in this context means, that the relative change of the magnetic field with time, as experienced by the UCN flying at a velocity v , is (much) smaller than ω_0 .

The spin flipping unit is positioned at the end of the field peak of B_0 close to the holding

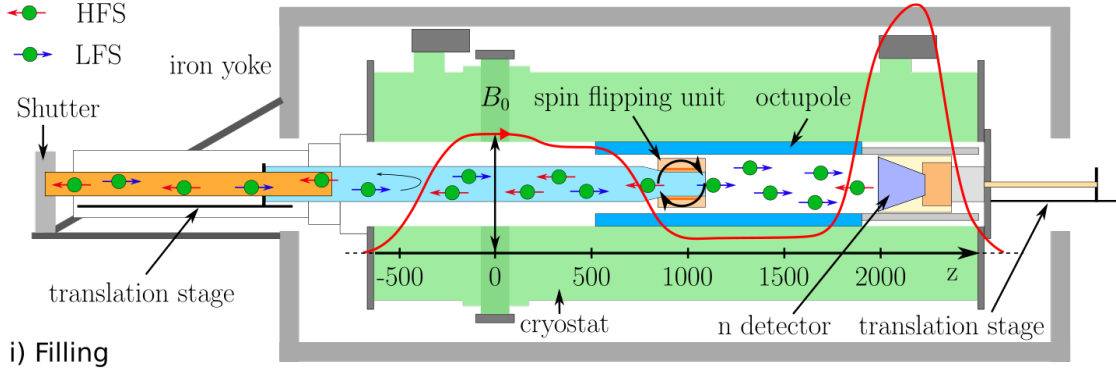


Figure 3.3: Schematic overview of the τ SPECT setup. The experiment is housed inside a cryostat (green) to cool down the superconducting coils to their operating temperature. The storage volume is defined by the superposition of B_0 (red line, direction shown by the red arrow) and the octupole field (position marked in blue). An iron yoke surrounds the cryostat to minimise stray fields. Neutrons enter the experiment through a shutter from the left and are transported by neutron guides (yellow and light blue). They get spin polarised in the B_0 field, HFS are accelerated into the high field, LFS are decelerated. The spin flipping unit converts HFS into storable LFS and is afterwards retracted from the storage volume by the spin flipper side translation stage to maintain purely magnetic conditions during storage. A neutron detector is located on the right, movable by the detector side translation stage. During the filling process, the detector remains outside the storage volume. The axis at the bottom represents the z -axis of the experimental coordinate system.

field, so that the spin flip can take place in low field gradients and thus adiabaticity is fulfilled. This means, however, that the SFU, and thus bulk material, is located inside the trap, which is not compatible with the concept of purely magnetic storage (cf. Ch. 2.2.4). Therefore, the SFU has to be retracted from the storage volume, which is done by the spin flipper side translation stage: A gear spindle driven wagon is connected to a stainless steel tube, which houses a quartz neutron guide and has the SFU attached to its rear end. By pulling at the steel tube, neutron guide and SFU are retracted until both come to rest in the high field outside the trap.

The neutron detector on the right side (cf. Ch. 3.4) can be moved into the trap by the detector side translation stage. The detector as well as the translation stages are the work of J. Kahlenberg and are discussed in detail in [Kah20].

Each measurement with τ SPECT can be divided into four steps, which are executed one after another:

1. **Filling:** During the filling process, the entrance shutter is open, the SFU is positioned inside the storage volume and the detector is in its so-called storage position in the high field of the second magnetic field peak (see Fig. 3.3). UCN are produced by a reactor pulse and are filled into the trap as long as the spin flipper is switched on and irradiates the transversal, oscillating magnetic field.
2. **Cleaning:** The shutter closes and the SFU is retracted from the storage volume (see Fig. 3.4, top). Now the trap is filled with LFS with energies below the trap

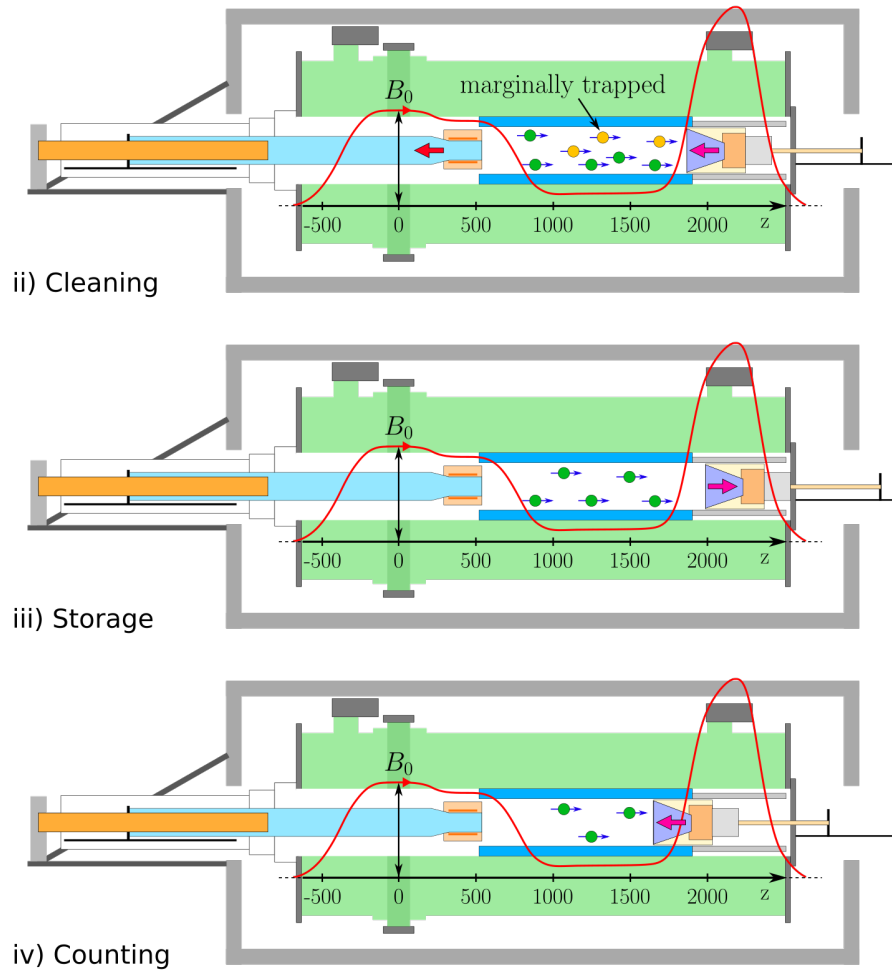


Figure 3.4: Measurement procedure in τ SPECT after the filling process has ended. Cleaning (top): The SFU is retracted from the storage volume to maintain purely magnetic conditions. The neutron detector drives to the edge of the storage volume and removes marginally trapped neutrons (yellow). Storage (middle): The detector drives back to the storage position and the neutrons can leave the trap only by β decaying. Counting (bottom): After storage, the detector drives to the counting position inside the storage volume and counts the remaining neutrons. Afterwards, detector and SFU drive back to their initial positions for a new measurement cycle.

potential but also such with higher energies but small reflection angles (marginally trapped neutrons). Since these neutrons have storage times on the order of the neutron lifetime (cf. Ch. 2.2.4), they have to be removed from the trap in advance. Therefore, the detector drives to the edge of the storage volume and absorbs all neutrons which have energies $E_n \gtrsim V_{\text{pot}} = \mu_n B(z)$ at this position and arrive at the detector within the cleaning duration. The parameters of this procedure (the cleaning position in the magnetic field and the cleaning duration) highly depend on how chaotic the neutron flight trajectories are and thus require careful optimisation. Details on this optimisation process can be found in Ch. 5.3.1.

3. **Storage:** The detector is pulled back to the storage position and the storage time begins, during which the neutrons can only leave the trap by β decaying (Fig. 3.4, middle). The storage time is varied between the measurements and typically ranges from $t_s = 20$ s to 2000 s.
4. **Counting:** After the storage time, the detector drives to the counting position located inside the storage volume and detects the remaining neutrons (Fig. 3.4, bottom). Afterwards, the detector is pulled back to the storage position again and the SFU drives to its filling position in preparation for a new measurement cycle.

The storage of UCN in the longitudinal magnetic field in τ SPECT was successfully demonstrated by J. Karch in a prototype measurement [Kar17]. Instead of the storage octupole, a quartz tube was used for radial confinement (Fermi potential²: $V_F = 90$ neV) resulting in a hybrid storage using magnetic and material walls. With the installation of the storage octupole in 2018 [Kah20], τ SPECT was upgraded to a purely magnetic storage experiment.

3.1.2 The spin flipping unit

The spin flipping unit is depicted in Fig. 3.5 in order to give an overview of the subcomponents discussed in detail afterwards. It consists primarily of an octupole magnet to reduce the radial field of the storage octupole (cf. Ch. 3.2.2) and the spin flipper that produces the B_1 field (cf. Ch. 3.3.1). The yellow line marks the centre of the spin flipper, to which the nominal spin flip position z_{SF} refers to. On the right, the front of the SFU, a ring

²An overview over the Fermi potentials of all material used in this work is found in Tab. B.1.

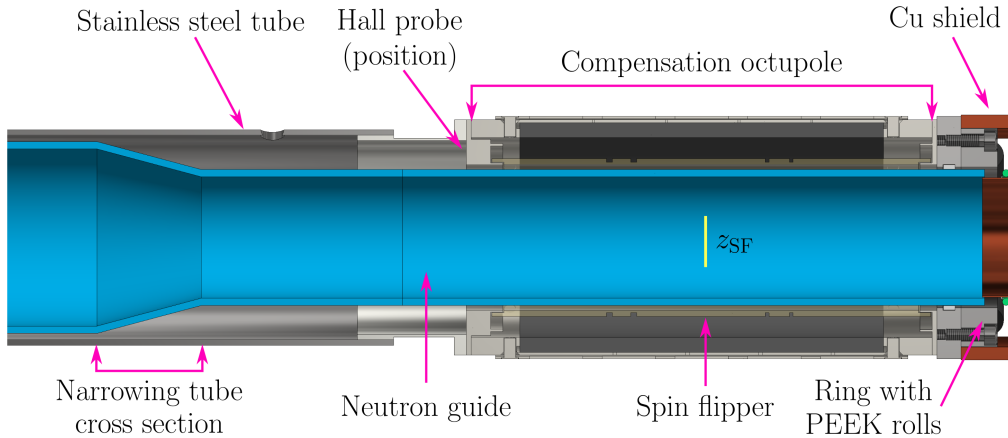


Figure 3.5: Overview of the SFU components. The spin flipper (centre position marked by z_{SF}) is surrounded by an octupole magnet (compensation octupole), which has a ring with four spring mounted rolls attached to its front as well as a Cu shield for neutron reflection. UCN are transported by the neutron guide, which is narrowing from $r = 36.5$ mm to $r = 25$ mm in front of the SFU due to spacial constraints. The SFU is moved in and out of the trap by a stainless steel tube, which is connected to the translation stage outside of the cryostat. A 1-axis Hall probe measures the longitudinal component of the magnetic field in τ SPECT.

with four spring-mounted rolls made of polyether ether ketone (PEEK) is mounted for supporting the weight of the SFU on the storage octupole surface. They are positioned at 45° with respect to the vertical axis to improve the gravitational force distribution. The UCN are transported from the left towards the storage volume by the neutron guide, which due to spacial constraints is narrowed from a diameter $r = 36.5$ mm to $r = 25$ mm in front of the SFU. The outer shell of the SFU is built from titanium ($V_F = -48$ neV), so that a copper shield is attached to the front ($V_F = 168$ neV) to reflect the neutrons inside the trap during the filling process. A stainless steel tube connects the compensation octupole to the translation stage outside the cryostat, so that the entire SFU can be moved out of the trap and back in. The longitudinal component of the magnetic field in τ SPECT is measured using a 1-axis Hall probe³ in a distance $\Delta z = -61.4$ mm from the spin flipper centre.

3.2 Compensation of the octupole field

3.2.1 Halbach octupoles

The two octupoles used in τ SPECT are based on the so-called Halbach array, a special arrangement of permanent magnets developed by Klaus Halbach [Hal80], in which the magnetic flux escapes only on one side and vanishes on the other side. Ideally, this is achieved by a continuously changing magnetisation direction in the material, as is shown in Fig. 3.6 (left) for an infinite linear Halbach array.

Halbach arrays in a cylindrical shape can be used for building magnets with a strong magnetic field on the inside and a vanishing field on the outside. Depending on the magnetisation change, arbitrarily high order multipoles can be constructed as shown in Fig. 3.6. Here, m refers to the number of pole pairs ($m = 1$: dipole, $m = 2$: quadrupole, and $m = 4$: octupole). Following Halbach's calculations in [Hal80], the amplitude of the magnetic field

³Arepec HHP-NA, <http://www.arepec.sk>

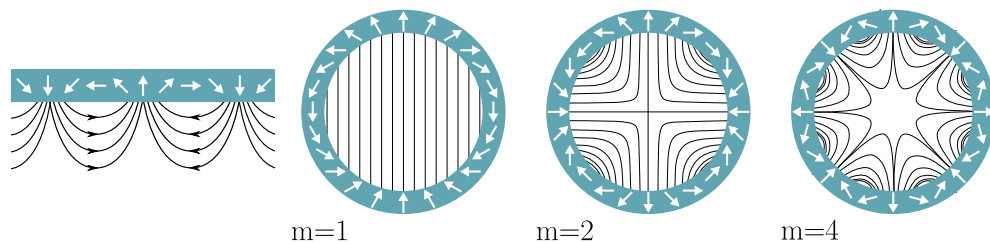


Figure 3.6: Ideal Halbach arrays of different shapes and orders. The magnetisation direction changes continuously and the magnetic flux escapes only on one side of the array. Left: An infinite linear Halbach array. The circular arrays show cuts through infinite Halbach cylinders with strong magnetic fields on the inside and vanishing fields on the outside. The multipole order is chosen by the magnetisation change per unit angle. From left to right: Infinite plane, dipole ($m = 1$), quadrupole ($m = 2$) and octupole ($m = 4$).

on a radius \vec{r} inside an infinite cylinder is given by

$$B = B_R \ln \left(\frac{r_i}{r_o} \right) \quad \text{for } m = 1 \quad (3.2a)$$

$$B(\vec{r}) = \left(\frac{\vec{r}}{r_i} \right)^{m-1} B_R \frac{m}{m-1} \left[1 - \left(\frac{r_i}{r_o} \right)^{m-1} \right] \quad \text{for } m \geq 2 \quad (3.2b)$$

with r_i and r_o the inner and outer radii of the Halbach cylinder, respectively, and B_R the magnetic remanence of the material. Unfortunately, infinite magnetic cylinders are not realisable and additionally a uniformly changing magnetisation on a continuous material is hard to manufacture. Approximating the ideal Halbach cylinder with discrete magnetic segments is a far easier method, as magnets with different sizes, strengths and magnetisation directions are commercially available, and the main task is their arrangement into a Halbach array. Due to the segmented structure, the magnetisation angle now changes discretely between the segments with

$$\alpha = (m + 1)\vartheta \quad (3.3)$$

where α is the magnetisation direction of the segment and ϑ its location angle [Blu16]. In case of a Halbach octupole with $m = 4$, this would result e.g. in a magnetisation by an angle $\alpha = 225^\circ$ at the location angle $\vartheta = 45^\circ$, or $\alpha = 450^\circ \hat{=} 90^\circ$ at $\vartheta = 90^\circ$ (0° assumed in vertical direction).

3.2.2 The magnetic octupoles in τ SPECT

The storage octupole⁴ is a discrete Halbach octupole consisting of 24 rings, each made from 32 segments of $\text{Sm}_2\text{Co}_{17}$ with a magnetic remanence of $B_R = 1.1$ T. It was designed by S. Dragisic, who chose this material, because it does not undergo a phase transition at low temperatures [Dra14]. Each ring is 57.5 mm long, so that the storage octupole has an overall length of 1380 mm; the inner radius is $r_{\text{SO}} = 54$ mm. The minimum magnetic field at $r = 53.5$ mm close to the octupole surface, which limits the magnetic trap, is extrapolated from the measurement results by J. Haack [Haa16] and found as $B_{\text{oct}}^{\text{min}} = 780$ mT.

However, while octupole fields fall off towards the centre rapidly due to the r^3 dependency (cf. Eq. 3.2b), in the radial range of the neutron guide significant transversal fields remain. Ch. 4.1.2 derives a criteria for efficient spin flipping in the presence of transversal fields as

$$k = \frac{\nabla_t B(r_{\text{max}})}{\nabla_z B(r = 0 \text{ mm})} \lesssim 3, \quad (3.4)$$

where $\nabla_t B(r_{\text{max}})$ is the transversal field gradient⁵ at the neutron guide radius r_{max} and $\nabla_z B(r = 0 \text{ mm})$ the longitudinal gradient at its centre.

⁴The octupole was manufactured and delivered by Arnold Magnetic Technologies AG, the used material is called Recoma28HE.

⁵In a symmetric octupole, the total magnetic field $B(r)$ on a circle with fixed radius r is constant and the orientation of this field changes continuously between radial and angular direction when using cylinder coordinates. The same is true for the total magnetic field gradient, which on this circle remains of equal amplitude but changes its orientation in the $r-\varphi$ plane. In a general notation, this gradient is thus referred to as transversal field gradient $\nabla_t B$ in this work.

Given the octupole field components B_r , B_φ and B_z in cylinder coordinates, as well as B_0 pointing along the z -axis, the total magnetic field is calculated as

$$|\vec{B}| = \sqrt{B_r^2 + B_\varphi^2 + (B_z + B_0)^2}. \quad (3.5)$$

The radial dependency of the longitudinal field B_0 is negligible close to the central axis and is thus not taken into account here. The total field in turn scales the components of the field gradient according to

$$\begin{aligned} \nabla B &= (\nabla_r B)\hat{e}_r + (\nabla_\varphi B)\hat{e}_\varphi + (\nabla_z B)\hat{e}_z \\ &= \frac{B_r}{|\vec{B}|} \frac{dB_r}{dr} \hat{e}_r + \frac{1}{r} \frac{B_\varphi}{|\vec{B}|} \frac{dB_\varphi}{d\varphi} \hat{e}_\varphi + \frac{B_z}{|\vec{B}|} \frac{dB_z}{dz} \hat{e}_z. \end{aligned} \quad (3.6)$$

If not stated otherwise, the radial and angular field gradients in this work are combined in the more general transversal field gradient

$$\nabla_t B = \sqrt{(\nabla_r B)^2 + (\nabla_\varphi B)^2}. \quad (3.7)$$

In order to estimate, whether spin flips are possible at the design position $z_{\text{SF}}(\text{design}) = 1100 \text{ mm}$ [Kah20], the parameter k in Eq. 3.4 is evaluated using the longitudinal and transversal field gradients at this position. At $I_{\text{main}} = 33 \text{ A}$, a magnetic field of $B_0 = 197.7 \text{ mT}$ and a longitudinal gradient $\nabla_z B(r = 0 \text{ mm}) = 0.4 \text{ mT/cm}$ are found. The field of the storage octupole is approximated analytically in Ch. A.5.1.2. Assuming the neutron quartz guide at $r_{\text{max}} = 36.5 \text{ mm}$ without the narrowed tube section (cf. Ch. 3.1.2) and calculating the octupole field at one of its poles (this corresponds to $B_\varphi = 0 \text{ mT}$), $\nabla_t B(r_{\text{max}}) = 154.2 \text{ mT/cm}$ is inferred. Inserting the gradients in Eq. 3.4 results in $k = 378$, so that at the design position the spin flip condition is highly violated.

With $\nabla_t B$ decreasing at smaller radii, a reduction of the neutron guide diameter only could be considered. However, in order to fulfill $k \simeq 3$, a radius of only $r = 13.3 \text{ mm}$ is necessary. In terms of neutron guide cross sections, this corresponds to a reduction by 87%, which is inefficient. Thus, it is unavoidable to reduce the octupole field itself in the spin flipping region.

To do this, a second octupole magnet (compensation octupole, CO) is used, which generates a magnetic field of the same shape as the storage octupole but is rotated by 45° around its longitudinal axis. Due to rotational symmetry, then opposing magnetic poles align, so that the remaining field after superposition should ideally vanish. The configuration is shown in Fig. 3.7 (left), the arrows mark the magnetisation direction of individual segments. The grey circle corresponds to the narrowed neutron guide with $r = 25.0 \text{ mm}$, which is required for the spin flipper to still fit between neutron guide and compensation octupole. The dimensions of the compensation octupole were optimised in [Ros17] along with theoretical studies concerning its precise alignment with the storage octupole. The results are briefly recapitulated here.

In order to receive the same behaviour upon cool down in τ SPECT, the compensation octupole has to be made of the same material as the storage octupole ($\text{Sm}_2\text{Co}_{17}$ (Recoma28HE) from Arnold Magnetic Technologies with a remanence of $B_R = 1.1 \text{ T}$). It is constructed from 5 rings, each containing 32 magnetic segments, and is in total 150 mm long. The outer radius of the compensation octupole is fixed to $r_{o,\text{CO}} = 47.0 \text{ mm}$ to leave space for a construction shell. The inner radius is determined analytically by using Eq. 3.2b

separately with the storage octupole and with the compensation octupole dimensions, leaving $r_{i,CO}$ the only free parameter. Equating the fields then results in $r_{i,CO} = 41.2$ mm.

The quality of the field compensation, however, relies heavily on a good orientation of the two octupoles with respect to each other. The main misalignments are

1. a non-perfect rotational orientation,
2. a non-perfect axial alignment,
3. variations in the position of each magnetic segment, and
4. fluctuations in the magnetisation angles and strengths of the segments.

The effects of the first two mentioned misalignments are shown on the right side of Fig. 3.7 in comparison with the magnetic fields without and with perfect compensation. The remaining field at perfect compensation arises from the discrete magnetic segmentation of the two octupoles. The compensation is evaluated at the neutron guide radius $r = 25$ mm and results in 99.7% for perfect alignment (reduction of the field from 96.96 mT to 0.33 mT), 93.0% for a radial misalignment by $\delta\varphi = 1.0^\circ$ and only 63.9% for an axial misalignment by $\delta y = -3.0$ mm in vertical direction (this would correspond to a sagging

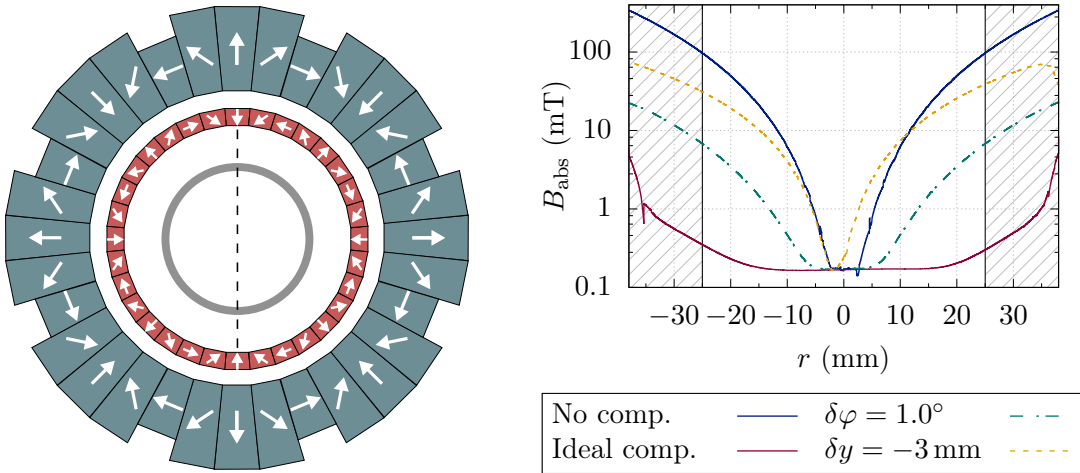


Figure 3.7: Principle of octupole field compensation and results from a FEM simulation using COMSOL Multiphysics[®]. Left: Storage octupole (blueish) and compensation octupole (red) with the arrows showing the magnetisation direction of individual segments. A rotation by 45° between the octupoles results in an alignment of opposing poles, so that the magnetic field inside ideally vanishes. The grey circle marks the position of the narrowed neutron guide. The field along the dashed line is used for analysing the compensation effect. Right: The absolute magnetic field on the analysis line without (blue) and with perfect compensation (red), a rotational offset by $\delta\varphi = 1.0^\circ$ (green) and an axial offset by $\delta y = -3.0$ mm in vertical direction (yellow dashed). For better clarity, the y axis is in logarithmic scale. The black lines correspond to the inner radius of the neutron guide, the shaded region is outside of neutron range.

of the compensation octupole). The values for the misalignments were chosen as rough estimations in anticipation of what we find in the experimental setup later.

As a result of this analysis a construction is required for τ SPECT, which keeps the orientation of the compensation octupole fixed and as close to the desired 45° as reasonably possible, and which centres the compensation octupole. At the same time mobility must be maintained, so that the compensation octupole (and thus the spin flipping unit) can be retracted from the storage volume.

The construction of the compensation octupole is discussed in detail in Ch. A.2, the finished octupole is shown in Fig. 3.8 (left). The right side depicts the front section of the SFU: Four spring-mounted PEEK rolls are attached to the compensation octupole via an adapting ring, on which it is moved on the storage octupole surface. The springs are used in an attempt to keep the axial offset due to gravity as small as possible, and to smoothen the movement over the segment edges of the storage octupole⁶. However, even though the springs were built from spring steel (the strongest material available for this purpose [Wor18]), the compensation octupole sagged visibly within the storage octupole⁷. Finally, a copper shield covers the entire front of the compensation octupole, apart from a circular cutout in the centre, through which the UCN can travel into the storage volume.

The orientation of the compensation octupole inside the storage octupole is set and maintained by a flange, which is welded to the first part of the translation stage as is shown in Fig. 3.9 (the construction is the work of J. Kahlenberg [Kah20]). This flange has four indentations 90° apart containing insets made from Teflon[®] (PTFE), which glide on a fixed rail construction. The SFU thus remains movable in z -direction with the gearing of the flange and the rails preventing rotation.

⁶According to [Haa16], small steps of up to 1.03 mm between adjacent rings of the storage octupole occur.

⁷During an optimisation of the alignment in 2020, the lower springs were removed and rolls with rigid axles were installed (cf. Ch. 5.2.1), but until then the axial misalignment could not be avoided.

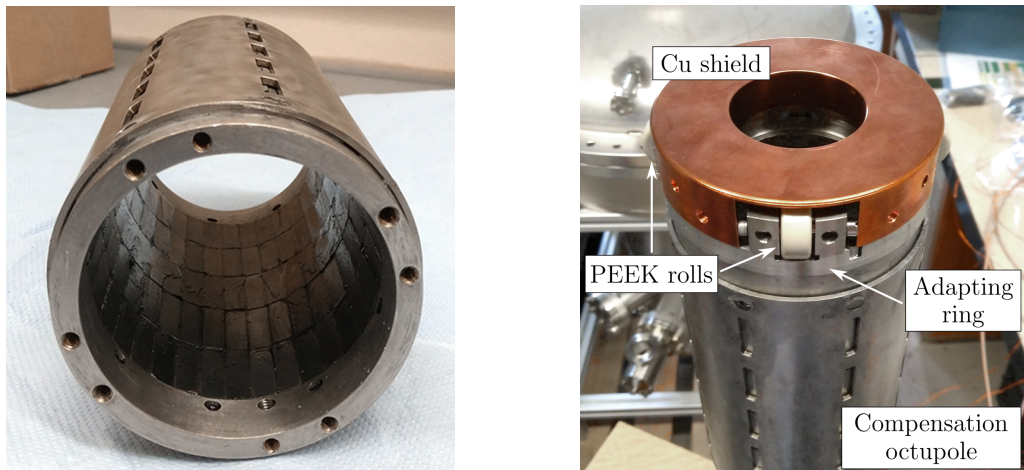


Figure 3.8: Finished compensation octupole (left) and front assembly of the SFU (right). Four spring-mounted PEEK rolls are connected to the compensation octupole via the adapting ring allowing the movement on the storage octupole surface and keeping the axial offset in the alignment small. The copper shield reflects neutrons during the filling process.

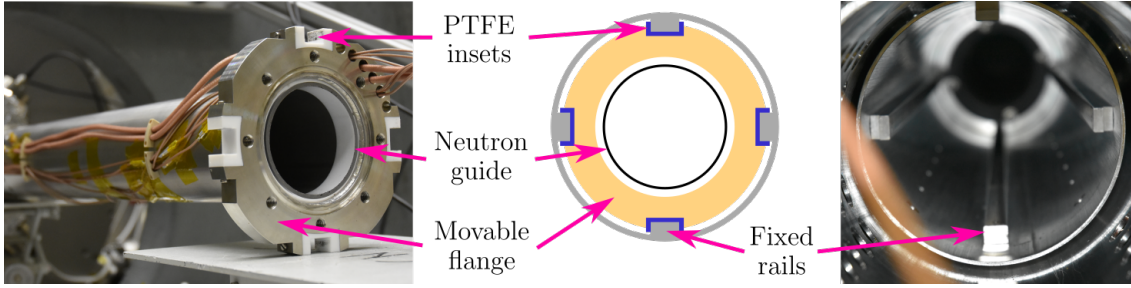


Figure 3.9: The gearing principle of the compensation octupole rotation fixation in a schematics (middle) as well as the relevant components prior to the final assembly in τ SPECT (left and right). A movable flange is welded to the stainless steel tube, to which other end the compensation octupole is connected. This flange has four indentations 90° apart, which enclose four fixed rails connected to the storage octupole. Additional PTFE insets increase the mobility in z -direction, while maintaining the rotational orientation of the compensation octupole. The construction is the work of J. Kahlenberg [Kah20].

3.2.2.1 Measurement of the compensated octupole field

After the construction of the compensation octupole was finished, the magnetic field of the storage octupole with and without compensation were measured and compared afterwards. The compensation octupole, including the adapting ring with the PEEK rolls and the copper shield, was mounted to the first part of the translation stage to secure the rotational orientation (cf. Fig. 3.9). With the storage octupole not having been installed in τ SPECT at that time, the compensation octupole was inserted from one side and the magnetic field measurement could be done from the other side of the storage octupole.

The setup is shown in Fig. 3.10, on the left a schematic view and on the right the experimental realisation from outside the storage octupole. The compensation octupole was positioned with its centre at what in τ SPECT corresponds to the design position for the filling process at $z_{\text{SF}}(\text{design}) = 1100 \text{ mm}$. The field measurement was done with a calibrated high-precision 3-axis Hall probe⁸ mounted on a probe holder. This holder was connected to a gear rack and was moved back and forth inside a guiding tube by a stepper motor. A plate was welded to the tube, which was then connected with screws to the mounting holes in the storage octupole. By rotation of the gear rack, and thus the probe holder and the Hall probe, the measurement angle could be adjusted. The angle adjustment plate fixed the orientation during individual measurements and allowed for equally distributed measurements in steps of $\Delta\varphi = 360^\circ/64 = 5.63^\circ$. At its front, the probe holder was shaped such as to fix the Hall probe on four different radii $r = \{10, 15, 20, 25\} \text{ mm}$. The measurement range along the z -axis was limited by two electrical end stops. The coordinate system of the measurement is cylindrical to reflect the octupoles' geometry. The angle $\varphi = 0^\circ$ is aligned with the upper mounting hole in the storage octupole and lies in the middle of two adjacent magnetic poles. Every measurement consisted of the following steps:

1. The radius was selected by mounting the Hall probe to the corresponding place on

⁸SENIS 3-Axis Hall Probe F3A-03KS10C, readout by 3-Axis Digital Teslameter 3MH3A-0.1%-2T [sen19]

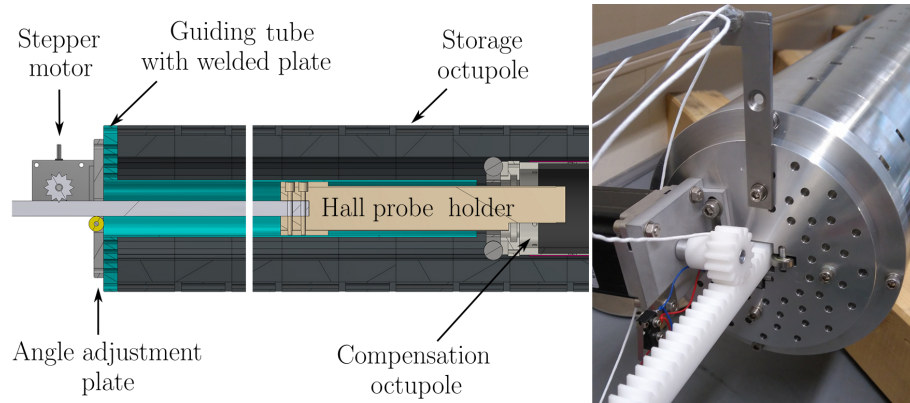


Figure 3.10: Setup for the magnetic field measurement with and without the compensation octupole. Left: The 3-axis Hall probe is mounted on a probe holder, which, connected to a gear rack, is moved back and forth inside the guiding tube (turquoise) by a stepper motor. The angular orientation of the gear rack and thus the holder and the probe itself is set and maintained by the angle adjustment plate. The measurement range is limited by two electrical end stops (not shown here). Right: A photograph of the measurement setup from the outside.

the probe holder.

2. The measurement angle was selected by rotating the angle adjustment plate.
3. The probe holder was moved out until the outer end stop was reached. This was the starting position.
4. A measurement point was taken every $\Delta z = 5(2)$ mm until the rear end stop was reached. The error is a conservative estimation from the manual distance measurement between the start position of the measurement and the front of the compensation octupole and the adjustment of the number of motor steps required per millimeter driving distance.
5. Finally, the probe holder was pulled back to the starting position.

Before mapping the magnetic field, an Allan deviation measurement was done to estimate the required measurement time for each data point (cf. Ch. A.2.3). The optimum was found at $t = 1.0$ s. A reproducibility check was done, measuring the same configuration at the arbitrary angle $\varphi = 293^\circ$ and $r = 25$ mm ten times in a row: The results shown in Fig. 3.11 refer to the absolute magnetic field⁹ B_{abs} and are in good agreement in a range up to $z_{\text{rel}} \sim 210$ mm, afterwards they spread to a maximum of $B_{\text{abs}}^{\text{max}} - B_{\text{abs}}^{\text{min}} = 0.83 \pm 0.02$ mT at the very end, which may be caused by gravitational sagging of the Hall probe holder. Taking this into account, the error in each field component was conservatively estimated as $\Delta B = 0.5$ mT.

⁹The error bars of the individual magnetic field measurements are estimated from the Allan deviation ($\sigma_B(1\text{ s}) \simeq 0.016$ mT at 128 internal averages, cf. Ch. A.2.3), which was assigned to each field component before calculating ΔB_{abs} by Gaussian error propagation.

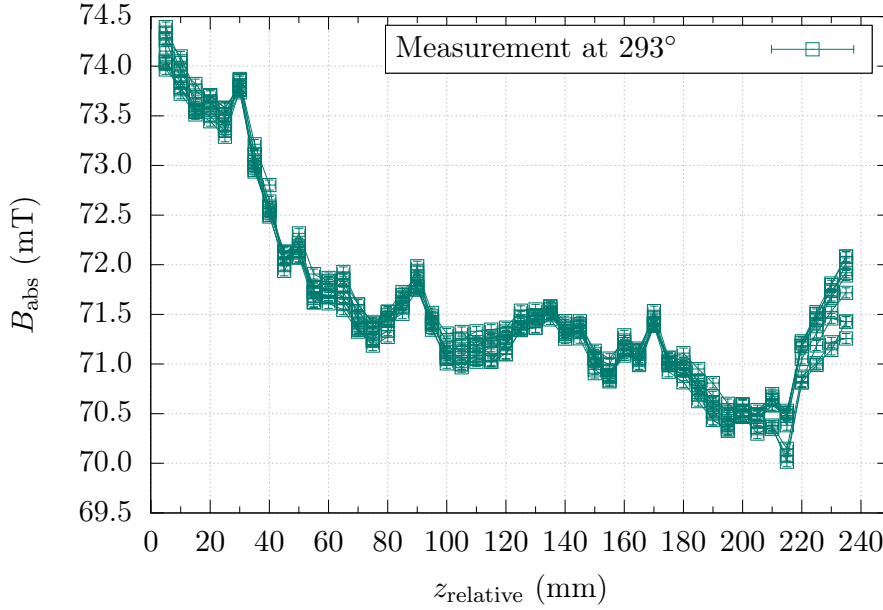


Figure 3.11: Reproducibility of the compensated magnetic field measurement. On a fixed angle of 293° and $r = 25$ mm, the measurement was repeated 10 times in a row. The results spread to a maximum of $B_{\text{abs}}^{\text{max}} - B_{\text{abs}}^{\text{min}} = 0.83 \pm 0.02$ mT on the right, which may be caused by gravitational sagging of the Hall probe holder. From this value, the error in each measured field component is estimated as $\Delta B = 0.5$ mT.

The octupoles as well as the rotational fixation of the translation stage show a 90° symmetry, so that four orientations of the compensation octupole inside the storage octupole are possible. The measurements and results of finding the best orientation are discussed in Ch. A.2.4, the optimum is found in 'orientation No. 4', which was chosen for all following measurements and also for the final assembly in τ SPECT.

During the uncompensated field measurement, the compensation octupole was pulled out of the measurement region as far as possible. The field was mapped on all four radii and at all available measurement angles. Afterwards, the compensation octupole was put back in position and the measurements were repeated.

Effectivity of the field compensation Fig. 3.12 depicts the measured radial field component at $r = 25$ mm without (left) and with field compensation (right) at the longitudinal position $z_{\text{rel}} = 120$ mm, which is roughly in the middle of the compensation octupole. While the uncompensated field shows eight poles as expected (multipole order $m = 4$, cf. Ch. 3.2.1), the number of poles of the remaining field after the compensation is reduced to six ($m = 3$).

To investigate this effect, the fields were additionally simulated using COMSOL Multiphysics[®], where the uncompensated field simulation confirms the octupole structure. In the compensated field simulation, a rotational and an axial offset were included in separate runs: With a rotational offset even by a comparably large but randomly chosen $\delta\varphi = 5^\circ$ the field remains of octupolar shape (the result is not shown here), whereas an axial misalignment by $\delta y = -3$ mm results in a hexapole field with both structure and field

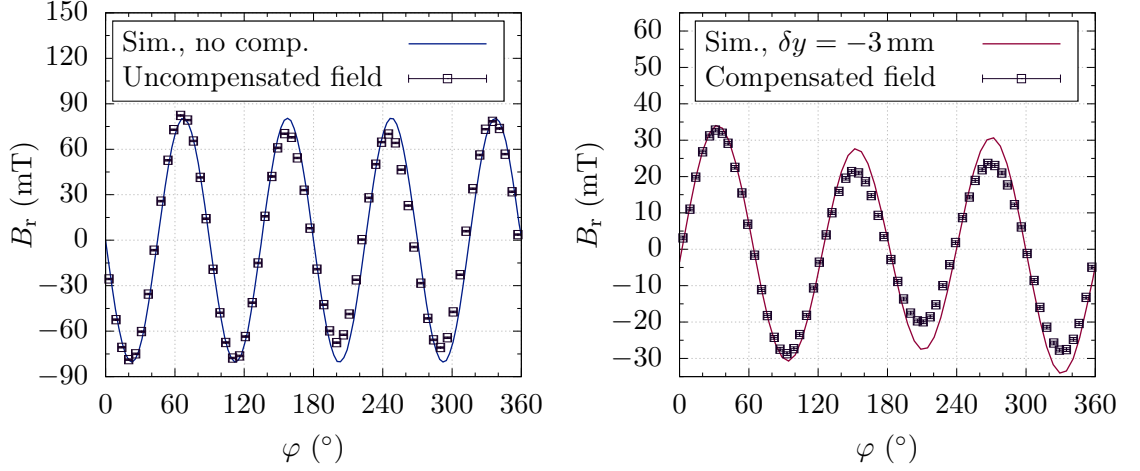


Figure 3.12: Radial magnetic field component without (left) and with field compensation (right). The black markers show the measurement results at $r = 25$ mm and $z_{\text{rel}} = 120$ mm, the solid lines are simulations using COMSOL Multiphysics[®] with an axial misalignment of the compensation octupole by $\delta y = -3$ mm in vertical direction. Without compensation the field shows an octupolar structure with multipole order $m = 4$, which is reduced to $m = 3$ when including the compensation octupole.

amplitude roughly matching the measurement results. In fact, Ch. A.5.1.2 deduces an analytic approximation of the compensated field, where an axial offset by $\delta y = -2.6$ mm and a rotational offset by $\delta\varphi = 0.2^\circ$ are deduced. Thus, the axial misalignment caused by the gravitational sagging of the compensation octupole does not only lead to a non-vanishing residual magnetic field but is also responsible for the reduction of the multipole order.

A map of the uncompensated and the compensated field at $r = 25$ mm is shown in Fig. 3.13, more measurement results for the radii 10, 15 and 20 mm can be found in Appendix B. Especially at the uncompensated field we find that the measured field at the top ($\varphi = 0^\circ$) is stronger than that at the bottom ($\varphi = 180^\circ$), which contradicts the

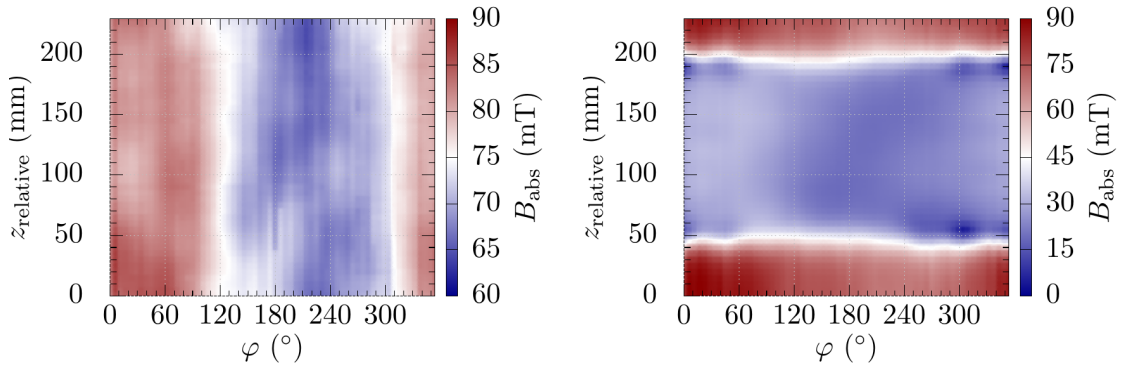


Figure 3.13: Octupole field map without (left) and with compensation (right) on a measurement radius $r = 25$ mm.

initial assumption that the Hall probe holder sagged due to gravity. A simulation using COMSOL Multiphysics[®] revealed, that if the centre of the measurement plane in $r - \varphi$ direction and the octupole axis are not fully aligned but offset by $\delta y \simeq +0.8$ mm in vertical direction, this behaviour can be explained (cf. Fig. B.1). Such an offset can occur e.g. if the guiding tube is not fully straight or welded not perfectly perpendicularly to the plate that connects it to the storage octupole (cf. Fig. 3.10).

In order to quantify the compensating effect, we focus on the region between $z_{\text{rel},1} = 60$ mm and $z_{\text{rel},2} = 180$ mm. The limits were chosen assuming an effective spin flipper length of 100 mm and including an offset of 10 mm on each side, and its centre position in the middle of the compensation octupole, here $z_{\text{rel}} = 120$ mm. The absolute magnetic field and gradient were calculated at each measurement point and afterwards the maximum and average values were determined. The results of this analysis are given in Tab. 3.1. The compensation C of each component B_i was calculated as $C = 1 - (B_{i,\text{comp.}}/B_{i,\text{uncomp.}})$. A weighted average yields a total compensation of the octupole field by 60.4(1.0)%.

As the measurement radius $r = 25$ mm of $B_{\text{abs,mean}}$ and $|\nabla_t B|_{\text{mean}}$ corresponds to the radius of the narrowed neutron guide (cf. Ch. 3.1.2), we can use the results to recalculate the spin flip parameter k in Eq. 3.4: Along with $B_0 = 197.7$ mT at the spin flip design position $z_{\text{SF}}(\text{design}) = 1100$ mm we find the total magnetic field $B = 199.3$ mT (cf. Eq. 3.5) and its gradients $\nabla_z B = 0.4$ mT/cm and $\nabla_t B = 3.6$ mT/cm (cf. Eq. 3.6). With $k = \nabla_t B / \nabla_z B = 9.0$, the spin flip condition is still violated on radii close to the neutron guide edges. However, as shown in detail in Ch. 4.1.2, when varying the position of the spin flip and thus the longitudinal gradient $\nabla_z B$, regions can be found where efficient spin flips are possible.

Table 3.1: Comparison of the uncompensated and compensated octupole field at $r = 25$ mm with respect to maximum and mean absolute fields and gradients. The error in the mean field and gradient are the standard deviation of the results of all evaluation positions. The gradients point in transversal direction according to Eq. 3.7. The compensation C was calculated using $C = 1 - (B_{i,\text{comp.}}/B_{i,\text{uncomp.}})$ with B_i the component of interest.

Component	Uncompensated field	Compensated field	Compensation C (%)
$B_{\text{abs,max}}$	83.7(5) mT	33.4(5) mT	60(1)
$B_{\text{abs,mean}}$	75(5) mT	25(4) mT	67(6)
$ \nabla_t B _{\text{max}}$	197(31) mT/cm	60(10) mT/cm	70(7)
$ \nabla_t B _{\text{mean}}$	112(54) mT/cm	29(15) mT/cm	74(18)

3.2.3 Zero-field points

Inside the storage octupole, the magnetic field is dominated by the transversal components B_r and B_φ , with the z -component being vanishingly small. However, the fringe field of the compensation octupole generates a longitudinal field, which, if on the order of magnitude of B_0 and pointing in the opposite direction, can lead to points with zero field at which the neutrons depolarise (cf. Ch. 2.2.4).

Fig. 3.14 is used for an estimation of possible zero-field points inside the neutron guide: $B_0(z)$ around $z_{\text{SF}}(\text{design})$ is added by components to the compensated octupole field at

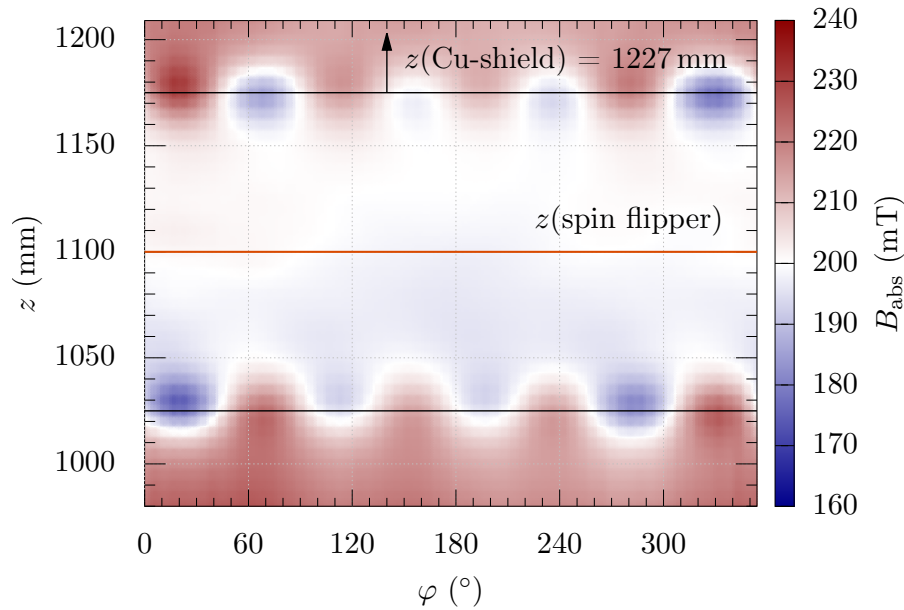


Figure 3.14: Superposition of the measured compensated octupole field at $r = 25$ mm and B_0 in order to investigate the neutron guide region for zero-field points. Seen from above, the neutrons enter from the bottom, the storage volume is located at the top. The lines correspond to the spin flipper centre (red) and the physical edges of the compensation octupole magnets (black). The absolute field drops nowhere to below $B_{\min} = 174$ mT, so that zero-field points and thus depolarisation at such points can be excluded.

$r = 25$ mm (cf. Tab. 3.1) and the absolute magnetic field is calculated. The position is chosen, because here, B_0 is close to its minimum value (at $I_{\text{main}} = 33$ A the minimum lies at $z(B_{0,\min}) = 1056$ mm with $B_{0,\min} = 196.6$ mT) and thus the compensation octupole has the largest impact. The y -axis corresponds to the longitudinal position in τ SPECT. The red line represents the centre of the spin flipper, the black lines mark the edges of the compensation octupole. The position of the copper shield ($z_{\text{Cu-shield}} = 1227$ mm) where the neutrons enter the storage volume lies outside of the measurement region. The fringe field is clearly visible in the wavy structure around the octupole edges. However, because the field is still dominated by $B_0(z)$, no results smaller than $B_{\min} \simeq 174$ mT are found.

As the magnetic field directly behind the copper shield could not be measured, it was simulated using COMSOL Multiphysics[®]. It was shown earlier in this chapter, that an axial offset by $\delta y = -3$ mm in the alignment of the compensation octupole e.g. due to gravitational sagging on the spring-mounted rolls (cf. Fig. 3.8) leads to a relatively large miscompensation (cf. Fig. 3.7). In comparison to smaller axial offsets, this field also generates the largest fringe fields, so that it is used as a worst-case scenario here. In the simulation, the highest values for B_z were found at the magnetic poles of the compensation octupole. Therefore, the field map was extracted from a vertical $r - z$ plane through the centre at $r = 0$ mm. As before, the B_0 field is added by components and the absolute field is calculated. The result is shown in Fig. 3.15.

The graphical overlay roughly depicts the front of the spin flipping unit. The magnetic field seen by the neutrons is delimited by the neutron guide. After the neutrons enter the

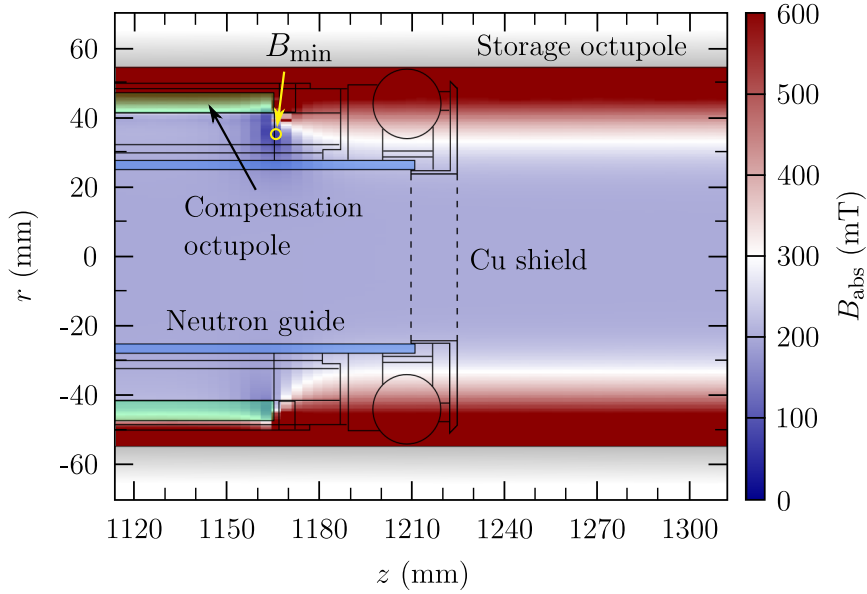


Figure 3.15: Simulation of the total magnetic field in τ SPECT, as a combination of the B_0 holding field and the worst case fringe field of the compensation octupole at an axial misalignment of $\delta y = -3$ mm. Shown is the shape of the SFU front with the compensation octupole (green), the storage octupole (grey), the neutron guide (blue) and the Cu shield. The field of the octupoles was simulated on a vertical $r-z$ plane through the centre at $r = 0$ mm and added to the B_0 field by components. The minimum is found as $B_{\text{abs}} = 20.8$ mT at the position marked by the yellow circle. In the area occupied by the neutrons within the neutron guide and on the right side of the Cu shield, zero-field points and thus depolarisation at such points can be excluded.

trap during the filling process, they are prevented from accessing the area of the fringe field by the Cu shield. The fringe field (the field minimum is found as $B_{\text{min}} = 20.8$ mT) is thus contained mostly by the material between the magnets themselves and the Cu shield and is negligible in regions accessible to neutrons.

We therefore conclude, that no zero-field points are created in the trap by inserting the compensation octupole in τ SPECT and depolarisation of the neutrons on such points can be excluded.

3.3 The spin flipper

The spin flip of UCN from high-field seekers to low-field seekers requires an oscillating magnetic field B_1 perpendicular to the static holding field B_0 . The first spin flipper used for τ SPECT was a so-called 'birdcage resonator', which was, however, later replaced by a pair of saddle coils (cf. Ch. 5.1).

3.3.1 Birdcage Resonators

In general, a homogeneous transversal magnetic field can be produced by a cosine-theta coil, which is shown schematically in Fig. 3.16. A direct current J through the coil wires generates a static magnetic field, whereas with an additional time modulation ($J(t) = J_0 \sin(\omega t)$) an oscillating transversal B_1 field with linear polarisation is produced. Circular polarisation of B_1 is obtained by using a second cosine-theta coil rotated by 90° in azimuthal direction and adding a 90° phase shift to the current ($J(t) = J_0 \sin(\omega t + \pi/2)$).

An similar oscillating or rotating B_1 field can also be generated using a birdcage resonator, which was presented by Cecil E. Hayes *et. al.* in 1985 [HES85]. It consists of two concentrically aligned end-rings, connected by an even number N (in τ SPECT $N = 8$) of evenly distributed straight segments, called 'rungs'. Birdcage resonators can be built in the so-called 'low-pass' and 'high-pass' design [GLSP02, HES85, HBD12, FBM00]. In a high-pass design, capacitances C are equally distributed over the end-rings, whereas in low-pass design, they are located within the rungs. Fig. 3.17 shows the shape of a birdcage resonator in low-pass design on the left (a) and the generated transversal magnetic field from a FEM simulation using COMSOL Multiphysics[®] on the right (c). A lumped element model of the birdcage resonator is depicted in the middle (b). The nodes A and A^* , as well as B and B^* , are connected and form the end-rings. They are joined by N repeated rungs including the capacitances C_R . The inductances L_1 and L_2 contain the self- and mutual inductances of the end-rings and rungs. Following [HES85], this circuit consists of N repeated loops, where each loop adds a phase shift $\Delta\phi(\omega)$ to the current, ω being the frequency of the excitation signal. A resonance condition is only fulfilled with periodic boundary conditions $\Delta\phi(\omega) = j2\pi$ with the resonance mode j an integer number. The

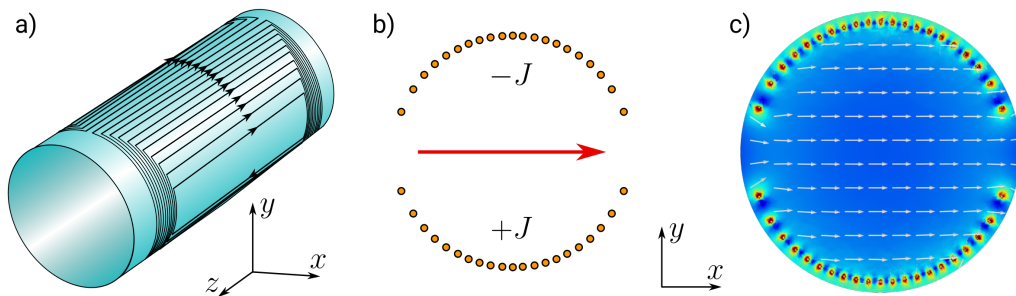


Figure 3.16: Schematic depiction of a cosine-theta coil (a) with a cut in xy -direction to show the distribution of wires on the cylindrical surface (b). The direction of the current J in the upper and lower half with respect to the drawing plane is indicated, the red arrow shows the direction of the resulting B_1 field. A simulation of the B_1 field (arbitrary units) using COMSOL Multiphysics[®] is depicted in c), the white arrows mark the direction of the local field.

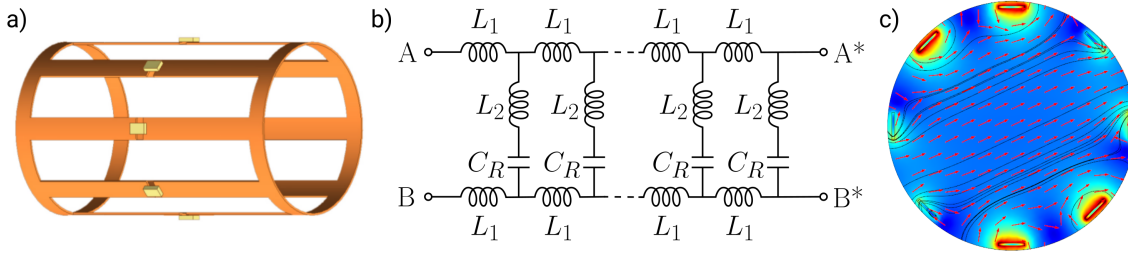


Figure 3.17: Birdcage resonator in low-pass design. a) The birdcage resonator, consisting of two concentric end-rings connected by eight rungs, and a capacitor located inside each rung. b) The corresponding lumped-element model with A and A^* as well as B and B^* connected to form the end-rings. For better visibility only four rungs are shown. c) The resulting transversal magnetic field in the sinusoidal mode.

frequency spectrum has a total of $N/2 + 1$ resonances, so that $1 \leq j \leq N/2 + 1$ [Lei97]. The mode required for τ SPECT is called the sinusoidal mode, which generates the sinusoidal current distribution. It is the highest mode of the frequency spectrum in the high-pass design (in τ SPECT with $N = 8$, this would result in $j = N/2 + 1 = 5$) and the lowest mode in low-pass design [HBD12] ($j = 1$).

A birdcage resonator can be excited either linearly or in quadrature. In linear excitation, two sinusoidal signals are used, which are applied at positions 180° apart and of which one is phase shifted by $\Delta\varphi = 180^\circ$. The result is a linearly (π) polarised magnetic field. In quadrature excitation, the two signals are applied at positions 90° apart and with a relative phase shift of $\Delta\varphi = 90^\circ$. The resulting magnetic field is circularly polarised and the rotational direction (σ^+ or σ^-) depends on the sign of the phase shift. The advantage of quadrature excitation over linear excitation is that the radio frequency (RF) power requirements for a certain B_1 amplitude is reduced by a factor of 2 [CHS83].

In the τ SPECT prototype measurement, a first version of a birdcage resonator used as spin flipper was successfully tested [Kar17]. It was built in high-pass design at linear RF coupling and operated at 10.24 MHz in a magnetic field of $B_0 = 350.7$ mT at $I_{\text{main}} = 56.7$ A. However, due to geometry and magnetic field changes, this spin flipper could not be used after the upgrade to purely magnetic storage of UCN.

3.3.2 The birdcage resonator for τ SPECT

Typically, birdcage resonators are best suited for operating frequencies of several 10 MHz [HES85, Lei97, HBD12], i.e. their resonance frequencies ranging from ~ 10 MHz to ~ 100 MHz. The required spin flipper frequencies of $f_{\text{SF}} \simeq 10$ MHz in τ SPECT are thus comparably low and only at the edge of the optimum operating range. With a birdcage resonator in high-pass design and the sinusoidal excitation in the highest frequency mode, this would mean that the entire frequency spectrum would have to be shifted down, resulting in an operation outside of the optimum range.

Therefore, a low-pass design was chosen for the new spin flipper, because with the sinusoidal excitation here in the lowest mode, the birdcage resonator remains in its optimum operating range and tuning to the required frequency is easier.

3.3.2.1 Construction and tuning

The birdcage resonator was soldered from 2 mm thick copper stripes for optimum heat distribution. Its dimensions are: Length $l = 100$ mm and inner diameter $d = 64$ mm. The capacitors had to fulfill the following parameters:

1. They required low dielectric losses to tolerate RF (this is quantified by the dissipation factor DF),
2. they must withstand high voltages, and
3. their capacitance should not change upon cool down ($300\text{ K} \rightarrow 200\text{ K}$), because the tuning of the resonance was done at room temperature but the operational temperature in τ SPECT was $T \simeq 200\text{ K}$.

The MC series by Cornell Dubilier¹⁰ with dielectric C0G(NP0)¹¹ fulfilled these requirements and were thus used: They have high quality factors of $Q > 2000$, resulting in low dissipation factors $DF = 1/Q < 5 \times 10^{-4}$, and withstand voltages of $U \geq 500\text{ V}$.

The assembled spin flipper is shown in Fig. 3.18 (left). In total, a capacitance of $C_R = 2.83\text{ nF}$ was inserted in each rung. The RF coupling was done capacitively using the tuning capacitors C_T . A PT1000 sensor was attached to the copper surface for temperature surveillance. A pick-up coil was added for operational checks after installation in τ SPECT. The right side of the figure shows the resulting resonance at $f_{\text{SF}} = 10.26\text{ MHz}$. It was

¹⁰The datasheet can be found here: <https://www.cde.com/resources/catalogs/MC.pdf>

¹¹C0G is the letter code of the *Electronic Industries Alliance* (EIA, ceased operations in Feb. 2011), NP0 is the name of the ceramic material. It is specified with a capacitance drift of $0 \pm 30\text{ ppm/K}$.

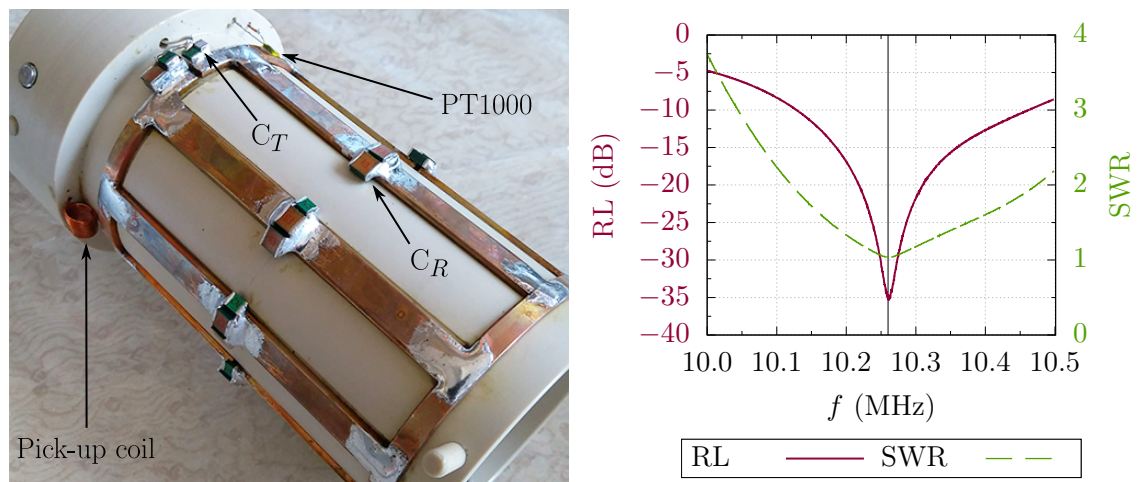


Figure 3.18: Finished birdcage resonator and resonance frequency after optimisation. Left: The birdcage resonator with capacitors C_R within the rungs and capacitors C_T for RF tuning. The PT1000 sensor and the pick-up coil are used for temperature and operational checks after installation in τ SPECT. Right: The resonance after optimisation. The resonance parameters are found to be $RL = -35\text{ dB}$ (the return loss is shown in red) and $SWR = 1.04 : 1$ (green dashed line) at a resonance frequency $f_{\text{SF}} = 10.26\text{ MHz}$.

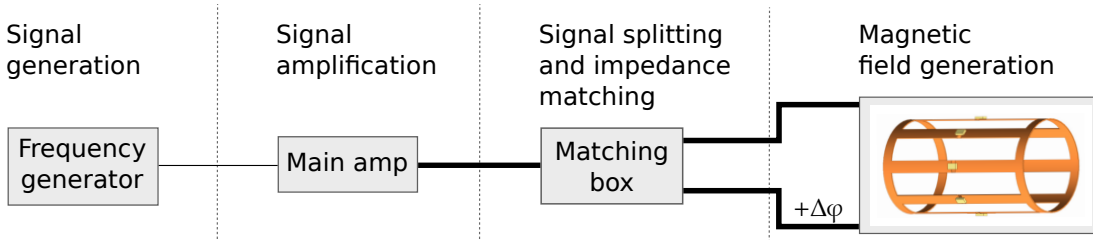


Figure 3.19: Signal scheme of the birdcage resonator. The RF signal is produced by a frequency generator and amplified afterwards. The signal splitting and impedance matching is done by the 'Matching Box'. The split signals are then coupled capacitively into the birdcage resonator with one of the signals phase shifted by $\Delta\varphi = 90^\circ$.

measured using a vector network analyser¹². The depth of the resonance is a crucial aspect when irradiating RF power into an electrical circuit: One parameter to use as a quantification is the return loss (RL), which gives the ratio of the reflected power at a load with respect to the irradiated power on a logarithmic scale. Values below $RL = -30$ dB refer to a reflected power fraction below 10^{-3} which we take as target upper limit. A second parameter is the standing wave ratio (SWR). It is a measure of impedance matching of loads to the characteristic impedance of a transmission line, the optimum would be $SWR = 1 : 1$. The resonance of the birdcage resonator was tuned using C_R and C_T , resulting in $R_L = -35$ dB and $SWR = 1.04 : 1$.

Finally, to complete the circuit, the connection between a frequency generator¹³, a power amplifier¹⁴ and the birdcage resonator was realised as shown in Fig. 3.19. A single RF signal was generated and amplified, and afterwards split into two lines inside the so-called 'Matching Box'. This box has the main purpose to match the circuit to the $Z = 50\Omega$ impedance of the amplifier. In a not fully matched circuit, the imaginary part of the complex impedance $Z = R + iX$, the reactance X , leads to the power reflections mentioned in the context of the return loss. It thus decreases the power stored inside the load (i.e. the spin flipper) and could in the worst case damage the power amplifier. Behind the matching box, one of the split signals is phase shifted by $\Delta\varphi = 90^\circ$ for quadrature excitation of the birdcage resonator. In the required frequency range, the wavelength is on the order of several meters, so that an easy way to achieve the phase shift is to insert a long cable to increase the travelling distance of the wave. The necessary length is calculated using

$$l = \frac{\lambda_c}{4} = \frac{c_0}{4f_{\text{SF}}\sqrt{\varepsilon_R}} = 5.1 \text{ m} \quad (3.8)$$

with λ_c the signal wavelength inside the cable, c_0 the speed of light in vacuum, f_{SF} the frequency and ε_R the dielectric constant of the cable. The division by 4 leads to the desired 90° shift. Experimentally, a phase shift of $\Delta\varphi = 90.25^\circ$ was realised (cf. Ch. A.3.1) with the amplitude in the shifted signal reduced by $\sim 3.6\%$. With these results, a slightly elliptically polarised B_1 field is to be expected inside the spin flipper.

¹²mini Radio Solutions miniVNA Tiny

¹³Rigol DG1032Z

¹⁴Dressler LPPA 13010 linear power amplifier

3.3.2.2 Cool down behaviour

In order for the B_0 field coils to become superconducting, they have to be cooled to below 9.2 K (cf. Ch. 3.1.1). Consequently, as the cryostat in which τ SPECT is located is a cold bore cryostat, also the temperature of the birdcage resonator and thus all of its components is reduced. Even though the capacitors of the birdcage resonator were chosen for their low temperature coefficient, the resonance frequency may drift due to spatial contraction of the birdcage resonator or changes in the resistance. Therefore, the impact on the frequency tuning was investigated in advance.

The spin flipper was mounted inside the compensation octupole, and the assembly was placed in a glass bowl filled with small glass spheres, which was hung into a Dewar with liquid nitrogen. The glass spheres were used to slow down the cooling process and to prevent the system from breaking of a cold shock. The resonance was measured every 5 – 15 min using the network analyser. The temperature was logged before and after each resonance measurement using the PT1000 sensor at the birdcage resonator. Fig. 3.20 shows the resonance frequency depending on the mean temperature at that time. The frequency error is a conservatively estimated reading error of $\Delta f = 5$ kHz and the temperature error is $\Delta T/2$ of each measurement pair, which is in the plot smaller than the point size.

Starting with room temperature and the resonance frequency $f = 10.260(5)$ MHz, the resonance is shifted upwards as the temperature drops. A linear fit on the cool down data

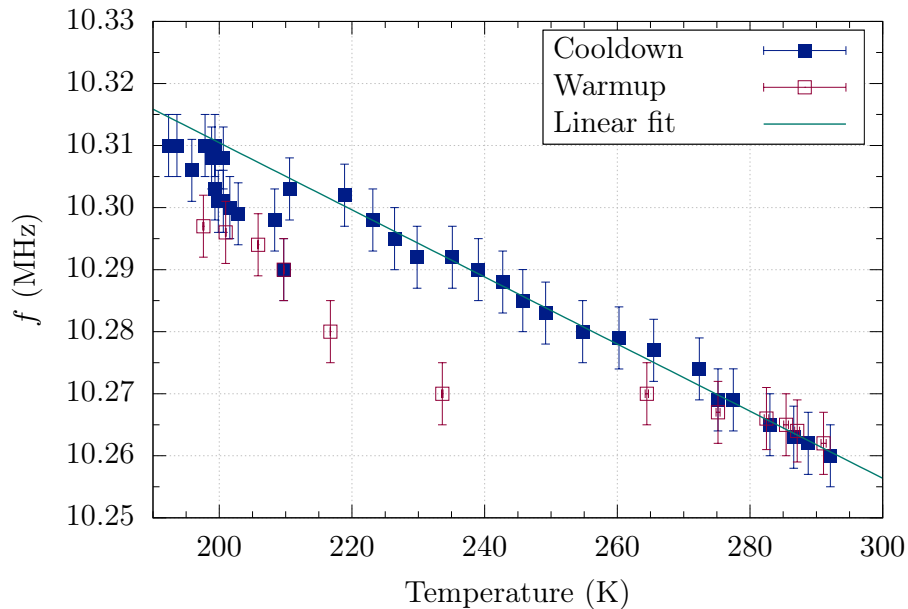


Figure 3.20: Cool down behaviour of the birdcage resonator. The resonance frequency and the temperature are measured every 5 – 15 min while the spin flipper, mounted inside the compensation octupole, is cooled down with liquid nitrogen (blue filled squares) and during the subsequent warm-up (red empty squares). The frequency error is estimated conservatively as 5 kHz, the temperature error is smaller than the point size. The line represents a linear fit to the data between room temperature and $T = 218$ K.

results in

$$f(T) = -aT + b \quad (3.9)$$

with T the temperature in K, and the fit parameters $a = 5.41(12) \times 10^{-4}$ MHz/K and $b = 10.42(0)$ MHz ($\chi^2/\text{ndf} = 0.06$). To avoid the spread at low temperatures, only data down to 218 K was included in the fit. If the spin flipper temperature in τ SPECT dropped to an estimated value of $T = 200$ K, the resonance was shifted to 10.312(2) MHz. This shift had to be taken into account in the choice of the spin flip position, which in case may have had to be corrected to smaller values where B_0 is higher. During warm-up, spin flipper and compensation octupole were taken out of the Dewar. The deviation in the data from the cool down phase might be caused by a different temperature distribution in the birdcage resonator. The final measurements at room temperature, however, show, that the resonance shift is reversible and purely temperature dependent.

3.3.3 The magnetic field of the birdcage resonator

A pick-up coil was used for the measurement of the magnetic field B_1 of the birdcage resonator: A time-varying magnetic field induces a voltage in this coil, which, after calibration with a well-known field, can in turn be used to deduce the B_1 field amplitude.

The calibration of such a pick-up coil is discussed in Ch. A.3.2. The coil was afterwards attached horizontally to a PEEK rod, in order to measure the transversal B_1 field. The measurement setup is shown in Fig. 3.21. The spin flipper was mounted inside the compensation octupole and connected to the signal generation electronics according to Fig. 3.19. The voltage induced in the pick-up coil was monitored using an oscilloscope. Before the field measurement, the quadrature excitation for the generation of circular field polarisation was confirmed by rotating the pick-up coil around the vertical axis. The induced voltage did not drop to zero at any time, which would be the case in a linearly polarised field with the pick-up coil axis oriented perpendicularly to the B_1 field. However, a voltage reduction was visible at 90° relative to the field maximum, indicating an elliptically polarised B_1 field.

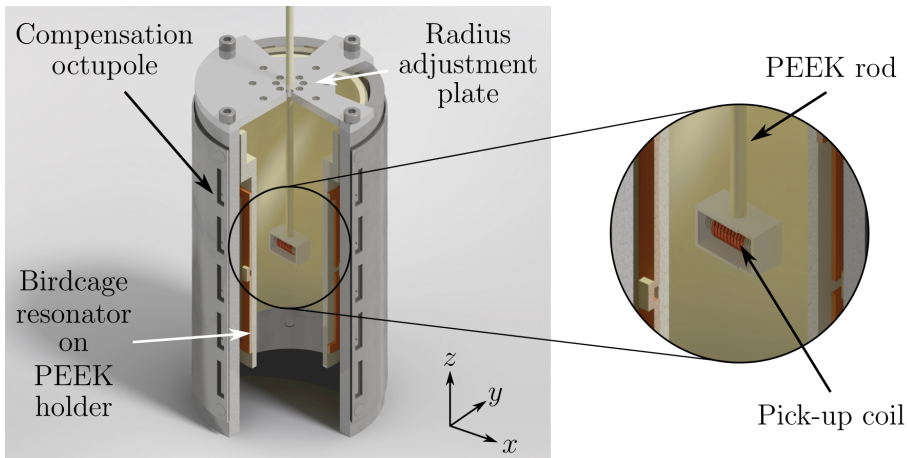


Figure 3.21: CAD rendering of the magnetic field measurement setup of the birdcage resonator. The B_1 field (circularly polarised) rotates in the $x - y$ plane. The pick-up coil (see inset) can be rotated around the vertical axis.

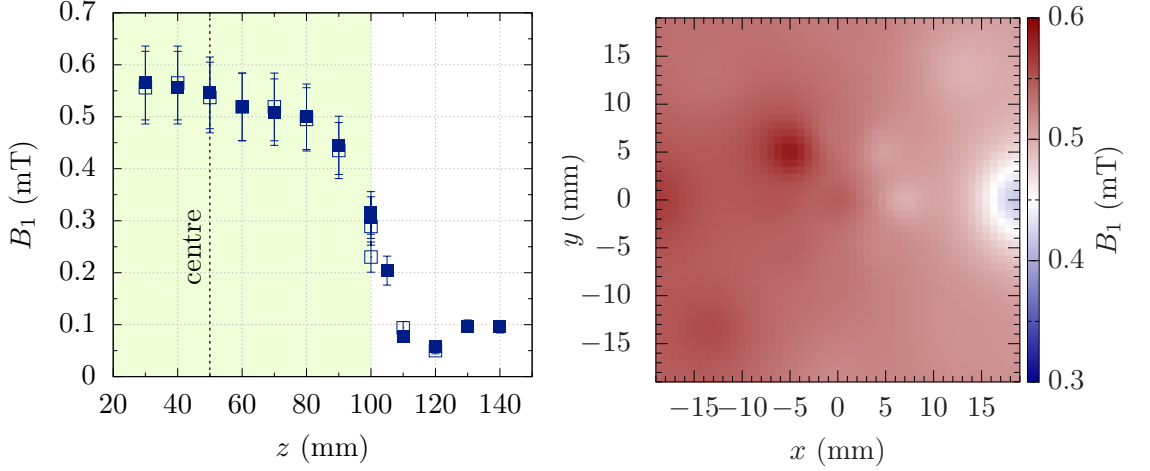


Figure 3.22: Magnetic field inside the birdcage resonator measured with the calibrated pick-up coil. Left: Results from a scan along the central axis ($r = 0$ mm, $\varphi = 0^\circ$), the z -axis is relative to the upper edge ($z = 0$ mm) of the birdcage resonator. The hollow points are measured on the way back to the starting point. The shaded area corresponds to the region covered by the birdcage resonator, its centre ($z = 50$ mm) is marked by the black dashed line. Right: Field on a horizontal plane through the centre of the birdcage resonator.

The measurement of the B_1 field was done in steps of $\Delta z = 10$ mm from the top of the birdcage resonator to the bottom on the measurement radii $r = \{0, 7, 19\}$ mm and at angles $\Delta\vartheta = 45^\circ$ apart. Therefore, the PEEK rod was plugged into the different holes in the radius adjustment plate (cf. Fig. 3.21, left). An RF input power of $P = 140$ W was used for all measurements. At every height, the pick-up coil was aligned first in order to measure the maximum induced voltage, the B_1 field amplitude was then calculated from the calibration in Eq. A.8. The scan along the central axis of the birdcage resonator ($r = 0$ mm, $\Delta\vartheta = 0^\circ$) is shown in Fig. 3.22 (left), the filled points are measured from top to bottom, the empty points back upwards. The relatively large error bars result from the conversion of the measured voltage to the B_1 field, which were calculated using Gaussian error propagation. The measurement starts only at $z = 30$ mm with respect to the birdcage upper edge, because at positions further upwards the radius adjustment plate impeded the cable connected to the pick-up coil. A related problem might be the reason for the comparably larger B_1 amplitude between $z = 30$ and 50 mm: The cable was taped to the PEEK rod directly above the pick-up coil for tension release of the solder points but could not be fixed elsewhere due to constraints in the measurement setup. At measurement positions close to the upper edge of the birdcage resonator, the weight and stiffness of the cable (an FEP coated RG 178 coaxial cable was used) might thus have slightly bent the relatively flexible PEEK rod, so that the measurement position was shifted away from the central axis, where the B_1 field was higher. In total, a field amplitude of $B_1 \gtrsim 0.5$ mT is reached over a wide range up to $\Delta z = 30$ mm from the birdcage centre.

The right side of Fig. 3.22 shows a field map on a horizontal cut plane through the centre of the birdcage resonator. Due to the finite size of the pick-up coil, the measured B_1 field is an average over the cross-sectional area in $x - y$ direction, which using the coil diameter $d \simeq 4.5$ mm and length $l \simeq 10$ mm is calculated as $A \simeq 45$ mm². The

measurement positions are discernible by the darker and lighter spots, in between the field was interpolated.

In conclusion, the measurement shows, that an elliptically polarised B_1 field was generated with amplitudes > 0.4 mT on the central axis (the ellipticity itself was, however, not measured directly). According to calculations described in detail in Ch. 4.1, this field amplitude is sufficient for a spin flip efficiency of $\varepsilon \geq 95\%$.

3.3.4 First experiences with the birdcage resonator and magnetic storage of UCN

The spin flipper was tested with UCN for the first time in beamtime *June2019*. However, this test was unsuccessful as no neutrons could be stored in τ SPECT. A possible explanation could be a wrong polarisation of the B_1 field (cf. Ch. 4.1.1.1) but the beamtime ended before the polarisation could be changed (this would have been attempted by switching the connections of the shifted and the unshifted excitation signal of the spin flipper, cf. Chs. 3.3.2.1 and A.3.1).

After the beamtime, functionality tests were done during which the birdcage resonator assembly was damaged, possibly due to overheating. The assembly was then removed from the τ SPECT cryostat for repairs. The birdcage resonator was re-soldered and all capacitors were replaced. The resonance frequency was then found to be $f_{\text{SF}} = 10.266$ MHz. It was shown in Ch. 3.3.2.2, that the spin flipper resonance frequency is shifted upwards with decreasing temperatures. After cool down, the temperature at the spin flipper was measured as $T \sim 215(10)$ K, which according to Eq. 3.9 results in $f_{\text{SF, theo.}} = 10.304(6)$ MHz, the measured resonance frequency was found at $f_{\text{SF, meas.}} = 10.315(5)$ MHz. Here, the additional shift compared to the theoretical prediction might be caused by changes in the capacitance due to vacuum conditions or the additional material surrounding the compensation octupole.

Due to undiscovered reasons, with this birdcage resonator only a linearly polarised B_1 field was realised. This could be caused by an additional phase shift by the circuit inside the matching box, so that the overall phase shift between the two excitation signals resulted in $\Delta\varphi = 0^\circ$ or 180° . This is not optimal, because the approximation of the spin flip efficiency ε_{SF} in Eq. 4.12 depends on the effective B_1 amplitude with $1 - 1/(1 + \eta B_1^4)$ (with η a proportionality factor of no further interest here). With a circularly polarised B_1 field, the full amplitude is effective for the spin flip, with linear polarisation, however, only a reduced amplitude of $B_1/\sqrt{2}$ is used (cf. Ch. 4.1.1.1 for a discussion about the B_1 field polarisation). To achieve the same spin flip efficiency as with a circularly polarised B_1 field, a stronger B_1 field - and thus higher RF power - is required.

The storage of UCN in the prototype measurement with τ SPECT using a spin flipper with a linearly polarised B_1 field was already successfully tested [Kar17]. During this measurement the spin flipper was positioned in a longitudinal gradient of only $\nabla_z B = 0.05(2)$ mT/cm and the storage octupole was not installed yet, so that no transversal magnetic field was present at that time.

The situation is different with the birdcage resonator presented here, however, in order to calculate the gradients, the required spin flip position needs to be found first. From the measured resonance frequency $f_{\text{SF}} = 10.315(5)$ MHz and the resonance condition $2\pi f_{\text{SF}} = \omega_0$ follows, that the total magnetic field must be $B = 353.8$ mT, the field was calculated using Eq. 3.1. The total field furthermore consists of the longitudinal B_0 field and the

compensated octupole field in transversal direction, which varies over the neutron guide cross section. As a result, the total magnetic field is not fixed over the cross section as well, resulting in a varying resonance frequency. The choice of a fixed value for the transversal field is thus accompanied by the necessity to optimise the spin flip position around the calculated position (cf. Ch. 3.6.3). As fixed value for the compensated octupole field the measurement result $B_{\text{abs,mean}} = 25(4)$ mT at $r = 25$ mm (cf. Tab. 3.1) is used. With

$$B(z_{\text{SF}}) = \sqrt{B_0(z_{\text{SF}})^2 + B_{\text{abs,mean}}^2} \quad (3.10)$$

the required spin flip position z_{SF} is found where $B_0(z_{\text{SF}})$ satisfies this equation. This is the case at $z_{\text{SF}} = 859$ mm, whereby in this work z_{SF} always refers to the centre of the spin flipper. The longitudinal and transversal gradients at this position are calculated as $\nabla_z B(r = 0 \text{ mm}) = 21.7$ mT/cm and $\nabla_t B(r = 25 \text{ mm}) = 2.1$ mT/cm, so that compared to the spin flipper used in the prototype measurement, a high spin flip efficiency using similar B_1 amplitudes cannot be assumed from the beginning. In terms of the parameter $k = \nabla_t B(r = 25 \text{ mm}) / \nabla_z B(r = 0 \text{ mm}) \sim 0.1$ the magnetic field itself does at least not violate the spin flip condition of Eq. 4.16.

From this discussion directly follows one of the major downsides of using a birdcage resonator as spin flipper in τ SPECT apart from its partly challenging construction: Once it is mounted inside τ SPECT, it cannot be tuned to a different resonance frequency and so the filling position with respect to B_0 is fixed. However, especially in an early stage of the experiment when the filling position is not optimised yet, a variation of the filling position is necessary if only for cross-checks. Using a cosine-theta coil as spin flipper, a frequency tuning outside of the experimental setup is significantly more straightforward. Therefore, the birdcage resonator was replaced by two saddle coils in approximation to cosine-theta coils in a second iteration (cf. Ch. 5.1).

With the birdcage resonator installed in τ SPECT for now, the first purely magnetic storage measurements of UCN were done in beamtime *Sept2019* and are shown at the end of this chapter (cf. Ch. 3.6.2).

3.4 The neutron detector

The magnetic field configuration in τ SPECT does not allow for an efficient extraction of neutrons from the trap and guidance towards a detector afterwards. Therefore, in-situ detection of UCN is necessary, which is challenging, because such a detector has to fulfil several requirements: It has to be suitable for cryogenic temperatures, high vacuum, and high magnetic fields of up to 2 T, it needs the ability to measure UCN efficiently also at low temperatures, and finally, it must be movable. The construction and characterisation of such a custom UCN detector is the work of J. Kahlenberg and is discussed in detail in [Kah20], so that here only aspects relevant for this work are summarised.

The detection principle is shown schematically in Fig. 3.23 (left). The essential part is a silver-doped zinc sulphide scintillator (ZnS:Ag, thickness $22.6 \mu\text{m}$) with an 80 nm thick layer of ^{10}B coating on the surface (the dimensions are not to scale). If a UCN impinges on this layer, it is absorbed in a $^{10}\text{B}(n, \alpha)^7\text{Li}$ reaction. The two charged particles α and ^7Li are emitted in opposite directions. One of them enters the scintillator, where in turn scintillation light is produced. A cone shaped light guide made from Polymethyl-

methacrylate (PMMA) guides this light towards a multi pixel photon counter (MPPC)¹⁵. The MPPC detects the photons and generates an analog signal, which is amplified by a signal shaper transferred to the outside of the cryostat, and digitised with a sampling rate of 10 MHz by an analog-to-digital converter (ADC). The data is then sent to PC via Ethernet, where it is written to file during a measurement run. Afterwards, an event detection algorithm analyses and extracts neutron events from the raw data. The algorithm is part of this work, its working principle and the optimisation is described in Ch. A.4.1. It offers an analysis independent of detector baseline drifts or slow noise, such as 50 Hz noise, which was a problem in early measurements with τ SPECT but is solved now.

A picture of the assembled detector¹⁶ is shown on the right side of Fig. 3.23. Here, the light cone is additionally covered with a thin metallised Mylar[®] foil to improve the light transport towards the MPPC. The movement of the detector in and out of the storage volume is realised by the detector side translation stage. In order to increase the mobility, spring-mounted rolls made from PEEK are attached on four sides of the cone. The analog signal of the MPPC is guided out of the cryostat by a vacuum feedthrough. Similar to the spin flipping unit, the longitudinal component of the magnetic field is measured using a 1-axis Hall probe¹⁷, which is mounted on the stabilising ring between the rolls at a distance $\Delta z = 76$ mm from the ^{10}B surface. An additional stainless steel cylinder (not shown here) is used to protect and stabilise the detector setup to the sides.

Comparison measurements with respect to a CASCADE-U detector¹⁸ ('gold standard')

¹⁵Hamamatsu S13361-6050AE-04, 16 channels in a 4x4 array.

¹⁶The picture was taken by J. Kahlenberg.

¹⁷Arepec HHP-NP, <http://www.arepec.sk>

¹⁸UCN detector by **cdt** CASCADE Detector Technologies GmbH, <https://n-cdt.com/>

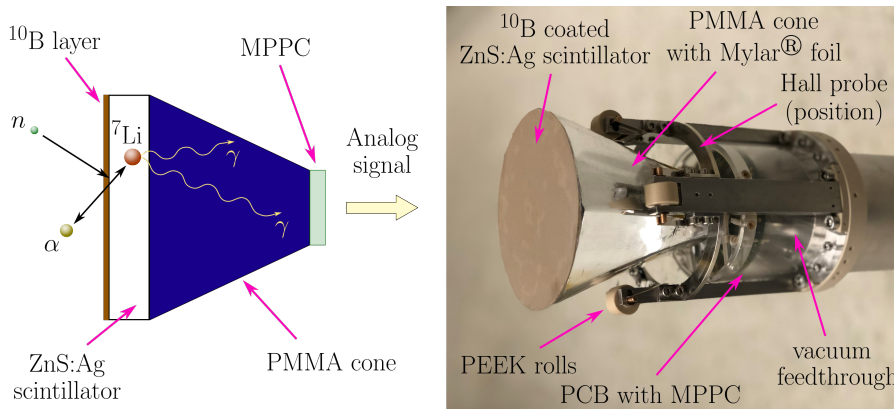


Figure 3.23: Detection principle (left) and setup of a custom UCN detector (right). UCN are captured by a ^{10}B layer, which is coated on a ZnS:Ag scintillator. One of the charged reaction products ($\alpha/{}^7\text{Li}$) produces scintillation light inside the scintillator. This light is transported towards an MPPC by a cone made from PMMA, which is covered with metallised Mylar[®] foil on the outside. Spring-mounted rolls centre the detector and increase its mobility while moving on the storage octupole surface. A Hall probe is used to measure the longitudinal magnetic field. A stainless steel cylinder (not shown) is mounted around the detector for protection and stabilisation to the sides. The detector is the work of J. Kahlenberg [Kah20].

yielded a comparable detection efficiency: UCN were stored in an aluminum storage bottle ($V_F = 54 \text{ neV}$, $V = 9.67(2) \text{ L}$ [Kah20]) for a storage time $t_s = 20 \text{ s}$ and counted afterwards. The UCN density measured with the CASCADE detector resulted in $\bar{\varrho}_{\text{UCN, CASCADE}} = 0.69(2) \text{ cm}^{-3}$ and the density measured with the newly built custom UCN detector in $\bar{\varrho}_{\text{UCN, det}} = 0.73(4) \text{ cm}^{-3}$ [Kah20]. Thus, the detection efficiency of the custom UCN detector compared with the CASCADE detector is

$$\frac{\varepsilon_{\text{UCN, det}}}{\varepsilon_{\text{UCN, CASCADE}}} = \frac{\bar{\varrho}_{\text{UCN, det}}}{\bar{\varrho}_{\text{UCN, CASCADE}}} = 1.06(7), \quad (3.11)$$

i.e. comparable within the error bars for the given UCN spectrum in this setup.

The MPPC of the custom UCN detector requires a reverse bias voltage, which has to be adjusted before measuring. With the MPPC consisting of a multitude of photodiodes operating in Geiger mode, the bias voltage V_{bias} needs to be larger than the so-called breakdown voltage V_{bd} [GH20]. It depends on the MPPC temperature, and so an additional PT1000 sensor on the MPPC PCB is used to adapt the bias voltage according to a theoretical model. The settings are such, that the minimum voltage corresponds to the nominal V_{bd} and the additional voltage, the overvoltage V_{over} , is adjusted manually. Ideally the breakdown voltage would be measured for every MPPC in the 4x4 array, and the bias voltage adapted individually as well. Unfortunately, this is not permitted in the current electronic design, so that an average breakdown voltage had to be inferred from data. The bias voltage is then given by

$$V_{\text{bias}} = V_{\text{bd}} + V_{\text{over}}. \quad (3.12)$$

The overvoltage was optimised in τ SPECT using $t_s = 50 \text{ s}$ storage measurements (cf. Ch. A.4.2). A suitable voltage range was found between $V_{\text{over}} = +3.0$ and $+4.5 \text{ V}$. At smaller values, the detection efficiency is reduced, whereas the detector noise increases with higher voltages. If not mentioned otherwise, all measurements in this work were done at $V_{\text{over}} = +3.5 \text{ V}$.

3.5 Slow control of the experiment

The sequence of every measurement run is controlled electronically in order to ensure exact timing of all involved components as well as reproducibility between individual measurements. This sequencing is done by the so-called 'Delay Box': It is triggered by the TRIGA reactor pulse electronics shortly before UCN production starts. It features 24 outputs with either $+5 \text{ V}$ TTL logic or $+24 \text{ V}$, which are switched on and off at adjustable times with respect to the trigger signal. In order to use these signals, however, all components involved in the experiment require the ability to either be triggered and perform predefined actions, or that they remain active as long as the output signal of the Delay Box is high. The main components to which this applies are listed in the following.

- **Data recording:** The ADC samples the detector's MPPC data with 14 bit at 10 Msps . This corresponds to roughly 20 MB/s , which would result in large files, if data recording was active also between measurements. Therefore, a TTL signal of the Delay Box is read by a GPIO bridge¹⁹, which starts data recording at the beginning of the measurement and stops it afterwards.

¹⁹The implementation of the bridge and the readout was done by Prof. D. Ries.

- **UCN shutter:** The shutter at the beamline entrance is moved by pressurised air. Its status being open or closed is controlled by a TTL signal, which switches the valve of the pressurised air. In order to prevent accidental opening of the shutter when the cryostat is evacuated but no beamline is attached, an interlock system was developed, which allows the shutter to open only, if the beamline pressure is below a certain threshold²⁰ (cf. Ch. A.7.2).
- **RF amplifier:** Efficient filling of UCN in τ SPECT depends on optimal start and stop times of the spin flipping B_1 field. The amplifier used with the birdcage resonator has a so-called blanking input, a TTL gate, which activates the output of the amplifier for the duration of a high TTL signal. The output power scales with the voltage amplitude of the frequency generator signal.
- **The translation stages:** Both the spin flipping unit and detector are moved by their translation stages, which are connected to stepper motors by gear chains. The controllers of the stepper motors offer the possibility to store predefined movement profiles, which are selected and triggered by TTL signals. Within these sets, driving velocities and positions are defined, which are the filling and storage position of the SFU, as well as the storage, cleaning, and counting positions of the detector. Encoders at both stepper motors are used for closed-loop surveillance, so that no motor steps are lost and position reproducibility is increased. With a dedicated readout and control program (cf. Ch. A.7.1), the status and current positions are monitored, and positions and velocities can be altered between measurements. Also, manual control of the stepper motors is possible remotely.
- **Pulse trigger:** The Delay Box is triggered to start a sequence if the reactor is ready for a new pulse. However, before the pulse, data recording has to be started and the shutter has to open. Therefore, the pulse trigger is delayed by 5 s, so that by then τ SPECT is ready for data taking.

All components (except for the detector bias voltage) can be configured remotely to allow changing of parameters while the reactor is active, inhibiting access to the devices. The sequence of one measurement run is shown in Fig. 3.24 and consists of the following steps:

1. As soon as the Delay Box is triggered, data recording begins and the shutter opens.
2. The pulse is triggered, which in the data is visible as a peak produced by thermal neutrons ('thermal peak'). As the detector start time varies on the 100 ms scale between measurements, this peak is used as time reference t_0 in data analysis²¹.
3. The RF amplifier is switched on at t_{fill} and remains on for the filling duration Δt_{fill} . After it is switched off, the filling process is finished. The shutter closes and the SFU is retracted from the storage volume.

²⁰Currently the threshold is set to $p = 8.6 \times 10^{-3}$ mbar.

²¹Between the time the Delay Box is triggered by the reactor electronics and the actual execution of the pulse a jitter of several milliseconds can occur, e.g. due to signal delays by long cables or the shoot-out of the pulse rod in the reactor (cf. Ch. A.1). The timing of all hardware components is relative to the Delay Box trigger, whereas the timing of all data analysis is referenced to the thermal peak. As this can cause inaccuracies in the experimental sequence, a dedicated detector is currently under construction, which detects the thermal peak and triggers the hardware accordingly.

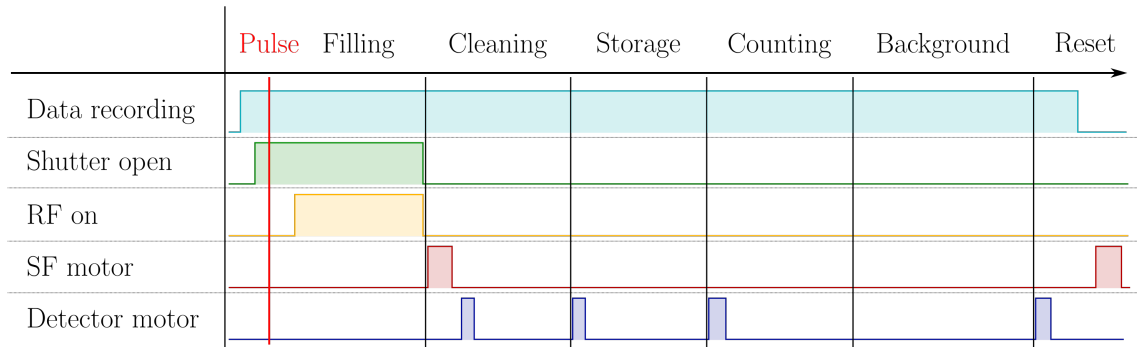


Figure 3.24: Schematics of TTL pulses and gates for individual components in τ SPECT. The TTL signals are provided by the Delay Box. The red line corresponds to the trigger of the pulse.

4. If spectrum cleaning is included in the measurement, the detector moves to the cleaning position at t_{clean} and remains there for the cleaning duration Δt_{clean} . When it is retracted back to its storage position, the storage time t_s begins.
5. Afterwards, the detector is moved to the counting position and measures the surviving neutrons. It remains at the counting position for around 150 s to allow for background measurements.
6. Finally, the experiment is reset for a new run: The detector drives back to the storage position and data recording stops. For so far unknown reasons, the movement of the SFU back to the filling position creates large noise peaks in the ADC data, so that this step was pushed to the very end of the sequence.

3.6 First operation of τ SPECT after commissioning

The components relevant for magnetic storage were installed in 2018/2019. A picture of the experiment from the side is shown in Fig. 3.25. The cryostat is housed inside the iron yoke to minimise stray fields. The yoke in turn is located on four truck lifts, so that the height of the experiment can be adjusted. The height is measured by a time-of-flight distance sensor²² permanently located at the lower edge of the yoke, which is controlled by a Teensy 3.2 microcontroller board. At maximum, a height of 2 m above the UCN source exit of the TRIGA reactor, indicated at the bottom left, is possible. The beamline connects the source exit to the UCN shutter. Characterisations and optimisations of the beamline are discussed in [Kah20], the beamlines used in this work are briefly presented in Ch. A.6. In the following, beamline No. 1 (also shown in the picture here) is used.

With a total of four turbo molecular pumps (TMPs), τ SPECT is evacuated to $\sim 1.3 \times 10^{-7}$ mbar. Inside the beamline, a pressure of $\sim 10^{-4}$ mbar is achieved, which is sufficient for the interlock system (cf. Ch. A.7.2) to allow opening the UCN shutter. Two cold heads at the top of the cryostat cool the superconducting coils down to $T \leq 10$ K. Details on the pumping concept, as well as the pumping and cool down behaviour of τ SPECT are found in [Kah20].

²²Adafruit VL53L0X

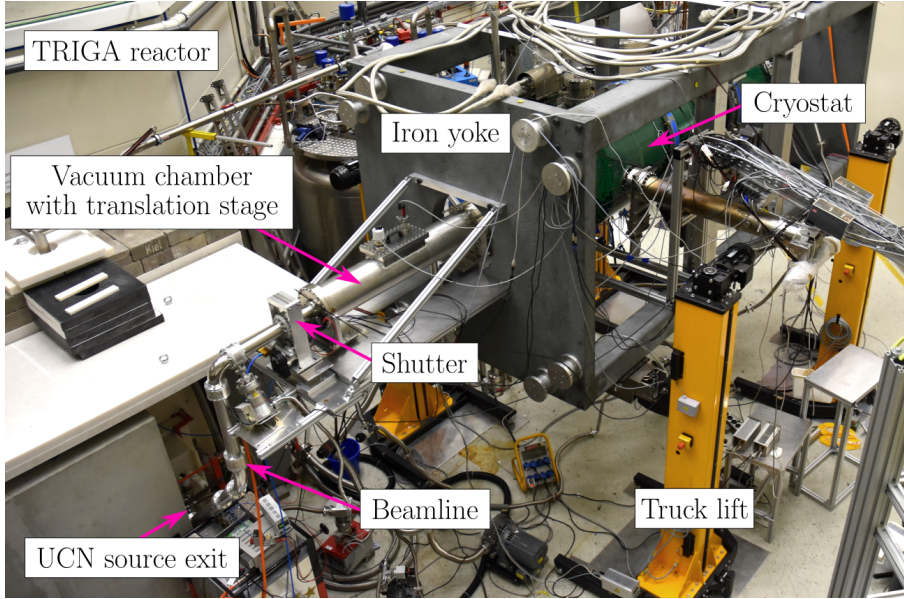


Figure 3.25: Experimental setup of the τ SPECT experiment as seen from the side.

3.6.1 Position calibration of the translation stages

The positions with respect to the z -axis in τ SPECT (cf. Fig. 3.3, here referred to as ' τ SPECT coordinates') are known theoretically taking a computer-aided design (CAD) model of the translation stages. Due to mechanical offsets in the construction of the translation stages which are not included or accounted for in this model, deviations in the real position are unavoidable. Furthermore, the only relevant parameter is the position of the spin flipping unit and the detector with respect to the magnetic field and not the position relative to mechanical components. Therefore, the two Hall probes at SFU and detector were used to measure the B_0 field²³ [Fra19] and from comparisons with the simulated field, the available positioning range was deduced. This range is limited by two electrical end stops. The outer end stop is the so-called 'zero-position', to which all further positions are related to (cf. Ch. A.7.1).

The calibration procedure for the SFU and detector translation stage was identical: From the zero-position onwards, magnetic field measurements were done in steps of $\Delta z = 10$ mm, on the detector side until the inner end stop was reached and on the SFU side around 2/3 of the total driving range. Because of its notably peaked shape, the B_0 field gradient was used for the calibration instead of the absolute B_0 field, and the measurement relative to the zero-position was shifted until it overlapped with the simulation.

The result is shown in Fig. 3.26, on the left for the SFU and on the right for the detector. The markers depict the calculated gradient from the measurement with the Hall probes. However, so far the calibration refers to the positions of the Hall probes and not the centre of the SFU and the detector surface themselves, so that an additional longitudinal offset has to be included in the calibration ($\Delta z_{\text{SFU}} = -61.4$ mm and $\Delta z_{\text{det}} = 76$ mm). The accessible range is thus given by the grey area, which for the SFU ranges from $z_{\text{SFU}} = 397$ mm to 1200 mm, and for the detector from $z_{\text{det}} = 1599$ mm to 1932 mm. The spikes in the measurement data are caused by the storage octupole fringe field. The position of these

²³The readout and the required electronics for the Hall probes were implemented by K. Franz.

spikes match the theoretical position of the storage octupole according to the CAD model (on the SFU side $z = 570$ mm and on the detector side $z = 1950$ mm) and thus confirm the calibration of the translation stages. In this work, all positions are hereafter given in calibrated τ SPECT coordinates.

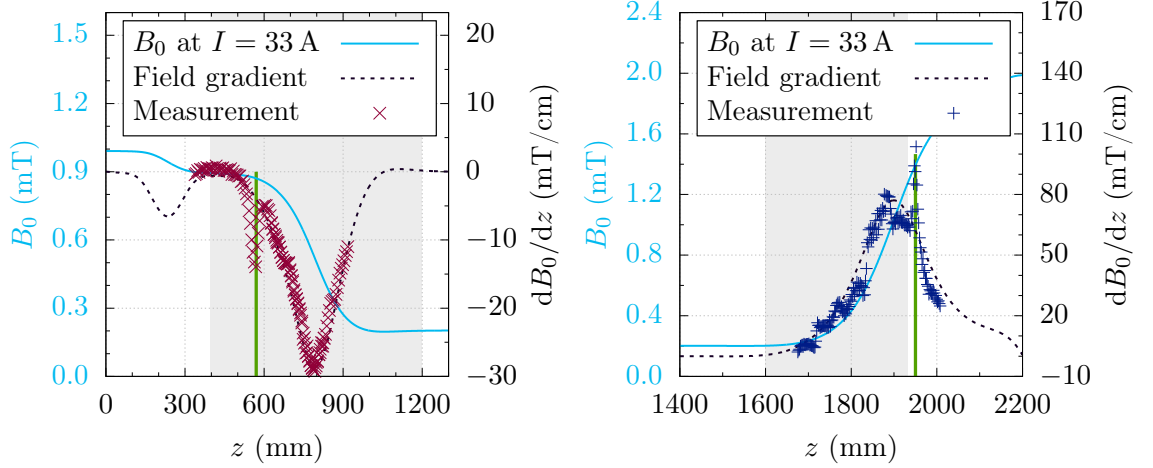


Figure 3.26: Calibration of the translation stage positions of the SFU (left) and the detector (right). The light blue lines refer to B_0 at $I_{\text{main}} = 33$ A (left axis), the black dashed lines are its gradient (right axis). From the magnetic field measurement with the 1-axis Hall probes, the gradient is calculated and the measurement position shifted until measurement and simulation overlap. The grey areas show the accessible range of SFU and detector, the offset at the outer positions arise from the positional offset of the Hall probes. The green lines mark the two edges of the storage octupole according to the CAD model. The spikes in the measurement at these positions confirm the calibration result.

3.6.2 The arrival spectrum

During storage measurements with τ SPECT, the arrival spectrum of neutrons in the detector follows a specific pattern, which is shown exemplary for a 50 s storage run including cleaning in Fig. 3.27. The thermal peak is not visible here because of the 1 s-binning and the large time range. Neutrons which are unstorable fly through the experiment and reach the detector immediately. This corresponds to the first high peak in the data. The spin flipper is switched on $t_{\text{fill}} = 2$ s after the reactor pulse trigger and remains on for $\Delta t_{\text{fill}} = 4$ s. Cleaning begins at $t_{\text{clean}} = 16$ s, so that the peak of cleaned neutrons is separable from the bunch of fast neutrons in the beginning (cf. Ch. 5.3.1 for the current status of the cleaning time optimisation). After a cleaning duration of $\Delta t_{\text{clean}} = 30$ s, the storage time begins. Subsequently, the surviving neutrons (this interval is also called the 'counting interval') and the background counts are measured.

The number of neutrons from the reactor varies between individual pulses, so that a normalisation of the measured neutron counts is necessary in order to compare the results afterwards. Three normalisation methods are presented and compared in Ch. 5.3.2. So far the best results are achieved normalising to the average pulse energy \bar{E}_{pulse} of the

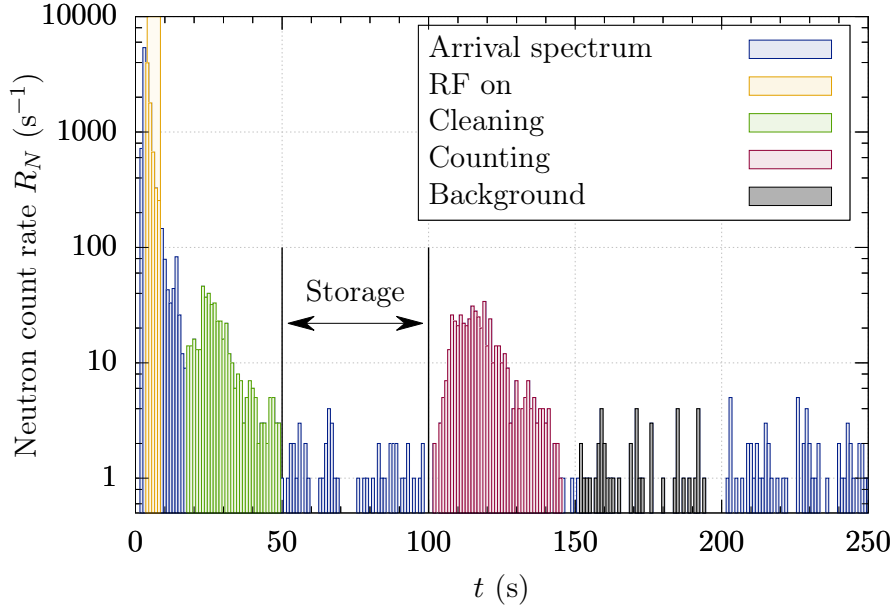


Figure 3.27: Neutron arrival spectrum of a 50s storage measurement with cleaning at 1s binning. The first bunch of neutrons corresponds to neutrons which are too fast to be stored and reach the detector immediately. The yellow area marks the time during which the spin flipper RF is switched on. Marginally trapped neutrons are removed from the trap during cleaning, they appear in the detector as the peak marked in green. After the storage time, the detector counts the remaining neutrons (red). The subsequent interval in grey is used for background measurements.

particular beamtime via

$$N = \frac{C_{\text{count}} - C_{\text{bg}}}{E_{\text{pulse}}} \bar{E}_{\text{pulse}} \quad (3.13)$$

with C_{count} the neutrons measured in the counting interval, C_{bg} the background counts, and E_{pulse} the energy of the specific pulse. The error of each measurement is calculated using statistical \sqrt{N} errors with Gaussian error propagation in the normalisation.

3.6.3 The first purely magnetic storage curve

The first storage curve using only magnetic fields for confining UCN in τ SPECT was measured in beamtime *Sept2019*. In order to achieve the maximum UCN density, the spin flipper power, position and timing were optimised in advance.

Dependency on RF power Generally, the spin flip efficiency ε_{SF} rises with the amplitude of B_1 until a maximum of 100% is reached (cf. Eq. 4.12 in Ch. 4.1). Before installing the spin flipper in τ SPECT, B_1 was measured depending on the irradiated RF power, which is shown on the left side of Fig. 3.28. The large error bars arise from the conversion of the measured induction voltage in the pick-up coil to B_1 (cf. Ch. 3.3.3). The line is a fit to the data according to

$$B_1(P) = a\sqrt{P} + b \quad (3.14)$$

with $a = 37.6(7) \times 10^{-3} \text{ mT}/\sqrt{\text{W}}$ and $b = 4.5(3) \times 10^{-2} \text{ mT}$ ($\chi^2 = 0.03$), and used for extrapolations to higher power (Ch. 5.1.1.2 derives the expected \sqrt{P} -behaviour of B_1). The right side of the figure shows the normalised number of stored neutrons after $t_s = 50 \text{ s}$ without cleaning depending on the RF power. It can be seen, that from $P \sim 270 \text{ W}$ onwards, the number of neutrons does not increase anymore within errors and a saturation is reached. This is the case, if ε_{SF} is close to 100 % and even though B_1 is increased further, no additional neutrons are available in the storable energy range (cf. Ch. 4.2 for the energy acceptance of the trap). However, in order not to damage the birdcage resonator or the matching circuit with high powers and thus too high heat loads, the measurements for the storage curve were done at $P = 185(5) \text{ W}$, which according to Eq. 3.14 corresponds to $B_1 = 0.56(1) \text{ mT}$. Here, a neutron saturation was reached to $79 \pm 9\%$.

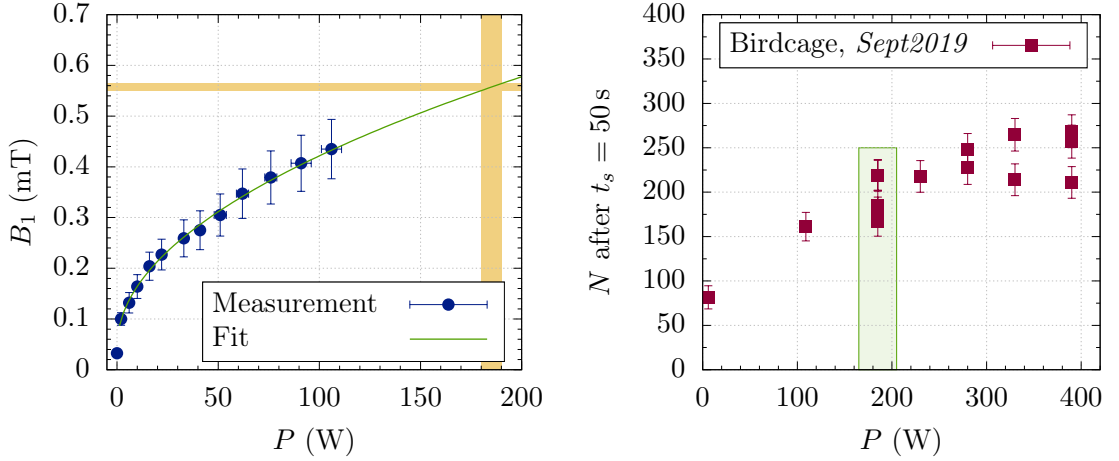


Figure 3.28: Left: Ex-situ measurement of the B_1 amplitude with respect to the irradiated RF power using the calibrated pick-up coil (blue bullets) with a fit according to Eq. 3.14 (green line). The yellow bands mark the parameters used for the storage curve ($P = 185(5) \text{ W}$ with $B_1 = 0.56(1) \text{ mT}$). Right: Number of stored neutrons after $t_s = 50 \text{ s}$ (red squares). From $P \sim 270 \text{ W}$ onwards, a saturation is reached within errors. The green box marks the power used for the storage curve.

Birdcage resonator position optimisation The optimum filling position for the given resonance frequency $f_{\text{SF}} = 10.315 \text{ MHz}$ was calculated as $z_{\text{SF}} = 859 \text{ mm}$ earlier in this section (cf. Ch. 3.6) using the simulation of the B_0 field and the measurement results of the compensated octupole field B_t (cf. Ch. 3.2.2.1). Thereby z_{SF} always refers to the centre of the spin flipper. However, the calculation requires a correct position calibration of the translation stage and does not take into account, that B_t might vary when moving the spin flipper (and thus the SFU) to a different longitudinal position.

Therefore, the filling position was optimised in τ SPECT using neutron storage measurements at $t_s = 50 \text{ s}$ without the cleaning procedure. Keeping the RF frequency constant, the filling position was varied around the calculated position and the number of stored

neutrons compared afterwards. The detector overvoltage was set to $V_{\text{over}} = +2.0$ V and the RF power to $P = 109$ W.

The result is shown in Fig. 3.29, the black empty circles are measured with the spin flipper switched off, resulting in 36(11) neutrons on average. These may be marginally trapped neutrons, which are independent of the filling process. With the spin flipper active, $N = 108 \pm 13$ neutrons were stored on average at filling positions between 839 and 879 mm. Here, the optimisation shows a plateau-shaped behaviour around the calculated position at $z_{\text{SF}} = 859$ mm. This can be explained by the length of the spin flipper: If the spin flipper centre is located at an offset with respect to the calculated optimum filling position, but due to its length the resonance condition $2\pi f_{\text{SF}} = \omega_0$ is still fulfilled inside the spin flipper volume, neutrons can be filled into the trap anyway.

However, during the beamtime, the ADC raw data showed 50 Hz noise, which could at that time not be filtered by the peak detection algorithm (cf. Ch. A.4.1 for a discussion about the problem of noise in the detector data). Therefore, the optimum filling position for the given frequency was then considered to be $z_{\text{SF}} = 879$ mm, what - lying within the plateau - was still in the optimum range.

RF timing optimisation After the reactor pulse, UCN travel through the beamline towards the storage volume. At the typical height of τ SPECT of $h = 1.5$ m above the source exit and using beamline No. 1 (cf. Ch. A.6), the length of the beamline between

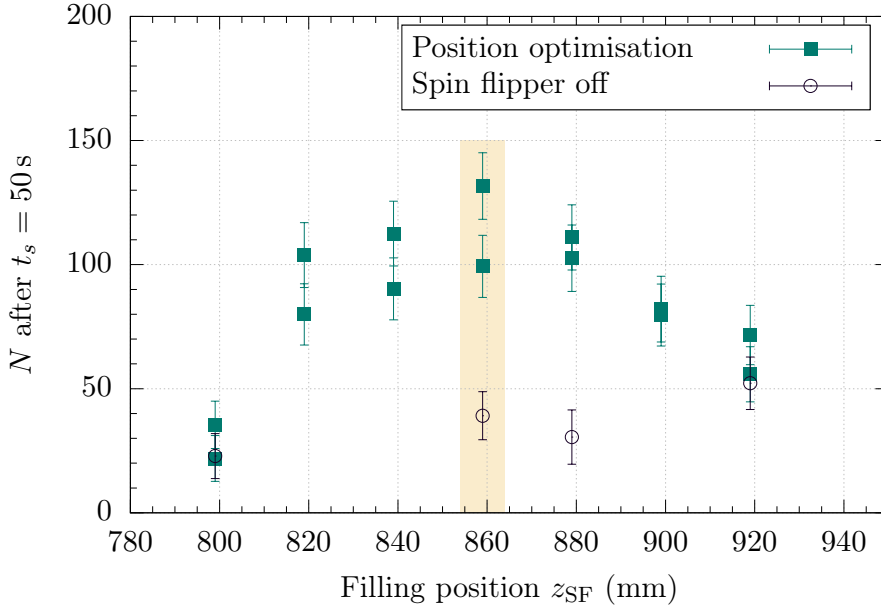


Figure 3.29: Spin flipper position optimisation of beamtime *Sept2019* using 50 s storage measurements at $V_{\text{over}} = +2.0$ V and $P = 109$ W. The measurements with spin flipper active (turquoise squares) show a plateau-like behaviour around the calculated optimum position at $z_{\text{SF}} = 859$ mm (yellow). The hollow black circles correspond to measurements with the spin flipper switched off. During the beamtime, the optimum position was considered to be $z_{\text{SF}} = 879$ mm due to 50 Hz noise in the ADC data which distorted the analysis.

the source and the spin flipper is estimated as $l_{\text{beamline}} \simeq 5.4$ m. Depending on their kinetic energy (and thus their velocity) and their trajectory angles relative to the axis of the UCN guide, the time it takes them to reach the spin flipper differs by several seconds. Therefore, it is necessary to optimise the time during which the spin flipper irradiates the B_1 field: As soon as neutrons in the storable energy range arrive at the spin flipper, it must be active already. Furthermore, leaving the RF switched on for too long causes on the one hand a high heat load in the birdcage resonator and the matching circuit, but it can also flip the already stored LFS back to HFS, if they enter the neutron guide again (back-diffusion) at the position the copper shield of the SFU.

This makes a timing optimisation necessary, which was done in beamtime *Nov2019* using 50 s storage measurements at $z_{\text{SF}} = 859$ mm and $P = 109$ W. The left side of Fig. 3.30 shows a neutron arrival spectrum in the first seconds of the measurement with three time windows relative to the thermal peak at t_0 , during which the spin flipper would be switched on. The right side depicts the normalised average number of neutrons N in the counting interval after $t_s = 50$ s depending on the filling start time t_{fill} . The optimum at $t_{\text{fill}} = 4$ s with $\Delta t_{\text{fill}} = 1$ s shows, that here most of the neutrons in the storable energy range arrive at the spin flipper. This is confirmed, if the interval between $t = 4$ and 5 s is included in longer filling durations, but filling starting earlier. From the plateau at later start times follows, that the neutrons do not arrive in a single bunch, but rather continuously due to different trajectory angles and thus different travelling durations inside the beamline. The filling duration $\Delta t_{\text{fill}} = 4$ s was measured with higher statistics at $t_s = 200$ s (cf. Fig. B.6) and yields similar results in comparison with $\Delta t_{\text{fill}} = 3$ s.

In conclusion, we do not find a clear optimum timing combination for the spin flipper, but rather an optimum range, which has to include the 4 – 5 s time interval. From the fact that we do not see a decrease in N with rising Δt_{fill} follows, that the filling duration was either not too long to spin flip a significant amount of the stored neutrons back to HFS,

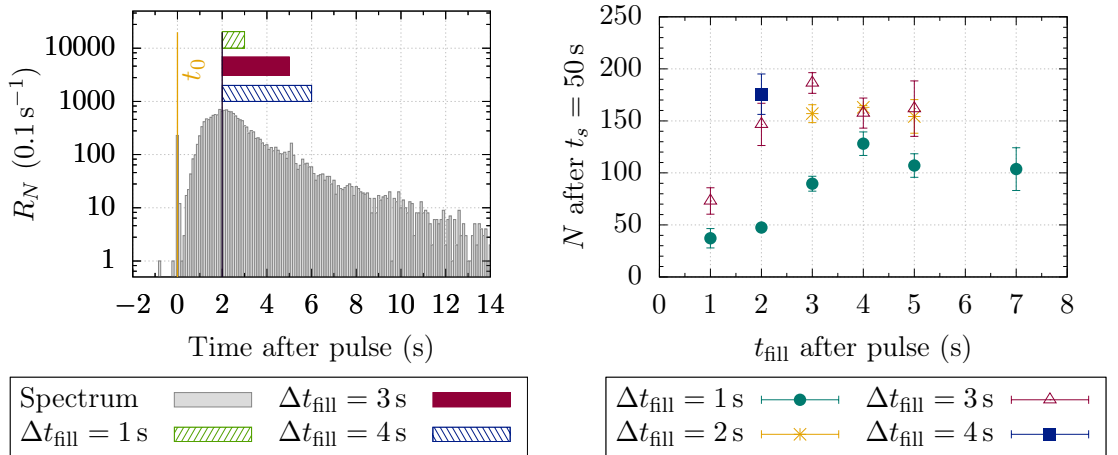


Figure 3.30: Left: Neutron arrival spectrum shortly after the reactor pulse at t_0 (yellow line) with 0.1 s binning. The boxes mark selected filling durations at a filling start time $t_{\text{fill}} = 2$ s. Right: Number of neutrons in the counting interval depending on t_{fill} for different filling durations. Without a clear optimum, the timing was set to $t_{\text{fill}} = 2$ s and $\Delta t_{\text{fill}} = 4$ s for all measurements in this work.

which during this time would have had to find their way back into the narrowed neutron guide, or that an equilibrium between filling and emptying of the trap was reached. If not mentioned otherwise, all measurements in this work were done with $t_{\text{fill}} = 2$ s and $\Delta t_{\text{fill}} = 4$ s.

The first storage curve with τ SPECT The storage curve was measured in beamtime *Sept2019* without cleaning and is shown in Fig. 3.31 with normalisation to the pulse energy. The shape follows an expected double exponential decay according to

$$N(t) = a_1 \exp(-t/\tau_1) + a_2 \exp(-t/\tau_2), \quad (3.15)$$

with the first term accounting for marginally trapped neutrons (cf. Ch. 2.2.4). Fitting this function to the measurement data yields the fit parameters given in Tab. 3.2. From these parameters follows, that around 145(21) neutrons were fully storable in τ SPECT. Given this number, we estimate in the following, how many and which measurement runs are required for a first result on the neutron lifetime with $\Delta\tau \lesssim 1.0$ s.

Table 3.2: The fit parameters of the storage curve measured in beamtime *Sept2019* as shown in Fig. 3.31. The fitting function is given by Eq. 3.15.

a_1	τ_1	a_2	τ_2	χ^2/ndf
400.2(57.8)	29.6(6.4) s	145.0(21.0)	476.9(79.7) s	1.53

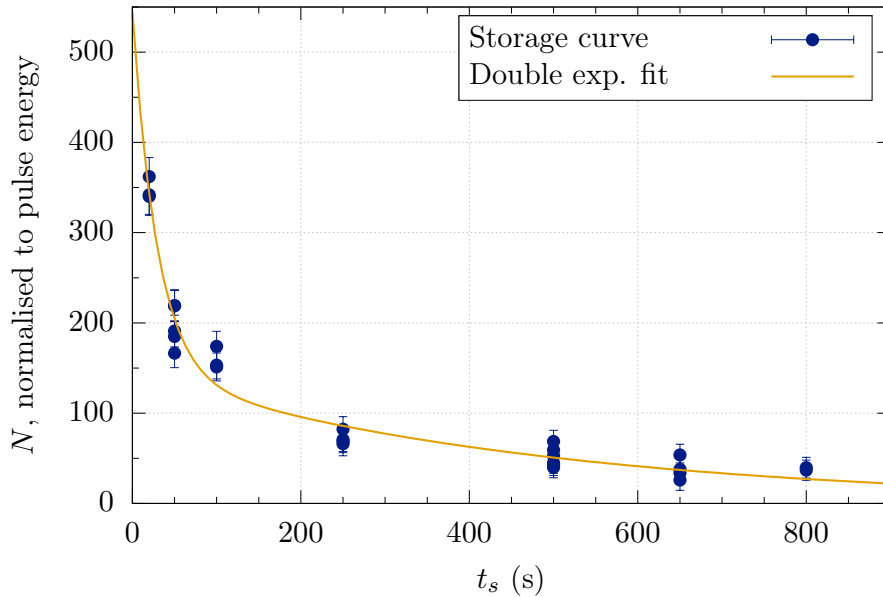


Figure 3.31: First purely magnetic storage curve measured in beamtime *Sept2019*. The neutron counts are normalised to the pulse energy. The double exponential fit according to Eq. 3.15 results in the fit parameters listed in Tab. 3.2.

3.6.4 Measurement time required for a first neutron lifetime result

The overall measurement duration $T_{\Delta\tau}$ depends on the one hand on the number of stored neutrons at $t_s = 0$ s, N_0 , but on the other hand also on which storage times are used for the storage curve. The simulation presented in the following attempts to give a rough estimation on the order of magnitude of $T_{\Delta\tau}$ until the uncertainty in the measured neutron lifetime drops to below $\Delta\tau_n = 1.0$ s.

To start with, we assume $N_0 = 1500$ simulated neutrons and $\tau_n = 880$ s, and roughly optimise, which and how many different storage times t_s are required for a minimum $T_{\Delta\tau}$. Therefore, we define measurement sequences consisting of a number of k different storage times. Using N_0 and τ_n , the number of neutrons $N(t_s)$ at each storage time is calculated using single exponential decay and adding statistical fluctuations with $\sigma = \sqrt{N}$. The sequence is repeated over and over, every time adding the results to the previous ones and thus increasing the data set with every step. After every iteration, the current data set is fitted with an exponential function. The quantity of interest is the required number of repetitions n , until $\Delta\tau_n$ is equal to 1.0 s or smaller.

However, n is not strictly representative for a minimum in $T_{\Delta\tau}$, because the latter depends on k and the storage times themselves. Therefore, first the measurement time for each sequence t_{seq} is calculated and with that the overall measurement time $T_{\Delta\tau} = nt_{\text{seq}}$. Each measurement is assumed to take the storage time and 200 s additionally to account for the filling, cleaning and counting procedure. Measurements with $t_s < 800$ s are assigned a fixed duration of 15 min, which is estimated as the required time interval between two reactor pulses. Tab. 3.3 lists the results of the optimisation process. The optimum is found for a sequence consisting of $t_s = [50, 100, 1000, 1500]$ s and results in a total measurement duration of $T_{\Delta\tau} = 974.3$ h.

Using this sequence, we have a look at the dependency on the initial number of neutrons N_0 . Fig. 3.32 shows the achieved uncertainty $\Delta\tau_n$ with respect to $T_{\Delta\tau}$. However, as quoting the measurement time in hours is impractical, $T_{\Delta\tau}$ was converted to the number of three-

Table 3.3: Simulated sequence optimisation in the determination of τ_n . $T_{\Delta\tau}$ is calculated as nt_{seq} with the optimum in bold print.

k	Storage times t_s	Required n	Time per sequence t_{seq}	Total time $T_{\Delta\tau}$
3	[50, 500, 1000] s	1720	50 min	1433.3 h
3	[50, 500, 1200] s	1380	54 min	1242.0 h
3	[50, 500, 1500] s	1210	59 min	1189.8 h
3	[100, 500, 1200] s	1480	54 min	1332.0 h
4	[50, 100, 800, 1500] s	860	76 min	1089.3 h
4	[50, 100, 900, 1000] s	1050	69 min	1207.5 h
4	[50, 100, 1000, 1500] s	740	79 min	974.3 h
4	[50, 100, 1200, 1500] s	720	83 min	996.0 h
4	[50, 200, 800, 1200] s	1280	69 min	1472.0 h
5	[50, 100, 500, 800, 1200] s	960	86 min	1376.0 h
5	[50, 200, 500, 800, 1200] s	1070	86 min	1533.7 h

weeks double-shift beamtimes at the TRIGA reactor²⁴. This calculation corresponds to the ideal case and does not take any downtime or delays by the reactor or the experiment into account, which would prevent a fully efficient use of the beamtime. Furthermore, additional storage times (especially longer ones with $t_s \sim 2000$ s) may be required to investigate systematic effects. The results of the simulation can therefore be only a first indication of the order of magnitude of $T_{\Delta\tau}$.

Nevertheless, from the fit results of the storage curve measured in beamtime *Sept2020* ($N_0 = a_2 = 145(21)$ neutrons, cf. Tab. 3.2), it becomes obvious already at this stage, that with a maximum of four beamtimes available per year, even after three years $\Delta\tau_n = 1.0$ s (black horizontal line) is unachievable. The primary goal for τ SPECT, after having shown that magnetic storage is successfully possible, is therefore to increase the UCN density in the trap.

²⁴A three-weeks double-shift beamtime consists of 9 full days à 16 hours and 4 half days à 8 hours measurement time, resulting in 176 h. The number of required beamtimes was calculated from $T_{\Delta\tau}/176$ h.

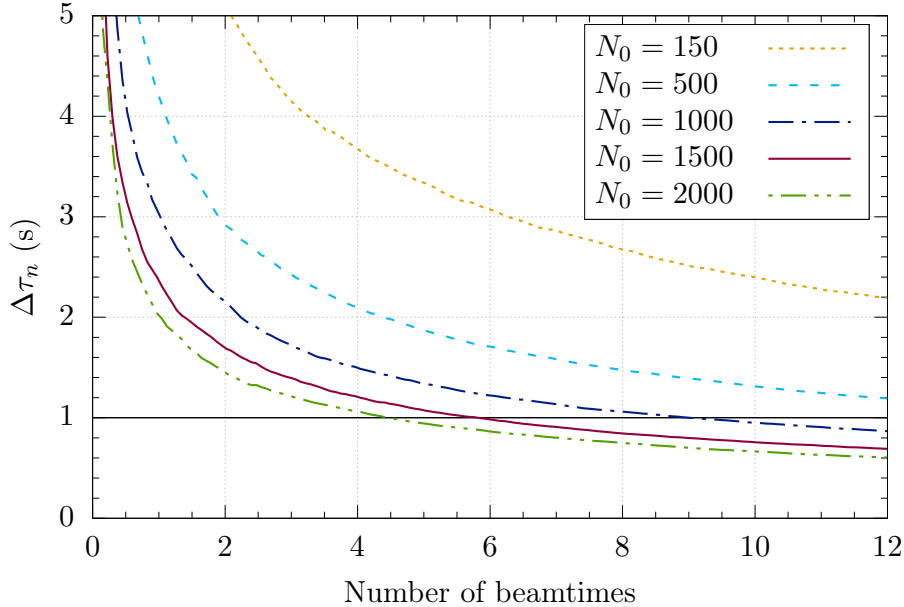


Figure 3.32: Simulated statistical sensitivity $\Delta\tau_n$ with respect to the number of double-shift beamtimes at the TRIGA reactor for selected initial values of N_0 . The target sensitivity of $\Delta\tau_n = 1.0$ s of phase I in τ SPECT is marked by the black line.

3.7 Summary

This chapter introduced the storage and measurement principle of the τ SPECT experiment and discussed the development of relevant components required for the filling process. Purely magnetic storage was successfully demonstrated and after the parameter optimisation of the spin flipper, a first storage curve was presented. The number of permanently stored neutrons was deduced from the fit parameters to this storage curve as $N = 145(21)$. After optimisation of the measurement sequence, however, so far more than three years of measurement time are required to achieve the intermediate target uncertainty of $\Delta\tau_n \leq 1.0\text{ s}$. Therefore, in the following chapters we will have a closer look at the filling process in theory and how optimisations are realised in τ SPECT.

Chapter 4

The theory of spin flip loading in τ SPECT

The neutron density achievable inside the τ SPECT storage volume depends on various factors, such as the neutron spectrum exiting the UCN source of the reactor and UCN transport through the beamline towards the experiment. However, without the filling process, which spin flips the high-field seeking neutrons into low-field seekers, none of the arriving neutrons would be permanently storable in the magnetic trap. This chapter gives a short theoretical introduction into the adiabatic fast passage spin flipper (cf. Ch. 4.1) and shows that the filling process itself depends on multiple parameters, such as the magnetic field polarisation of the spin flipper (cf. Ch. 4.1.1.1), the presence of transversal gradients (cf. Ch. 4.1.2), and the spin flip position with respect to the B_0 field (cf. Ch. 4.2).

4.1 Spin flipping using adiabatic fast passage

The motion of a neutron spin \vec{S} in a magnetic field \vec{B} without relaxation¹ is generally described by (adapted from [Blo46])

$$\frac{d\vec{S}}{dt} = \gamma (\vec{S} \times \vec{B}) \quad (4.1)$$

from which the precession with the Larmor frequency $\omega_0 = -\gamma B$ arises. If the field changes slowly enough, the orientation of the neutron spin is able to follow the magnetic field direction adiabatically. This is the key element of the adiabatic fast passage spin flipper, which goes back to V. Luschikov in 1970 [LT84] and which is applied in the UCN filling process in τ SPECT.

4.1.1 Adiabatic fast passage spin flipping in longitudinal fields

The magnetic field in τ SPECT in the spin flipping region consists of a superposition of static and dynamic fields. The static field is produced by the longitudinal $\vec{B}_0(z)$ field, which in this region is assumed to have a constant negative gradient, and the transversal

¹In general, relaxation terms are included in the Bloch equations but are only applicable to spin ensembles, in which the overall magnetisation is taken into account. This is not the case for individual particles, such as UCN, where the spin \vec{S} is conserved.

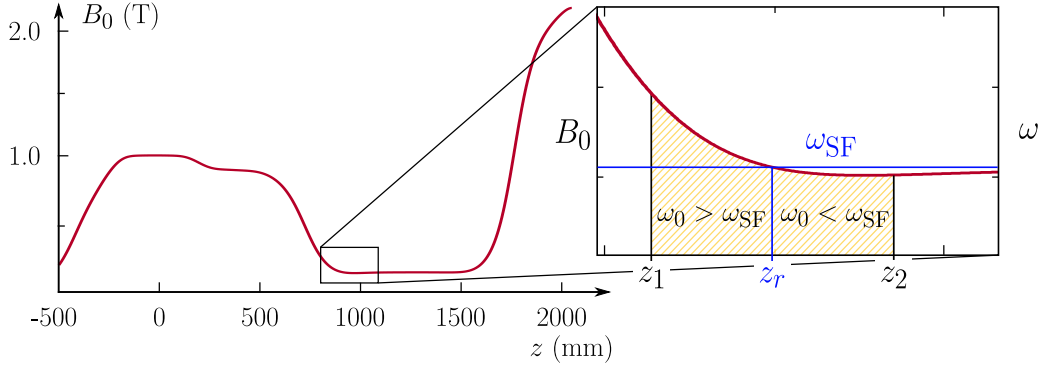


Figure 4.1: The longitudinal magnetic field $\vec{B}_0(z)$ (red line) with the inset showing a zoomed-in view of the spin flipping region (yellow area) limited by the positions z_1 and z_2 . In between, the $\vec{B}_1(z)$ field rotates at a frequency ω_{SF} . At the resonance position z_r (blue), the Larmor frequency is $\omega_0 = \gamma B_0(z) = \omega_{\text{SF}}$.

compensated octupole field $\vec{B}_t(r, \varphi, z)$. For simplicity, the transversal field is ignored for now. The dynamic field $\vec{B}_1(t)$, generated by the spin flipper, is rotating in the xy -plane at a frequency ω_{SF} . The spin flipping region is limited by the length of the spin flipper, starting at z_1 and ending at z_2 , as shown by the yellow shaded area in Fig. 4.1; outside this region $\vec{B}_1(t) = 0$ is assumed, neglecting the declining fringe field. In the lab frame the total magnetic field is written as

$$\vec{B}(z, t) = B_0(z)\hat{z} + B_1 [\cos(\omega_{\text{SF}}t)\hat{x} + \sin(\omega_{\text{SF}}t)\hat{y}], \quad (4.2)$$

with B_1 circularly polarised. In order to simplify this equation, it is convenient to go to a reference frame rotating at the spin flipper frequency ω_{SF} . The \hat{z}' -axis of this frame remains parallel to \hat{z} . In the co-rotating frame, $\vec{B}_1(t)$ becomes static and is oriented along one of the remaining axes, in this case \hat{x}' .

With \vec{B}_0 depending strongly on z , this applies to the corresponding Larmor frequency as well and we can write $\omega_0 = \omega_0(B_0(z)) = \omega_0(z)$. In the co-rotating frame, this frequency is transformed into an apparent - or reduced - Larmor frequency [Kee02]

$$\omega_{\text{red}}(z) = \omega_0(z) - \omega_{\text{SF}}. \quad (4.3)$$

The apparent magnetic field, also called the reduced field, then follows as $\vec{B}'_{\text{red}}(z) = (-\omega_{\text{red}}(z)/\gamma)\hat{z}'$. The addition of \vec{B}'_1 results in the effective field $\vec{B}'_e(z)$ given by

$$\vec{B}'_e(z) = \vec{B}'_{\text{red}}(z) + \vec{B}'_1 = \left[B_0(z) + \frac{\omega_{\text{SF}}}{\gamma} \right] \hat{z}' + B_1 \hat{x}'. \quad (4.4)$$

A vector diagram of the effective field is shown in Fig. 4.2. The $\vec{B}_0(z)$ field is reduced by the magnetic field equivalent $\omega_{\text{SF}}/\gamma$ of the reference frame rotation. The vector addition of the reduced field $\vec{B}'_{\text{red}}(z)$ and \vec{B}'_1 results in the effective magnetic field $\vec{B}'_e(z)$. The angle θ between $\vec{B}'_e(z)$ and the \hat{z}' -axis can be written as

$$\tan(\theta) = \frac{B'_1}{B_0(z) + \frac{\omega_{\text{SF}}}{\gamma}} = \frac{\omega_1}{-\omega_{\text{red}}(z)}. \quad (4.5)$$

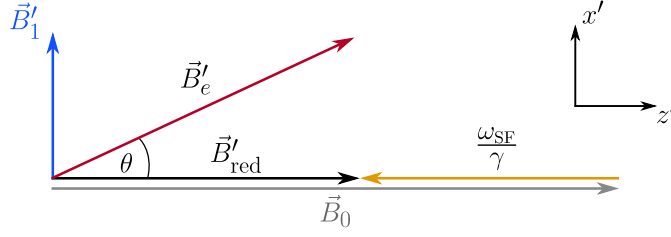


Figure 4.2: The magnetic fields involved in the spin flipping process without transversal fields (the lengths of the vectors are not to scale). By transformation to a reference frame rotating at ω_{SF} , the $\vec{B}_0(z)$ field (grey), aligned with the z' -axis, is reduced by a field equivalent of magnitude $\omega_{\text{SF}}/\gamma$ (yellow). In this frame, $\vec{B}'_1(z)$ (blue) always points along the x' -axis. The superposition of $\vec{B}'_1(z)$ and the reduced field $\vec{B}'_{\text{red}}(z)$ (black) results in the effective field $\vec{B}'_e(z)$ (red). θ is defined as the angle between $\vec{B}'_e(z)$ and the z' -axis.

We now consider a position z_r inside the spin flipping region with $z_1 \leq z_r \leq z_2$, at which the Larmor frequency of the neutron equals the irradiated spin flipper frequency according to

$$-\gamma B_0(z_r) = \omega_0 = \omega_{\text{SF}}. \quad (4.6)$$

This is the resonance position, marked by the blue lines in Fig. 4.1. Due to the negative gradient of $\vec{B}_0(z)$, at any $z < z_r$, $\omega_0(z)$ is larger than ω_{SF} and therefore $\omega_{\text{red}}(z) > 0$. Consequently, at $z > z_r$, $\omega_{\text{red}}(z) < 0$ because $\omega_0(z) < \omega_{\text{SF}}$. This results in the denominator of Eq. 4.5, and thus $\tan(\theta)$, changing sign.

If θ changes slowly enough, the neutron spin follows $\vec{B}'_e(z)$ while flying through the resonance as shown in Fig. 4.3. Here, the vector sum of $\vec{B}'_{\text{red}}(z)$ and $\vec{B}'_1(z)$ gives the direction of $\vec{B}'_e(z)$. From the simplified condition $\vec{B}'_1 = 0$ outside the spin flipping region, and consequently $\vec{B}'_e(z) \parallel \vec{B}_0(z)$, follows, that the neutron spin is (anti-)aligned with $\vec{B}_0(z)$ in front of as well as behind the spin flipper. This can only be realised if the neutron spin

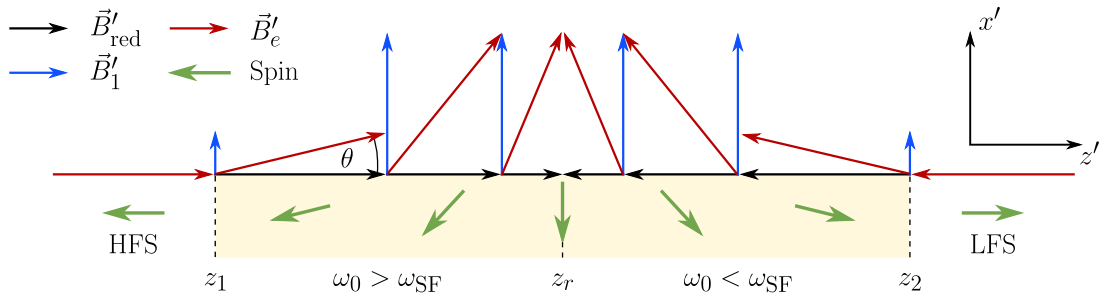


Figure 4.3: Spin motion during the adiabatic fast passage spin flip. Initially, the spin (green) of a HFS is aligned anti-parallel with $\vec{B}'_e(z)$ (red). Inside the spin flipping region between z_1 and z_2 (yellow shaded area) the \vec{B}'_1 field (blue) points along \hat{x}' and tilts $\vec{B}'_e(z)$ by an angle θ . On the left side of the resonance at z_r , the reduced field $\vec{B}'_{\text{red}}(z)$ is positive, on the right side it becomes negative, causing the orientation of $\vec{B}'_e(z)$ to change sign. Thus, the neutron spin, following $\vec{B}'_e(z)$ adiabatically, exits the spin flipper as a LFS.

is rotated by 180° in between.

The condition of θ , and thus the orientation of $\vec{B}'_e(z)$, changing slowly enough is quantified by the so-called adiabaticity parameter

$$\alpha = \left| \frac{\gamma \vec{B}'_e(z)}{\dot{\theta}(z)} \right| \gg 1. \quad (4.7)$$

In words, this means that if the effective Larmor frequency $|\gamma \vec{B}'_e(z)|$ is (much) larger than the change of the field orientation with time, $\dot{\theta}(z)$, a spin flip is likely. Assuming a neutron flying in z -direction at a velocity v and using

$$\frac{d}{dt} \vec{B}_0(z) = \frac{\partial \vec{B}_0(z)}{\partial z} \frac{\partial z}{\partial t} = \nabla \vec{B}_0(z) v, \quad (4.8)$$

$\dot{\theta}$ as defined in [LT84] can be rewritten as

$$\dot{\theta} = \frac{|\nabla \vec{B}'_e(z)| v \cdot |\vec{B}'_1|}{|\vec{B}'_e(z)|^2}. \quad (4.9)$$

On resonance at z_r , $\vec{B}'_{\text{red}}(z) = 0$ and so $|\vec{B}'_e(z)|^2 = |\vec{B}'_1|^2$ in Eq. 4.9 is minimal, which leads to a maximum field change $\dot{\theta}$. In combination with Eq. 4.7, α is minimal as well and can then be simplified as

$$\alpha = \frac{\gamma B_1'^2}{|\nabla \vec{B}_0| v}. \quad (4.10)$$

The spin flip efficiency ε can be estimated as a probability to follow the magnetic field adiabatically. This efficiency is deduced in [Rob71] and written in [HBD12] as

$$\varepsilon = 1 - \underbrace{\frac{1}{1 + \alpha^2} \sin^2 \left(\frac{\sqrt{1 + \alpha^2}}{2} \pi \right)}_{\leq 1}. \quad (4.11)$$

In case of $\varepsilon_{\text{SF}} \lesssim 1$, the oscillating \sin^2 term can be omitted, so that after insertion of the minimum α on resonance (Eq. 4.10) and further simplification, the spin flip efficiency can be approximated as

$$\varepsilon_{\text{SF}} \geq 1 - \frac{(\nabla B_0)^2 v^2}{(\nabla B_0)^2 v^2 + \gamma^2 B_1^4}. \quad (4.12)$$

This equation is, however, not valid for smaller ε_{SF} , in case of which a numerical solution of the Bloch equation (cf. Eq. 4.1) is necessary. It can only be used to investigate the fundamental dependencies with respect to v , ∇B_0 and B_1 . From the denominator for example follows directly, that a large spin flip efficiency with $\varepsilon_{\text{SF}} \lesssim 1$ is only achievable if

$$\gamma^2 B_1^4 \gg (\nabla B_0)^2 v^2, \quad (4.13)$$

which is not trivial regarding the rather large gradients of $\mathcal{O}(\nabla B_0) \sim 10 \text{ mT/cm}$ in τSPECT^2 .

²In order to give an example, the required B_1 amplitude for a neutron at $v = 1 \text{ m/s}$ and $\nabla B_0 = 10 \text{ mT/cm}$ is calculated as $B_1 \gg 0.7 \text{ mT}$.

Apart from not being useful in calculations of $\varepsilon_{\text{SF}} < 1$, Eq. 4.12 does furthermore not take into account the velocity distribution and flight trajectories of neutrons, as well as external forces such as gravity and the Stern-Gerlach force. Therefore, in order to estimate the spin flip efficiency in τ SPECT, a Monte Carlo simulation of the spin flip process was done, which is presented in Ch. 4.1.2.

4.1.1.1 Influence of the B_1 field polarisation on the spin flip efficiency

The functionality of the adiabatic fast passage spin flipper relies on a resonance of the irradiated B_1 field frequency with the Larmor frequency ω_0 . This resonance, however, does not only depend on the condition $\omega_{\text{SF}} = \omega_0$ but also on the polarisation of the B_1 field.

We can understand the polarisation of a magnetic field as the superposition of two counter-rotating fields B^+ and B^- . In this picture, σ^+ polarisation is realised, if B^- is equal to zero, and vice versa for σ^- polarisation. Fig. 4.4 illustrates the resulting overall field polarisation depending on the ratio of B^+ and B^- . The upper row corresponds to circular polarisation, where in this case the total B_1 field equals B^+ . With an additional B^- component, elliptic polarisation is achieved as long as $B^+ \neq B^-$. Here, the ellipticity and the net rotational direction of the field depend only on the result of $B^+ - B^-$. Linear (π) polarisation results from $B^+ = B^-$, as in this case the vertical vector components cancel and only the horizontal components remain.

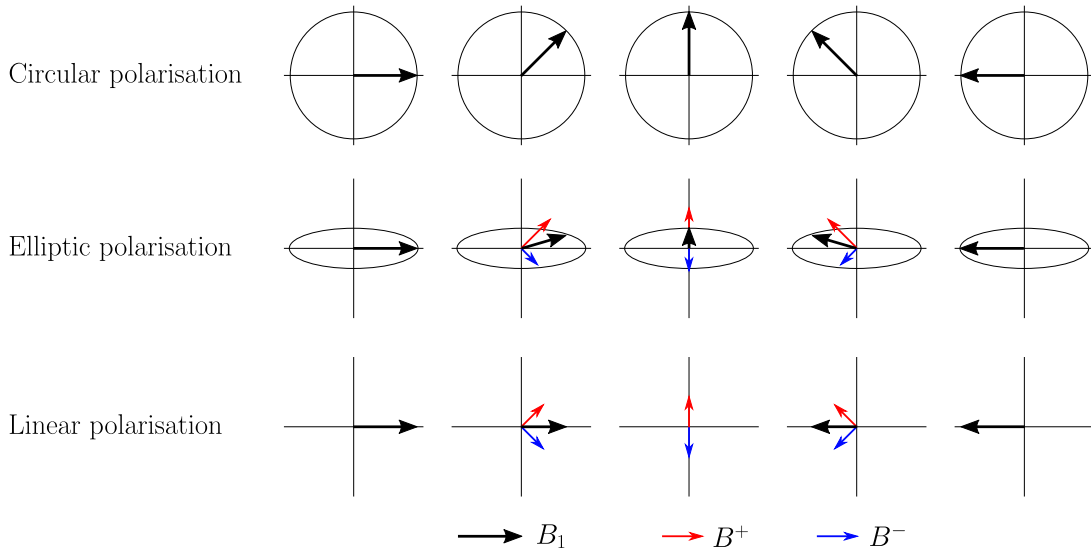


Figure 4.4: Schematic depiction of field polarisation. Every polarisation is understood as two counter-rotating circularly polarised fields B^+ (red) and B^- (blue). If one of those components is equal to zero, the resulting field is also circularly polarised (top row). The black arrow shows the direction of the magnetic field at different time steps. With $B^+ = B^-$, the vertical vector components of B^+ and B^- cancel, and the magnetic field is linearly polarised (bottom row). Any other combination of B^+ and B^- leads to elliptic polarisation (middle row) with the rotation direction determined by the dominant polarisation component.

In the context of efficient UCN spin flipping, the polarisation of the B_1 field is a crucial parameter: We assume circular polarisation $B_1 = B^+$, here σ^+ , matching the direction of the Larmor precession (cf. Eq. 4.2). The reference frame then rotates at $+\omega_{\text{SF}}$ resulting in the resonance $\omega_0(z_r) = \omega_{\text{SF}}$ and thus causing $\omega_{\text{red}}(z_r)$ to vanish (cf. Eqs. 4.3 and 4.6). This is a necessary condition for adiabatic fast passage spin flipping. In addition, with σ^+ polarisation the whole B_1 amplitude contributes to the spin flip efficiency ε_{SF} (cf. Eq. 4.12).

As soon as we add a counter-rotating field B^- by changing the field polarisation, but keep the B_1 amplitude constant, i.e. $B_1 = \sqrt{(B^+)^2 + (B^-)^2}$, the co-rotating field component B^+ , which causes the spin flip, is reduced, and thus also ε_{SF} is reduced. This is because the counter-rotating field does not affect the spin flip: The corresponding reference frame rotates at $-\omega_{\text{SF}}$ (i.e. in opposite direction with respect to the Larmor precession), and therefore the necessary resonance condition $\omega_{\text{red}}(z_r) = 0$ is never fulfilled. Consequently, in the extreme case with B_1 consisting only of the counter-rotating field, no spin flip is possible.

4.1.2 The spin flip efficiency in a Monte Carlo simulation

Coming back to the spin flip efficiency, we will now have a look at the Monte Carlo simulation, which is used to estimate the dependencies of the filling process in τ SPECT.

The magnetic fields implemented in this simulation are analytical approximations of the τ SPECT fields (cf. Ch. A.5.1), and both Stern-Gerlach and gravitational forces are included. In order to reduce the calculation time, the simulation begins at $z = 755$ mm rather than in front of the first magnetic field peak of B_0 (this would correspond to $z = -1500$ mm). In addition, the transversal magnetic field is replaced by an ideal hexapole field (cf. Ch. 3.2.2.1), so that the field amplitude is easily scalable. This allows for a variation of the transversal fields and gradients without altering the principle field shape.

Spin flipping depending on the field parameter k A set of 4000 neutrons was defined with randomised start positions in the $x - y$ plane within the neutron guide ($r = \sqrt{x^2 + y^2} \leq 25$ mm), equally distributed velocities between 1 and 4 m/s, flight angles up to $\theta_{\text{max}} = 25^\circ$ relative to the z -axis, and the spin $\vec{S} = -1\vec{z}$ corresponding to the high-field seeking state. Those neutrons were simulated to fly through the spin flipper at a given field configuration (consisting of B_0 and a varying B_t as static fields, and $B_1(t)$ as the dynamic field) during which the Bloch equation without spin relaxation [Blo46] (cf. Eq. 4.1) was used to track the spin motion. Afterwards, the spin flip efficiency was calculated by counting the number of spin flipped neutrons N_{LFS} ($\vec{S} = +1\vec{z}$; corresponding to low-field seekers) and dividing by the total number of simulated neutrons N ($\vec{S} = -1\vec{z}$), resulting in

$$\varepsilon_{\text{SF}}(\%) = \frac{N_{\text{LFS}}}{N} \cdot 100. \quad (4.14)$$

The condition for a successful spin flip was a change of sign in the direction of the spin after passage through the spin flipper. However, as the neutron spin was only analysed at the end of the simulation, ε_{SF} inferred with this method corresponds to everything that happened in between start and end point of the simulation, and therefore refers to an integral spin flip efficiency over the total spin flipper volume. If we now vary the

amplitude of the hexapole field to investigate its influence on the spin flip efficiency, the entire field in the simulation region changes, which makes a comparison of the results difficult. Furthermore, if we want to transfer the results from the simulation to τ SPECT, we need to find a quantity, which characterises the magnetic field in the spin flipping region.

Therefore, we define a field parameter $k(z_{\text{SF}})$ as the ratio between the transversal gradient of the total magnetic field at the neutron guide surface (within the narrowed tube this is at $r = 25$ mm) and the longitudinal gradient at $r = 0$ mm, both evaluated at the nominal position of the spin flipper, z_{SF} . In short, this parameter reads

$$k(z_{\text{SF}}) = \frac{\nabla_t B(r = 25 \text{ mm}, z = z_{\text{SF}})}{\nabla_z B(r = 0 \text{ mm}, z = z_{\text{SF}})}. \quad (4.15)$$

In τ SPECT, $k(z_{\text{SF}})$ is calculated using the simulation of B_0 and the results $B_{\text{abs,mean}}$ and $|\nabla_t B|_{\text{mean}}$ from the compensated field measurement (cf. Tab. 3.1), from which the gradients of the total magnetic field B are deduced. The compensated field measurement, however, was done at a rather low resolution with $\Delta r = 5$ mm, $\Delta\varphi = 5.63^\circ$ and $\Delta z = 5$ mm, so that in order to compare the field parameters of the Monte Carlo simulation with that calculated from the measurement, $B_{\text{abs,mean}}$ and $|\nabla_t B|_{\text{mean}}$ from the analytical hexapole field were calculated using the same resolution.

The results from the simulation are shown in Fig. 4.5. Within each plot, the spin flip position and the RF frequency were kept constant; in the simulation shown on the left side $z_{\text{SF}} = 980$ mm and $f_{\text{SF}} = 6.098$ MHz, an on the right side $z_{\text{SF}} = 1020$ mm and $f_{\text{SF}} = 5.846$ MHz. The position refers to the centre of the spin flipper, the frequencies

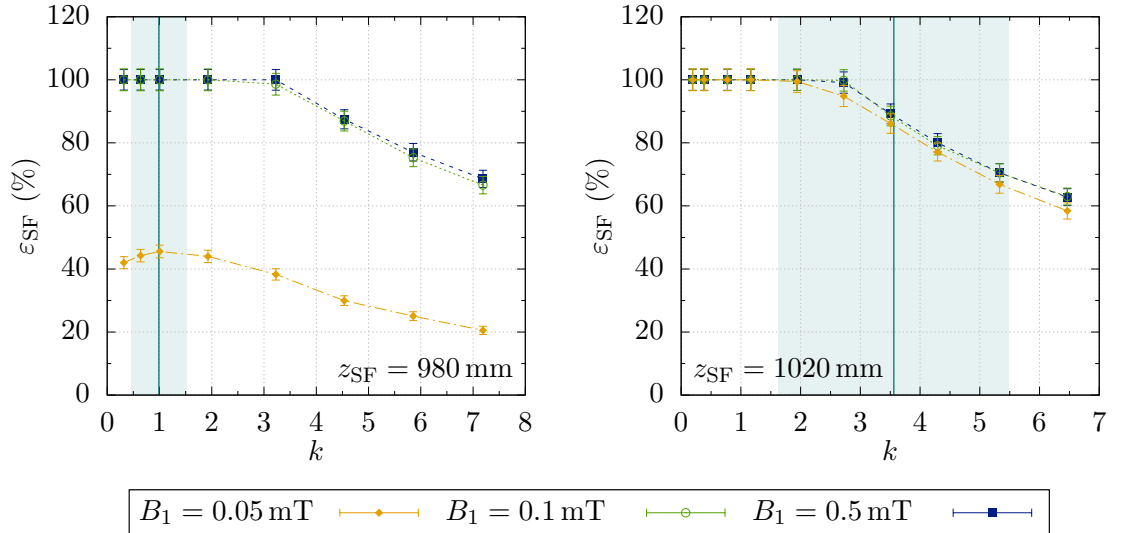


Figure 4.5: Spin flip efficiency ε_{SF} depending on the field characterisation parameter $k(z_{\text{SF}})$ for different B_1 amplitudes inferred from a Monte Carlo simulation. The left side refers to the spin flip position $z_{\text{SF}} = 980$ mm, the right side to 1020 mm. The vertical green line represents $k(z_{\text{SF}})$ in τ SPECT calculated from the compensated field measurement data, the green shaded region corresponds to its uncertainty. From ε_{SF} dropping from $k(z_{\text{SF}}) \simeq 3$ onwards at all B_1 amplitudes, the spin flip field condition in Eq. 4.16 is deduced.

were calculated separately as described in Ch. 5.1.1.1, using $B_{\text{abs,mean}}$ (cf. Tab. 3.1) in the determination of the absolute magnetic field $B(z_{\text{SF}})$. In order to investigate the dependency of the spin flip efficiency on the transversal field B_t , here expressed by $k(z_{\text{SF}})$ (cf. Eq. 4.15), the analytic hexapole field was scaled to different amplitudes such that the corresponding field parameter results in values between roughly $k(z_{\text{SF}}) = 0$ and 7. Finally, the simulation was repeated for the three spin flipper field amplitudes, $B_1 = 0.5$ mT, 0.1 mT and 0.05 mT.

From the simulation follows, that up to $k(z_{\text{SF}}) \simeq 3$ the spin flip efficiency remains on a constant level within errors at both spin flip positions, with the level depending only on the amplitude of B_1 : At $z_{\text{SF}} = 1020$ mm, all B_1 amplitudes suffice for $\varepsilon_{\text{SF}} \simeq 100\%$ at low values of $k(z_{\text{SF}})$, whereas at $z_{\text{SF}} = 980$ mm the amplitude $B_1 = 0.05$ mT results only in around 50% efficiency. This can be explained by the higher longitudinal field gradient at $z_{\text{SF}} = 980$ mm (here, $\nabla_z B = 3.6$ mT/cm compared to $\nabla_z B = 1.0$ mT/cm at $z_{\text{SF}} = 1020$ mm), which causes the condition in Eq. 4.13, now written as $\gamma^2 B_1^4 / (\nabla B_0)^2 v^2 \gg 1$ not to be sufficiently fulfilled anymore³.

From $k(z_{\text{SF}}) \simeq 3$ on, however, ε_{SF} decreases with rising $k(z_{\text{SF}})$ regardless of the B_1 amplitude. This causes a problem, as we see when calculating $k(z_{\text{SF}})$ for the total magnetic fields in τ SPECT at both spin flip positions. The results $k(980 \text{ mm}) = (0.99 \pm 0.53)$ and $k(1020 \text{ mm}) = (3.56 \pm 1.93)$ are shown in Fig. 4.5 by the green line and the green shaded box; the errors are calculated from the uncertainty in the compensated field measurement using Gaussian error propagation. With $k(1020 \text{ mm}) > 3$ in τ SPECT thus a reduced efficiency of the filling process needs to be expected.

In order to explain this phenomenon, we compare the magnetic field maps of a small $k(z_{\text{SF}})$ and a large one at both spin flip positions, as shown in Fig. 4.6. The maps were generated using a superposition of the analytical approximation of B_0 (cf. Ch. A.5.1.1) and the analytical hexapole field, which was scaled to result in the following field parameters: The top row refers to $z_{\text{SF}} = 980$ mm with $k(980 \text{ mm}) = 0.6$ (left) and $k(980 \text{ mm}) = 5.9$ (right), the bottom row refers to $z_{\text{SF}} = 1020$ mm with $k(1020 \text{ mm}) = 0.4$ (left) and $k(1020 \text{ mm}) = 3.5$ (right). The lines mark the edges of the spin flipper; the black curves show the positions, where the resonance condition $\omega_0 = 2\pi f_{\text{SF}}$ is fulfilled with a tolerance of $\Delta f_{\text{SF}} = 3$ kHz. As we see, this resonance band is significantly curved at larger $k(z_{\text{SF}})$. With the neutrons flying on random trajectories, it is possible for them to hit the resonance condition multiple times (an exemplary trajectory is depicted in turquoise). We can therefore distinguish three different possibilities for the neutron spin to evolve:

1. High B_1 amplitudes result in high individual spin flip efficiencies each time the resonance condition is hit. With an uneven number of spin flips an initial HFS exits as storable LFS.
2. With the same argumentation but an even number of spin flips, the neutron is not storable, because it leaves the spin flipper as a HFS.
3. With smaller B_1 amplitudes, the spin is not flipped entirely when hitting the resonance, so that reduced efficiencies multiply. This might be the case also in the B_1 fringe field outside the spin flipper.

³Giving an example for a neutron with $v = 1$ m/s and inserting $B_1 = 0.05$ mT as well the respective gradients, we find the relations $\gamma^2 B_1^4 / (\nabla B_0)^2 v^2 \simeq 1.62 \gtrsim 1$ at $z_{\text{SF}} = 980$ mm and $\gamma^2 B_1^4 / (\nabla B_0)^2 v^2 \simeq 20.98 \gg 1$ at $z_{\text{SF}} = 1020$ mm.

In conclusion, the spin flip position has to be chosen in a way, so that ε_{SF} is not reduced by the magnetic field configuration at that position. Going back to Fig. 4.5, we define the limit such, that $k(z_{\text{SF}})$, calculated with the average field and gradient of the compensated field measurement, does (also within errors) not exceed $k(z_{\text{SF}}) = 3$. In total, this results in the spin flip field condition

$$k(z_{\text{SF}}) + |\Delta k(z_{\text{SF}})| \leq 3. \quad (4.16)$$

In order to apply this condition to τ SPECT, we take a look at the magnetic field gradients, which depend on the longitudinal position. Fig. 4.7 shows B_0 at $I_{\text{main}} = 33$ A on the left axis, and the longitudinal and transversal gradients $\nabla_z B(r = 0 \text{ mm})$ and $\nabla_t B(r = 25 \text{ mm})$ on the right axis. The transversal gradient was calculated using the average fields and gradients of the compensated field measurement (cf. Tab. 3.1). For comparability reasons, both gradients are depicted as absolute values. As the transversal field is only present within the range of the storage octupole ($570 \text{ mm} \leq z \leq 1950 \text{ mm}$), $|\nabla_t B(r = 25 \text{ mm})| = 0 \text{ mT/cm}$ at $z < 570 \text{ mm}$. The spin flip field condition of Eq. 4.16 is fulfilled

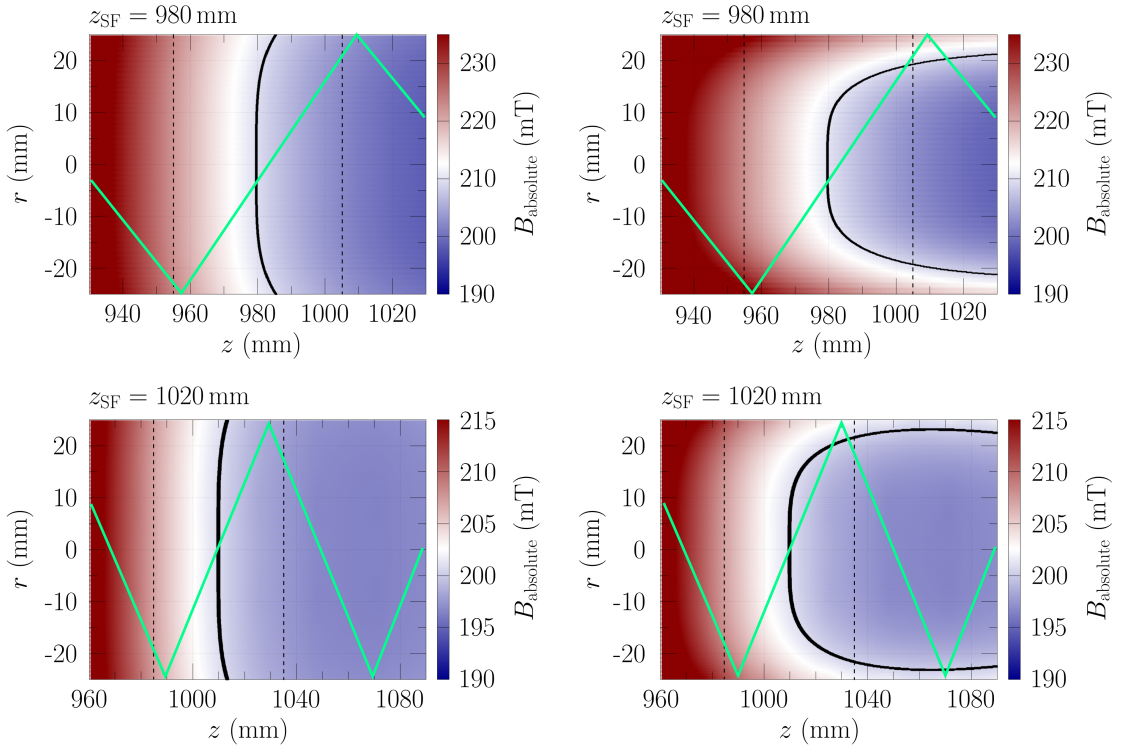


Figure 4.6: Resonance bands in the spin flipping region depending on the field parameter $k(z_{\text{SF}})$ at $z_{\text{SF}} = 980 \text{ mm}$ (top row, left: $k(z_{\text{SF}}) = 0.6$ and right: $k(z_{\text{SF}}) = 5.9$) and $z_{\text{SF}} = 1020 \text{ mm}$ (bottom row, left: $k(z_{\text{SF}}) = 0.4$ and right: $k(z_{\text{SF}}) = 3.5$). The fields are a superposition of the analytical approximation of B_0 and the scalable transversal hexapole field. The vertical dashed lines mark the physical edges of the spin flipper, the black curves show the positions, where the resonance $\omega_0 = 2\pi f_{\text{SF}}$ is fulfilled within $\Delta f_{\text{SF}} = 3 \text{ kHz}$. A neutron flying on arbitrary trajectories (turquoise lines) can be spin flipped more than once depending on the curvature of the resonance band.

within the shaded region, the maximum possible position at $z_{\text{SF,max}} = 1004$ mm is marked by the red line. Spin flip positions further inside the trap should be avoided, because here ε_{SF} is expected to drop. The first storage curve, presented in Ch. 3.6.3, was measured at $z_{\text{SF}} = 879$ mm, which lies well within the allowed range, whereas the design position at $z_{\tau} = 1100$ mm would not have been realisable without reducing the spin flip efficiency. However, with the approach using the average transversal fields and gradients and $k(z_{\text{SF}})$ a rough estimation, the energetically most advantageous position which is not limited by transversal gradients should be confirmed experimentally as well.

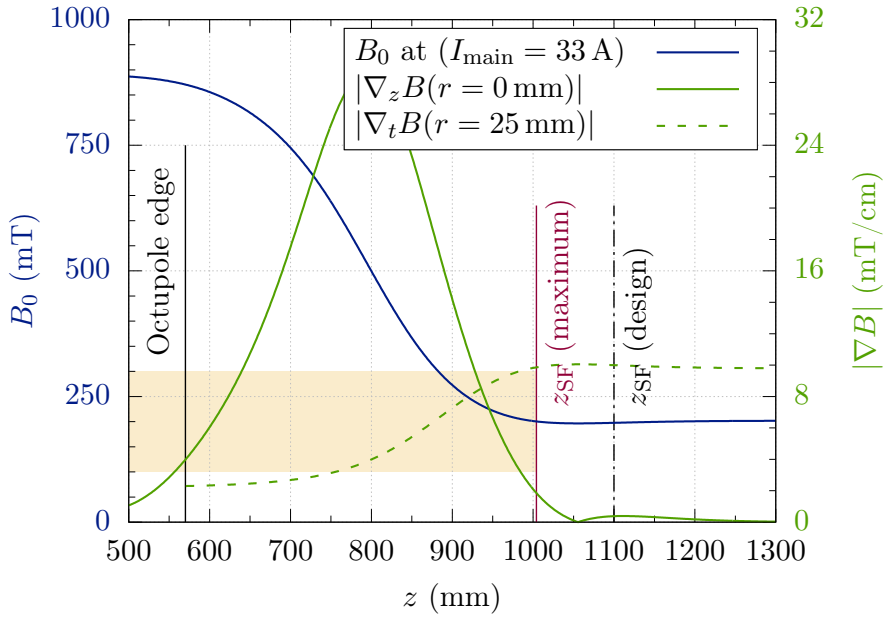


Figure 4.7: Constraints on the spin flip position by the field gradients in τ SPECT at $I_{\text{main}} = 33$ A. The B_0 field is shown in blue (left axis), the gradients (green) are plotted on the right axis as absolute values for comparability reasons. $\nabla_z B(z)$ is evaluated at $r = 0$ mm and $\nabla_t B(z)$ at $r = 25$ mm using the average compensated field components of Tab. 3.1. Outside of the storage octupole ($z < 570$ mm, black solid line) $|\nabla_t B(r = 25 \text{ mm})| = 0$ mT/cm. The spin flip field condition deduced from the MC simulation (cf. Eq. 4.16) is fulfilled up to $z_{\text{SF}}(\text{max}) = 1004$ mm (yellow shaded region and red line). The spin flip design position $z_{\text{SF}}(\text{design})$ (black dashed line) lies outside this region and should not be used.

Spin flipping depending on the B_1 amplitude The Monte Carlo simulation was not only helpful in calculating the spin flip efficiency depending on the transversal field, it could also be used to estimate how ε_{SF} scales with the B_1 amplitude. As mentioned in Ch. 4.1.1, the analytic approximation of ε_{SF} in Eq. 4.12 can only be applied for $\varepsilon_{\text{SF}} \lesssim 1$ and additionally does not take any forces or flight trajectories into account. Therefore, the simulation at $z_{\text{SF}} = 980$ mm with the field parameter $k = 1.0$ was repeated with varying B_1 amplitudes. The spin flip efficiency was calculated as before, using Eq. 4.14. The result is shown in Fig. 4.8. It shows, that between $B_1 \simeq 0.045$ mT and 0.060 mT ε_{SF} increases

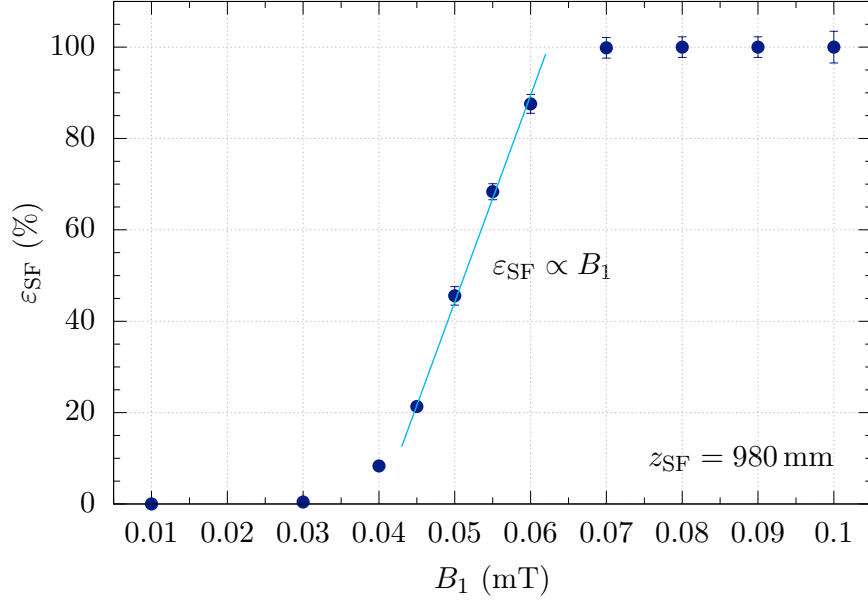


Figure 4.8: Spin flip efficiency ε_{SF} depending on the B_1 amplitude as inferred from the Monte Carlo simulation at $z_{\text{SF}} = 980$ mm. The transversal hexapole field was scaled to yield a field parameter $k = 1.0$. The result is shown by the blue markers, ε_{SF} was calculated using Eq. 4.14. In a range between $B_1 \simeq 0.045$ mT and 0.06 mT, a linear dependency is observed (light blue line). At higher B_1 amplitudes, ε_{SF} saturates at 100 %.

approximately linearly⁴ with B_1 until it saturates at 100 % from $B_1 \simeq 0.07$ mT onwards.

4.2 The energy acceptance of the UCN trap in τ SPECT

We have seen, that the magnetic fields, both static and dynamic, have to fulfil certain requirements in order to allow for efficient spin flipping of UCN. This is, however, only one aspect of the filling process. In addition, the energy of incoming UCN has to be in a range, which is storable in the magnetic trap after the spin flip. This range is limited by the maximum kinetic energy a UCN may have when entering τ SPECT, a quantitative description of which is derived in the following.

4.2.1 Derivation of the maximum storable energy (without gravity)

We begin with a neutron in the high field seeking state at an initial kinetic energy $E_{\text{kin},0}$ in front of the first magnetic field peak of B_0 . Here, $B_0(z) = 0$ T and thus the magnetic potential energy is $V_{\text{magn},0}(z) = -|\mu_n|B_0(z) = 0$ neV as well (cf. Eq. 2.5). We define this potential as reference for later potential difference calculations. Furthermore, gravity is included only in a second step and ignored for now.

⁴The line is a linear fit to the data in this range according to $\varepsilon_{\text{SF}} = a \cdot B_1 + b$ with $a = 4523.4(129.3)$ %/mT and $b = -182.0(6.3)$ % ($\chi^2/\text{ndf} = 1.07$).

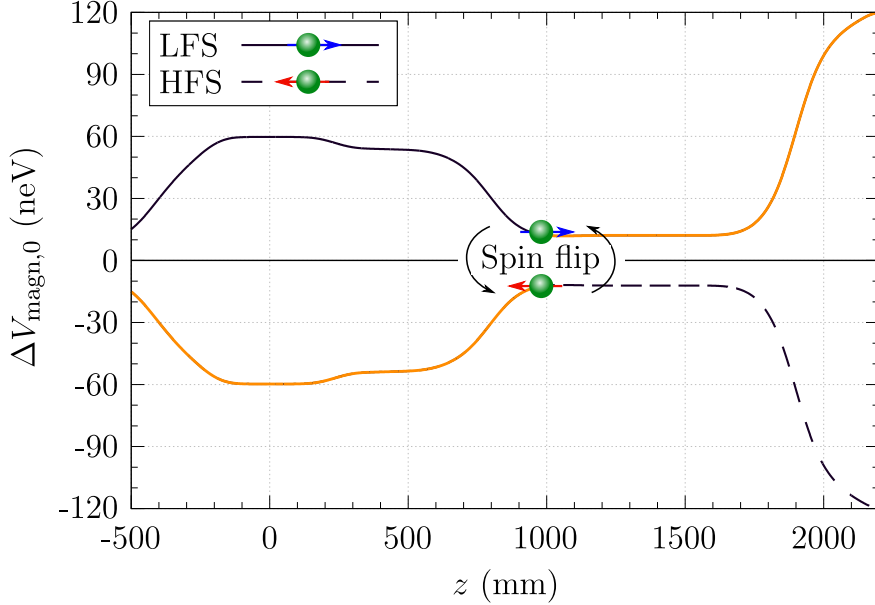


Figure 4.9: Magnetic potential difference in τ SPECT relative to $V_{\text{magn}} = 0$ neV as seen by a HFS (black dashed line) and a LFS (black solid line) at $I_{\text{main}} = 33$ A. Conserving energy, the HFS (LFS) is accelerated (decelerated) in the increasing magnetic field, and vice versa as the field drops. Due to the spin flip at z_{SF} , the potential energy difference with respect to $V_{\text{magn},0} = 0$ neV changes sign. The potential as seen from an initial HFS spin flipped to a LFS is marked in yellow.

With the magnetic moment of the HFS aligned parallel with B_0 (cf. Ch. 2.1.4 and Fig. 3.3), the magnetic field appears as a potential well as is shown in Fig. 4.9. This means, that the neutron - while flying along the z -axis - is first accelerated, and decelerated again afterwards⁵. We consider the spin flipper to be located in the low field region behind the first magnetic field peak. Here, the potential difference with respect to $V_{\text{magn},0}(z)$ is negative and given by $\Delta V_{\text{magn},0}(z_{\text{SF}}) = -|\mu_n|B_0(z_{\text{SF}})$ (z_{SF} is again the nominal position of the spin flipper). This results in the neutron having been accelerated to a larger extent than it was decelerated afterwards, leading to an additional kinetic energy at the spin flip position of $E_{\text{kin}}(z_{\text{SF}}) = |\mu_n|B_0(z_{\text{SF}})$.

After the spin flip, the magnetic moment is aligned anti-parallel with B_0 , so that $\Delta V_{\text{magn},0}(z_{\text{SF}}) = |\mu_n|B_0(z_{\text{SF}})$ becomes positive. The total energy of the neutron directly after the spin flip can thus be summarised as

$$\begin{aligned} E(z_{\text{SF}}) &= E_{\text{kin},0} + E_{\text{kin}}(z_{\text{SF}}) + \Delta V_{\text{magn},0}(z_{\text{SF}}) \\ &= E_{\text{kin},0} + 2|\mu_n|B_0(z_{\text{SF}}). \end{aligned} \quad (4.17)$$

If this energy is smaller than the potential of the magnetic trap of $V_{\text{pot}} = 47$ neV, the neutron is storable. Given a specific spin flip position - and thus a specific magnetic field $B_0(z_{\text{SF}})$ - we can calculate a maximum allowed initial kinetic energy

⁵For simplicity, we assume cylindrical symmetry, so that effects from the transversal fields cancel.

$$E_{\text{kin},0}^{\text{max}}(z_{\text{SF}}) = 47 \text{ neV} - 2|\mu_n|B_0(z_{\text{SF}}), \quad (4.18)$$

which still results in a storable neutron after the spin flip. Taking for example the filling position used for the first purely magnetic storage curve with the birdcage resonator (cf. Ch. 3.6.3), $z_{\text{SF}} = 879 \text{ mm}$, we find $B_0(879 \text{ mm}) = 306.7 \text{ mT}$, which inserted into Eq. 4.18 results in $E_{\text{kin},0}^{\text{max}}(879 \text{ mm}) = 10.0 \text{ neV}$. From the incoming UCN spectrum, thus only those neutrons can be stored, which have kinetic energies in front of the first magnetic field peak with $0 \text{ neV} \leq E_{\text{kin},0} \leq 10.0 \text{ neV}$. This range is in this work called the energy acceptance $\Delta E_{\text{kin},0}$ of the trap. Considering the neutron density at low energies

$$\varrho(E) \sim \sqrt{E}, \quad (4.19)$$

the number of neutrons in the storable energy range scales with $\varrho_{\text{UCN}} \sim E^{3/2}$ [GRL91]. With $E_{\text{kin},0}^{\text{max}}(879 \text{ mm}) = 10.0 \text{ neV}$, the storable phase space is thus very small. This gets even worse since we additionally have to take gravity into account.

4.2.2 The maximum storable energy depending on gravity

The storage octupole and the neutron guide are aligned concentrically⁶, but they have different radii ($r_{\text{guide}} = 25 \text{ mm}$ compared to $r_{\text{SO}} = 54 \text{ mm}$), which results in a height difference of $s_0 = 29 \text{ mm}$ between the bottom of the neutron guide and the bottom of the storage octupole. This is illustrated in Fig. 4.10. We assume a neutron being spin flipped to the low-field seeking state at a certain height $s = s_0 + \Delta s$, with Δs limited by the neutron guide and ranging from 0 mm to $2r_{\text{guide}} = 50 \text{ mm}$. Inside the storage octupole this neutron falls down and is accelerated by gravity until the repulsive Stern-Gerlach force prevails and the neutron is reflected. In the worst case, this reflection occurs only a short distance above the bottom of the storage octupole, so that the neutron is accelerated by $\Delta V_{\text{grav}} = s \cdot 102.4 \text{ neV/m}$ beforehand.

This has to be taken into account in the calculation of the allowed initial kinetic energy, so that Eq. 4.18 is extended to

$$E_{\text{kin},0}^{\text{max}}(z_{\text{SF}}, \Delta s) = 47 \text{ neV} - 2|\mu_n|B_0(z_{\text{SF}}) - (s_0 + \Delta s) \cdot 102.4 \text{ neV/m} \quad (4.20)$$

resulting in a maximum for $\Delta s = 0 \text{ mm}$ at a given spin flip position. The dependency of $E_{\text{kin},0}^{\text{max}}(z_{\text{SF}}, \Delta s = 0 \text{ mm})$ on z_{SF} is shown in Fig. 4.11.

Taking again our example at $z_{\text{SF}} = 879 \text{ mm}$, we see that the already low maximum initial energy of formerly 10.0 neV decreases further to $E_{\text{kin},0}^{\text{max}}(879 \text{ mm}) = 7.0 \text{ neV}$ when we include gravity in the consideration. If we were able to position the spin flipper in a lower magnetic field $B_0(z_{\text{SF}})$, the maximum storable energy would increase to up to $E_{\text{kin},0}^{\text{max}}(1004 \text{ mm}) = 19.9 \text{ neV}$. This value is calculated at the maximum allowed spin flip position $z_{\text{SF}} = 1004 \text{ mm}$ limited by the condition in Eq. 4.16, where we find $B_0(1004 \text{ mm}) = 200 \text{ mT}$.

⁶It is shown in Ch. A.5.1.2, that the compensation octupole, and with it the neutron guide, is positioned at an axial offset of $\delta y = -2.6 \text{ mm}$. Nevertheless, concentric alignment is assumed here for simplicity.

4.2.3 The storable fraction of the neutron energy spectrum

In order to estimate the expected increase of the storable phase space when positioning the spin flipper in a lower magnetic field, Eq. 4.19 is integrated according to

$$N(E) = \int_{E_{\min}}^{E_{\max}} \varrho(E) dE. \quad (4.21)$$

However, because of the dependency on Δs of the total neutron energy after spin flip, not all energy intervals may be treated equally as is shown in the following example calculation.

We assume the maximum allowed spin flip position at $z_{\text{SF}} = 1004 \text{ mm}$ where $B_0(z_{\text{SF}}) = 200 \text{ mT}$ (cf. Fig. 4.11). Rewriting Eq. 4.20, and inserting $B_0(z_{\text{SF}})$ and $s_0 = 29 \text{ mm}$ results in

$$\begin{aligned} E_{\text{kin},0}(z_{\text{SF}}, \Delta s) &\leq 47 \text{ neV} - 2|\mu_n| \cdot 200 \text{ mT} - (29 \text{ mm} + \Delta s) \cdot 102.4 \text{ neV/m} \\ &\leq 47 \text{ neV} - 24.1 \text{ neV} - 3.0 \text{ neV} - \Delta s \cdot 102.4 \text{ neV/m} \\ &\leq 19.9 \text{ neV} - \Delta s \cdot 102.4 \text{ neV/m}. \end{aligned} \quad (4.22)$$

With $\Delta s = 0 \text{ mm}$, we find the already known maximum initial energy $E_{\text{kin},0}^{\text{max}}(1004 \text{ mm}) = 19.9 \text{ neV}$. Using Eq. 4.22 and Fig. 4.12 (left), we can distinguish four cases:

1. Neutrons with $E_{\text{kin},0} > 19.9 \text{ neV}$ are not storable under any conditions.
2. Neutrons with $E_{\text{kin},0} = E_{\text{kin},0}^{\text{max}} = 19.9 \text{ neV}$ are storable only, if they are spin flipped at $\Delta s = 0 \text{ mm}$ within the neutron guide.
3. Neutrons which are spin flipped at the maximum $\Delta s = 50 \text{ mm}$ are storable, if $E_{\text{kin},0} \leq 19.9 \text{ neV} - 50 \text{ mm} \cdot 102.4 \text{ neV/m} = 14.8 \text{ neV}$. This energy is called $E'_{\text{kin},0}$ and is furthermore the limiting energy, up to which the spin flip height inside the neutron guide does not matter and all neutrons are storable.

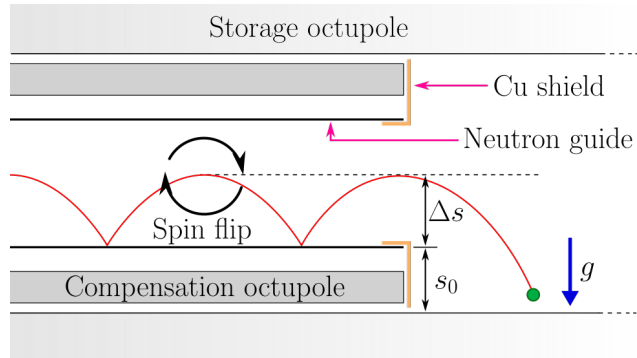


Figure 4.10: Schematics of the spin flipping unit front section for an estimation of the gravitational acceleration of neutrons after spin flip. The SFU with Cu shield (orange), compensation octupole and neutron guide is aligned concentrically with the storage octupole (light grey). The height of the neutron guide lower edge above the bottom of the storage octupole is $s_0 = 29 \text{ mm}$. A neutron (trajectory shown in red) is spin flipped at additional height Δs within the neutron guide. When entering the trap, it can thus be accelerated by gravity (blue arrow) by up to $\Delta V_{\text{grav}} = (s_0 + \Delta s) \cdot 102.4 \text{ neV/m}$.

4. Neutrons with $E'_{\text{kin},0} < E_{\text{kin},0} < E_{\text{kin},0}^{\text{max}}$ can be stored only, if they are spin flipped below a certain height $\Delta s = \Delta s_{\text{max}}$, so that Eq. 4.22 would still be fulfilled. Assuming an equal distribution of neutrons over the neutron guide cross section, this means, that only a fraction of neutrons is storable, which calculates as the ratio between the area up to Δs_{max} and the full cross section of the neutron guide.

These conditions have to be accounted for when integrating the neutron spectrum. Therefore, Eq. 4.21 is extended by a weighting function

$$w(E_{\text{kin},0}) = \begin{cases} 1 & \text{for } E_{\text{kin},0} \leq E'_{\text{kin},0} \\ 1 - \left[\frac{\cos^{-1}\left(1 - \frac{E'}{r \cdot p}\right) r^2 - \left(r - \frac{E'}{p}\right) \sqrt{2r \frac{E'}{p} - \left(\frac{E'}{p}\right)^2}}{\pi r^2} \right] & \text{for } E'_{\text{kin},0} < E_{\text{kin},0} \leq E_{\text{kin},0}^{\text{max}} \\ 0 & \text{for } E_{\text{kin},0} > E_{\text{kin},0}^{\text{max}} \end{cases} \quad (4.23)$$

with $E' = E_{\text{kin},0} - E'_{\text{kin},0}$ and $p = 102.4 \text{ neV/m}$. The storable phase space is then calculated as

$$\varrho_{\text{UCN}}(E) = \int_{E_{\text{min}}}^{E_{\text{max}}} \varrho(E) w(E) dE, \quad (4.24)$$

which corresponds to the blue shaded fraction in Fig. 4.12 (right). Relative to the storable phase space achievable with the birdcage resonator, this would result in an increase by

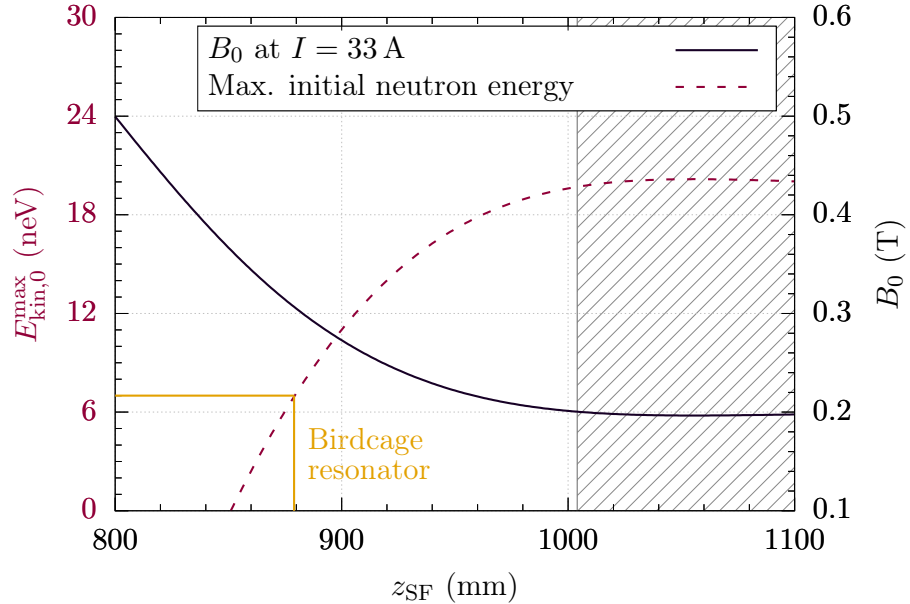


Figure 4.11: Maximum initial kinetic energy $E_{\text{kin},0}^{\text{max}}(z_{\text{SF}}, \Delta s = 0 \text{ mm})$ depending on the spin flip position z_{SF} (red dashed line). The right axis shows B_0 at $I_{\text{main}} = 33 \text{ A}$ (black line). The grey shaded region marks the positions, where the spin flip field condition of Eq. 4.16 is violated. The yellow line refers to the measurements with the birdcage resonator in beamtime *Sept2020* at $z_{\text{SF}} = 879 \text{ mm}$.

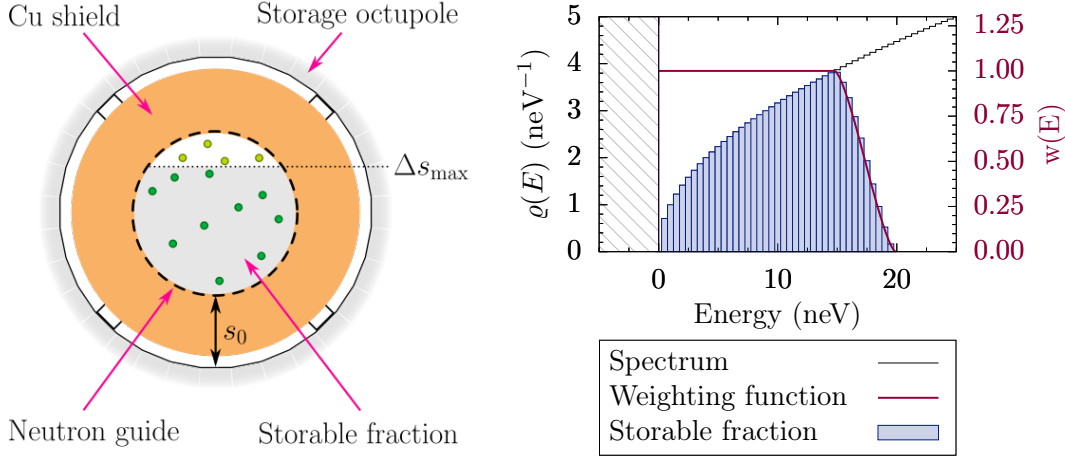


Figure 4.12: Left: Schematics of the SFU front section in the $x - y$ plane as seen from inside the trap. The minimum distance between storage octupole and the concentrically aligned neutron guide is $s_0 = 29$ mm. Neutrons in a small energy range close to the upper limit of the energy acceptance are only storable, if they are spin flipped below Δs_{\max} , the storable fraction of all neutrons in this range is marked by the gray region. Right: Simulated neutron energy distribution following a \sqrt{E} -behaviour (black) and the weighting function of Eq. 4.23 resulting from the spin flip height dependency inside the neutron guide (red, shown on the right axis). In combination, only the blue shaded part of the spectrum is storable in τ SPECT.

$$g = \frac{\int_{0 \text{ neV}}^{19.9 \text{ neV}} \varrho(E) w(E) dE}{\int_{0 \text{ neV}}^{7.0 \text{ neV}} \varrho(E) w(E) dE} \approx 7.4. \quad (4.25)$$

Even this being only an approximation, we can conclude that the filling position must be in the lowest magnetic field which still allows for efficient spin flipping (cf. Ch. 4.1.2) in order to store as many neutrons in the trap as possible.

4.2.4 Implications for the birdcage resonator

The optimisation of the filling position in τ SPECT implies that the resonance frequency of the spin flipper needs to be adapted, so that the resonance condition $2\pi f_{\text{SF}} = \omega_0$ is still fulfilled. This is illustrated in Fig. 4.13: The left axis shows $B_0(z)$ in the region behind the first magnetic field peak, the right axis refers to the corresponding resonance frequency calculated as $f_{\text{SF}} = \omega_0/(2\pi) = \gamma B_0(z_{\text{SF}})/(2\pi)$. The inset is a detailed view of the region around a weak field minimum at $z = 1056$ mm, which plays a role in the discussion in Ch. 5.2.1. Within the grey shaded region, the spin flip field condition of Eq. 4.16 is violated. The marked position shows the position calculated from the resonance frequency of the birdcage resonator ($z_{\text{SF}} = 859$ mm, cf. Ch. 3.3.4)⁷. In the allowed spin flipping region up to $z_{\text{SF}} = 1004$ mm, we find frequencies in a range $\sim 5.5 \text{ MHz} \leq f_{\text{SF}} \leq 10 \text{ MHz}$.

⁷The measurements using the birdcage resonator were done at $z_{\text{SF}} = 879$ mm but without adapting the resonance frequency, so that we refer to the theoretical optimum position here.

The birdcage resonator was built in a low-pass design (cf. Ch. 3.3.1), for which it was experimentally determined, that increasing the capacities within the rungs decreases the resonance frequency. However, in order to shift the resonance frequency over several MHz, additional capacities in the nF-range would have been required, which was a problem for the following reasons:

1. Inserting variable capacitors would have been a rather flexible solution for a tuning to various different frequencies, however, such capacitors range typically only up to ~ 100 pF, which is too small for the required frequencies in τ SPECT.
2. Replacing the already mounted capacitors by such with higher capacity was not optimal, because the Q -value (cf. Ch. 3.3.2.1) decreases with rising capacity, which makes them more and more unsuitable for applications involving RF.
3. We could have added further capacitors with $C \sim 1$ nF in parallel to the existing ones. However, due to the size of the capacitor housing (the edges have lengths of one to several millimeters), only a small number of capacitors would have fitted between the copper plates of the birdcage resonator and the compensation octupole, which in turn would have limited the adjustable frequency range.

In addition, every tuning to a different resonance frequency implied a reconstruction of the birdcage resonator outside of τ SPECT, which would have been cumbersome and time-consuming. Using a birdcage resonator for an optimisation of the filling position was thus not the optimum solution. An alternative was found by replacing the birdcage resonator with an externally frequency tunable double saddle coil, which is presented in Ch. 5.

4.3 Summary

This chapter presented the theory of the adiabatic fast passage spin flipper in longitudinal magnetic fields as well as the dependency on the polarisation of the rotating B_1 field. Since calculations regarding a spin flip efficiency are possible only numerically, Monte Carlo simulations were done in order to estimate the influence of the transversal field amplitude of the compensated octupole field. In terms of measurable quantities, the condition on the magnetic field configuration at the spin flip position was found as $k(z_{\text{SF}}) + |\Delta k(z_{\text{SF}})| \leq 3$, which in τ SPECT is fulfilled up to $z_{\text{SF}} = 1004$ mm. From an energy analysis before and after the spin flip, the maximum allowed initial kinetic energy of storable UCN was deduced. With the birdcage resonator, this maximum energy is calculated as $E_{\text{kin},0}^{\text{max}}(879 \text{ mm}) = 7.0 \text{ neV}$, which is constrained by its fixed frequency ω_{SF} and thus the fixed spin flip position in the magnetic field. It was estimated, that if the spin flip position was in a lower magnetic field, the storable phase space could be increased, however, this makes a frequency tunable spin flipper necessary. Such a spin flipper is realised as double saddle coils and presented in the next chapter.

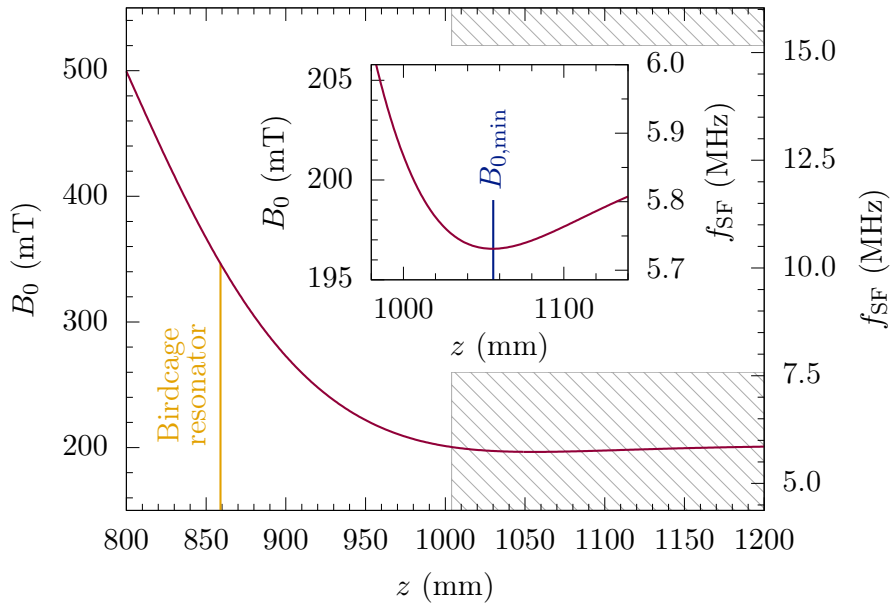


Figure 4.13: Magnetic field B_0 (left axis) and corresponding required spin flipper frequency f_{SF} (right axis) as function of the spin flip position z_{SF} at $I_{\text{main}} = 33$ A. The yellow line marks the theoretical spin flip position for the birdcage resonator, $z_{\text{SF}} = 859$ mm, calculated from its resonance frequency $f_{\text{SF}} = 10.315$ MHz. Within the grey shaded region the spin flip field condition of Eq. 4.16 is violated. The inset shows a detailed view of the area around the magnetic field minimum B_0^{min} at $z = 1056$ mm (blue line).

Chapter 5

Optimisation of spin flip loading in τ SPECT

The calculations in Ch. 3.6.4 showed, that the number of neutrons in the magnetic trap needs to be increased in order to reduce the overall measurement time for a first neutron lifetime measurement with $\Delta\tau_n \leq 1.0$ s. This can in theory be achieved by using spin flip positions further inside the trap where $B_0(z_{\text{SF}})$ is smaller, which leads to an increase in the maximum energy - and consequently the number of neutrons - storable in the trap.

As we have seen at the end of the previous chapter, changing the resonance frequency of the birdcage resonator is not reasonably possible in the required range of several MHz. Therefore, the birdcage resonator is replaced by a frequency tunable spin flipper built from a pair of saddle coils, which is presented in the first part of this chapter. The second part deals with an optimisation of the normalisation and the spectrum cleaning procedure.

5.1 Spin flipping using a double saddle coil

The shape of a saddle coil is shown on the left in Fig. 5.1. It is the simplest approximation to a cosine-theta coil (cf. Ch. 3.3.1), consisting of two opposite rectangles of wire on a cylindrical surface as shown in Fig. 5.1 (left). Its characteristics are a length l , a bending radius $d/2$ and an opening angle ϕ . With a constant current flowing through the wire, a static magnetic field is generated as shown by the red arrow in the left figure and the white arrows in the field map on the right, which is the result of a FEM simulation using COMSOL Multiphysics[®]. Using a sinusoidal current at a frequency f_{SF} leads to a linear oscillation of the magnetic field. A second saddle coil is added, rotated by 90° , as shown in the middle of Fig. 5.1. This second coil superimposes a second linearly oscillating field perpendicular to the first one. The coils are excited individually at the same frequency f_{SF} and amplitude, but with a phase shift $\Delta\varphi$. With this phase shift, the polarisation of the resulting magnetic field can be adjusted to linear π -polarisation ($\Delta\varphi = 0^\circ$ or 180°), circular σ^\pm -polarisation ($\Delta\varphi = \pm 90^\circ$) or elliptical polarisation at any other values.

The spin flipper was built as this double saddle coil assembly and is shown in Fig. 5.2 (left). The coils are wound on a holding cylinder made from PEEK with special millings to simplify the construction. Two pick-up coils are added for functionality checks, as well as a PT1000 sensor on the backside for temperature surveillance. The dimensions of the two coils are $l = 60$ mm, $d/2 = 31.5$ mm and $\phi = 120^\circ$. The value for the opening angle arises

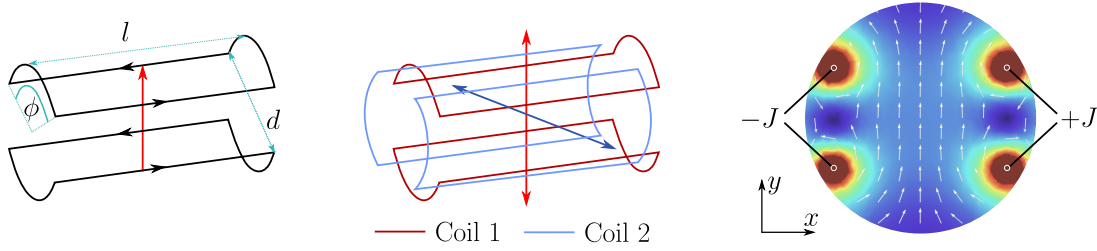


Figure 5.1: Schematics of a single saddle coil and the double saddle coil assembly. Left: A single saddle coil of length l , bending radius $d/2$ and opening angle ϕ , carrying a constant current (black arrows) generates a static magnetic field (red arrow). Middle: The same saddle coil is now shown in red. By adding a second saddle coil (blue), rotated by 90° and using sinusoidal excitation, a field superposition of two linearly oscillating magnetic fields can be achieved. A phase shift in the excitation signals changes the polarisation of the resulting B_1 field. Right: Simulation of the B_1 field at direct current (arbitrary units) using COMSOL Multiphysics[®], the white arrows show the direction of the field.

from the analytic optimum found in [GM70], leading to the most homogeneous field in the centre of the coil, which is, however, deduced for $l/d = 2$. With l/d being approximately 1 in our case, [SVMT06] quotes an optimum of $\phi = 135^\circ$. Regarding the spin flipper for τ SPECT, this leaves room for improvement. The coils are positioned with a longitudinal offset of 10 mm to reduce cross-talk. Therefore, the effective length of the spin flipper is $l_{\text{eff}} = 50$ mm. The excitation circuit is shown on the right side of Fig. 5.2. The sinusoidal signal is produced by the two output channels of a frequency generator¹, the phase shift is added to channel No. 2. The signals are amplified in two stages², because the main amplifiers require an input power of at least 1 W. Both tuning and impedance matching of the saddle coils to $|Z| = 50 \Omega$ (cf. Ch. 3.3.2.1) are done by amateur radio tuners³ outside of the experiment. This is the main improvement with respect to the birdcage resonator, where the resonance frequency was fixed by the capacitors mounted within the rungs (cf. Fig. 3.18). Finally, after passing bidirectional couplers, the two signals generate the magnetic field inside the spin flipper. The couplers are used for signal monitoring and for adjusting the signal phase and amplitudes.

5.1.1 Increasing the UCN density in τ SPECT

The saddle coil spin flipper was mounted inside the compensation octupole in τ SPECT and tested with neutrons for the first time in beamtime *Feb2020*. In the following, the optimisation of the spin flip position with respect to B_0 in order to increase the energy acceptance (cf. Ch. 4.2.1) is shown; afterwards, we have a look at the characterisation of the spin flipper. If not mentioned otherwise, all measurement results refer to the background

¹Frequency generator: Siglent SDG2042X

²Pre-amplification: K-N-E 10W-QRP power amplifier, max. output 10 W
Main amplification: RM Italy HLA300 V plus, max. output 300 W

³Frequency tuning: MFJ-969 Versa Tuner II

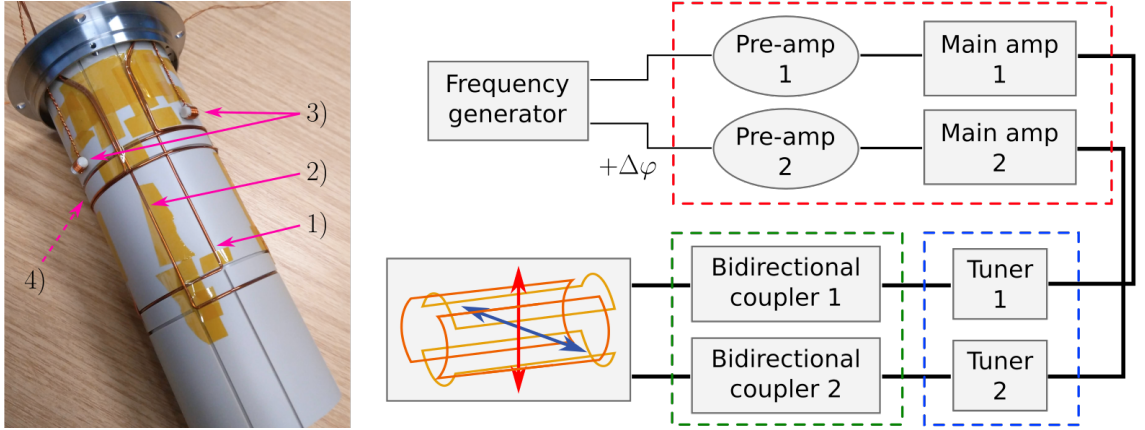


Figure 5.2: The finished saddle coil spin flipper and the excitation circuit. Left: The saddle coils (1) and (2) are wired onto a holding tube. Two pick-up coils (3) and a PT1000 sensor (4) (not shown) are used for functionality and temperature checks. Right: The excitation signals (with the adjustable phase shift $\Delta\varphi$ added to channel No. 2) are produced by a frequency generator and amplified (red dashed box). Two amateur radio tuners tune and match the saddle coils to $|Z| = 50 \Omega$ at the desired frequency (blue dashed box). After passing the bidirectional couplers (green dashed box), which are used for phase and amplitude adjustments, the signals generate the magnetic field inside the spin flipper.

subtracted UCN counts N in the counting interval normalised to the average pulse energy of the specific beamtime.

5.1.1.1 The optimum filling position relative to B_0 in τ SPECT

The optimisation of the spin flipper filling position was done using 50s storage measurements without cleaning at $z_{\text{SF}} = [900, 935, 959, 980, 1020]$ mm. The height of τ SPECT was $h = 1.47$ m with beamline No. 2 (cf. Ch. A.6). At each position, the required RF frequency $\omega_{\text{SF}} = 2\pi f_{\text{SF}}$ was calculated to match $\omega_0(z_{\text{SF}}) = |-\gamma B(z_{\text{SF}})|$, with $B(z_{\text{SF}})$ the total magnetic field at the nominal spin flip position calculated using Eq. 3.10. Furthermore, the signal phase $\Delta\varphi$ at the bidirectional couplers was set to $+90^\circ$ and the RF power to $P \geq 50$ W, where saturation of the trap is reached (see Ch. 5.1.1.2 further below for details on the optimisation processes).

The results are shown in Fig. 5.3 as average and standard deviation of multiple measurements with normalisation to the average pulse energy. The measurements in beamtime *Sept2019* using the birdcage resonator were re-normalised to beamtime *Feb2020*. At the rather short storage time, also with the spin flipper switched off again an average of $N_{\text{SF_off}} = 60 \pm 8$ UCN were detected. The grey shaded region shows the positions $z_{\text{SF}} > 1004$ mm, where $\nabla_t B(r = 25 \text{ mm}, z_{\text{SF}}) > 3\nabla_z B(r = 0 \text{ mm}, z_{\text{SF}})$ and thus the spin flip field condition $k(z_{\text{SF}}) > 3$ (cf. Eq. 4.16) is violated. It is apparent, that N significantly increases when z_{SF} is shifted to positions further inside the storage octupole where B_0 is lower. By performing the spin flip at $z_{\text{SF}} = 980$ mm, 4.3 ± 0.6 times more neutrons could be stored in comparison to the measurements with the birdcage resonator. The decline in N at $z_{\text{SF}} = 1020$ mm furthermore confirms, that positions where the field condition is

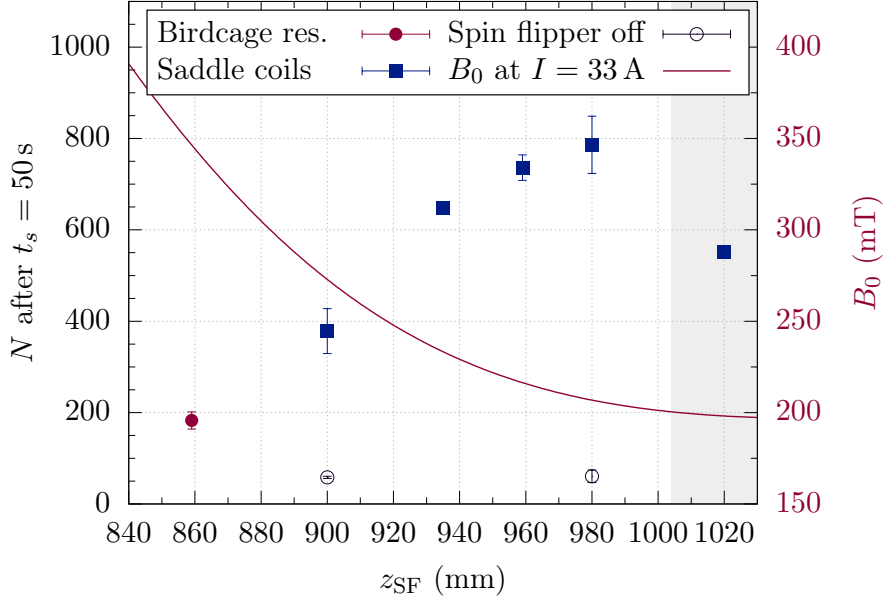


Figure 5.3: Number of stored neutrons N after 50s storage depending on the spin flip position z_{SF} , normalised to the average pulse energy. Compared to the birdcage resonator measurement (red circle), the frequency tunable saddle coil spin flipper allows for spin flip positions, where N increases up to a factor of ~ 4 (blue squares). Each data point is the average value and standard deviation of multiple measurements at that position. With the spin flipper switched off, $N_{\text{SF, off}} = 60 \pm 8$ UCN are measurable (open circles). The range with $k_{\text{mean}} + |\Delta k_{\text{mean}}| > 3$ is marked by the grey area. Here, as expected from the MC simulation, ε_{SF} drops and N is reduced by $\sim 25\%$.

violated should be avoided as here the spin flip efficiency decreases.

Therefore, we take $z_{\text{SF}} = 980 \text{ mm} = z_{\text{SF, opt}}$ as temporary optimum filling position. Here we find the energy acceptance of the trap as

$$\Delta E_{\text{kin},0} = [0 \text{ neV}, 18.9 \text{ neV}]. \quad (5.1)$$

5.1.1.2 Optimisation of the saddle coil parameters

Each new spin flip position requires the optimisation of three parameters in order to guarantee, that the spin flipper is maximally efficient. These parameters are in principle the frequency, the RF power and the polarisation of B_1 .

The spin flipper frequency The optimum spin flip position for the birdcage resonator measurements in Ch. 3.6.3 was calculated from its fixed resonance frequency (cf. Ch. 3.3.4). In this calculation, we used the simulation of B_0 and the measurement result of the compensated octupole field $B_{\text{abs, mean}} = 25(4) \text{ mT}$ at $r = 25 \text{ mm}$ (cf. Tab. 3.1). However, since the transversal field (and consequently the total field and the resonance frequency) is not fixed over the neutron guide cross section, a position optimisation around the target position was required in order to confirm this approach (cf. Ch. 3.6.3).

With the saddle coil spin flipper, the process is reversed compared to the birdcage resonator, but a similar argumentation holds: We start with a fixed target spin flip position z_{SF} and calculate the total magnetic field $B(z_{\text{SF}})$ using Eq. 3.10 again, inserting $B_0(z_{\text{SF}})$ and the compensated octupole field $B_{\text{abs,mean}} = 25(4)$ mT at $r = 25$ mm. From the corresponding Larmor frequency $\omega_0(z_{\text{SF}}) = |-\gamma B(z_{\text{SF}})|$ (cf. Eq. 3.1), the required RF frequency $\omega_{\text{SF}} = 2\pi f_{\text{SF}}$ is deduced and the spin flipper tuned accordingly. The maximum spin flip efficiency is achieved if the resonance $\omega_0(z_{\text{SF}}) = 2\pi f_{\text{SF}}$ lies inside the spin flipper, so that the maximum B_1 amplitude is useful. With an infinitely long saddle coil this would always be the case, however, with the spin flipper of finite length, fringe effects occur: If the spin flipper is positioned such that the resonance lies within the fringe field at the edges of the saddle coils, the amplitude of B_1 is reduced and the field points increasingly in longitudinal direction. As only the projection of B_1 perpendicular to the longitudinal B_0 field is effective for the spin flip (cf. Ch. 4.1), the spin flip efficiency decreases. Outside of the spin flipper fringe field B_1 drops eventually to zero - here no spin flip is possible anymore.

The optimisation of the resonance lying inside the spin flipper can be done by choosing a fixed spin flip position and vary the RF frequency (this moves the position of the resonance relative to the spin flipper), however, retuning the spin flipper during beamtimes is rather time-consuming. The other possibility is to keep the RF frequency fixed and instead vary the position of the spin flipper relative to the position of the resonance.

The result of such a spin flip position optimisation is shown in Fig. 5.4: The target position was $z_{\text{SF}} = 900$ mm at which the resonance frequency was calculated as $f_{\text{SF}} = 8.021$ MHz. The plateau-shaped behaviour, that we saw with the birdcage resonator as

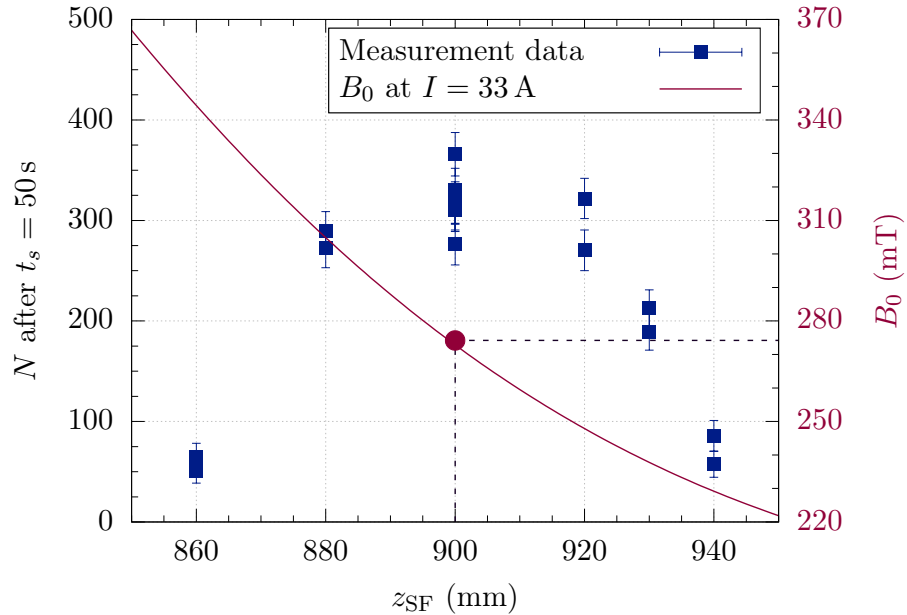


Figure 5.4: Saddle coil spin flip position optimisation around $z_{\text{SF}} = 900$ mm at $f_{\text{SF}} = 8.021$ MHz using 50 s storage measurements and an RF power of 50 W. The blue squares show the measurement results on the left axis, normalised to the average pulse energy. The red line depicts the B_0 field at $I_{\text{main}} = 33$ A, referring to the right axis. The target spin flip position is marked by the red circle, which is confirmed as optimum by the measurement results.

well (cf. Fig. 3.29), is visible within errors between $z_{\text{SF}} \approx 880$ and 920 mm, which is slightly smaller than the effective spin flipper length of $l_{\text{eff}} = 50$ mm. At positions beyond this region, the resonance lies only within the fringe field of the spin flipper, so that the effective B_1 amplitude does not suffice for a maximum spin flip efficiency anymore. Consequently, the number of neutrons storable in the trap decreases.

To summarise, with the target position lying well within the measured plateau, we can confirm this position as the optimum for the given RF frequency.

The dependency on RF power Under the assumption of neglectable transversal gradients ($\nabla_t B \ll \nabla_z B$), the spin flip efficiency ε_{SF} for neutrons at a given velocity depends only on $\nabla_z B$ and the B_1 amplitude (cf. Eq. 4.12). At each spin flip position, $\nabla_z B$ in the centre of the spin flipper is a fixed parameter, so that ε_{SF} depends only by B_1 (this dependency was also simulated at one selected spin flip position $z_{\text{SF}} = 980$ mm as was shown in Ch. 4.1.2).

In τ SPECT, the amplitude of B_1 is scaled by the irradiated RF power, which is in turn adjusted by the signal amplitude of the frequency generator. The maximum RF power, that can be irradiated, depends on the impedance matching of the spin flipper to $|Z| = 50 \Omega$ (cf. Ch. 3.3.2.1). If the spin flip position is changed the resonance frequency must be adapted to the magnetic field at the new position, so that $\omega_0(z_{\text{SF}}) = |-\gamma B(z_{\text{SF}})| = 2\pi f_{\text{SF}}$ remains valid.

Consequently, every time the spin flipper is retuned, its performance with respect to power needs to be measured. This serves as a quality check for the impedance matching, because the main amplifiers enter a fail-safe mode if the reflected power becomes too large and would have to be restarted.

Furthermore, the power output of the amplifiers depends on the frequency as well. During measurements with τ SPECT the experimental area is not accessible, so that the power output cannot be read directly, which would be required e.g. when changing the B_1 amplitude. Therefore, a look-up table is required at each frequency, which relates the input signal amplitude to the resulting output power.

In order to measure the performance, the spin flipper was switched on manually for 6 s independently of UCN production. The irradiated power is read from the analog displays of the tuners and the voltage measured with the pick-up coils at the spin flipper is monitored while the signal voltage is raised.

Fig. 5.5 shows an example of the resulting dependency between the induced voltage in the pick-up coils U_{pp} (peak-to-peak voltage) and the RF power at the two frequencies $f_{\text{SF},1} = 8.021$ MHz (corresponding to $z_{\text{SF},1} = 900$ mm) and $f_{\text{SF},2} = 6.098$ MHz ($z_{\text{SF},2} = 980$ mm). The errors are estimated from the reading uncertainties. In both cases, irradiating up to at least 100 W was safely possible with the dependency following a \sqrt{P} -behaviour, as confirmed by the two fits of shape⁴ $U(P) = a\sqrt{P}$. This behaviour is explained using the proportionality in Ampère's law $B \propto I$ (cf. Eq. A.6), $P = UI/2$ for alternating current, and Ohm's law $U = RI$, resulting in the relation

$$P \propto I^2 \propto B_1^2. \quad (5.2)$$

⁴The fit parameters are $a = 0.1490(21) \text{ V}/\sqrt{\text{W}}$ for $f_{\text{SF},1}$ ($\chi^2/\text{ndf} = 0.92$) and $a = 0.1350(12) \text{ V}/\sqrt{\text{W}}$ for $f_{\text{SF},2}$ ($\chi^2/\text{ndf} = 0.35$).

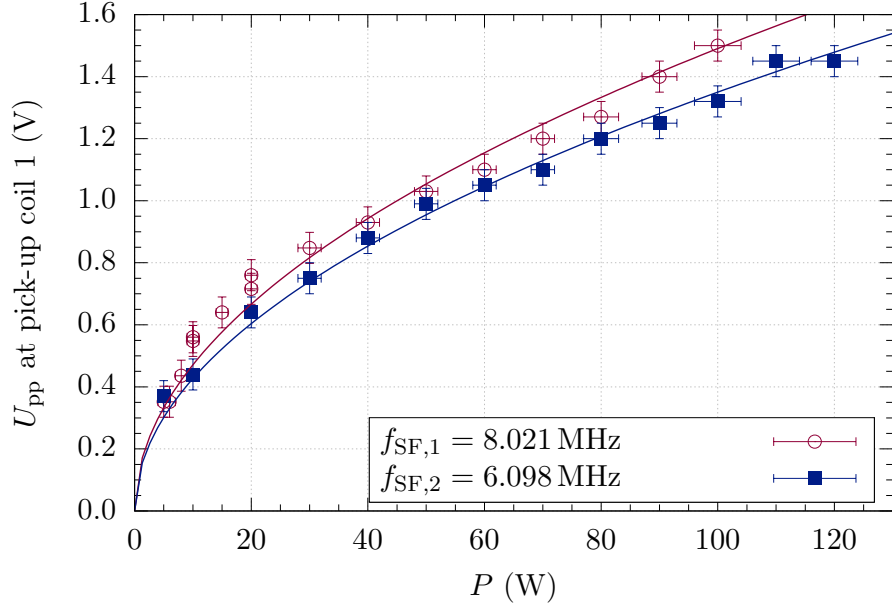


Figure 5.5: Pick-up coil voltage at the saddle coil spin flipper depending on the input RF power at $f_{\text{SF},1} = 8.021$ MHz (red, corresponding to $z_{\text{SF},1} = 900$ mm) and $f_{\text{SF},2} = 6.098$ MHz (blue, $z_{\text{SF},2} = 980$ mm). The lines are \sqrt{P} fits, confirming the expected proportionality deduced in Eq. 5.3.

The voltage induced in the pick-up coils on the other hand depends linearly on B_1 according to Maxwell-Faraday's induction law (cf. Eq. A.3). In terms of measurable parameters then follows

$$\sqrt{P} \propto B_1 \propto U_{\text{ind}}. \quad (5.3)$$

For τ SPECT, this means, that the RF power does in fact generate the B_1 field in the saddle coils and is not dissipated in the impedance matching circuit of the tuners. However, since the pick-up coils have not been calibrated, a direct deduction of the B_1 amplitude is not possible. Therefore, the number of storable neutrons N after $t_s = 50$ s was measured depending on the irradiated RF power, and thus B_1 . Saturation of the trap with UCN is expected as soon as B_1 is high enough to reach the full spin flip efficiency of $\varepsilon_{\text{SF}} \simeq 1$. An example of such measurement results is shown in Fig. 5.6, again for $z_{\text{SF},1} = 900$ mm and $z_{\text{SF},2} = 980$ mm, where we can distinguish two major effects:

1. At $z_{\text{SF},1}$ the longitudinal gradient is higher than at $z_{\text{SF},2}$ ($\nabla_z B(z_{\text{SF},1}) = 14.0$ mT/cm compared to $\nabla_z B(z_{\text{SF},2}) = 3.6$ mT/cm), so that a higher B_1 amplitude is required for maximum spin flip efficiency and thus saturation of the trap is reached at higher RF powers.
2. The maximum storable energy $E_{\text{kin},0}^{\text{max}}$ is larger at $z_{\text{SF},2}$ ($E_{\text{kin},0}^{\text{max}}(z_{\text{SF},2}) = 18.9$ neV compared to $E_{\text{kin},0}^{\text{max}}(z_{\text{SF},1}) = 11.0$ neV, cf. Ch. 4.2), resulting in a higher number of neutrons in the storable energy range. Therefore, at $z_{\text{SF},2}$, N in saturation reaches a higher level.

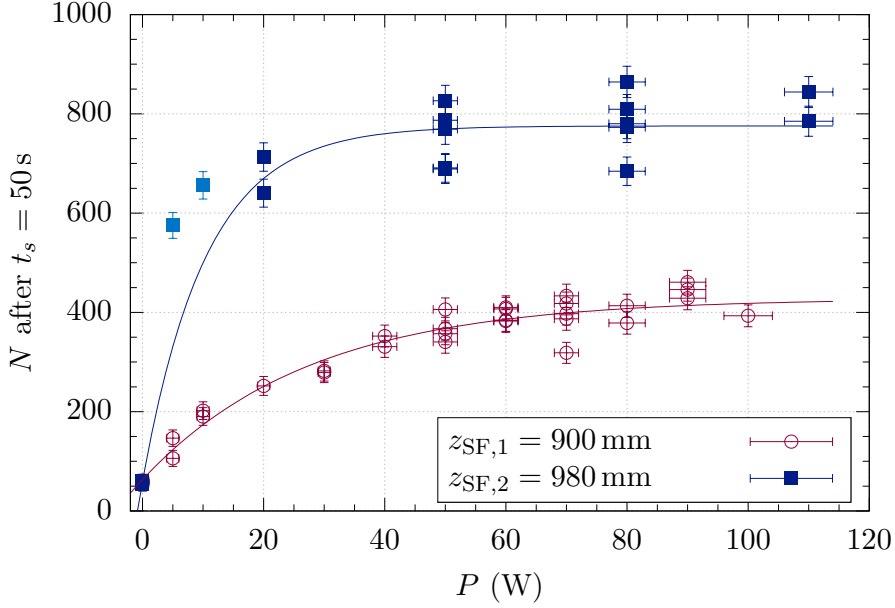


Figure 5.6: Number of storable neutrons depending on the irradiated RF power at $z_{\text{SF},1} = 900$ mm (red) and $z_{\text{SF},2} = 980$ mm (blue). The data shows a saturation behaviour, with N increasing with P as long as $N(P) < N_{\text{sat}}$, and N_{sat} given by the energy acceptance at the individual spin flip position. The lines are saturation fits according to Eq. 5.4 with the fit parameters listed in Tab. 5.1. The light blue data points are not included in the fit for $z_{\text{SF},2}$.

Both data sets are fitted using a saturation function of the shape

$$N(P) = N_{\text{sat}} \left(1 - \exp \left[-\frac{P}{P_{1/e}} \right] \right) + N_{\text{SF_off}} \quad (5.4)$$

with N_{sat} the number of storable neutrons in saturation, $P_{1/e}$ the characteristic RF power at which $1/e$ of the saturation is reached, and $N_{\text{SF_off}}$ the offset at $P = 0$ W. The light blue data points are not included in the fit at $z_{\text{SF},2}$ due to the limited statistics. The fit parameters are listed in Tab. 5.1. As from $P \simeq 50$ W onwards the measurement results of each set are consistent within errors, we assume, that here saturation of the trap is fulfilled sufficiently. It can thus be confirmed, that the saddle coil spin flipper reaches full efficiency well within its safely operational range. If not mentioned otherwise, all measurements in this work using the saddle coils were done in saturation.

Table 5.1: Results of the saturation fits in Eq. 5.4 to the measurements depicted in Fig. 5.6.

f_{SF}	N_{sat}	$P_{1/e}$	$N_{\text{SF_off}}$	χ^2/ndf
8.021 MHz	364.9 ± 14.5	27.7 ± 3.5 W	63.1 ± 8.6	1.55
6.098 MHz	716.9 ± 21.9	10.5 ± 2.1 W	58.7 ± 13.8	3.34

The dependency on the signal phase shift $\Delta\varphi$ Successful spin flipping depends on the polarisation of the B_1 field, as was shown in Ch. 4.1.1.1, because when expressing the polarisation as two counter-rotating fields, only the B^+ component is on resonance with the neutron Larmor precession. By changing the phase shift $\Delta\varphi$ between the saddle coil excitation signals, the fraction of the B^+ - and B^- -component in the resulting B_1 field is varied.

The phase dependency was measured in beamtime *June2020* using 200 s storage measurements at $z_{\text{SF,opt}} = 980$ mm and a reduced RF power of 20 W (we will see why in a moment). The rather long storage time was chosen in an attempt to avoid counting the spin flipper independent neutrons $N_{\text{SF_off}}$, because at perfect σ^- polarisation, the spin flip efficiency should go down to zero and thus the trap should be empty. The resulting dependency of N on $\Delta\varphi$ is shown in Fig. 5.7 with the x -axis corresponding to the phase difference measured at the bidirectional couplers.

The leftmost three measurement points are repeated on the right to enhance the visibility of the periodic structure of the data. The grey bands roughly indicate the estimated field polarisation at the respective phase shift. The data roughly follows the shape of the modulus of a cosine function, so that a fit of the form

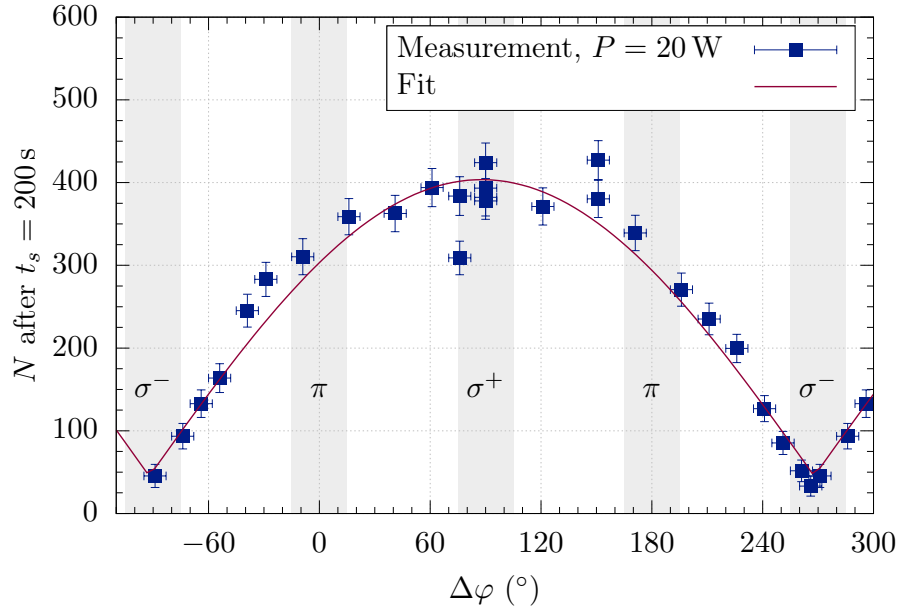


Figure 5.7: Number of stored neutrons after $t_s = 200$ s depending on $\Delta\varphi$ as measured at the bidirectional couplers with normalisation to the average pulse energy. The spin flipper was set to $f_{\text{SF}} = 6.098$ MHz at $z_{\text{SF}} = 980$ mm and $P = 20$ W. The red line is a fit of the modulus of a cosine function (cf. Eq. 5.5). The maximum number of neutrons was measured at $\Delta\varphi = 90^\circ$, which corresponds to σ^+ polarisation of the B_1 field. The opposite σ^- polarisation is thus found at -90° and 270° , where no spin flip is possible and $N = N_{\text{SF_off}}$. In the centre between these two extremes (0° and 180°), linear polarisation of B_1 is realised. Here, the effective B_1 amplitude is reduced to a factor of $1/\sqrt{2}$.

$$N(\Delta\varphi) = N_{\sigma^+} \left| \cos \left(\frac{1}{2} (\Delta\varphi - \varphi_0) \right) \right| + N_{\text{SF_off}} \quad (5.5)$$

is applied with the optimum found at $\varphi_0 = (87.9 \pm 2.3)^\circ$ and $N_{\sigma^+} = 358.4 \pm 14.9$ ($\chi^2/\text{ndf} = 0.89$). Given the non-vanishing parameter $N_{\text{SF_off}} = 45.2 \pm 9.3$ either not all spin flipper independent neutrons could be eliminated or perfect σ^- polarisation was not achieved⁵. Linear polarisation is found at $\Delta\varphi(\sigma^+) \pm 90^\circ$. From $B^+ = B^-$ (cf. Ch. 4.1.1.1) follows $B_1 = \sqrt{2(B^+)^2}$, so that here the useful component for spin flipping is reduced to $B^+ = B_1/\sqrt{2}$. The factor $1/\sqrt{2}$ is also visible in the reduction of N . The direct proportionality between N - and consequently ε_{SF} - and B_1 is only possible if ε_{SF} depends linearly on B_1 , which contradicts Eq. 4.12. In the Monte Carlo simulation in Ch. 4.1.2 on the other hand such an approximately linear dependency between ε_{SF} and B_1 was found when increasing the B_1 amplitude until ε_{SF} saturated at 100% (cf. Fig. 4.8). Therefore, as long as the spin flipper is operated at an RF power which is not in the trap saturation range (see also Ch. 5.1.1.2), the optimum phase $\Delta\varphi$ has to be found to achieve maximum spin flip efficiency.

If we raise the power to the saturation regime, the cosine behaviour of N vanishes and ε_{SF} becomes independent of $\Delta\varphi$ in a wide range around the optimum: This is shown in Fig. 5.8 as the result of measurements with $P = 80$ W and a storage time of 50 s. The fit corresponds to a function of shape

⁵This could have been investigated by measuring the number of neutrons in the trap after $t_s = 200$ s with the spin flipper switched off, which was not done in this case.

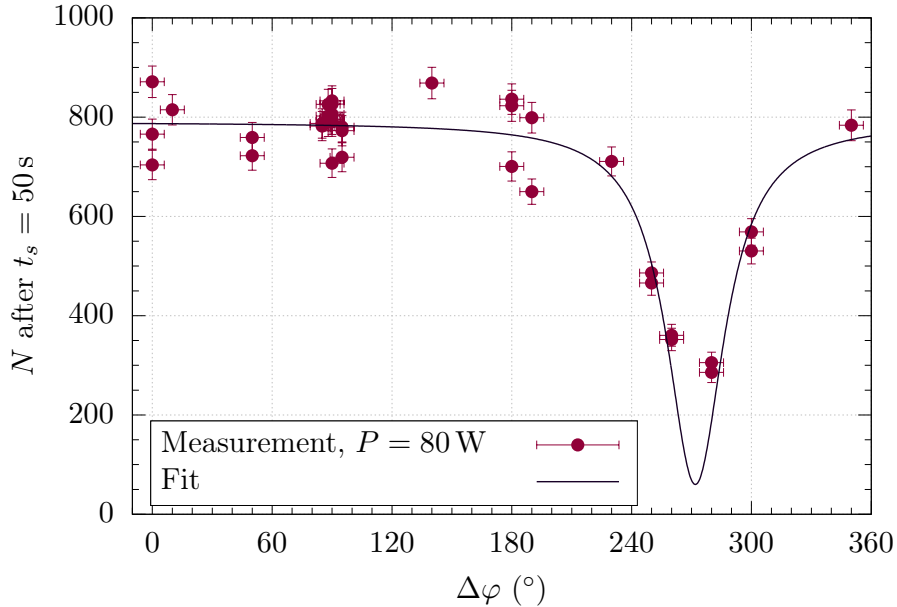


Figure 5.8: Number of stored neutrons after $t_s = 50$ s (red) depending on $\Delta\varphi$ at $P = 80$ W with normalisation to the average pulse energy. With the RF power in the saturation regime, ε_{SF} is maximum over a wide range up to $\Delta\varphi \simeq 220^\circ$. The black line corresponds to a fit of the function in Eq. 5.6.

$$N(\Delta\varphi) = N_{\text{sat}} \left(1 - \frac{w^2}{w^2 + (2\Delta\varphi - 2\Delta\varphi_0)^2} \right) + N_{\text{SF off}} \quad (5.6)$$

with the number of neutrons in saturation $N_{\text{sat}} = 730.0 \pm 10.6$, a fixed offset $N_{\text{SF off}} = 60$, and a dip at $\Delta\varphi_0 = (271.9 \pm 3.4)^\circ$ with a half width of $w = (35.2 \pm 5.9)^\circ$ ($\chi^2/\text{ndf} = 2.60$). The reason for this independency is that at high powers also a reduced B^+ -component still suffices to achieve maximum spin flip efficiencies.

5.2 Implications for measurements with τ SPECT

The measurements using the double saddle coil spin flipper showed, that it is sufficient to know the correct spin flip position with respect to B_0 within several 10 mm due to the length of the saddle coils. Also as soon as the RF power is in the saturation regime and $\Delta\varphi$ is roughly close to the optimum, the spin flipper reaches maximum efficiencies.

Maximum efficiencies were also obtained with the birdcage resonator (cf. Ch. 3.6), however, due to its fixed resonance frequency a variation of the spin flip position was not possible and the storable phase space was limited by the maximum initial kinetic energy $E_{\text{kin},0}^{\text{max}}$ (879 mm). In comparison, the number of storable neutrons after 50 s storage time could be increased by a factor of ~ 4 to $N = 786 \pm 63$ at the optimum filling position $z_{\text{SF,opt}} = 980$ mm. In addition to these results, two further optimisations were attempted, which are discussed in the following.

5.2.1 Improving the compensation of the octupole field

In the process of finding an analytic approximation of the compensated octupole field (cf. Ch. A.5.1.2), the rotational and axial offsets between storage and compensation octupole are estimated as $\delta\varphi = 0.2^\circ$ and $\delta y = -2.6$ mm. The rather large axial misalignment arises from a full compression of the springs at the lower two rolls, on which the spin flipping unit is moved on the storage octupole surface (cf. Ch. 3.1.2), which was already visible in the setup for the compensated field measurement (cf. Ch. 3.2.2.1). By adding 3.5 mm thick cylinders under the springs, the spring deflection is decreased and full compression occurs earlier, so that the axial offset can be reduced as is shown in Fig. 5.9 (left).

The left half of the figure refers to the initial situation, the right half corresponds to the configuration including the cylinders. Considering the 45° arrangement of the rolls with respect to the vertical axis, the axial offset is reduced by $3.5 \text{ mm} \times \cos(45^\circ) = 2.47$ mm. As a conservative estimation, this value is rounded down, leaving a remaining axial offset of $\delta y = -0.2$ mm.

Due to time issues, the resulting magnetic field after centring could not be measured and was simulated using COMSOL Multiphysics[®] instead. The right side of Fig. 5.9 shows the compensated field measurement data at $r = 25$ mm obtained in Ch. 3.2.2.1 for reference and an according simulation with $\delta\varphi = 0.2^\circ$ and $\delta y = -2.6$ mm, as well as a simulation with $\delta y = -0.2$ mm corresponding to the resulting field after centring the compensation octupole. It was discussed in Ch. 3.2.2.1, that an axial offset is responsible for the reduction in the multipole order of the compensated field. Therefore, due to the small but still present offset δy after centring the compensation octupole the hexapole shape remains.

In order to quantify the effect of the centring on the compensated magnetic field, the mean field and gradients of both measurement and simulations were calculated and are

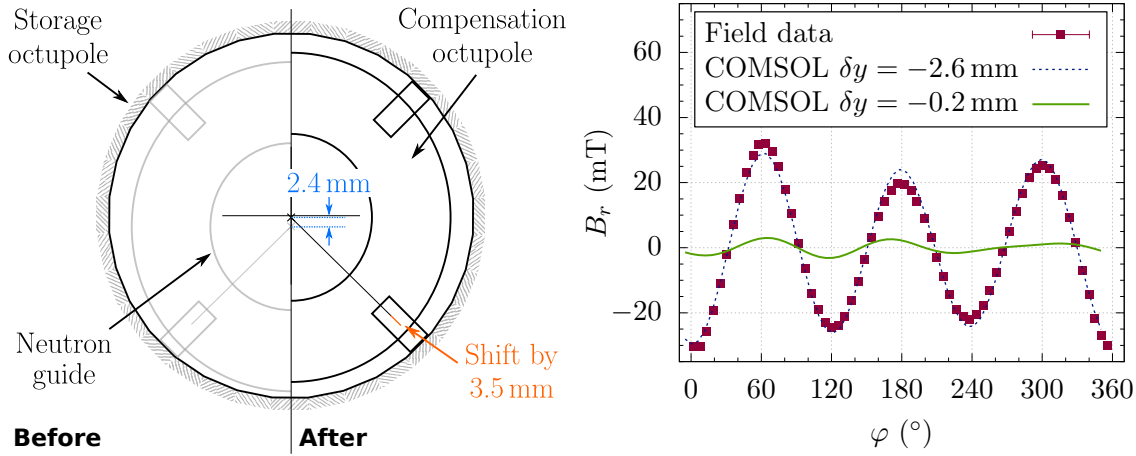


Figure 5.9: Centring principle of the compensation octupole and simulation of the effect on the compensated magnetic field. Left: Split view of the alignment of compensation octupole and neutron guide with respect to the storage octupole before (grey, left half) and after centring (black, right half). The position of full compression of the springs under the lower two rolls is shifted inwards by 3.5 mm using stainless steel cylinders (indicated in orange). The compensation octupole is thus lifted by 2.4 mm from $\delta y = -2.6$ mm to -0.2 mm. Right: Radial component of the compensated octupole field measurement at $r = 25$ mm (red data points) and the corresponding simulation using COMSOL Multiphysics[®] with $\delta\varphi = 0.2^\circ$ and $\delta y = -2.6$ mm (blue dashed line). Assuming $\delta y = -0.2$ mm after centring results in the field shown by the green solid line.

listed in Tab. 5.2. The results of measurement and simulation of the uncentred compensation are consistent within errors. Comparing the absolute mean field and gradient $B_{\text{abs,mean}}$ and $|\nabla_t B|_{\text{mean}}$ of the simulated fields, the compensation is improved by a factor of 12.2 ± 4.5 and 11.8 ± 4.6 , respectively. On average, the centring improves the field compensation by a factor of 12.0 ± 3.2 . Including these results in the total magnetic field in τ SPECT and calculating k according to Eq. 4.16, we find that the maximum allowed spin flip position is shifted from formerly 1004 mm to 1055 mm at $I_{\text{main}} = 33$ A.

The effect of the centring was measured with neutrons in beamtime *Dec2020* using 50 s storage measurements at the so far optimum spin flip position $z_{\text{SF}} = 980$ mm and three positions closer to the trap minimum ($z_{\text{SF}} = [1005, 1020, 1030]$ mm). At each position, the required RF frequency was calculated as described in Ch. 5.1.1.2, with the total magnetic field (cf. Eq. 3.10) consisting of $B_0(z_{\text{SF}})$ in longitudinal direction and $B_{\text{abs,mean}}$ at $r = 25$ mm obtained from the simulated field results after centring. Furthermore, the spin flip position as well as the B_1 polarisation were optimised as described in the previous section, and the RF power was raised to the saturation regime.

The result is shown in Fig. 5.10, each data point corresponds to the average of a set of measurements, the error is the standard deviation of these measurements. The data obtained in beamtime *Feb2020* are depicted for reference with a re-normalisation to the average pulse energy of beamtime *Dec2020*. Here, the compensation octupole was still misaligned by $\delta y = -2.6$ mm. After centring the compensation octupole, the high level

Table 5.2: Storage octupole field before and after centring. The measurement data is taken from Tab. 3.1, the simulation results are obtained using COMSOL Multiphysics[®] with misalignments of $\delta\varphi = 0.2^\circ$ in both simulations, and $\delta y = -2.6$ mm (uncentred) and $\delta y = -0.2$ mm (centred). All values refer to a radius of $r = 25$ mm. Regarding the absolute magnetic field and gradient, an average improvement of the field compensation by a factor of 12.0 ± 3.2 is achieved.

	Measurement uncentred	Simulation uncentred	Simulation centred
$B_{\text{abs,mean}}$	25 ± 4 mT	26.8 ± 2.2 mT	2.2 ± 0.8 mT
$ \nabla_t B _{\text{mean}}$	29 ± 15 mT/cm	24.8 ± 2.1 mT/cm	2.1 ± 0.8 mT/cm

of stored neutrons N is confirmed at $z_{\text{SF}} = 980$ mm, even though the absolute number is reduced by around 17%. In retrospect, a HD-contamination of the D_2 gas within the UCN source (cf. Ch. A.1) is held responsible for this reduction. The expected increase in N at spin flip positions further inside the trap could, however, not be realised, rather the contrary is the case: With $N(1020 \text{ mm}) = 44(5)$, the value is on the same level as the result obtained with the spin flipper switched off ($N_{\text{SF_off}} = 46(1)$), which means that effectively, no storable LFS were produced. The situation is similar at $z_{\text{SF}} = 1030$ mm ($N(1030 \text{ mm}) = 67(6)$).

We can exclude, that at these positions the RF signal did not reach the saddle coils but was dissipated, e.g. within the tuners, by comparing the induced voltages in the pick-up coils: The measured spin flip positions as well as the corresponding RF frequencies and the induced voltages in the pick-up coils, U_{pp} , are summarised in Tab. 5.3, with the error in the voltage arising from reading uncertainties from the oscilloscope⁶. From Eq. A.5 follows, that with a given fixed field amplitude of B_1 and a decreasing RF frequency, U_{pp} must increase. The measured voltages being consistent within errors, however, indicate a slight reduction of B_1 when decreasing the frequency. Nevertheless, from the fact, that at $z_{\text{SF}} = 980$ mm and 1005 mm UCN were stored, we can deduce, that also at $z_{\text{SF}} = 1020$ mm a B_1 field was irradiated, which would have been sufficient to fill the trap with a number of neutrons distinguishable from $N_{\text{SF_off}}$.

Even though this was not the original intention, a successful centring of the compen-

⁶Compared to the pick-up coil signals in Fig. 5.5 with $U_{\text{pp}}(f_{\text{SF}} = 6.098 \text{ MHz}) = 1.2 \text{ V}$ at 80 W, a significant signal reduction is visible. This is caused by a shift in the self-resonances of the pick-up coils due to the installation of isolated vacuum feedthroughs for the BNC connections in τ SPECT.

Table 5.3: RF frequencies and induced pick-up coil voltages U_{pp} at the spin flip positions used in beamtime *Dec2020*. The voltage at $z_{\text{SF}} = 1030$ mm was not measured.

	$z_{\text{SF}} = 980$ mm	$z_{\text{SF}} = 1005$ mm	$z_{\text{SF}} = 1020$ mm	$z_{\text{SF}} = 1030$ mm
RF frequency	6.030 MHz	5.903 MHz	5.776 MHz	5.753 MHz
U_{pp}	250(20) mV	234(20) mV	226(20) mV	-

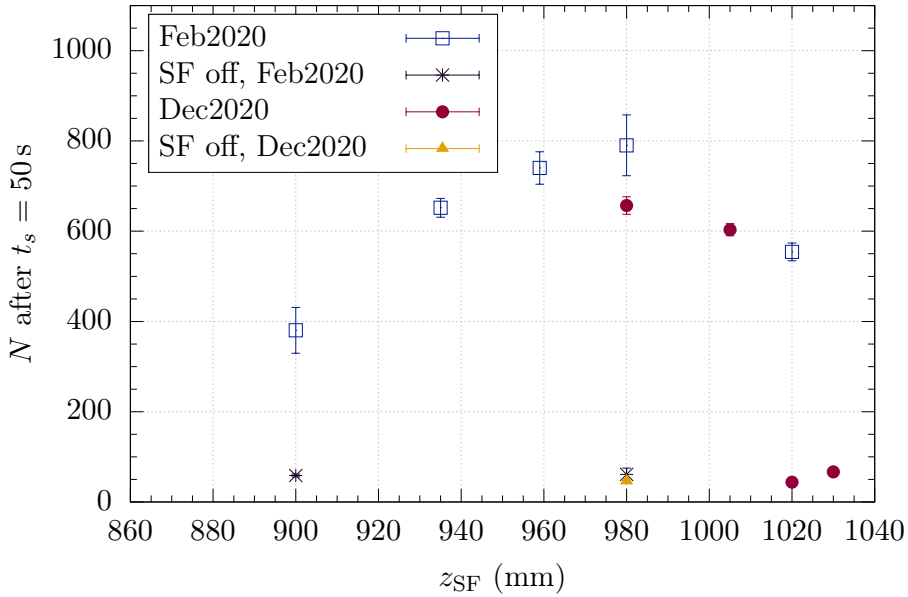


Figure 5.10: Number of stored neutrons after $t_s = 50$ s depending on the spin flip position before ($\delta y = -2.6$ mm, blue hollow squares) and after the centring of the compensation octupole ($\delta y = -0.2$ mm, red bullets). The data from beamtime *Feb2020* was re-normalised to the average pulse energy $\bar{E}_{Dec2020} = 9.47 \pm 0.16$ MWs. The measurement positions $z_{\text{SF}} \geq 1020$ mm are close to the field minimum of B_0 , so that after centring the compensation octupole, UCN are spin flipped twice. Therefore, no storable neutrons are produced and N is on the same level as the measurements with the spin flipper switched off (yellow and black markers).

sation octupole can explain this phenomenon: From Fig. 5.9 (right) follows, that after centring the compensation octupole, $B_{\text{abs,mean}} \simeq 3$ mT remain at $\delta y = -0.2$ mm, so that at $B_0(z) \sim 200$ mT the total magnetic field $B(z) = \sqrt{B_0(z)^2 + (B_{\text{abs,mean}})^2} \simeq B_0(z)$, which means that the transversal field becomes neglectable. It was shown in Fig. 4.13, that $B_0(z)$ decreases to a minimum at $z = 1056$ mm (here, $B_0^{\text{min}} = 196.6$ mT at $I_{\text{main}} = 33$ A), and increases again further inside the storage volume. Due to the length of the spin flipper, configurations can be found, where two lines⁷ occur, on which the resonance $\omega_0 = 2\pi f_{\text{SF}}$ is fulfilled - one in front of and one behind the minimum of B_0 . Without centring the compensation octupole, the transversal field gradients were comparably high, which resulted in a curvature of the resonance lines, so that neutrons could be spin flipped multiple times depending on their trajectories (cf. Ch. 4.1.2), some exiting the spin flipper as high-field seeker and some as low-field seeker. The result was a reduced number of $N = 551(10)$ neutrons in the trap at $z_{\text{SF}} = 1020$ mm in beamtime *Feb2020*.

After centring the compensation octupole, the two resonance lines are nearly straight, so that the neutrons are spin flipped twice regardless of their trajectory. This means that usually storable LFS after a first spin flip are flipped back to the high-field seeking state.

⁷The line shape does only apply in a two-dimensional view, which is used as simplification here. In three dimensions, the line must be rotated about the z -axis, resulting in a resonance plane. A curved resonance line would result in a cone shaped surface plane in three dimensions.

The trap thus remains empty apart from the filling process independent neutrons $N_{\text{SF_off}}$.

In [Kar17], the magnetic field minimum in B_0 was eliminated by additional longitudinal compensation coils, so that efficient spin flips were possible in this region. Currently, these coils are not operational due to a short circuit, which emerged during the installation of hardware components into τ SPECT (storage octupole, spin flipper side translation stage, etc.). If they would be replaced and the magnetic field minimum removed, the filling position could be further optimised.

5.2.2 Reduction of the current in the main coils

With the energy acceptance depending directly on the magnetic field at the spin flip position, a current reduction, and thus a reduction of $B(z_{\text{SF}})$, leads to an increase in $E_{\text{kin},0}^{\text{max}}$ (cf. Eq. 4.20).

The left side of Fig. 5.11 shows the maximum storable neutron energy $E_{\text{kin},0}^{\text{max}}(z_{\text{SF}})$ at $I_{\text{main}} = 31$ A and 33 A in a region around the current optimum spin flip position at $z_{\text{SF}} = 980$ mm (here, $E_{\text{kin},0}^{\text{max}}(33 \text{ A}) = 18.9$ neV). After centring the compensation octupole, the spin flip condition inferred from the MC simulation (cf Eq. 4.16) is fulfilled up to $z_{\text{SF,max}} = 1055$ mm. However, with no significant number of neutrons stored from $z_{\text{SF}} = 1020$ mm onwards in beamtime *Dec2020* (cf. Fig. 5.10), the spin flip position was kept⁸ at $z_{\text{SF}} =$

⁸After the discussion at the end of the previous section (cf. Ch. 5.2.1), filling positions with $z_{\text{SF}} > 980$ mm can be made possible if the field minimum of B_0 is eliminated.

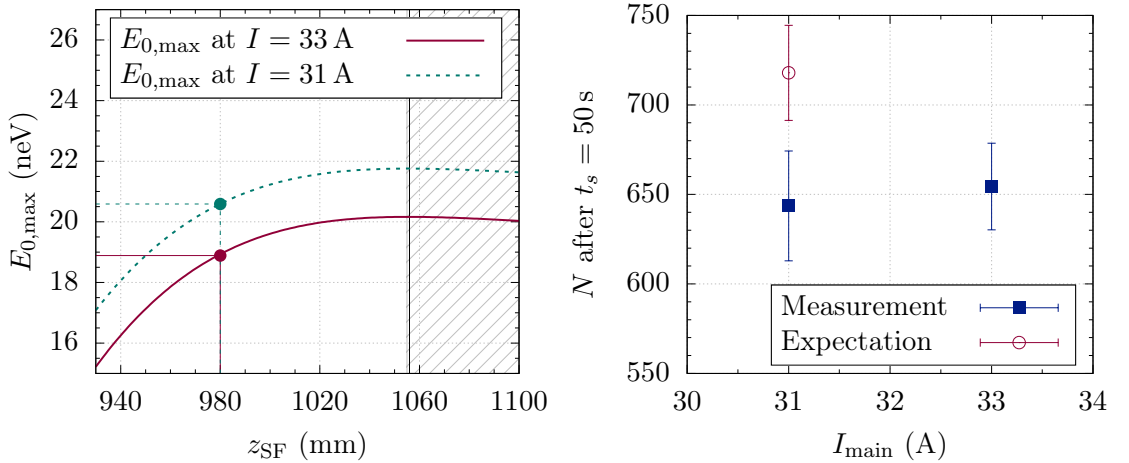


Figure 5.11: Influence of a reduction of I_{main} and experimental result. Left: The maximum storable energy in the spin flipping region at $I_{\text{main}} = 33$ A (red solid line, current optimum marked at $z_{\text{SF}} = 980$ mm) and 31 A (turquoise dashed line). After centring the compensation octupole, spin flip positions up to $z_{\text{SF}} = 1055$ mm are possible (up to the grey shaded region). The vertical line at $z = 1056$ mm marks the position, where $\nabla_z B(z) = 0$ mT/cm. Right: Results of 50 s storage measurements depending on I_{main} after optimisation of the spin flipper parameters shown as average values and standard deviations of all measurements taken into account (blue). Instead of the expected increase (red hollow circle), $N(31 \text{ A})$ is consistent with $N(33 \text{ A})$ within errors.

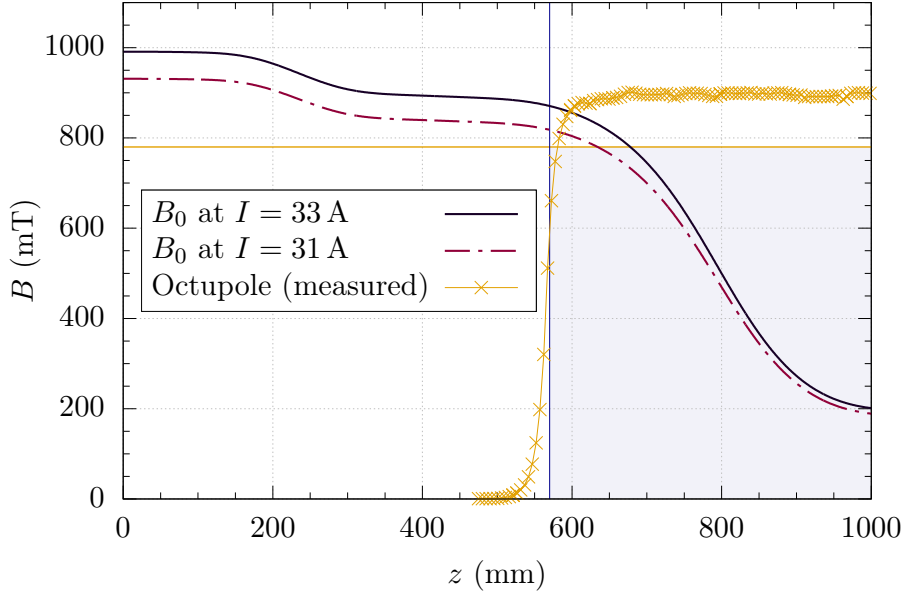


Figure 5.12: Magnetic fields around the spin flipper side storage octupole edge: B_0 at $I_{\text{main}} = 33$ A (black solid line) and 31 A (red dashed line), and the measured octupole field B_{oct} rescaled to $r = 53.5$ mm (yellow markers) at the measurement angle $\phi = 216^\circ$. The yellow horizontal line corresponds to the minimum field of the octupole $B_{\text{oct}}^{\text{min}} = 780$ mT, which was measured at a different azimuth angle. The physical edge of the octupole is marked by the vertical line.

980 mm. Here, $E_{\text{kin},0}^{\text{max}}$ increases to 20.6 neV when reducing the current to $I_{\text{main}} = 31$ A, which using Eq. 4.25 leads to an expected increase in the number of neutrons in the trap by $g \simeq 14.0\%$.

A comparison measurement was done in beamtime *Dec2020*, during which beamline No. 3 (cf. Ch. A.6) was used with τ SPECT at a height $h = 1.557$ m. The spin flipper was operated in the saturation regime ($P \geq 50$ W) and the spin flip position was optimised (cf. Ch. 5.1.1.2). The simulation results of Tab. 5.2 after centring were included in the total magnetic field and the required RF frequencies calculated as $f_{\text{SF},31\text{A}} = 5.665$ MHz and $f_{\text{SF},33\text{A}} = 6.030$ MHz. The remaining neutrons after $t_s = 50$ s were counted and normalised to the pulse energy. For statistical reasons, the measurements of the position optimisation between $z_{\text{SF}} = 970$ mm and 990 mm were averaged, yielding a total of 9 measurements at $I_{\text{main}} = 33$ A (cf. Fig. B.7) and 8 measurements at $I_{\text{main}} = 31$ A. The result is shown in Fig. 5.11 (right) with the errors the standard deviation. Instead of the expected increase in N when reducing the current, $N(31\text{ A}) = 644(31)$ is consistent within errors with $N(33\text{ A}) = 654(25)$.

An explanation for this observation might be found looking at the trap potential at both currents: Fig. 5.12 shows $B_0(z)$ at $I_{\text{main}} = 33$ A and 31 A, as well as one of the field measurements⁹ of the storage octupole along the z -axis at the azimuth angle $\phi = 216^\circ$ (the vertical direction corresponding to $\phi = 0^\circ$ [Haa21]), which was rescaled to $r = 53.5$ mm

⁹The measurement was done by J. Haack [Haa16].

(cf. Ch. 3.1). The yellow line corresponds to the minimum field of the octupole¹⁰ at $B_{\text{oct}}^{\text{min}} \simeq 780$ mT. At both currents, B_0 exceeds this line still within the range of the storage octupole. However, at 31 A the crossing point of B_0 and B_{oct} lies further outside and already in the fringe field of the storage octupole, so that compared to B_0 at 33 A, the trap potential is reduced in this region. This effect might oppose the increasing energy acceptance and (in case of no other loss mechanisms) would be of approximately equal strength here, as follows from the comparable results in N .

With no improvement found when decreasing the current, $I_{\text{main}} = 33$ A is retained for now. In future measurements, a variation of the current to 32 A or even 34 A could be considered in order to investigate an optimum trade-off between a maximum energy acceptance and a reduction of the storage potential in the fringe region of the trap.

5.2.3 Summary of the optimum parameters for τ SPECT

So far, this chapter discussed the available parameters for spin flipping using double saddle coils and showed, to what extent these parameters have to be optimised. The saddle coils were found to perform maximally efficient while additionally being easy to handle due to the possibility of external tuning and impedance matching. Consequently, switching back to a birdcage resonator in a final design is not necessary.

Furthermore, the compensation octupole was centred inside the storage octupole, which lead to an almost vanishing transversal field. However, with now being sensitive to the magnetic field minimum of B_0 at $z = 1056$ mm, the expected increase in the number of storable neutrons N could not be realised yet, probably due to the neutrons being spin flipped a second time and thus resulting in unstorable high-field seekers. A reduction of the current in the superconducting coils producing the B_0 field did also not lead to the expected increase in N yet.

Nevertheless, with this newly gained knowledge, we can derive new optimisation possibilities:

1. After reparation of the longitudinal correction coils, the magnetic field minimum of B_0 can be eliminated, so that the neutrons are spin flipped only once. This would allow us to position the spin flipper further inside the trap, where $B_0(z_{\text{SF}})$ is lower and the energy acceptance - and thus N - increases.
2. If filling positions further inside the trap are possible, the combination of current in the superconducting coils and filling position can be optimised to maximise the energy acceptance in the trap.
3. The dimensions of the narrowed neutron guide (the inner radius is $r = 25$ mm, cf. Ch. 3.1.2)) was originally chosen to fit the birdcage resonator between the guide and the compensation octupole. The saddle coils take up less room in comparison, so that both the spin flipper including its holding tube (cf. Fig. 5.2, left) and the narrowed neutron guide in the range of the spin flipper can be built with a larger radius. Taking as example an increase in the bending radius of the saddle coils of $dr = 1.5$ mm from $d/2 = 31.5$ mm to 33 mm and assuming a thickness of the wire of $d_w = 1.2$ mm still results in a distance to the compensation octupole ($r_i = 41.2$ mm, cf. Ch. 3.2.2) of

¹⁰The minimum was found in a measurement along the z -axis at a different azimuth angle.

7 mm, which is approximately the same distance as when the birdcage resonator was installed. Increasing the neutron guide radius by the same amount would increase the areal cross section in the narrowed region by 12 %, which is beneficial for neutron transmission.

For the time being we will, however, continue with the optimum parameters for the saddle coils, that we found so far. These parameters are listed in Tab. 5.4.

Table 5.4: Summary of the optimum spin flipper parameters as inferred from Chs. 5.1.1.1 and 5.1.1.2 at the time of writing this thesis.

Parameter	Value
Spin flip position z_{SF}	980 mm
RF frequency f_{SF}	6.098 MHz
RF power P_{SF}	80 W
RF phase $\Delta\varphi$	90°
Current I_{main}	33 A

5.3 Current status and preparatory studies regarding a lifetime measurement

A storage curve using the optimised parameters (cf. Tab. 5.4) is shown in Fig. 5.13, normalised to the average pulse energy. The following double exponential function was fitted to the data points:

$$N(t) = a_1 \exp(-t/\tau_1) + a_2 \exp(-t/\tau_2), \quad (5.7)$$

the fit parameters are listed in Tab. 5.5. For direct comparison, the results from the storage curve obtained in beamtime *Sept2019* are included in the figure and the table. It can be seen, that the number of permanently storable neutrons a_2 increased by a significant factor of 5.1(9) and the storage time τ_2 by a factor of 1.5(3), even though it is not yet comparable to the neutron lifetime (remember, that the current PDG average is $\tau_n = 879.4(6)$ s). This improvement - especially in τ_2 - may be caused by the different UCN energy spectrum at the now larger energy acceptance, or because in beamtime *Sept2019* long storage times of $t_s > 800$ s could not be measured due to limited statistics. However, regardless of the large relative errors in a_1 and τ_1 , we see from the fact that the fit still gives reasonable results, that β decay is not yet the only loss channel.

Ch. 2.2.3 summarises the occurring losses in magnetic storage of UCN as 1) non-adiabatic spin flips, and 2) marginally trapped neutrons. Non-adiabatic spin flips can occur in magnetic fields with large gradients or if $B \simeq 0$ mT, in both cases the adiabaticity parameter¹¹

$$\alpha = \frac{\gamma B^2}{|\nabla B|v} = \frac{\omega_0}{\dot{\theta}} \quad (5.8)$$

¹¹The adiabaticity parameter is here written in a more general way than in Eq. 4.10, which referred to the rotating reference frame of the spin flipper.

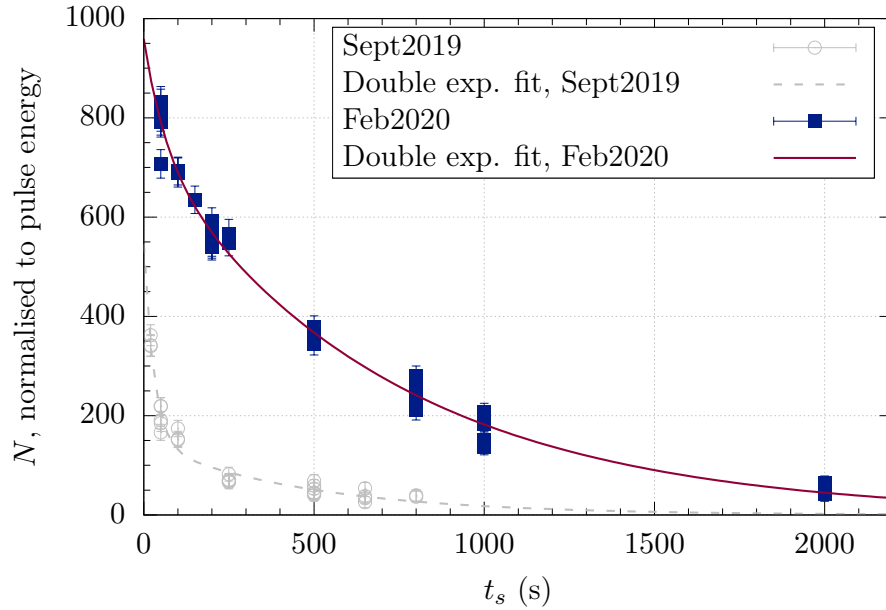


Figure 5.13: Storage curve measured with optimised parameters of the single spin flip technique in beamtime *Feb2020* at $z_{\text{SF}} = 980$ mm (blue squares), normalised to the average pulse energy. The red line is a double exponential fit to the data according to Eq. 5.7, the fit parameters are listed in Tab. 5.5. The grey bullets correspond to the results from beamtime *Sept2019* using the birdcage resonator at $z_{\text{SF}} = 879$ mm. A significant improvement in both storage time τ_2 and permanently stored neutrons a_2 is achieved.

approaches $\alpha \simeq 0$. The right side of this equation is obtained after division by B and with $\dot{\theta} = |\nabla B|v/B$ the change of the field orientation. The longitudinal field is always larger than $B_0^{\text{min}}(1056 \text{ mm}) = 196.6 \text{ mT}$ at $I_{\text{main}} = 33 \text{ A}$, so that for the total field $B \simeq 0 \text{ mT}$ can only be fulfilled where longitudinal field components opposite to B_0 and of similar amplitude occur. This could in principle be the case in the fringe field of the compensation octupole when the spin flipping unit is in its filling position, or at the edges of the storage octupole.

It was shown in Ch. 3.2.3 already, that the fringe field of the compensation octupole is retained within its holding construction, so that $B \gg 0 \text{ mT}$ is fulfilled in this region. In order to investigate the total magnetic field at the edges of the storage octupole, a simulation of the octupole field at $r = 53.5 \text{ mm}$ was done with COMSOL Multiphysics[®]

Table 5.5: Fit parameters of the storage curve measured in beamtime *Feb2020* as shown in Fig. 5.13. The fit function is given by Eq. 5.7. The first row corresponds to the results from beamtime *Sept2019*, which are listed for comparison.

Beamtime	a_1	τ_1	a_2	τ_2	χ^2/ndf
<i>Sept2019</i>	400.2(57.8)	29.6(6.4) s	145.0(21.0)	476.9(79.7) s	1.53
<i>Feb2020</i>	217.8(105.3)	64.5(61.7) s	740.7(49.5)	713.1(46.9) s	1.38

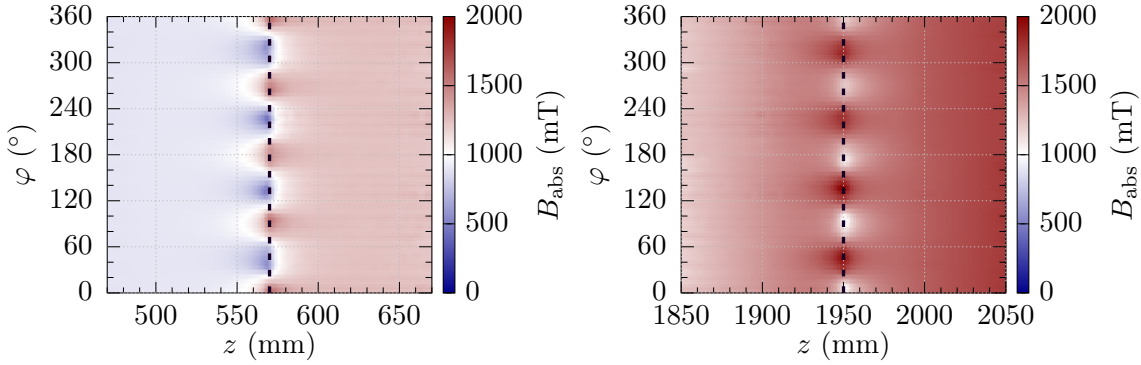


Figure 5.14: Magnetic field in the fringe region of the storage octupole on the spin flipper side (left) and on the detector side (right). The field of the octupole was simulated at $r = 53.5$ mm using COMSOL Multiphysics[®] and superimposed on the B_0 field at $I_{\text{main}} = 33$ A by components. The absolute field of this superposition is shown here. The physical edges of the storage octupole at $z = 570$ mm and $z = 1950$ mm are marked by the black dashed lines. The field minima in the region within the storage octupole are found as $B_{\text{abs}}^{\text{min}} = 418.2$ mT on the spin flipper side and $B_{\text{abs}}^{\text{min}} = 771.8$ mT on the detector side.

and the superposition with B_0 calculated by components. The resulting total magnetic field B_{abs} is shown in Fig. 5.14, on the left at the edge of the storage octupole on the spin flipper side and on the right at the edge on the detector side. On the spin flipper side, the field is always larger than $B_{\text{abs}}^{\text{min}} = 418.2$ mT, on the detector side we find $B_{\text{abs}} \geq 771.8$ mT, where the analysis was constrained to the region within the storage octupole, i.e. $z \geq 570$ mm and $z \leq 1950$ mm, respectively. The nominal trapping region is limited in longitudinal direction by the positions where $B_0(z) = B_{\text{oct}}^{\text{min}} = 780$ mT, which is the case at $z = 677$ mm on the spin flipper side and $z = 1865$ mm on the detector side. The fringe field of the storage octupole does therefore not reach into the trap and we can conclude, that $B \gg 0$ mT is fulfilled in the entire trap.

In order to estimate the influence of the field gradients on non-adiabaticity, we assume a neutron at velocity v on a circular orbit in the $x - y$ plane (z constant) at radius r and ignore the longitudinal field B_0 for now. Within one closed orbit, the total field B - now consisting only of the storage octupole field - then turns between the radial ($B = B_r$) and the angular direction ($B = B_\varphi$) 16 times, each corresponding to a rotation by an angle $\Delta\theta = 90^\circ$. This is shown in the middle of Fig. 5.15 in (a). The velocity of the field change is then given by

$$\dot{\theta} = \Delta\theta \cdot \frac{v}{l} \quad (5.9)$$

with l the track length of one turn. If we include the B_0 field, the neutron still experiences a change in the field orientation, however, $\Delta\theta$ reduces accordingly as is shown in Fig. 5.15 in (b). The extreme case $B_0 \gg B_{\text{oct}}$ leads to $\Delta\theta \sim 0^\circ$.

Using $\dot{\theta}$ and the Larmor frequency of the neutron, $\omega_0 = |-\gamma B|$, [SLK⁺17] introduces a depolarisation time τ_{dep} as

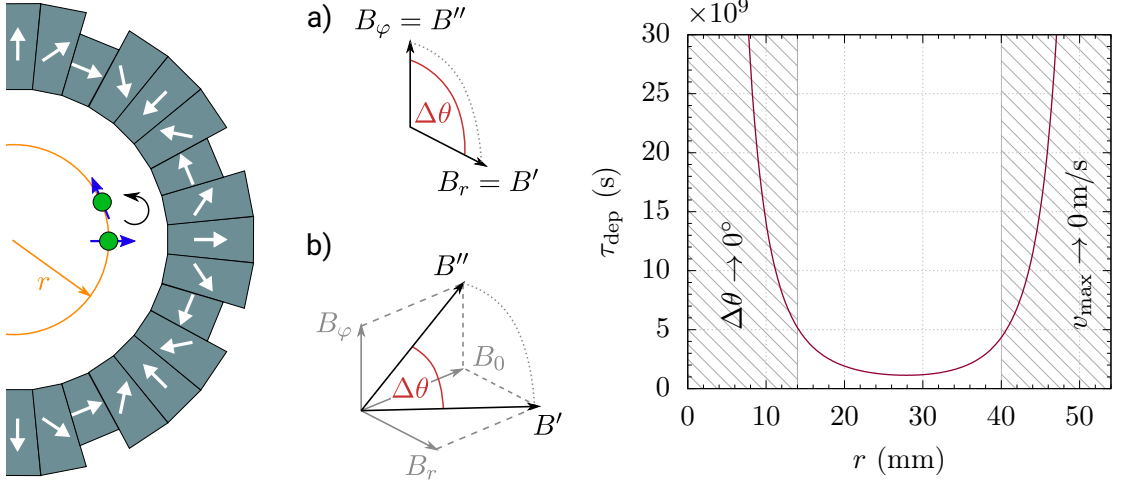


Figure 5.15: Magnetic field change seen by a neutron on a circular orbit. Left: A neutron (green) flies on a closed orbit at radius r (orange) in the $x - y$ plane of the storage octupole. Within a full rotation of the neutron the octupole field turns 16 times. Middle: The change in orientation of the total field before (B') and after (B'') a single turn of the octupole field without (a) and with the longitudinal B_0 field (b). In the first case $\Delta\theta = 90^\circ$ and in the second $\Delta\theta < 90^\circ$ depending on the amplitude of B_0 . Right: The depolarisation time τ_{dep} as calculated from Eq. 5.11 depending on the orbit radius; in all cases the maximum velocity for a storable neutron was used. The minimum is found at $\tau_{\text{dep}}(r = 27.9 \text{ mm}) = 1.13 \times 10^9 \text{ s} \gg \tau_n$, so that depolarisation by non-adiabatic spin flips can be excluded in τ SPECT.

$$\frac{1}{\tau_{\text{dep}}} = \frac{1}{t_s} \sum_{i=1}^n \frac{\dot{\theta}^2}{4\omega_0^2} \quad (5.10)$$

with n the number of turns the neutron encountered on a given orbit during the total storage time t_s (the variable names are adapted to match the notation used in this work).

To calculate an example, we assume a neutron on a closed orbit at $r = 30 \text{ mm}$ and $z = 1056 \text{ mm}$, where $B_0(z) = B_0^{\text{min}} = 196.6 \text{ mT}$. Here we find $B_{\text{oct}} = 134.5 \text{ mm}$ (cf. Eq. A.17), resulting in a total magnetic field of $B = 238.2 \text{ mT}$. As the total energy of the neutron in the trap must fulfil $E_{\text{kin}} + |\mu_n|B \leq 47 \text{ neV}$ (gravity is neglected here for simplicity), we find the maximum allowed neutron velocity as $v_{\text{max}} = 2.5 \text{ m/s}$. Using the dot product of the two vectors containing the field components before and after each turn of the octupole field, the rotation angle is calculated as $\Delta\theta = 47.1^\circ$ and with $l = 30 \text{ mm} \cdot 2\pi/16 = 11.8 \text{ mm}$ we end up with $\dot{\theta} = 174.2 \text{ rad/s}$. The Larmor frequency is given by $\omega_0 = 4.364 \times 10^7 \text{ rad/s}$ and the number of turns encountered in a storage time of $t_s = 880 \text{ s}$ by $n = v_{\text{max}} \cdot t_s / l = 1.864 \times 10^5$. Simplifying Eq. 5.10 and putting in the numbers results in a depolarisation time of

$$\tau_{\text{dep}} = \frac{t_s}{n} \frac{4\omega_0^2}{\dot{\theta}^2} = 1.18 \times 10^9 \text{ s}. \quad (5.11)$$

This calculation was repeated for different radii within the storage octupole, the result is shown on the right side of Fig. 5.15. The strong increase in τ_{dep} at small radii is caused

by $B_{\text{oct}} \ll B_0$ and thus $\Delta\theta \sim 0^\circ$ and that at large radii by $v_{\text{max}} \sim 0$ m/s as otherwise the neutron's total energy would exceed the trap potential. In all cases $\tau_{\text{dep}} \gg \tau_n$, so that non-adiabatic spin flips can be excluded in τ SPECT, which, however, needs to be proven in a separate simulation as well.

Consequently, the only remaining loss mechanism is the escape of marginally trapped neutrons, i.e. neutrons with kinetic energies (slightly) higher than the trap potential, $E_{\text{kin}} \gtrsim V_{\text{pot}}$ (cf. Ch. 2.2.4). As long as these neutrons fly under such angles, that their velocity component v_\perp normal to the magnetic field potential is small resulting in $E_\perp = 1/2 m_n v_\perp^2 \lesssim V_{\text{trap}}$, they are reflected and can thus be quasi-trapped on a time scale of tens to hundreds of seconds until they eventually escape. In an attempt to eliminate this loss channel, the UCN spectrum in the trap must be cleaned and the marginally trapped neutrons removed before the actual storage time begins.

5.3.1 Optimisation of the cleaning process

In the cleaning process, the detector is moved to the cleaning position z_{clean} in the fringe region of the trap where $B_0(z_{\text{clean}}) \simeq B_{\text{oct}}$, where it remains for a cleaning duration Δt_{clean} . Neutrons which fly under such angles that $E_\perp \gtrsim V_{\text{pot}}(z_{\text{clean}}) \approx 47$ neV can reach the detector, are absorbed at the ^{10}B layer and thus counted and removed from the trap. Neutrons with lower energies do not arrive at the detector and remain in the trap, so that the magnetic field potential at the cleaning position is equal to a cut-off energy up to which the trap is filled with neutrons. After cleaning is finished, the detector is moved back to the storage position and the storage time begins (cf. Chs. 3.1.1 and 3.5 for the procedure in a schematic view and the slow control structure).

During cleaning, one attempts to extract also those neutrons with $E_{\text{kin}} \sim E_\perp \gtrsim 47$ neV, however, such neutrons require close to perpendicular trajectories relative to the magnetic field in order to be able to reach the detector. This means that the more chaotic the particle trajectories are the higher is the probability for large incident angles, and thus the shorter is the duration required to clean all marginally trapped neutrons from the trap. In contrast, at more orderly trajectories the required cleaning duration increases until in the extreme case of closed orbits the neutrons take infinitely long to reach the detector, so that they cannot be cleaned at all. In total, the cleaning process in τ SPECT therefore depends on two parameters:

1. The cleaning duration: It must be long enough so that the detector is not moved back to the storage position before all marginally trapped neutrons have been removed.
2. The cleaning position: In order to include an energetic safety margin, the cut-off energy must be below the actual trap potential of $V_{\text{pot}} = 47$ neV, otherwise small energy changes of the stored neutrons (e.g. through microphonic heating by vibrations of the magnetic field) can lead to remaining time-dependent losses. On the other hand, the cut-off energy should be as large as possible, so that the number of storable neutrons reaching the detector as well is not reduced more than necessary, as this would be counterproductive with respect to statistical sensitivity.

Starting with an optimisation of the cleaning position, we first have to find the position of the storage volume edge in τ SPECT, which can in principle be calculated from the simulated B_0 field (the position is then found where $B_0(z) = B_{\text{oct}}^{\text{min}} = 780$ mT, which is

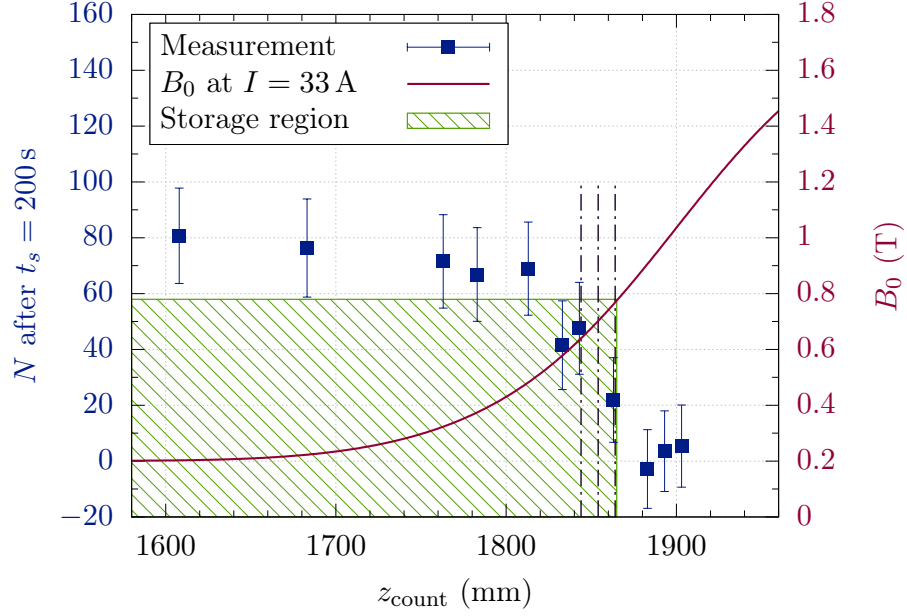


Figure 5.16: Dependency of the average number of detected neutrons on the detector counting position (blue squares, referring to the left axis). The data was obtained in beamtime *Nov2019* and is normalised to the average pulse energy. The B_0 field at $I_{\text{main}} = 33$ A is shown in red for reference (right axis), the green shaded region marks the storage volume limited by the position, where $B_0(1865 \text{ mm}) = B_{\text{oct}}^{\text{min}} = 780$ mT. Starting on the right, the detected number of neutrons increases as soon as the counting position reaches the storage volume and saturates from $z_{\text{count}} = 1810$ mm on, where all neutrons in the trap are counted. The vertical black dashed lines refer to the cleaning positions used during the optimisation process ($z_{\text{clean},1} = 1844$ mm, $z_{\text{clean},2} = 1854$ mm and $z_{\text{clean},3} = 1864$ mm).

the case at $z = 1865$ mm, cf. Fig. 3.2). However, a direct measurement with UCN leads to more reliable results, so that the dependency of the number of detectable neutrons on the counting position z_{count} was measured in beamtime *Nov2019* using 200 s storage measurements.

The results¹² are shown in Fig. 5.16, B_0 is given at $I_{\text{main}} = 33$ A in the region of the detector, the green shaded box marks the position of the storage volume with the height equal to $B_{\text{oct}}^{\text{min}}$. Seen from the right, N is compatible with zero counts up to $z_{\text{count}} = 1880$ mm, which means, that at those counting positions, the magnetic field is too high for any stored neutron to reach the ^{10}B layer. At counting positions further inside the trap, N increases up to a saturation from $z_{\text{count}} = 1810$ mm onwards. The edge of the storage volume is thus found in the region between $z_{\text{count}} = 1810$ mm and 1880 mm, so that the cleaning position must be located somewhere here as well.

Three cleaning positions were investigated so far ($z_{\text{clean},1} = 1844$ mm, $z_{\text{clean},2} = 1854$ mm and $z_{\text{clean},3} = 1864$ mm), which are shown by the vertical dashed lines in Fig. 5.16. Further-

¹²During the beamtime, the birdcage resonator was installed, so that with the spin flip position restricted to $z_{\text{SF}} = 879$ mm the counting statistics is rather low. The principle dependency on the the counting position is, however, not afflicted.

more, the cleaning duration was varied between $\Delta t_{\text{clean}} = 20$ s, 30 s and 40 s, each starting at $t_{\text{clean}} = 16$ s relative to the trigger executing the reactor pulse (cf. Ch. 3.5), so that the cleaned neutrons, which appear in the detector data as additional peak ('cleaning peak'), are well separable from the faster, not storable neutrons arriving directly after the reactor pulse (cf. Fig. 3.27). The cleaning intervals are depicted in Fig. 5.17 with respect to an arrival spectrum with and without cleaning (the cleaning position was $z_{\text{clean},2} = 1854$ mm).

In order to find the optimum combination of cleaning duration and position, storage curves were measured in beamtime *June2020* at optimised spin flipper parameters (cf. Tab. 5.4). An example with all three cleaning positions at $\Delta t_{\text{clean}} = 30$ s is shown in Fig. 5.18. The data points are background subtracted with the background error included in the error bars and normalised to the pulse energy. The solid and dashed lines correspond to a single and a double exponential fit to the results of $z_{\text{clean},2}$, respectively (cf. Eq. 5.7, for the single exponential fit only the first term is used). The fit parameters, also for the remaining positions, are listed in Tab. 5.6. The same procedure with $\Delta t_{\text{clean}} = 20$ s and 40 s is shown in Fig. B.8 for completeness with the fit parameters in Tabs. B.3 and B.4 leading to no improved results, so that we focus on $\Delta t_{\text{clean}} = 30$ s here.

In τ SPECT, a good cleaning procedure is characterised by a large a_1 , so that the fraction of permanently storable UCN which are removed in the process as well is small, and a long τ_1 (in the ideal case, $\tau_1 = \tau_n$). First of all, we see from the errors in the fit parameters, that in all three cases the double exponential fit does not give reasonable results. Furthermore, the values of τ_1 are comparable to $\tau_2 = 713.1(46.9)$ s from the storage curve without

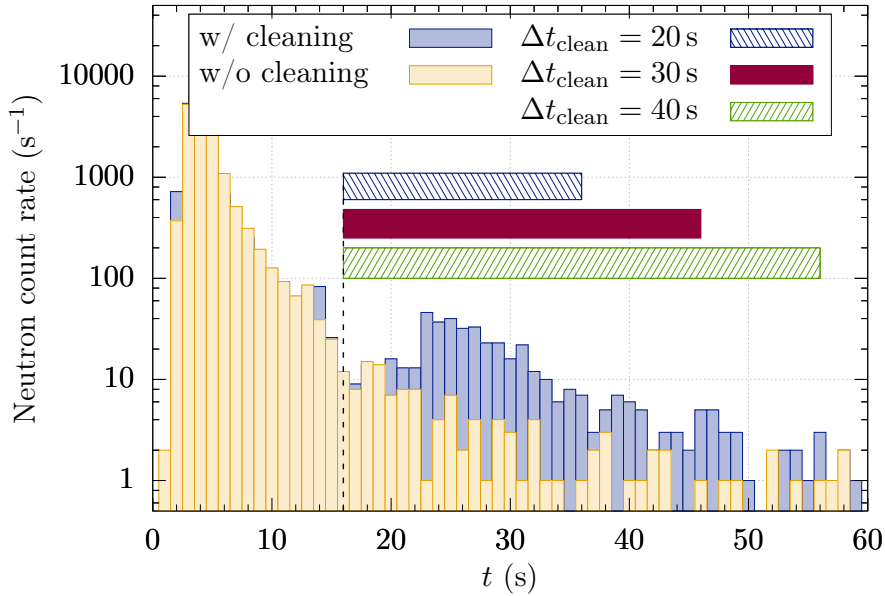


Figure 5.17: Neutron arrival spectra in the detector at 1 s binning with and without the cleaning procedure (blue and yellow, respectively, cleaning position: $z_{\text{clean},2} = 1854$ mm). The cleaning start time is in all cases set to $t_{\text{clean}} = 16$ s after the reactor pulse trigger in order to separate the cleaning peak from the bunch of faster neutrons. The cleaning optimisation process includes durations of $\Delta t_{\text{clean}} = 20$ s, 30 s and 40 s, indicated by the shaded boxes. In the arrival spectrum with cleaning shown here, Δt_{clean} was set to 30 s.

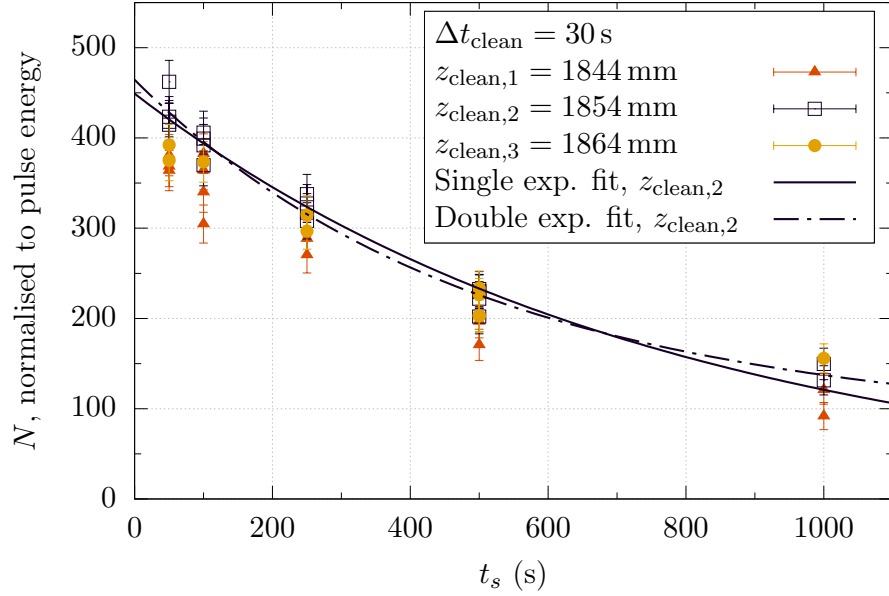


Figure 5.18: Background subtracted storage curves measured with cleaning of duration $\Delta t_{\text{clean}} = 30$ s at the cleaning positions $z_{\text{clean},1} = 1844$ mm (\blacktriangle), $z_{\text{clean},2} = 1854$ mm (\square) and $z_{\text{clean},3} = 1864$ mm (\bullet). The solid line corresponds to a single exponential fit to the results at $z_{\text{clean},2}$, the dashed line to a double exponential fit to the same data. The fit parameters are listed in Tab. 5.6.

cleaning (cf. Tab. 5.5). We can therefore draw the first conclusion, that the cleaning procedure definitely removed marginally trapped neutrons, which were responsible for the short decay time in the measurement without cleaning. Apart from that, an analysis of which position is superior to the others is difficult, because due to the limited statistics and the large error bars (especially in the decay constants), all measurement results are more or less compatible. Extending the measurement duration was, however, not possible within the beamtime, so that increased statistics still have to be gathered in the future.

Table 5.6: Fit results of single and double exponential functions (cf. Eq. 5.7) to the storage curves measured at $\Delta t_{\text{clean}} = 30$ s at the cleaning positions $z_{\text{clean},1} = 1844$ mm, $z_{\text{clean},2} = 1854$ mm and $z_{\text{clean},3} = 1864$ mm. The corresponding measurement data is shown in Fig. 5.18.

z_{clean}	a_1	τ_1	a_2	τ_2	χ^2/ndf
1844 mm	397.3(11.3)	708.4(54.0) s			1.16
1844 mm	324.2(1632.0)	495.4(1676.0) s	83.1(1654)	3252.8(1.3e5) s	1.29
1854 mm	449.1(8.3)	762.4(36.4) s			0.69
1854 mm	349.0(559.2)	472.4(585.2) s	115.4(570.5)	5201.6(8.4e4) s	0.49
1864 mm	403.2(14.2)	874.3(76.0) s			0.98
1864 mm	306.7(580.6)	465.6(815.3) s	116.1(597.7)	2.6e5(2.4e8) s	0.66

In order to analyse, whether the length of the cleaning duration is in the right order of magnitude, the data of the cleaned storage curve at $z_{\text{clean},2}$ and $\Delta t_{\text{clean}} = 30$ s was fitted with a double exponential function (cf. Eq. 5.7) but this time fixing $\tau_2 = 880$ s $\approx \tau_n$. From the fit parameters $a_1 = 68.4(18.2)$, $a_2 = 400.7(19.2)$ and $\tau_1 = 160.7(123.1)$ s ($\chi^2/\text{ndf} = 0.58$) follows, that longer cleaning durations of $\Delta t_{\text{clean}} \sim 200$ s are worth investigating as well.

An additional difficulty in the cleaning procedure is the rather symmetric shape of the trap due to the cylindrical storage octupole: This symmetry simplifies the formation of closed or quasi-closed orbits of marginally trapped neutrons, which then occupy only a small range in the longitudinal direction and which do not reach the detector within the cleaning duration. This problem could be assessed, if the total experimental setup was slightly tilted to break the symmetry of the trap. The neutrons would then be gravitationally accelerated in the direction of the detector and either their energy would exceed the magnetic potential and they would escape, or they could be cleaned from the trap.

In conclusion, a cleaning at a duration of $\Delta t_{\text{clean}} = 30$ s successfully removes as many marginally trapped neutrons, that no obvious double exponential behaviour is visible anymore. By the time of writing this work, however, an optimum still needs to be found.

5.3.2 Optimising the data normalisation

The determination of the neutron lifetime in τ SPECT is a relative measurement (cf. Ch. 3.6.4), which requires the initial number of neutrons $N_0(t_s = 0$ s) to be equal at each measurement run. If this is the case, only statistical fluctuations have to be taken into account when measuring at different storage times. However, additional fluctuations e.g. in the UCN production can occur, which increase the error $\Delta\tau_n$ of the neutron lifetime, so that they have to be compensated for by normalising the measurements to a parameter, which is subject to the same fluctuations.

The reactor power is directly connected to the thermal neutron flux Y_{th} . The resulting number of UCN emerging from the source, $Y_{\text{UCN}}(E_{\text{UCN}})$, depends on Y_{th} , but is influenced by fluctuations $f(E_{\text{UCN}}, \dots)$ caused by changes in the sD_2 crystal, such as deformation or varying temperatures upon heat load. Therefore, $Y_{\text{UCN}}(E_{\text{UCN}}, \dots) = Y_{\text{th}} \cdot f(E_{\text{UCN}}, \dots)$. One way to take these fluctuations into account is an in situ normalisation by counting a fraction of the stored UCN after a certain storage time ($t \sim 100$ s) and measuring the storage curve with the remaining UCN in the trap [SKF⁺18].

This method was investigated in [Kah20] using material wall storage in a stainless steel bottle ($V_F = 190$ neV) and gave reasonable results. However, the counting statistics was significantly higher due to the high trap potential, so that removing a fraction of the stored UCN for normalisation was not a problem. As long as the counting statistics using magnetic storage is still comparably low (which is the case by the time of writing this thesis), a different normalisation method has to be found. The following three normalisation methods are investigated, quantities called C correspond to the background subtracted neutron counts in a given interval without normalisation, N refers to normalised data:

1. Normalisation to the reactor power and therefore Y_{th} ,
2. Normalisation to higher energy neutrons in the arrival spectrum C_{arrival} , and

3. Normalisation to the cleaned UCN.

In order to compare the different methods, identical 500 s storage measurements at optimised spin flipper parameters (cf. Tab. 5.4) from beamtime *June2020* are used with cleaning at $z_{\text{clean},2} = 1854$ mm and $\Delta t_{\text{clean}} = 30$ s. After background subtraction, the neutrons in the counting interval C_{count} are normalised to the cleaned UCN counts C_{clean} , the neutron counts C_{arrival} in an interval between 0 s and 2 s after the thermal peak¹³, and the pulse energy E_{pulse} . The results are multiplied by an average value of the normalisation parameter for comparability reasons. In summary

$$N_{\text{pulse}} = \frac{C_{\text{count}}}{E_{\text{pulse}}} \bar{E}_{\text{pulse}} \quad (5.12a)$$

$$N_{\text{arrival}} = \frac{C_{\text{count}}}{C_{\text{arrival}}} \bar{C}_{\text{arrival}} \quad (5.12b)$$

$$N_{\text{clean}} = \frac{C_{\text{count}}}{C_{\text{clean}}} \bar{C}_{\text{clean}} \quad (5.12c)$$

with statistical counting errors \sqrt{C} in all intervals as well as in the background counts, and $\Delta E_{\text{pulse}} = 0.1$ MWs ([Hel21], the error of the pulse energy is a conservative estimation). The total error is calculated using Gaussian error propagation. The normalised results of the 500 s storage measurements are shown in Fig. 5.19, on the left with normalisation to E_{pulse} (cf. Eq. 5.12a), in the middle with normalisation to C_{arrival} (cf. Eq. 5.12b) and on the right with normalisation to C_{clean} (cf. Eq. 5.12c). It is slightly visible, that the normalisation method influences the size of the error bars, them being smallest with a normalisation to the pulse energy and largest using a normalisation to C_{clean} .

With a perfect normalisation method, the resulting fluctuations of the measurements should be of statistical nature only, i.e. $\sigma_N = \sqrt{N}$. Any deviation from this relation indicates, that the normalisation method does not fully compensate the non-statistical fluctuations in the data, making it less suitable for a permanent usage in τ SPECT. This deviation is calculated as

$$r = \left(\frac{\sigma_N}{\sqrt{N}} - 1 \right) \cdot 100 \%, \quad (5.13)$$

resulting in $r(E_{\text{pulse}}) = 5 \%$, $r(C_{\text{arrival}}) = 49 \%$ and $r(C_{\text{clean}}) = 43 \%$. The normalisation to the higher energy neutron counts and the cleaned UCN are both unsuitable in the current state, because they leave fluctuations of $\sim 45 \%$ in addition to the statistical uncertainties.

The smallest deviation is found for a normalisation to the pulse energy, which is surprising, because as this method is based on a measurement of the thermal neutron flux, it is energetically furthest away from the UCN energies in τ SPECT in comparison. The order of magnitude of a remaining fluctuation after normalisation of $\mathcal{O}(1 \%)$ as inferred in [Kah20] is, however, roughly confirmed if we take into account the limited statistics of only 9 measurements. Nevertheless, as soon as the relative statistical precision in the measurement

¹³The interval could not be chosen at later times, because during some pulses the RF signal of the spin flipper created noise in the detector data, which could not be filtered by the peakfinding algorithm (cf. Ch. A.4.1)

$$\frac{\sqrt{\bar{N}}}{N} = \frac{1}{\sqrt{\bar{N}}} \quad (5.14)$$

improves to below a factor σ_N/\bar{N} , the overall error is not purely statistically dominated anymore. With a normalisation to the pulse energy, this is the case from $N = 200$ counts onwards.

Therefore, with an improved counting statistics, the normalisation method needs to be adapted, which requires further investigation of a better and independent normalisation method: This can be done by preventing the spin flipper RF signal from coupling into the detector data, so that later and longer time intervals are made available for a normalisation to the higher energy neutrons. Other options would be an additional monitoring UCN detector in the region of the beamline, or detection of the low-field seeking neutrons, which are reflected from the high magnetic field peak during the filling process (cf. Ch. 3.1.1). Depending on the counting statistics, the in situ normalisation discussed at the beginning of this section could be considered as well.

However, with so far no improved normalisation method found, other arrival spectrum intervals not available in many, and cleaning not included in most measurements, all results in this work are normalised to the average pulse energy of the respective beamtime (cf. Tab. B.2 for a list of the average pulse energies in the time frame of this work).

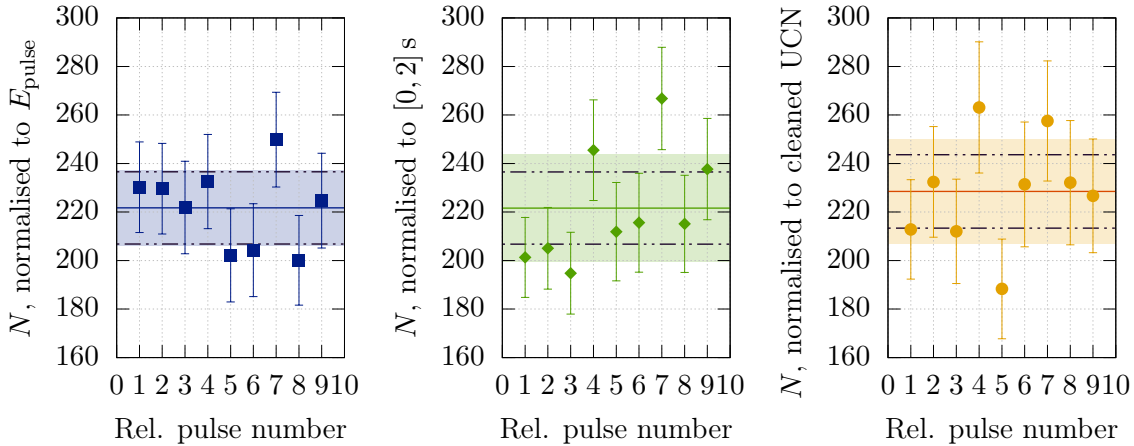


Figure 5.19: Comparison of all 500 s storage measurements with identical parameters in beamtime *June2020* with normalisation to the reactor pulse energy (left), higher energy neutrons from the arrival spectrum in the detector (middle) and the cleaned UCN (right). The solid horizontal lines correspond to the average value \bar{N} of the distribution after normalisation, the coloured regions mark the range within the standard deviation, $\bar{N} \pm \sigma_N$. The range with purely statistical fluctuations $\sqrt{\bar{N}}$ lies within the black dash-dotted lines. The deviation between σ_N and $\sqrt{\bar{N}}$ is calculated using Eq. 5.13 resulting in $r(E_{\text{pulse}}) = 5\%$, $r(C_{\text{arrival}}) = 49\%$ and $r(C_{\text{clean}}) = 43\%$.

5.4 Status of the required measurement time for $\Delta\tau_n = 1$ s

After the upgrade from the birdcage resonator to the double saddle coil spin flipper and thus the possibility to raise the energy acceptance in the trap, the initial number of neutrons N_0 after spectrum cleaning could be increased to ~ 450 (the value is inferred from the single exponential fit to the results at $z_{\text{clean}} = 1854$ mm and $\Delta t_{\text{clean}} = 30$ s, cf. Tab. 5.6). With this result, the required measurement duration $T_{\Delta\tau}$ (cf. Ch. 3.6.4) until $\Delta\tau_n = 1.0$ s is reached still calculates to roughly three years; here again assuming the ideal case of a fully efficient use of each beamtime without taking downtimes into account. Realistically achievable would be an overall measurement duration of rather one year, so that additional methods have to be found to further increase the neutron density in the trap.

Several options to do this were already identified earlier in this chapter (cf. Ch. 5.2.3), but the question remains, whether their combined effect on N_0 is sufficient. Therefore, additionally a modified filling technique was implemented and investigated, which is presented in the following chapter.

Chapter 6

The Double Spin Flip Technique

The filling process as it was done so far (we now call it the single spin flip technique, sSF) accelerates high-field seeking neutrons and decelerates them again until they reach the spin flipper. Even though this method was proven to work successfully, it has at least two downsides: 1) It does not decelerate the neutrons to the same extent as it accelerated them in the beginning, always leaving them with an additional kinetic energy depending on the spin flip position (cf. Ch. 4.2); and 2) With the energy acceptance ranging from 0 neV to the filling position dependent upper limit of ~ 20 neV, only the lowest fraction of the incident UCN spectrum is useful for the storage in τ SPECT. With the number of neutrons in a given energy interval rising with $E^{3/2}$ (this follows from integration of Eq. 4.19), thus accessing a higher energy range of the spectrum and transforming this one to the storable energy range could lead to an increase in the neutron density in τ SPECT.

6.1 Energy considerations in the double spin flip technique

The idea is to start with higher energetic LFS neutrons and to decelerate them twice by intermediately spin flipping them to the high-field seeking state¹. This requires an additional spin flipper in the high field region of B_0 , which is referred to as 'Spin Flipper 1' (SF1); the spin flipper used so far is then 'Spin Flipper 2' (SF2).

6.1.1 The energy acceptance in the double spin flip technique

We derive the energies involved for this double spin flip technique (dSF) by means of Fig. 6.1 similar to the considerations with the sSF technique. SF1 is located around $z_{\text{SF1}} = 0$ mm where $B_0(33 \text{ A}) = 1.020 \text{ T}$, resulting in a potential energy difference $\Delta V_{\text{magn},0}(z_{\text{SF1}}) = |\mu_n|B_0(z_{\text{SF1}}) = 61.52 \text{ neV}$ relative to $V_{\text{magn}} = 0 \text{ neV}$ in front of the first magnetic field peak. SF2 remains at its optimised position $z_{\text{SF2}} = 980 \text{ mm}$ with $B_0(33 \text{ A}) = 0.207 \text{ T}$ and thus $\Delta V_{\text{magn},0}(z_{\text{SF2}}) = |\mu_n|B_0(z_{\text{SF2}}) = 12.48 \text{ neV}$. The total initial energy of a neutron in front of the first magnetic field peak is

$$E_0 = E_{\text{kin}} + V_{\text{magn}}(B_0(z)) = E_{\text{kin},0} \quad (6.1)$$

with $V_{\text{magn}}(B_0(z < 500 \text{ mm})) = 0 \text{ neV}$ (cf. Fig. 6.1). A low-field seeking UCN is decelerated

¹The idea to use this technique in τ SPECT and first considerations were put up by Prof. W. Heil.

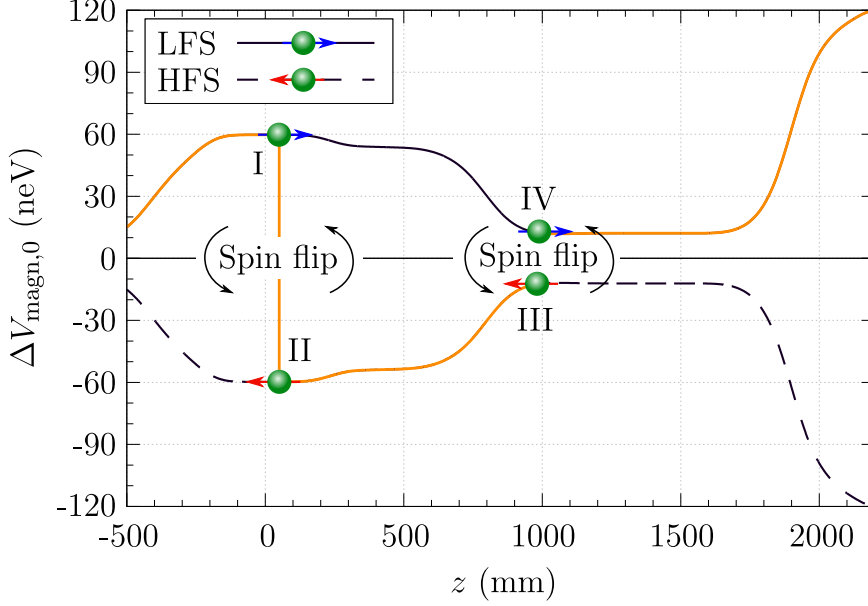


Figure 6.1: Magnetic field potential difference in τ SPECT relative to $V_{\text{magn}} = 0 \text{ neV}$ ($B_0 = 0 \text{ T}$) as seen by a HFS (black dashed line) and a LFS (black solid line) at $I_{\text{main}} = 33 \text{ A}$. An initial LFS is decelerated as the potential energy rises (yellow line). At SF1, the neutron is converted to a HFS and $\Delta V_{\text{magn},0}$ changes sign (from Pos. I to II). The HFS neutron is again decelerated and at SF2 $\Delta V_{\text{magn},0}$ changes sign again (from Pos. III to IV). In total, the kinetic energy of the neutron is reduced by 110.56 neV at $z_{\text{SF2}} = 980 \text{ mm}$, the remaining magnetic potential energy after SF2 results in 12.48 neV .

due to the rising potential. At z_{SF1} , immediately before the spin flip (Pos. I), the total energy of the neutron is given by

$$\begin{aligned} E &= E_{\text{kin},0} - \Delta E_{\text{kin}}(z_{\text{SF1}}) + \Delta V_{\text{magn},0}(z_{\text{SF1}}) \\ &= E_{\text{kin},0} - |\mu_n|B_0(z_{\text{SF1}}) + |\mu_n|B_0(z_{\text{SF1}}). \end{aligned} \quad (6.2)$$

The spin flip (Pos. II) does not change the kinetic energy $E_{\text{kin}}(z_{\text{SF1}})$, but with the neutron now in the high-field seeking state, its total energy is

$$E = \underbrace{E_{\text{kin},0} - |\mu_n|B_0(z_{\text{SF1}})}_{E_{\text{kin}}(z_{\text{SF1}})} - |\mu_n|B_0(z_{\text{SF1}}). \quad (6.3)$$

On its way to SF2, the HFS is further decelerated, so that we can write for the kinetic energy $E_{\text{kin}}(z_{\text{SF2}})$ at the second spin flipper (Pos. III)

$$\begin{aligned} E_{\text{kin}}(z_{\text{SF2}}) - |\mu_n|B_0(z_{\text{SF1}}) + |\mu_n|B_0(z_{\text{SF1}}) - |\mu_n|B_0(z_{\text{SF2}}) &= E_{\text{kin}}(z_{\text{SF1}}) - |\mu_n|B_0(z_{\text{SF1}}) \\ E_{\text{kin}}(z_{\text{SF2}}) &= E_{\text{kin},0} - 2|\mu_n|B_0(z_{\text{SF1}}) + |\mu_n|B_0(z_{\text{SF2}}), \end{aligned} \quad (6.4)$$

where the last line was obtained using Eq. 6.3. This yields $E_{\text{kin}}(z_{\text{SF2}}) = E_{\text{kin},0} - 110.56 \text{ neV}$ for $|\mu_n|B_0(z_{\text{SF1}}) = 61.52 \text{ neV}$ and $|\mu_n|B_0(z_{\text{SF2}}) = 12.48 \text{ neV}$. Thus the initial kinetic energy $E_{\text{kin},0}$ of the neutron (LFS) is reduced by 110.56 neV until it reaches SF2 as HFS after being spin flipped once. From this value, we can directly infer the lower limit of the energy acceptance, because neutrons with $E_{\text{kin},0} < 110.56 \text{ neV}$ diffuse backwards before reaching SF2.

For the upper limit, we have to add the magnetic potential at z_{SF2} , $|\mu_n|B_0(z_{\text{SF2}})$, and include gravity the same way as was done in the considerations with the single spin flip technique (cf. Ch. 4.2.2). The neutrons cannot enter the trap below the minimum height between neutron guide and storage octupole, so that the minimum gravitational potential $V_{\text{grav}} = s_0 \cdot 102.4 \text{ neV/m} = 3.0 \text{ neV}$ needs to be taken into account in any case. Including additional entrance heights Δs we can write the condition on storable energies in τ SPECT after the second spin flipper (Pos. IV) as

$$E = (E_{\text{kin},0} - 110.56 \text{ neV}) + |\mu_n|B_0(z_{\text{SF2}}) + (s_0 + \Delta s) \cdot 102.4 \text{ neV/m} \leq 47 \text{ neV}. \quad (6.5)$$

Neutrons at a maximum initial kinetic energy are then storable only if $\Delta s = 0 \text{ mm}$, this energy is $E_{\text{kin},0}^{\text{max}} = 142.07 \text{ neV}$. In total, the energy acceptance using the double spin flip technique is thus given as

$$\Delta E_{\text{kin},0} = [110.56 \text{ neV}, 142.07 \text{ neV}]. \quad (6.6)$$

In order to compare this range to the energy acceptance deduced when using only SF2 alone, $E_{\text{kin},0} = [0 \text{ neV}, 18.9 \text{ neV}]$ (cf. Eq. 5.1), we integrate the neutron density $\varrho \sim \sqrt{E}$ (cf. Eq. 4.19) in the range of the energy acceptances of both filling techniques. Using Eq. 4.25 and the weighting function $w(E)$ in Eq. 4.23 to account for gravity, we find a theoretical gain by a factor of

$$g = \frac{\int_{142.07 \text{ neV}}^{110.56 \text{ neV}} \sqrt{E} \cdot w(E) dE}{\int_{0 \text{ neV}}^{18.9 \text{ neV}} \sqrt{E} \cdot w(E) dE} \approx 7.2. \quad (6.7)$$

6.1.2 The problem with the beam divergence

The estimation above is only valid in a one-dimensional consideration: The B_0 field is oriented along the z -axis, which causes the Stern-Gerlach force to act only on the longitudinal z -component of the neutron velocity² v_z . Taking a neutron beam, which is fully parallel to the z -axis, the deceleration within the double spin flip technique is maximally efficient. This is not the case anymore when we add transversal components of the neutron momenta in the consideration as is shown on the basis of Fig. 6.2 (left).

The red line shows B_0 at $I_{\text{main}} = 33 \text{ A}$ in the declining part of the first field hump. We assume a neutron flying at velocity v and an angle θ relative to the z -axis. The velocity can then be split into a longitudinal component $v_z = v \cos(\theta)$ and a transversal component $v_t = v \sin(\theta)$. Converting from velocities to energies, we use $E \propto v^2$.

Assuming again an initial kinetic energy $E_{\text{kin},0}$ (cf. Eq. 6.1), we can write the longitudinal energy component as $E_z = E_{\text{kin},0} \cos^2(\theta)$ and the transversal component as

²Strictly speaking, deceleration and acceleration by the Stern-Gerlach force due to the octupole field happens as well. For simplicity, this is assumed to average out over the cross section of the neutron guide.

$E_t = E_{\text{kin},0} \sin^2(\theta)$. With the Stern-Gerlach force acting only on E_z , the energy after the second spin flip (Pos. IV, cf. Fig. 6.1) is given as

$$E'_z = E_z - 110.56 \text{ neV} = E_{\text{kin},0} \cos^2(\theta) - 110.56 \text{ neV} \quad \text{and} \quad (6.8a)$$

$$E'_t = E_t = E_{\text{kin},0} \sin^2(\theta). \quad (6.8b)$$

From Eq. 6.8a follows, that for a finite θ , a minimum energy $E_{\text{kin},0}^{\text{min}} \geq 110.56 \text{ neV} / \cos^2(\theta)$ is required, because otherwise E'_z turns negative and the neutron diffuses back before reaching SF2. For example, a neutron at $E_{\text{kin},0} = 125 \text{ neV}$ flying at $\theta = 15^\circ$ has a longitudinal energy $E'_z = +6.1 \text{ neV}$ after the second spin flip, whereas the same neutron flying at 20° would end up with $E'_z = -0.2 \text{ neV}$ and therefore does not even reach SF2.

Assuming $E_{\text{kin},0} \geq E_{\text{kin},0}^{\text{min}}$, the total neutron energy after the second spin flip is given as

$$(E_{\text{kin},0} \cos^2(\theta) - 110.56 \text{ neV}) + E_{\text{kin},0} \sin^2(\theta) = (E_{\text{kin},0} - 110.56 \text{ neV}). \quad (6.9)$$

The storable energy therefore does not depend on θ and using Eq. 6.5, we find that the maximum energy remains at $E_{\text{kin},0}^{\text{max}} = 142.07 \text{ neV}$. However, the kinematic acceptance of incoming UCN is restricted to energies in a range

$$\Delta E_{\text{kin},0}^{\text{kinem.}} = [110.56 \text{ neV} / \cos^2(\theta), 142.07 \text{ neV}]. \quad (6.10)$$

At the critical angle $\theta_c = 28.1^\circ$ the minimum energy calculates as $E_{\text{kin},0}^{\text{min}} = 142.07 \text{ neV} = E_{\text{kin},0}^{\text{max}}$, so that from here on the kinematic acceptance is zero.

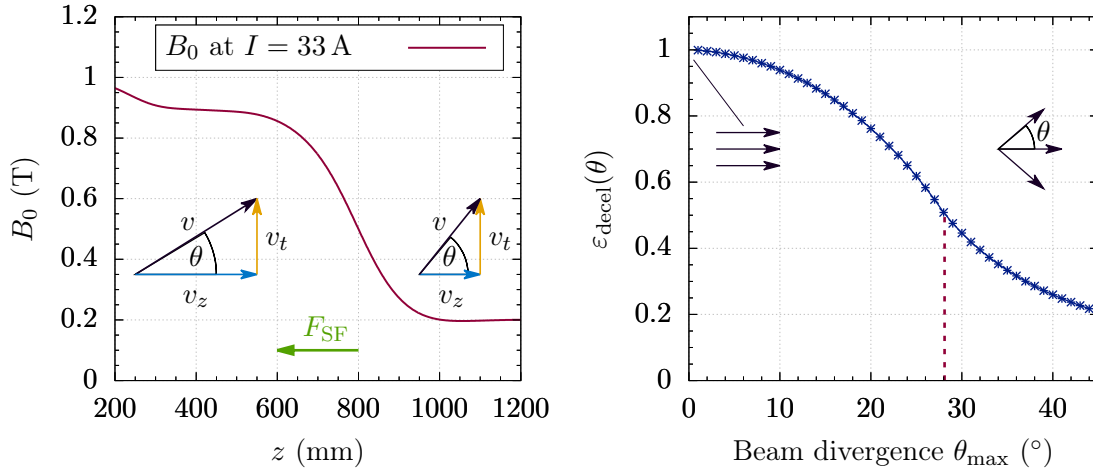


Figure 6.2: Influence of the neutron beam divergence θ_{max} on the deceleration efficiency $\varepsilon_{\text{decel}}(\theta)$ using the double spin flip technique. Left: A neutron flying at energy E and an angle θ relative to the z -axis with energy components $E_z = E \cos^2(\theta)$ (blue) and $E_t = E \sin^2(\theta)$ (yellow). The deceleration by the Stern-Gerlach force acts only upon $E_z(\theta)$, leaving $E_t(\theta)$ unchanged, which decreases the kinematic acceptance (cf. Eq. 6.10). Right: Deceleration efficiency $\varepsilon_{\text{decel}}(\theta)$ calculated using Eq. 6.12. The angle $\theta = 0^\circ$ refers to an entirely parallel neutron beam, here maximum deceleration occurs. At the critical angle $\theta_c = 28.1^\circ$ (red dashed line) the kinematic acceptance becomes zero, neutrons flying at larger angles cannot be stored in any case.

In the following, we will quantify the efficiency of the deceleration depending on the beam divergence θ_{\max} , i.e. the maximum angle of neutron trajectories occurring in the beam, so that $-\theta_{\max} \leq \theta \leq \theta_{\max}$. Therefore, we use again a \sqrt{E} -behaviour of the UCN density (cf. Eq. 4.19) and integrate over the kinematic acceptance between $110.56 \text{ neV} / \cos^2(\theta)$ and 142.07 neV . The resulting number of neutrons $n(\theta)$ is then weighted by $\sin(\theta)d\theta$ and integrated over the solid angle according to

$$Y(\theta_{\max}) = \frac{\int_0^{2\pi} \int_0^{\theta_{\max}} n(\theta) \sin(\theta) d\theta d\varphi}{\int_0^{2\pi} \int_0^{\theta_{\max}} \sin(\theta) d\theta d\varphi}, \quad (6.11)$$

with the storable UCN yield $Y(\theta_{\max})$. The deceleration efficiency is obtained after division by the result for a neutron beam at $\theta_{\max} = 0^\circ$ (i.e. the ideal situation of a parallel incoming beam) as

$$\varepsilon_{\text{decel}}(\theta_{\max}) = \frac{Y(\theta_{\max})}{Y(\theta_{\max} = 0^\circ)}. \quad (6.12)$$

Fig. 6.2 (right) shows the dependency of $\varepsilon_{\text{decel}}$ on θ_{\max} up to $\theta_{\max} = 45^\circ$. The critical angle θ_c , from which the kinematic acceptance is empty, is marked by red dashed line. However, we find $\varepsilon_{\text{decel}} > 0$ also for $\theta_{\max} \geq \theta_c$ because those neutrons in the beam with smaller flight angles ($\theta < \theta_c$) still contribute to a non-vanishing UCN yield $Y(\theta_{\max})$.

Nevertheless, with $\varepsilon_{\text{decel}}$ depending on θ_{\max} and the double spin flip technique relying strongly on the deceleration of UCN, we have to take $\varepsilon_{\text{decel}}$ into account when comparing the filling techniques regarding any expected gain (cf. Eq. 6.7). This applies all the more so, if we consider, that with the single spin flip technique initial high-field seeking neutrons experience a net acceleration by $|\mu_n|B_0(z_{\text{SF2}}) = 12.48 \text{ neV}$ (cf. Ch. 4.2.1) on their way to SF2. Due to this boost in longitudinal direction, the divergence (and consequently back diffusion) of the incident UCN beam even decreases as opposed to the double spin flip technique, and the transmission improves.

The calculation of $\varepsilon_{\text{decel}}$ as it was done so far can be a rough guide for estimations with the double spin flip technique, however, neither transversal fields nor gravity were taken into account yet. Therefore, the influence of the beam divergence on the filling efficiency is investigated additionally using the Monte Carlo simulation described in Ch. A.5.

The energy distribution of simulated neutrons follows a \sqrt{E} -behaviour (cf. Eq. 4.19), the starting positions in $x - y$ direction are evenly distributed over the neutron guide cross section and the initial flight angles are randomly chosen from a range $[-\theta_{\max}, \theta_{\max}]$, with θ_{\max} again the beam divergence. The simulation starts in front of B_0 , so that a direct comparison between the single (sSF) and the double spin flip technique (dSF) is possible. The spin flipper field amplitudes are set to $B_1 = 0.5 \text{ mT}$, only during the sSF simulation SF1 is switched off. After passing SF2, the neutrons are analysed with respect to their final energy and their spin state and storable low-field seeking neutrons are counted.

The fraction of storable neutrons N_{LFS} with respect to the total number of simulated neutrons N was calculated as $n_{\text{LFS}} = N_{\text{LFS}}/N$ for both filling techniques. The result is shown on the left side of Fig. 6.3 (left) as a function of the beam divergence θ_{\max} . While the results of the single spin flip technique, $n_{\text{LFS}}^{\text{sSF}}(\theta_{\max})$, are within errors roughly independent of θ_{\max} , $n_{\text{LFS}}^{\text{dSF}}(\theta_{\max})$ decreases significantly for larger beam divergences using the double spin flip technique. From the ratio³

³In the previous calculations on $\varepsilon_{\text{decel}}$ only the deceleration by the Stern-Gerlach force was taken into

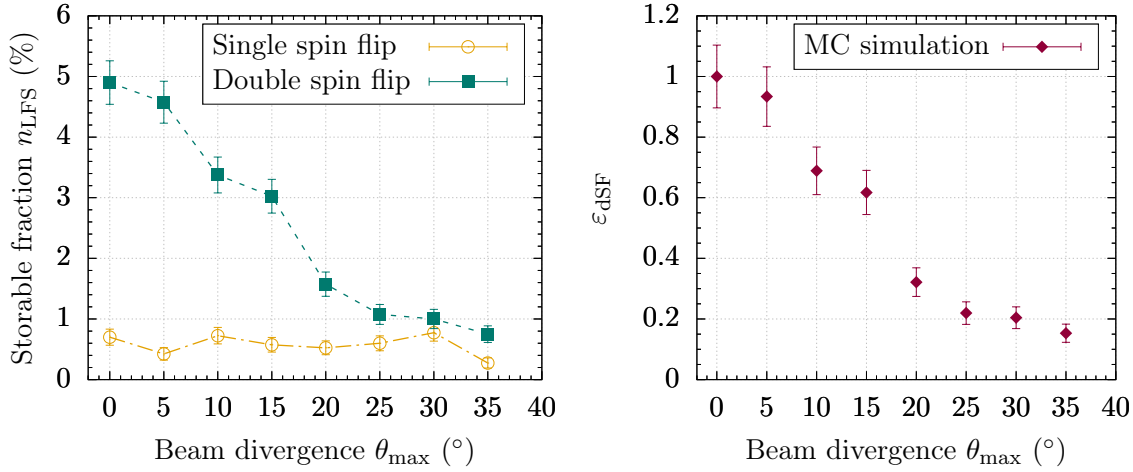


Figure 6.3: Single and double spin flip technique in a Monte Carlo simulation and inferred deceleration efficiency $\varepsilon_{\text{dSF}}(\theta_{\text{max}})$. Left: The fraction of storable neutrons n_{LFS} yielded with the sSF (yellow) and the dSF technique (turquoise) depending on the beam divergence θ_{max} at the entrance of τ SPECT. Since the kinematic acceptance in Eq. 6.10 decreases with θ_{max} , a significant reduction in $n_{\text{LFS}}^{\text{dSF}}$ is visible. Right: The filling efficiency for the dSF technique relative to an initially fully parallel UCN beam ($\theta_{\text{max}} = 0^\circ$), calculated as $n_{\text{LFS}}^{\text{dSF}}(\theta_{\text{max}})/n_{\text{LFS}}^{\text{dSF}}(\theta_{\text{max}} = 0^\circ)$.

$$\varepsilon_{\text{dSF}}(\theta_{\text{max}}) = \frac{n_{\text{LFS}}^{\text{dSF}}(\theta_{\text{max}})}{n_{\text{LFS}}^{\text{dSF}}(\theta_{\text{max}} = 0^\circ)} \quad (6.13)$$

we can deduce, how the beam divergence influences the filling efficiency compared to a parallel incoming UCN beam. The result is shown on the right side of Fig. 6.3. We find, that the efficiency using the double spin flip technique as inferred from the Monte Carlo simulation depends even stronger on the beam divergence than $\varepsilon_{\text{decel}}$ (cf. Fig. 6.2), which takes only energy ranges into account. This confirms, that the beam divergence of the incoming UCN beam must be as small as possible for the double spin flip technique to work efficiently. In τ SPECT, we can, however, not measure the beam divergence directly, so that $\varepsilon_{\text{dSF}}(\theta_{\text{max}})$ remains an open parameter.

6.1.3 The optimum height for the double spin flip technique

The unknown beam divergence furthermore complicates the choice of an optimum height for the operation of τ SPECT. The neutrons exit the UCN source at a minimum energy of $E \simeq 105$ neV due to the boost in longitudinal direction by the Fermi potential of the $s\text{D}_2$ crystal (cf. Ch. A.1.1). Therefore, if τ SPECT was operated at source level, no neutrons would be found in the storable energy range between 0 neV and 18.9 neV if the single spin flip technique was used (cf. Eq. 5.1). By guiding the UCN upwards after they exit

account, so that an isolated analysis with respect to θ_{max} was possible. In the Monte Carlo simulation, additional effects such as the spin flip efficiency itself, UCN transport through the guides and gravity are included in the consideration, so that instead of a deceleration efficiency $\varepsilon_{\text{decel}}$ a more general ratio ε_{dSF} is given.

the source, they are gravitationally decelerated, so that the number of neutrons which can be stored in the trap increases with height⁴. However, gravity acts - similarly to the Stern-Gerlach force in the consideration before - only on the longitudinal component of the neutron velocity (longitudinal in this case meaning the vertical direction aligned with the direction of the force), leaving transversal components unchanged. With additional height thus the beam divergence increases.

In [Kah20], the optimum height was found as $h = 1.83$ m in an independent measurement using a test setup with an aluminum storage bottle ($V_F = 54$ neV) at different heights. However, as suitable neutron guides were not available to connect the UCN source to the entrance of τ SPECT, the nominal height was determined as $h = 1.59$ m. In this work, the typical height of τ SPECT is on average rather $h = 1.50$ m, which is because of multiple reconstructions and the use of different shapes of the beamlines (cf. Ch. A.6).

Even though a direct height optimisation with τ SPECT has not been done so far, the results inferred from the test setup can be related to τ SPECT, because the single spin flip technique is largely insensitive to the beam divergence (cf. Fig. 6.3, left). This is not the case when using the double spin flip technique: The goal is an incident UCN spectrum at the entrance of τ SPECT with the highest number of neutrons in the storable energy range (cf. Eq. 6.6), low transmission losses and a low beam divergence to maximise the filling efficiency. Those three aspects will not have their respective optimum at the same height, so that an experimental optimisation of the operating height of τ SPECT will be required.

6.2 Double spin flipping in practice

Now that we have discussed which energy range is storable in τ SPECT using the double spin flip technique, and how strongly this technique depends on the beam divergence, we have a look at the experimental realisation and first measurement results.

6.2.1 Position constraints and design of the additional spin flipper

The new spin flipper is located in the high field plateau of B_0 , where according to Eq. 6.4 the largest deceleration occurs and therefore the highest gain is expected. This is, however, also the range, where the moving flange of the spin flipper side translation stage is guided by the rail system (cf. Fig. 3.9), which makes a fixed installation of SF1 in this region difficult. Therefore, it is to be mounted within the stainless steel tube of the translation stage (cf. Ch. 3.1.2) and is thus movable but installed in a fixed distance to SF2. Due to the mechanical constraints by the translation stage, the possible locations of SF1 are limited as shown in Fig. 6.4 (left). The B_0 field is given at $I_{\text{main}} = 33$ A. The position of SF1 (centre position) is decided to be $z_{\text{SF1}} = 50$ mm for the following reasons:

1. The position is in the maximum region of B_0 and the edge of the storage octupole is 520 mm away, so that fringe field effects are negligible.
2. A small but well-defined longitudinal field gradient is required for spin flipping using adiabatic fast passage (cf. Ch. 4.1). More specifically, the gradient must not have a zero transition inside the spin flipping region as this would increase the chance of hitting the resonance condition $\omega_{\text{SF1}} = \omega_0$ twice, resulting in spin flips back to the

⁴This assumption is only valid in the low energy part of the UCN spectrum, where $\rho \sim \sqrt{E}$.

initial state. The *a*SPECT experiment [BAGB⁺20], however, used two gradient coils C3 and C5 in this region, which are located at $z_{C3} = -118$ mm and $z_{C5} = 118.5$ mm. If connected in anti-Helmholtz configuration, they generate the well-defined gradient we require for the spin flip. By variation of the currents in both coils individually, the size of the gradient can be adjusted.

The effect of the additional coils on the total magnetic field and its gradient is shown on the right side of Fig. 6.4 with $I_{\text{main}} = 33$ A in all cases and the currents I_{C3} and I_{C5} set to $[0, 0]$ A as well as $[20, -10]$ A and $[30, -10]$ A. Magnetic fields are shown by solid lines and refer to the left axis, gradients are depicted as dashed lines on the right axis. As a target gradient, $\nabla_z B_0 \simeq -0.5$ mT/cm was chosen, which is met at $z_{\text{SF1}} = 50$ mm for the respective gradient coils current setting $I_{C3} = 20$ A and $I_{C5} = -10$ A ($\nabla_z B_0(z_{\text{SF1}}) = -0.48$ mT/cm). With a total magnetic field of 1.022 T in the centre of SF1, the required RF frequency results in $f_{\text{SF1}} = 29.799$ MHz.

In order to mount SF1 within the translation stage, a section of the stainless steel tube housing the quartz glass neutron guide was cut out on a length of 200 mm and replaced by a holding construction⁵. A schematic drawing as well as the finished spin flipper and the assembly within the tube are depicted in Fig. 6.5. The spin flipper is constructed and controlled in the same way as SF2 (cf. Ch. 5.1). Given the larger diameter of the quartz

⁵An identical stainless steel tube was used, replacing the original one for later reusability.

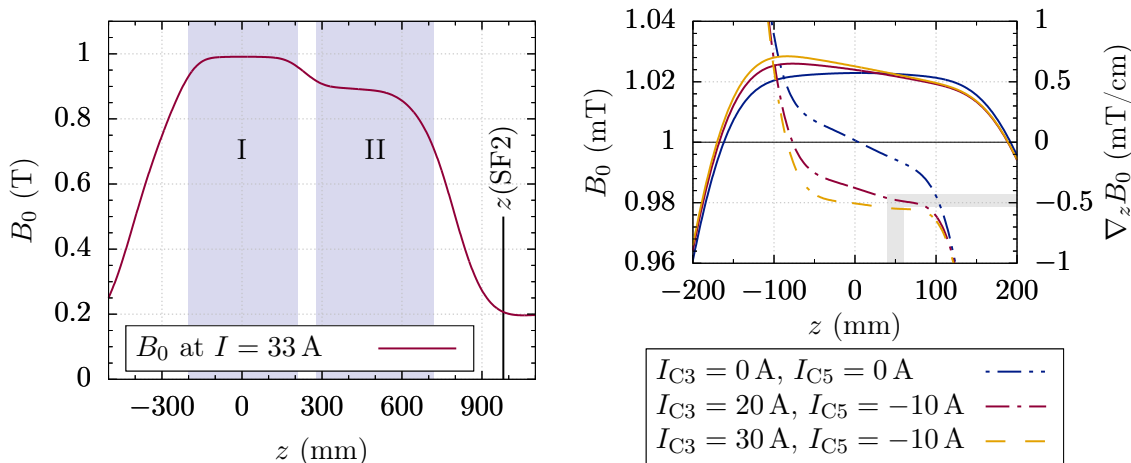


Figure 6.4: Positioning of SF1 and configuration of $\nabla_z B_0$. Left: SF1 is to be mounted within the translation stage in a fixed distance to SF2 and in the high field region of B_0 (red line). The mechanical constraints allow for two regions (I and II, marked by the grey shaded regions), in which SF1 can be positioned. The black line shows the optimum position of SF2 at $z_{\text{SF2}} = 980$ mm. Right: The magnetic field at $I_{\text{main}} = 33$ A in region I without (blue) and with the gradient coils C3 and C5 at different currents (red and yellow). Solid lines correspond to the magnetic field (left axis), dashed lines to the respective field gradients (right axis). The target gradient of $\nabla_z B_0 = -0.5$ mT/cm is achieved at $I_{C3} = 20$ A and $I_{C5} = -10$ A without further optimisation. The chosen position of the SF1 coils lies within region I with the SF1 centre at $z_{\text{SF1}} = 50$ mm. This results in a fixed distance to SF2 (centre) of 930 mm.

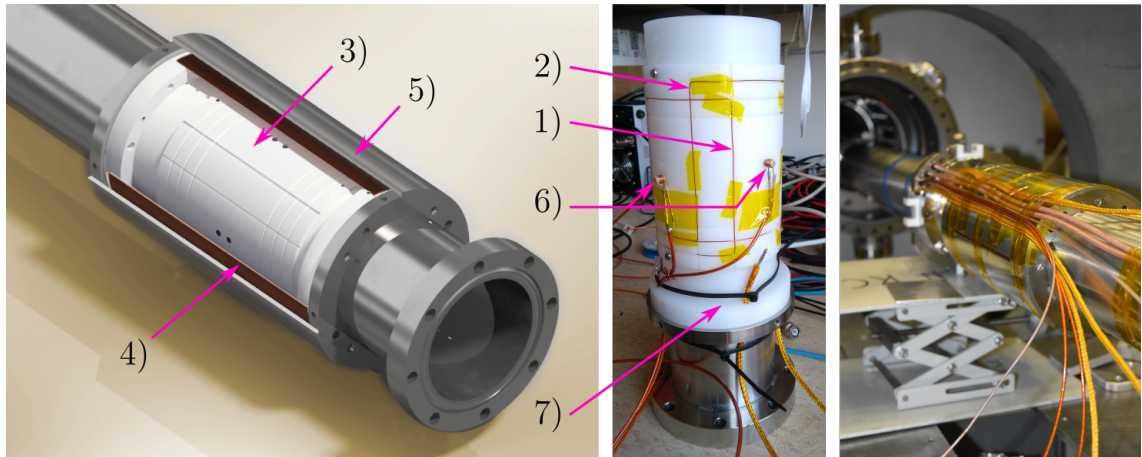


Figure 6.5: The setup of SF1. Left: Cut view of the CAD model, middle: The inner part of the construction, and right: The finished spin flipper prior to installation in τ SPECT. The two saddle coils (1) and (2) are wound on a holder made from POM (3) and are surrounded by a copper shield (4). The setup is mounted within the modified stainless steel tube of the translation stage housing the neutron guide (quartz tube, not shown). A stainless steel cylinder (5) ensures a rigid connection of the two pipe sections of the translation stage. In the (longitudinal) centre of the saddle coils, two pick-up coils (6) are installed for functionality checks. A Hall probe (position shown at 7) is added for magnetic field measurements.

tube compared to the narrowed tube at SF2⁶, the dimensions of the individual saddle coils are $d/2 = 46$ mm, $\phi = 120^\circ$ and $l = 80$ mm. With again a longitudinal displacement of the saddle coils by 10 mm (cf. Ch. 5.1), the effective length of SF1 is $l_{\text{eff}} = 70$ mm. The coils are wound on a cylindrical holder made from polyoxymethylene (POM), a grounded RF shield made from copper is used to retain the B_1 field inside. Both the SF1 holding tube and the RF shield are fixed only on one side, the other one flexibly mounted to reduce material stress during cool down. Finally, a 3 mm thick stainless steel cylinder connects the two ends of the cut tube of the translation stage. Longitudinal slits are added around its circumference for vacuum pumping purposes. Two pick-up coils are used for functionality checks during operation. A 1-axis Hall probe allows for measurements of the magnetic field in the longitudinal direction around SF1; it is located at $r_{\text{HP, SF1}} = 50 \pm 2$ mm and $\Delta z_{\text{HP, SF1}} = 88 \pm 1$ mm from the spin flipper centre.

6.2.2 Optimisation of the SF1 parameters

The double spin flip technique was implemented and tested for the first time in beamtime *Dec2020*. All measurements presented in this context refer to the UCN counts N after 50 s storage time, normalised to the average pulse energy.

In order to have the full spin flip efficiency with SF2, it was set to the optimum parameters listed in Tab. 5.4, the timing of the RF pulse was set to $t_{\text{fill}}(\text{SF2}) = 2$ s after pulse and a duration of $\Delta t_{\text{fill}}(\text{SF2}) = 4$ s (cf. Ch. 3.6.3). Two different heights of τ SPECT

⁶The outer diameter of the quartz tube is $d = 79$ mm as compared to the outer diameter of the narrowed guide of $d = 56$ mm (cf. Ch. 3.1.2).

above source level were investigated, $h_1 = 0.814$ m and $h_2 = 1.557$ m using beamline No. 3 for easy height adaptations (cf. Ch. A.6). Due to time restrictions⁷, however, detailed characterisation and optimisation measurements with respect to the SF1 parameters were not possible. Instead, we took steps to increase N as much as possible in the short time available. These steps included a variation of the signal phase shift $\Delta\varphi(\text{SF1})$ and the RF power P_{SF1} at SF1, a position optimisation and two different combinations of the RF timing.

The number of neutrons depending on the SF1 efficiency: In order to understand how to interpret the measurement results from this optimisation, we first recapitulate, what happens if we switch on SF1, especially if it does not operate at full efficiency. For this purpose, we focus on the RF power at SF1, as $\sqrt{P} \propto B_1$ and the efficiency ε_{SF1} scaling with B_1 (cf. Eq. 5.3 and Ch. 4.1.2). The dependencies on $\Delta\varphi(\text{SF1})$ and the spin flip position can be deduced from these findings afterwards. We assume SF2 operating in full saturation ($P_{\text{SF2}} \geq 50$ W, Fig. 5.6) and the timing of both spin flippers at equal onset and duration.

1. At $P_{\text{SF1}} = 0$ W SF1 is effectively switched off and the trap is filled by spin flipping high-field seeking UCN to low-field seekers using SF2 alone with the single spin flip technique. We call the number of neutrons in the trap therefore $N = N_{\text{sSF}}$.
2. If $P_{\text{SF1}} = P_{\text{sat}}$ high enough such that SF1 is fully efficient, the trap is filled using only the double spin flip technique, which means UCN being spin flipped from LFS to HFS at SF1 and back to LFS at SF2. Increasing P_{SF1} further then does not lead to a further increase in N_{dSF} and a saturation behaviour is reached.
3. If P_{SF1} is raised from $P_{\text{SF1}} = 0$ W onwards, the probability of spin flipping neutrons at SF1 rises, so that the number of neutrons filled into the trap using the double spin flip technique increases and we can write $N_{\text{dSF}} = N_{\text{dSF}}(P_{\text{SF1}})$. At the same time N_{sSF} decreases, which is because at SF1 some of the HFS are spin flipped to LFS. At SF2 these neutrons have then been accelerated in total to $E_{\text{kin}}(z_{\text{SF2}}) \geq 110.56$ neV (cf. Eq. 6.4 at opposite signs in the magnetic contribution), so that even if they were not spin flipped again (in this case this would be back to unstorable HFS), their energy would be too high to be stored in the trap. Therefore, $N_{\text{sSF}} = N_{\text{sSF}}(P_{\text{SF1}})$ depends on the RF power at SF1 as well. In the regime $0 \text{ W} < P_{\text{SF1}} < P_{\text{sat}}$ the trap is therefore filled with both spin flip techniques at different fractions, depending on the RF power of SF1.
4. Some neutrons independent of the filling process, $N_{\text{SF_off}}$, are detected after the storage time of $t_s = 50$ s in any case.

Summarising these findings in one equation, we can write the number of neutrons in the trap depending on the RF power at SF1 as

$$N(P_{\text{SF1}}) = N_{\text{dSF}}^{\text{sat}} \left(1 - \exp \left[-\frac{P_{\text{SF1}}}{P_{1/e}^{\text{SF1}}} \right] \right) + N_{\text{sSF}}^{\text{sat}} \left(\exp \left[-\frac{P_{\text{SF1}}}{P_{1/e}^{\text{SF2}}} \right] \right) + N_{\text{SF_off}}. \quad (6.14)$$

⁷Only two half-days of one-shift beamtime was available per measured height, which corresponds to roughly 15 pulses each.

Here, $P_{1/e}$ is the respective characteristic RF power at which $1/e$ of the saturation is reached, and N^{sat} is the neutron counts which would be measured at the respective filling technique in saturation.

At SF1 both HFS and LFS can be spin flipped, however, potentially at different efficiencies, because ε_{SF1} depends on the UCN velocity v (cf. Eq. 4.12). If we consider the energy acceptance for the single and the double spin flip technique ($\Delta E_{\text{kin},0}^{\text{sSF}} = [0 \text{ neV}, 18.9 \text{ neV}]$ and $\Delta E_{\text{kin},0}^{\text{dSF}} = [110.56 \text{ neV}, 142.07 \text{ neV}]$, cf. Eqs. 5.1 and 6.6), we find that at SF1 the HFS used in the first case have been accelerated to $\Delta E_{\text{kin}}^{\text{sSF}}(z_{\text{SF1}}) = [61.52 \text{ neV}, 80.42 \text{ neV}]$, and the LFS in the second case have been decelerated to $\Delta E_{\text{kin}}^{\text{dSF}}(z_{\text{SF1}}) = [49.04 \text{ neV}, 80.55 \text{ neV}]$. We may therefore assume, that the probability of spin flipping a neutron of either category is approximately equal, so that the change in N_{sSF} when increasing P_{SF1} should be similar to the change in N_{dSF} . We can then write $P_{1/e}^{\text{SF1}} \simeq P_{1/e}^{\text{SF2}} = P_{1/e}$ and simplify Eq. 6.14 to

$$N(P_{\text{SF1}}) = N_{\text{dSF}}^{\text{sat}} + N_{\text{SF_off}} - (N_{\text{dSF}}^{\text{sat}} - N_{\text{sSF}}^{\text{sat}}) \exp\left[-\frac{P_{\text{SF1}}}{P_{1/e}}\right]. \quad (6.15)$$

All in all, if we now vary the settings of SF1, we have to keep in mind that we measure only the result of a combination of both filling techniques, which complicates the isolated analysis of individual parameters.

The signal phase shift $\Delta\varphi$ The dependency of the filling process on the signal phase shift $\Delta\varphi(\text{SF1})$ was characterised at both heights. The results are shown in Fig. 6.6, the left side referring to h_1 and the right side to h_2 , both measured at $P_{\text{SF1}} = 80 \text{ W}$ and at the filling position⁸ $z_{\text{SF2}} = 980 \text{ mm}$. The RF timing configuration at SF1 was set equal to that of SF2 ($t_{\text{fill}}(\text{SF1}) = 2 \text{ s}$ and $\Delta t_{\text{fill}}(\text{SF1}) = 4 \text{ s}$). It turned out, that this configuration is not optimal, because UCN at the upper limit of the kinematic acceptance (cf. Eq. 6.10) can reach SF1 before it is switched on. This problem is discussed in more detail in Ch. 6.2.2.

Due to time constraints, a variation of $\Delta\varphi(\text{SF1})$ at h_1 was only possible in a small range, where no significant dependency was visible. Also at h_2 the results at σ^+ and π polarisation are comparable within errors, except for the increase at $\Delta\varphi(\text{SF1}) \simeq 180^\circ$. One possible explanation for this constant level would be that SF1 was in saturation and also the reduced effective B_1 amplitude at the non-optimal phase shift was still sufficient for full spin flip efficiency (cf. Ch. 5.1.1.2); this is, however, unlikely as will be shown in Ch. 6.2.2. Presumably, the effective B_1 amplitude of SF1 rather changed such, that the respective fractions of neutrons filled with the single or the double spin flip technique balance out, so that the total number of UCN in the trap remained constant.

The decline in N at $\Delta\varphi(\text{SF1}) = 270^\circ$ indicates, that here the wrong ('off-resonant') σ^- polarisation is found (cf. Ch. 4.1.1.1), where effectively no spin flip at SF1 is possible and the trap is filled only by the single spin flip technique. Compared to the considerations in Ch. 6.2.2 this has the same effect as setting $P_{\text{SF1}} = 0 \text{ W}$. Indeed, when we switched off SF1 on purpose to compare the single and the double spin flip technique (cf. Ch. 6.2.3) a comparable average number of $N = 657(20)$ neutrons⁹ was measured (cf. Tab. 6.2).

⁸The position of SF1 is implied by the fixed distance of 930 mm with respect to SF2. With z_{SF2} determining the energy acceptance more significantly, we mainly refer to this quantity.

⁹The difference to the $N \simeq 780$ neutrons in beamtime *Feb2020* is at the time of writing attributed to a HD-contamination of the D_2 gas within the UCN source (cf. Ch. A.1).

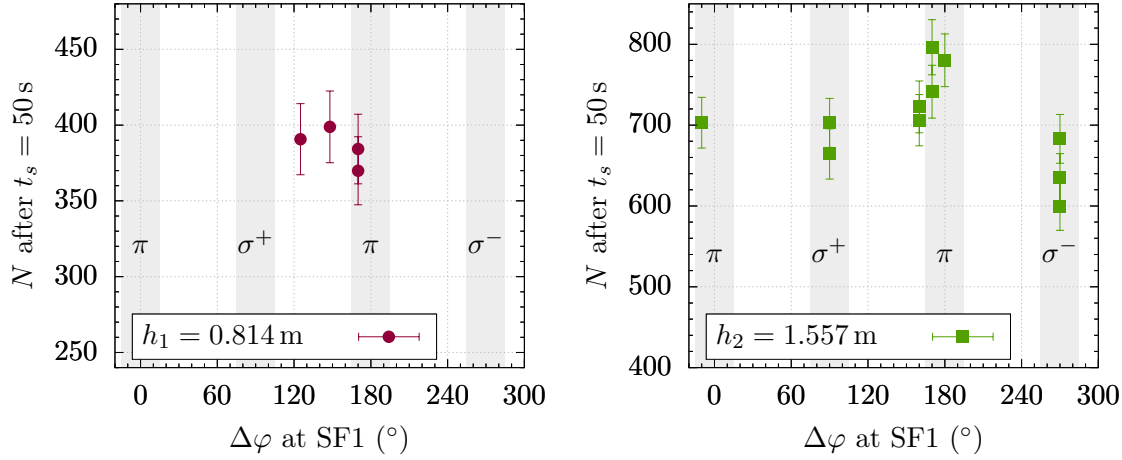


Figure 6.6: Phase optimisation at SF1 with the double spin flip technique in use at two different heights: h_1 (left) and h_2 (right). The position of SF1 was $z_{\text{SF1}} = 980$ mm ($z_{\text{SF2}} = 50$ mm) and the applied RF power was $P_{\text{SF1}} = 80$ W. The RF timing of SF1 for both heights was set to equal values as SF2 ($t_{\text{fill}} = 2$ s and $\Delta t_{\text{fill}} = 4$ s). A variation of the phase at h_1 was possible only in a small range due to time restrictions. At h_2 the results at σ^+ and π polarisation are roughly comparable, with exception of the increase in N at $\Delta\varphi(\text{SF1}) \simeq 180^\circ$, which cannot be explained yet. The decrease at $\Delta\varphi(\text{SF1}) = 270^\circ$ results from the 'off-resonant' σ^- polarisation, so that effectively only SF2 fills the trap using the single spin flip technique.

Only the increase in N at $\Delta\varphi(\text{SF1}) \simeq 180^\circ$ can so far not be explained, though it may be possible that here the combination of all parameters of SF1 lead to an improved filling efficiency.

Timing optimisation of the double spin flip technique So far, both spin flippers are switched on $t_{\text{fill}} = 2$ s after pulse. However, if we consider the upper limit of the energy acceptance $E_{\text{kin},0}^{\text{max}} = 142.07$ neV (cf. Eq. 6.6), which corresponds to velocities of $v \simeq 5.2$ m/s, we find, that the fastest neutrons storable with the double spin flip technique can reach SF1 from $t = 0.9$ s after the reactor pulse onwards. Here, the length of the beamline is estimated as ~ 4.5 m at h_1 and a direct flight path of the neutrons is assumed. If SF1 is not yet active when these neutrons arrive, they are excluded from the filling process.

Therefore, the timing was improved ('optimised') and both spin flippers were switched on directly at the pulse trigger ($t_{\text{fill}} = 0$ s) as is shown in Fig. 6.7 (left). Furthermore, as the goal was to maximise N in the limited amount of time, we changed the spin flipper duration to $\Delta t_{\text{fill}}^{\text{SF1}} = 5$ s and $\Delta t_{\text{fill}}^{\text{SF2}} = 6$ s, i.e. SF2 remained switched on for one second longer than SF1. The single spin flip technique requires UCN at lower energies, which reach SF2 later than those needed for the double spin flip technique. Therefore, during the first five seconds after pulse the trap is filled using the double spin flip technique (or if SF1 is not fully efficient at least with both single and double spin flip technique), while during the additional second afterwards SF2 alone adds neutrons in the energy range up to $E_{\text{kin},0}^{\text{max}} = 18.9$ neV (cf. Eq. 4.20) on top.

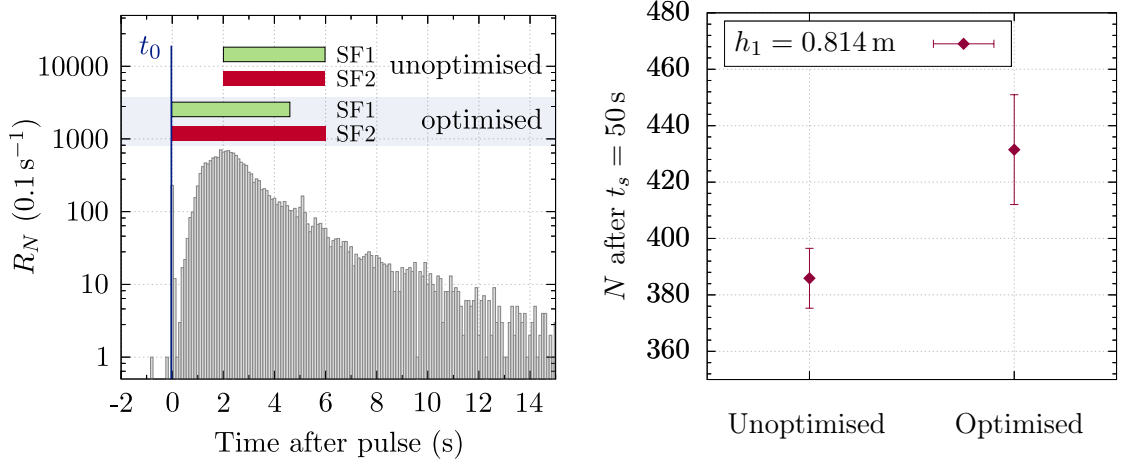


Figure 6.7: Timing optimisation using the double spin flip technique. Left: Arrival spectrum with neutron count rate R_N relative to the thermal peak at t_0 (blue line), binning: 0.1 s. The coloured boxes mark the time during which the spin flippers are active at unoptimised (top) and optimised timing configuration (bottom); green referring to SF1, red to SF2. Right: Number of neutrons after $t_s = 50 \text{ s}$ measured at h_1 using the unoptimised and the optimised timing of the spin flippers. Shown are average and standard deviation of n measurements ($n = 4$ at unoptimised timing, $n = 2$ at optimised timing). An increase by $\sim 12(6)\%$ is visible with the optimised spin flipper timing configuration.

The different timings are summarised again in Tab. 6.1, their effect on the number of neutrons in the trap was investigated, however, only at h_1 so far. The result¹⁰ is shown on the right side of Fig. 6.7, an increase by $\sim 12(6)\%$ was achieved with the optimised timing.

This measurement confirms, that a deliberate combination of the two filling techniques improves the number of neutrons in the trap, so that further investigations should be done, especially at h_2 at which τ SPECT is typically operating.

¹⁰The data point labeled 'unoptimised' is the average and the standard deviation of all results from the phase dependency measurement at h_1 (cf. Fig. 6.6, left).

Table 6.1: Timing of spin flippers 1 and 2 used with the double spin flip technique in beamtime *Dec2020* as onset $t_{\text{fill}}^{\text{SF}}$ and duration $\Delta t_{\text{fill}}^{\text{SF}}$. SF2 at the optimised timing is on for one second longer, during which the trap is additionally filled using the single spin flip technique alone.

Timing	$t_{\text{fill}}^{\text{SF1}}$	$\Delta t_{\text{fill}}^{\text{SF1}}$	$t_{\text{fill}}^{\text{SF2}}$	$\Delta t_{\text{fill}}^{\text{SF2}}$
'unoptimised'	2 s	4 s	2 s	4 s
'optimised'	0 s	5 s	0 s	6 s

The dependency on the spin flip position Both spin flippers only work efficiently, if they are placed at the right position in the B_0 field, so that the respective resonance condition $2\pi f_{\text{SF}} = \omega_0$ (cf. Eq. 4.6) is fulfilled. Similar to the measurements discussed in Ch. 5.1.1.2, the spin flip position was varied and the effect on N investigated after filling the trap with the double spin flip technique. SF2 was again operated at optimum parameters (cf. Tab. 5.4), $\Delta\varphi(\text{SF1})$ was set to the measured optimum at each height¹¹ (cf. Fig. 6.6) and $P_{\text{SF1}} = 80$ W. The RF frequency of both spin flippers was kept constant during the entire measurement. The measurement results are shown on the left side of Fig. 6.8. At h_1 the optimised timing configuration of the spin flippers was used (cf. Tab. 6.1), while the measurements at h_2 were still done at unoptimised timing. This is not ideal for direct comparisons between the heights, however, finding an optimum within one height should be possible nonetheless.

With the fixed distance between the two spin flippers, a position optimisation of SF1 was only possible within the optimum plateau in the position dependency of SF2, which is between $z_{\text{SF2}} = 970$ mm and 1000 mm (cf. Fig. B.7). At h_2 we find the optimum confirmed at $z_{\text{SF2}} = 980$ mm, since the result at $z_{\text{SF2}} = 970$ mm is at best on a comparable level. A similar behaviour was expected at h_1 , so that here we skipped measuring at $z_{\text{SF2}} = 970$ mm

¹¹This is $\Delta\varphi(\text{SF1}, h_1) = 148^\circ$ at h_1 and $\Delta\varphi(\text{SF1}, h_2) = 170^\circ$ at h_2 .

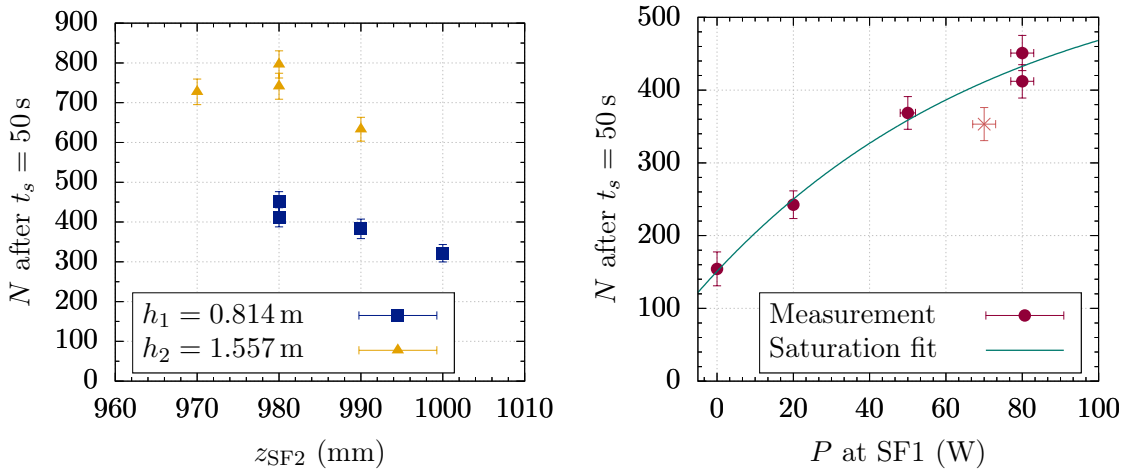


Figure 6.8: Optimisation of the filling position and the RF power of SF1 using the double spin flip technique. Left: Dependency of N after $t_s = 50$ s on the filling position at h_1 (■) and h_2 (▲), given in terms of z_{SF2} due to the fixed distance between the spin flippers. Both measurement series were done at optimum SF2 parameters and $P_{\text{SF1}} = 80$ W. h_1 was measured at optimised timing of the spin flippers, h_2 at unoptimised timing. The calculated optimum position at $z_{\text{SF2}} = 980$ mm ($z_{\text{SF1}} = 50$ mm), is confirmed at h_2 . At h_1 no data was taken at $z_{\text{SF2}} < 980$ mm due to time constraints. Right: Dependency of N on the RF power at SF1 (●) measured at h_1 and $z_{\text{SF2}} = 980$ mm ($z_{\text{SF1}} = 50$ mm) using optimised timing of the spin flippers. The turquoise line is a saturation fit according to Eq. 6.16. The measurement marked as (×) is not included in the fit. Despite the low statistics, it is estimated, that neutron saturation of the trap is not reached yet at $P_{\text{SF1}} = 80$ W.

due to time constraints. From the fixed distance of $\Delta z = 930$ mm between the two spin flippers follows the optimum position of SF1 at $z_{\text{SF1}} = 50$ mm, which confirms the design position in Ch. 6.2.1.

The dependency on the RF power The number of neutrons in the trap depends on the RF power used with SF1 as was discussed in the introduction of this section (cf. Ch. 6.2.2). In order to investigate, whether saturation of the trap was reached at P_{SF1} already, the RF power was decreased as is shown on the right side of Fig. 6.8. The measurement was done only at h_1 and at optimised timing. This is again not ideal if we are interested in the saturated number of neutrons achievable with using only the double spin flip technique. However, those neutrons that are filled into the trap using the single spin flip technique after SF1 has been switched off are independent of the RF power, so that they appear only in an additional offset.

Despite the limited statistics, a significant decrease in N with a reduction of P_{SF1} is visible. Even though Eq. 6.15 can be used to describe the general dependency of N on P_{SF1} , its parameters $N_{\text{sSF}}^{\text{sat}}$ and $N_{\text{dSF}}^{\text{sat}}$ as well as $N_{\text{SF_off}}$ are independent of P_{SF1} , so that they cannot be distinguished when applying a corresponding fit to the measurement results. Therefore, we simplify Eq. 6.15 further and receive

$$N(P_{\text{SF1}}) = a - b \left(\exp \left[-\frac{P}{P_{1/e}} \right] \right), \quad (6.16)$$

which results in the fit parameters $a = N_{\text{dSF}}^{\text{sat}} + N_{\text{SF_off}} = 591.3(171.1)$, $b = N_{\text{dSF}}^{\text{sat}} - N_{\text{sSF}}^{\text{sat}} = 440.4(162.9)$ and $P_{1/e} = 78.4(51.1)$ W ($\chi^2/\text{ndf} = 0.81$).

In Ch. 5.1.1.2, we found that when using the single spin flip technique saturation is reached with SF2 from $P_{\text{SF2}} \simeq 50$ W onwards (cf. Fig. 5.6). This does not seem to be the case with the double spin flip technique so far, which might be the result of a lower spin flip efficiency ε_{SF1} as compared to ε_{SF2} . From Eq. 4.12 follows, that the spin flip efficiency depends in principle on three parameters:

1. The longitudinal gradient $\nabla_z B_0$: We find $\nabla_z B_0(z_{\text{SF1}}) = -0.5$ mT/cm at SF1 and $\nabla_z B_0(z_{\text{SF2}}) = -3.6$ mT/cm at SF2. With the spin flip efficiency generally improving with decreasing gradients, we can exclude the gradients as a reason for a low ε_{SF1} .
2. The neutron velocity v : Between SF1 and SF2, neutrons used with either single or double spin flip technique are in the high-field seeking state, so that they are decelerated on the way to SF2. Consequently, the UCN velocity is higher at SF1 as compared to SF2, resulting in a reduced ε_{SF1} .
3. The B_1 amplitude: The current carrying wires of the SF1 saddle coils are located at a larger radius ($d/2 = 46$ mm) than the ones of SF2 ($d/2 = 31.5$ mm), so that B_1 at the centre ($r = 0$ mm) is smaller at SF1 than at SF2 (assuming equal power in both cases¹²), which results in a reduced ε_{SF1} as well.

¹²This is confirmed in a simulation with COMSOL Multiphysics®, which resulted in $B_1^{\text{SF1}}/B_1^{\text{SF2}} \sim 0.6$ (both fields evaluated at $r = 0$ mm). Using the relation $\sqrt{P} \propto B_1$ (cf. Eq. 5.3) we find that $P_{\text{SF1}} \simeq (1/0.6)^2 P_{\text{SF2}} = 2.78 P_{\text{SF2}}$ is required to reach equal B_1 amplitudes in SF1 and SF2. With saturation at SF2 reached at $P_{\text{SF2}} = 50$ W, this results in $P_{\text{SF1}} = 138$ W.

In conclusion, arguments (2) and (3) can explain why SF1 does not operate in saturation yet and in both cases a higher RF power helps to increase the spin flip efficiency. This makes an even more thorough impedance matching of SF1 necessary in future measurements.

6.2.3 The filling techniques in comparison

In the introduction of this chapter (cf. Ch. 6.1) the theory behind the double spin flip technique was discussed along with constraints regarding the UCN beam divergence. As the beam divergence at the entrance of τ SPECT could not be measured directly for an estimation of the expected increasing factors between the single and the double spin flip technique, comparison measurements of both techniques were done which are presented in the following.

At heights h_1 and h_2 , 50 s storage measurements were done and the spin flipper parameters were adjusted to the optimum values known so far: SF1 was set to $z_{\text{SF1}} = 50$ mm, $P_{\text{SF1}} = 80$ W, and $\Delta\varphi(\text{SF1}) = 148^\circ$ at h_1 and $\Delta\varphi(\text{SF1}) = 170^\circ$ at h_2 ; SF2 was set to $z_{\text{SF2}} = 980$ mm, $P_{\text{SF2}} = 80$ W, and $\Delta\varphi(\text{SF2}) = 90^\circ$. In order to allow for a direct comparison of the two filling techniques, both spin flippers were switched on $t_{\text{fill}} = 2$ s after pulse for a duration of $\Delta t_{\text{fill}} = 4$ s, corresponding to the unoptimised timing (cf. Tab. 6.1). The measurement results are shown in Fig. 6.9 as the average value and the standard deviation of all measurements done with the respective configuration. The results are also listed in Tab. 6.2. The ratio r is calculated as $N(\text{dSF})/N(\text{sSF})$. These values, however, include the

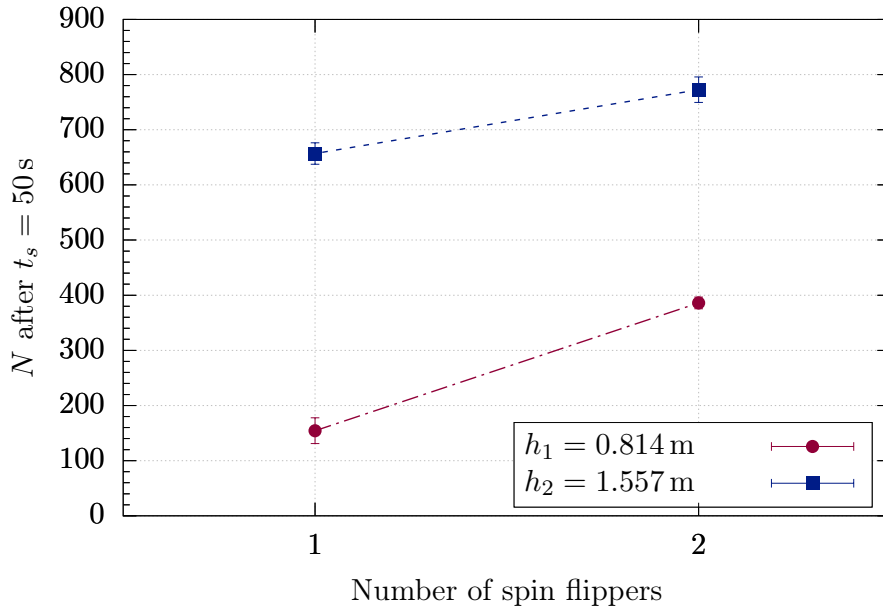


Figure 6.9: Comparison between the single (#1) and the double spin flip technique (#2) at heights $h_1 = 0.814$ m (red) and $h_2 = 1.557$ m (blue) using 50 s storage measurements at optimised spin flipper parameters. In all measurements the unoptimised timing configuration was used ($t_{\text{fill}} = 2$ s and $\Delta t_{\text{fill}} = 4$ s). The results and increasing factors between the two techniques are listed in Tab. 6.2, after subtraction of $N_{\text{SF_off}}$ an estimated gain of 3.46(1.17) at h_1 and 1.19(7) at h_2 is achieved.

Table 6.2: Results of the filling technique comparison measurement at h_1 and h_2 . The ratio $r = N(\text{dSF})/N(\text{sSF})$ includes the filling process independent neutrons $N_{\text{SF_off}} = 60 \pm 8$. They were subtracted from the results N before calculating the ratio R (right column). With the possibly height dependent $N_{\text{SF_off}}$ not measured at h_1 , the results are to be considered estimations.

Height	$N(\text{sSF})$	$N(\text{dSF})$	r	R ($N_{\text{SF_off}}$ subtracted)
$h_1 = 0.814 \text{ m}$	154.29 ± 23.35	385.90 ± 10.60	2.50(39)	3.46(1.17)
$h_2 = 1.557 \text{ m}$	656.88 ± 19.35	772.60 ± 23.11	1.18(5)	1.19(7)

filling process independent neutrons $N_{\text{SF_off}}$, so that the average value of $N_{\text{SF_off}} = 60 \pm 8$ obtained in beamtime *Feb2020* was subtracted from all results before calculating the ratio R in the right column. Strictly speaking, $N_{\text{SF_off}}$ could be height dependent but was not measured at h_1 yet.

As we are interested in maximising the number of neutrons in the trap, we will focus on h_2 here. Experimentally, an increasing factor of $R(h_2) = 1.19(7)$ was realised when switching from the single spin flip technique to the double spin flip technique. This is certainly in large contrast to the theoretical prediction $r_{\text{theo}} = 7.2$ (cf. Eq. 6.7), nevertheless this value was calculated using the storable energy ranges only without taking into account further effects such as the beam divergence θ_{max} (cf. Ch. 6.1.2) or the trap saturation. However, the fact that an increase in N was measurable indicates, that the double spin flip technique works in principle and now needs to be further optimised.

6.3 Future optimisation of the double spin flip technique

The measurements done with the double spin flip technique so far were intended as proof of concept with only a rough parameter optimisation of SF1 done in the short amount of time. This keeps several options open to improve the UCN density in τ SPECT which are presented in the following without claim of completeness.

Increasing the spin flip efficiency of SF1

The single spin flip measurements were done in trap saturation, i.e. at full efficiency ε_{SF2} of SF2 ($P_{\text{SF2}} = 80 \text{ W}$). From the considerations in Ch. 6.2.2 follows, that maximum efficiency of SF1 was probably not achieved yet if a similar dependency of N on P_{SF1} is assumed at h_2 as was measured at h_1 (cf. Fig. 6.8). In order to improve ε_{SF1} , higher RF power irradiation must be made possible by a more thorough impedance matching.

The spin flip efficiency furthermore depends on the gradient at SF1, which was adjusted to $\nabla_z B_0(z_{\text{SF1}}) = -0.5 \text{ mT/cm}$ by the gradient coils C_3 and C_5 . The size of this gradient was, however, only an estimated starting value and was neither optimised nor even varied yet.

Decreasing the beam divergence

In Ch. 6.1.2, we saw how strongly the effectiveness of the double spin flip technique depends on the beam divergence, so that a reduction of θ_{\max} is expected to have a significant impact on the UCN density in τ SPECT.

The gravitational deceleration between the UCN source exit and the shutter at the entrance of τ SPECT shifts the energy spectrum down, however, at the same time the beam divergence increases (cf. Ch. 6.1.3). The divergence angle depends amongst others on the type of reflection, the ideal case would be purely specular reflection (as opposed to diffuse reflection) but which requires a very high quality of the neutron guide inner surface. In the current beamline setting (beamline No. 3, cf. Ch. A.6), two 90° bends are used, which shall be replaced by specularly reflecting mirrors consisting of $^{58}\text{NiMo}$ coated float glass plates. As shown in Fig. 6.10, a reduction of the beam divergence would be expected since the transversal velocity components of the neutrons do not evolve as strongly as with the bent tube¹³. First prototypes of reflecting mirrors are currently under construction.

Furthermore, neutrons at higher energy are required for the double spin flip technique than for the single spin flip technique. As these neutrons have been gravitationally decelerated already when they reach the entrance of τ SPECT, their energy at UCN source level ($h = 0$ m) is even higher. Calculating a simplified example, a neutron with $E_{\text{kin},0}(h_2) = 142.07$ neV at the entrance of τ SPECT was decelerated from initially $E_{\text{kin}}(h = 0 \text{ m}) = 301.5$ neV. With the current beamline consisting of stainless steel tubes ($V_F = 190$ neV), this neutron may be lost if it impinges on the walls at large scattering angles. Therefore, it could be considered to coat the beamline with ^{58}Ni ($V_F = 335$ neV) or $^{58}\text{NiMo}$ ($V_F = 310$ neV). However, the surface quality - more specifically its roughness - depends on the coating method and from comparison measurements in [Kah20] follows, that the UCN transmission through the currently used stainless steel guides is still better than through a tube made from SiO_2 with NiMo coating. Thus, if the advantages of the high Fermi potential of ^{58}Ni is countered by a higher fraction of diffuse reflection resulting from

¹³This is only the case under the assumption of specular reflection.

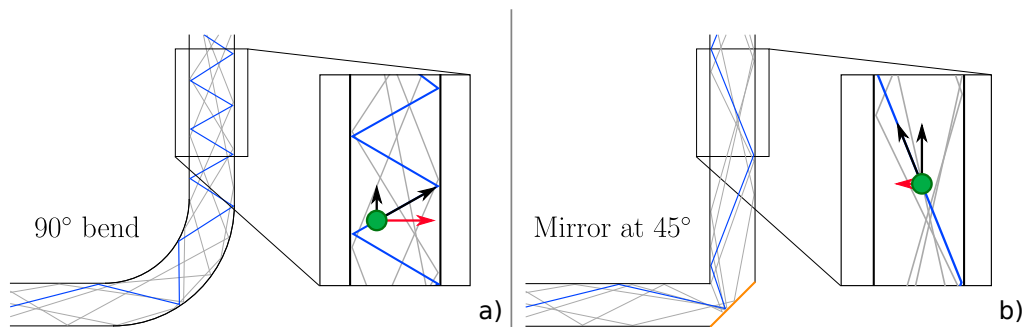


Figure 6.10: Schematics of neutron transmission through a 90° bent tube (a) and using a 45° mirror (b). Due to many reflections inside the bend, the transversal component of the neutron velocity (red arrow) increases faster when using the bend than with the mirror, where only one reflection is required to guide the neutrons upwards. In order to decrease the beam divergence at the entrance of τ SPECT, both bends in the beamline are thus to be replaced by mirrors in the future.

a rougher surface, nothing can be won. The optimisation of the beamline (which includes the neutron guides within τ SPECT) is therefore currently under investigation.

Combining the single and double spin flip technique

UCN in the energy range of the single spin flip technique ($\Delta E_{\text{kin},0} = [0 \text{ neV}, 18.9 \text{ neV}]$, cf. Eq. 5.1) reach τ SPECT later than those UCN used for the double spin flip technique ($\Delta E_{\text{kin},0} = [110.56 \text{ neV}, 142.07 \text{ neV}]$, cf. Eq. 6.6). By switching off SF1 earlier than SF2, both filling techniques are combined, which at h_1 already resulted in a 12(6)% increase using the 'optimised' timing configuration in Tab. 6.1. This method is thus worth investigating at h_2 as well.

In conclusion, the double spin flip technique was successfully tested as proof of concept and resulted in an increase in N by 19% already after a very rough parameter optimisation. The implementation of the steps mentioned above will show, to what extent this filling method can be further improved.

Chapter 7

Summary and Outlook

In this work the filling process in the neutron lifetime experiment τ SPECT was investigated and optimised. After the storage octupole had been installed in 2018, UCN storage using only magnetic fields was possible in the trap with a volume of ~ 10 L and a trap depth of $V_{\text{pot}} = 47$ neV. The measurement principle and the development of additional components required for the filling of the trap with UCN are discussed. The filling process involves the spin flip of high-field seeking neutrons to the low-field seeking state, which is done by an adiabatic fast passage spin flipper. It was estimated that spin flips in the transversal magnetic field of the storage octupole are not efficiently possible. In order to counter this effect, a second octupole was built and installed, which was able to compensate the transversal field by 60.4(1.0)%. Due to gravity, it was axially misaligned with the storage octupole by $\delta y = -2.6$ mm in vertical direction.

Two different types of spin flipper were investigated throughout the last years, the first one was a so-called birdcage resonator with a fixed resonance frequency of ~ 10 MHz. First storage experiments of UCN using this spin flipper were successful, the fit to a storage curve at optimised filling parameters and at $z_{\text{SF}} = 879$ mm yielded an initial number of permanently stored neutrons $N(t = 0\text{ s}) = 145.0(21.0)$ and a decay time of $\tau = 476.9(79.7)$ s; the measurement was done without spectrum cleaning of marginally trapped neutrons. Apart from this systematic error, a measurement of the neutron lifetime with an uncertainty of $\Delta\tau_n = 1.0$ s would not have been possible in a reasonable amount of time though.

Since analytic calculations regarding the adiabatic fast passage spin flipper are only valid for spin flip efficiencies $\lesssim 1$ and parameters such as the neutron velocity distribution or external forces are not taken into account, Monte Carlo simulations of the spin flip were carried out. These simulations allowed for investigations of the influence of the remaining transversal field on the spin flip efficiency. It was found, that ε_{SF} decreases regardless of the B_1 amplitude of the spin flipper if the transversal field gradient at the neutron guide radius is more than three times larger than the longitudinal field gradient in the centre of the guide. This led to the restriction of allowed spin flip positions with $z \leq 1004$ mm.

From energy considerations in the total filling process followed, that the maximum initial neutron velocity that is only just storable in the trap depends on the magnetic field at the spin flip position. The storable energy range for the birdcage resonator was calculated as 0 to 7 neV, which compared to the trap potential of 47 neV was rather low. In order to increase the neutron density, the spin flipper had to be positioned in a lower magnetic field. This was not possible without having to reconstruct the birdcage resonator, so that it was

unsuitable for further optimisation processes.

The spin flipper was thus replaced by a double saddle coil, that could be tuned to varying resonance frequencies externally. It allowed for spin flip positions in lower magnetic fields, where an increase in the number of neutrons stored in the trap by a factor of ~ 4 was achieved at the optimum position $z_{\text{SF}} = 980$ mm. Furthermore, its additional parameters RF power (which corresponds to the B_1 amplitude) and signal phase shift $\Delta\varphi$ were fully understood and optimised.

The compensation of the storage octupole field was improved by reducing the axial misalignment between the two octupole axes to $\delta y = -0.2$ mm. Simulations estimated an improvement in the compensation by another factor of ~ 12 . This allowed for spin flip positions close to the minimum of the B_0 field. However, no stored neutrons were measured here, which might be due to a second spin flip back to the high-field seeking state behind the field minimum.

By reducing the current in the superconducting coils from $I_{\text{main}} = 33$ A to 31 A, and thus decreasing the magnetic field at the spin flip position, a higher energy acceptance for incoming neutrons was expected. No increase in the number of neutrons could be found though, which could be caused by a reduction of the field potential in the fringe region of the trap.

First systematic investigations regarding a cleaning procedure were done, employing three different cleaning positions and three cleaning durations up to $t_{\text{clean}} = 40$ s. In all cases, the cleaning had a visible effect as the population of neutrons leaving the trap on time scales much shorter than the neutron lifetime could be decreased drastically.

The determination of the neutron lifetime from a storage curve of relative measurements requires a normalisation of the data. Three methods were investigated in this work, currently a normalisation to the pulse energy of the reactor gives the best results where non-statistical fluctuations of $\sim 5\%$ remain.

With the installation of an additional double saddle coil in the high field region of the first B_0 field peak the double spin flip technique was implemented. It relies on a two-stage deceleration of neutrons initially in the low-field seeking state. From the neutron energy distribution follows a significant increase in the number of storable neutrons. However, the effectiveness of this technique depends heavily on the divergence of the incident neutron beam, since the deceleration acts only on the longitudinal component of the neutron motion. Compared to the previous single spin flip technique, an increase in the neutron density by $\sim 19\%$ could be achieved in a proof of concept measurement.

Outlook

By replacing the bent tubes in the beamline with specularly reflecting mirrors, it will be attempted to reduce the beam divergence and thus increase the efficiency of the double spin flip technique. The mirrors are currently under construction and will be ready for investigation soon. A dedicated normalisation detector is currently under construction, which is planned to be located in the upper part of the beamline. Simulations on UCN transmission through the beamline are ongoing.

In the meantime, the cleaning procedure was further improved by prolonging the cleaning duration to $\Delta t_{\text{clean}} = 200$ s. A storage curve was measured in beamtime *June 2021* as shown in Fig. 7.1 with cleaning at $z_{\text{clean}} = 1854$ mm. A step-wise increase in the number of

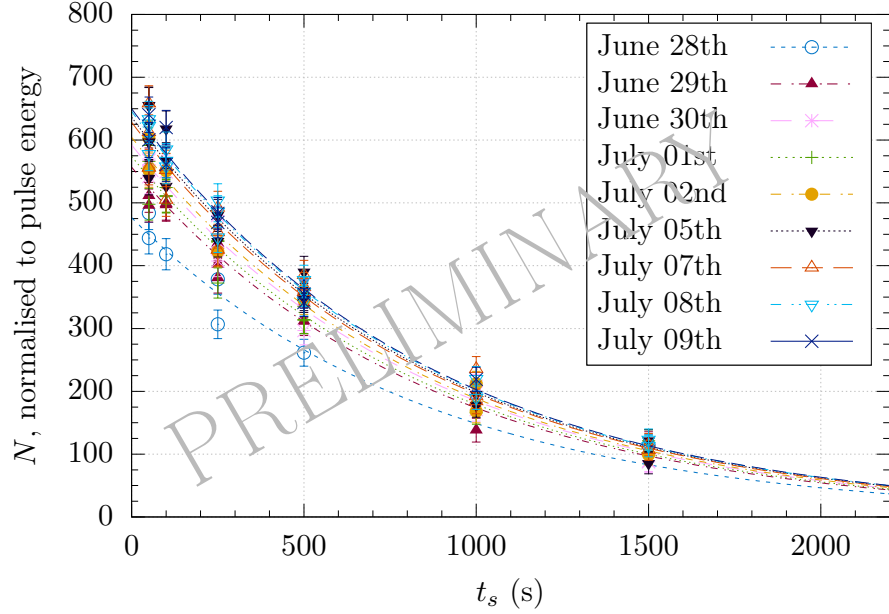


Figure 7.1: Storage curve measured in beamtime *June2021* with multi-dimensional single exponential fit. The data was split by days, the fit taking into account a parameter for the amplitude of each day and a common decay constant which yielded $\tau = 858.59(15.52)$ s. The remaining fit results are listed in Tab. B.5.

neutrons was observed with each new day (probably due to improved UCN production by reformation of the sD_2 crystal), so that the data set was split by days. A multi-dimensional single exponential fit of the form

$$N(t) = a_1^i \exp(-t/\tau) \quad (7.1)$$

was applied, with a_1^i corresponding to the initial number of neutrons at each separate day, and τ the decay constant common in all data sets (cf. Tab. B.5 for the fit results). With $\tau = 858.59(15.52)$ s ($\chi^2/\text{ndf} = 1.14$) a significant improvement compared to the measurements at shorter cleaning duration ($\Delta t_{\text{clean}} \leq 40$ s, cf. Ch. 5.3.1) was achieved as this result is close to the expected neutron lifetime $\tau_n \simeq 880$ s and measured with a higher precision. In the future, further investigations will be made. In addition, simulations on the cleaning procedure for finding the optimum cleaning position and duration are currently in progress.

Appendix A

Further contents, procedures and constructions

A.1 The UCN source D at the TRIGA reactor

Source D at the TRIGA reactor is a pulsed source for ultracold neutrons (cf. Ch. 2.1.2). Between the pulses, the reactor is kept in steady-state mode at $P = 50 \text{ W}$ [KRR⁺17], which is maintained by three control rods filled with a strong neutron absorbing material (in Mainz, this is Cadmium)¹. The sudden shoot out of one of the control rods (the 'pulse rod') using pressurised air leads to a short-term excess of reactivity and a sharp increase of the reactor power up to $P = 250 \text{ MW}_{\text{peak}}$ with a reactor period on the order of a few milliseconds. The temperature in the fuel rods rises quickly, leading to a fast decrease in reactivity. The result is a short neutron pulse with a width (FWHM) of $\sim 30 \text{ ms}$ and a total pulse energy of up to $E_{\text{pulse}} = 10 \text{ MWs}$. A maximum of 12 pulses per hour is legally allowed, so that in principle one pulse every 5 min would be possible. However, it was observed that the stability regarding UCN output increases if the time between pulses is roughly 12 min, which for τSPECT is no limitation as many measurements take longer than this time anyway.

A.1.1 The setup of the UCN source

A schematic drawing of the UCN source is depicted in Fig. A.1, based on Fig. 1 in [KSB⁺14] (dimensions are not to scale). The reactor core consists of multiple fuel rods, which are made from uranium zirconium hydride (UZrH). It is surrounded by a graphite reflector, a water pool and a concrete shielding. The UCN source is installed inside a drilling through the shielding and reaches close to the core. The fast neutrons from the fission of the uranium atoms ($E > 1 \text{ MeV}$) are thermalised by the hydrogen in the fuel rod material and the surrounding water. The thermal neutrons in turn maintain the fission chain reaction. The heat load in the fuel rods ($T \sim 600 \text{ K}$ [Hel21, Ebe21]) leads to upscattering of the thermalised neutrons to higher energies, so that the fission cross section decreases and the chain reaction stops.

¹A thorough introduction into the physics and operating properties of TRIGA reactors is found on the website of the International Atomic Energy Agency (IAEA): <https://ansn.iaea.org/> (accessed Feb 2nd, 2021).

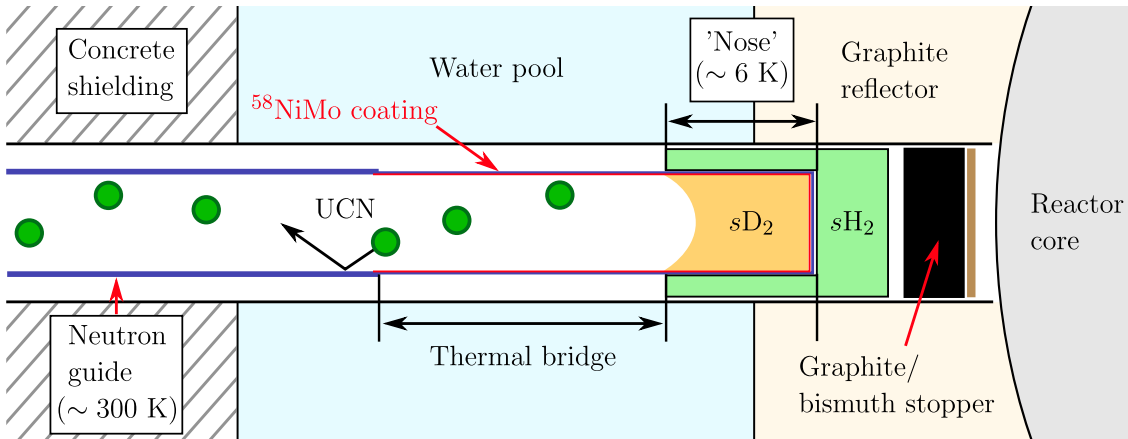


Figure A.1: 'Nose' region of UCN source D, based on Fig. 1 in [KSB⁺14]. The cup-shaped end of the source ('nose') is cooled to $T \simeq 10$ K, where a $s\text{H}_2$ (pre-moderator) and a $s\text{D}_2$ crystal (main moderator) are frozen out. Thermal neutrons scatter inelastically at the moderators and enter the neutron guide as UCN. In the region of the thermal bridge, the wall thickness is reduced for thermal decoupling. A graphite/bismuth stopper shields the crystals from high heat load by fast neutrons and γ radiation. The neutron guide is made from stainless steel tubes with $^{58}\text{NiMo}$ coating in the region of the thermal bridge.

In order to moderate the thermal neutrons down to the ultracold energy regime, two crystals are frozen out at the cup-shaped end of the source ('nose'): A hydrogen crystal as pre-moderator ($T_f(s\text{H}_2) = 14.0$ K) and a deuterium crystal as main moderator ($T_f(s\text{D}_2) = 18.7$ K). Therefore, the nose must be cooled with liquid helium ($T(l\text{He}) \leq 4.2$ K)².

The neutrons scatter inelastically via phonon interaction with the $s\text{H}_2$ crystal and are converted to energies which have a high scattering cross section with the atoms in the $s\text{D}_2$ crystal. Here they are further downscattered to ultracold energies ($T_{\text{UCN}} \simeq 3$ mK). In this process the quality and shape of the $s\text{D}_2$ crystal are important: Under good conditions the time the neutrons spend within the crystal is small due to a low diffuse reflection rate (\sim ms) and does not suffice to bring them to thermal equilibrium with the crystal ($T_{s\text{D}_2} \simeq 6 - 8$ K). Thus the source D is a superthermal UCN source. Furthermore, during the short time within the crystal, absorption by the deuterium atoms and upscattering is small, if the deuterium is in the energetic ground state ([UTM⁺05] 'ortho-state' with total spin $J = 0$) and if the crystal is not amorphous (this would lead to increased diffuse scattering and thus prolong the time spent within the crystal). When the neutrons finally leave the crystal they are accelerated because of the potential difference between the $s\text{D}_2$ crystal ($V_F = 105$ neV) and vacuum. Therefore, the UCN energy spectrum in the beamline starts at $E \simeq 105$ neV.

In the region of the so-called thermal bridge, the wall thickness of the neutron guide is reduced (length ~ 500 mm) for thermal decoupling of the room temperature part of the UCN guide from the 'nose' containing the $s\text{H}_2$ and $s\text{D}_2$ crystals. A graphite/bismuth stopper between the source and the core shields the crystals from heat load caused by

²The freeze out temperatures for H_2 and D_2 were obtained from <https://chem.libretexts.org/>, the boiling temperature for $l\text{He}$ from <https://www.rsc.org/>.

epithermal neutrons and γ radiation [KSB⁺14].

The source was upgraded in 2017 [KRR⁺17] to increase the UCN output, during which neutron guides with improved surface roughness³ were installed. Furthermore, the initial natural NiMo coating of the nose ($V_F = 220$ neV) was replaced by a coating made from ⁵⁸NiMo ($V_F = 311$ neV) and the coating region was extended to include the thermal bridge.

A.2 Construction of the compensation octupole

A.2.1 The selection of the magnetic segments

The compensation octupole required a total of 160 magnetic segments (32 in each of the five rings) which were ordered from Arnold Magnetic Technologies AG including an overhead of 45%. From the discretisation of the Halbach array follows a magnetic rotation by 45° between the segments (cf. Eq. 3.3), which in turn for symmetry reasons is realisable using segments of only 5 different magnetisation directions (cf. Fig. A.2, middle). Assuming perfect orientation of the segments within the Halbach array, the most homogeneous magnetic field is generated if only segments are used, which have the most similar magnetic remanence. Therefore, all segments were magnetically measured using a calibrated 3-axis Hall probe (cf. Ch. 3.2.2.1) before the assembly of the compensation octupole.

³Instead of electropolished stainless steel tubes of hygienic class HE4 ($R_a \leq 0.4 \mu\text{m}$), hygienic class HE5 ($R_a \leq 0.25 \mu\text{m}$) was used for the total of ~ 3.8 m length out of the reactor shielding [KRR⁺17]. The surface roughnesses are taken from <https://www.sks-online.com/>.

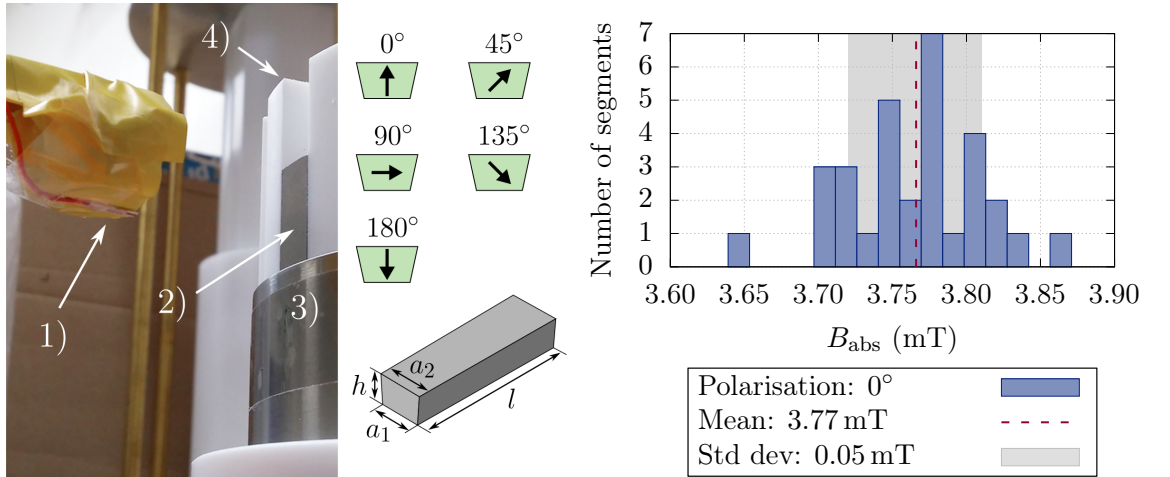


Figure A.2: Field measurement of the magnetic segments. Left: Measurement setup with a distance between segment (2) and Hall probe (1) of $d = 33$ mm. The segment is held by a PTFE construction aid (4) and one of the titanium rings of the compensation octupole holding shell (3). Middle: The five segment magnetisations required for the compensation octupole. The black arrows mark the magnetisation direction. The dimensions of a single segment are depicted at the bottom with $l = 30$ mm, $a_1 = 7.8$ mm, $a_2 = 9$ mm and $h = 5.8$ mm. Right: Distribution of the absolute magnetic field of the vertically (0°) magnetised segments around the common mean value of $B_{\text{main}}(0^\circ, d = 33 \text{ mm}) = 3.77(5)$ mT.

Fig. A.2 shows the measurement setup on the left and the resulting histogram for the absolute magnetic field of the vertically (0°) magnetised segments on the right. The measurement distance was $d = 33$ mm from the middle of the segments, which is roughly equal to their longest side ($l = 30$ mm, cf. Fig. A.2, bottom). This is a problem, because with the magnetic field of the segment decreasing with $\sim d^3$, a displacement in the exact position of the segment by only $\delta d = 0.1$ mm can cause fluctuations in the measured field by $\delta B \simeq 0.04$ mT (the dependency on d^3 and the values result from a FEM simulation using COMSOL Multiphysics[®]). However, at larger measurement distances the field would have been too small to be significantly distinguishable from noise.

The mean value of the results is found as $B_{\text{abs,mean}}(0^\circ, d = 33 \text{ mm}) = 3.77(5)$ mT. The measurement was repeated for all magnetisation directions and, finally, the required number of segments was chosen from the regions around the mean values.

A.2.2 Construction of the compensation octupole

After identifying the most similar magnetic segments, they were distributed over five individual titanium rings, which make the holding shell of the compensation octupole. The rings contain a gearing construction with precision cutouts between adjacent rings in order to keep the relative rotation of the rings fixed (cf. Fig. A.3 left). The end rings are longer by 20 mm on each side, so that the fringe field of the compensation octupole is contained mainly inside the material. The fixation in axial direction is done by a titanium holding cylinder, which is connected to the end rings on both sides. The vertical slits in the holding cylinder were originally intended to fit additional magnetic platelets to further improve the field compensation, which were, however, never used.

The glue (two-component epoxy resin Epo Tek 301-2) requires 48 hours to fully harden, so that a construction aid was needed, which on the one hand helped placing the magnetic segments properly, and on the other hand kept them in position during the curing time

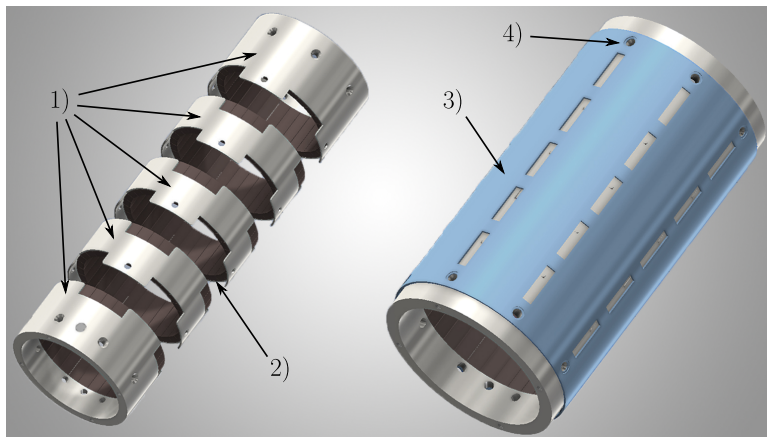


Figure A.3: Gearing principle of the compensation octupole rings. The magnetic segments (2) are glued into three inner and two outer rings made from titanium (1). When pushing the rings together for the final assembly, the overlapping material of the rings are integrated into adjacent indents, maintaining the alignment of the octupoles. A titanium holding cylinder (3) is pulled over the rings and connected to the end rings via studs (4).

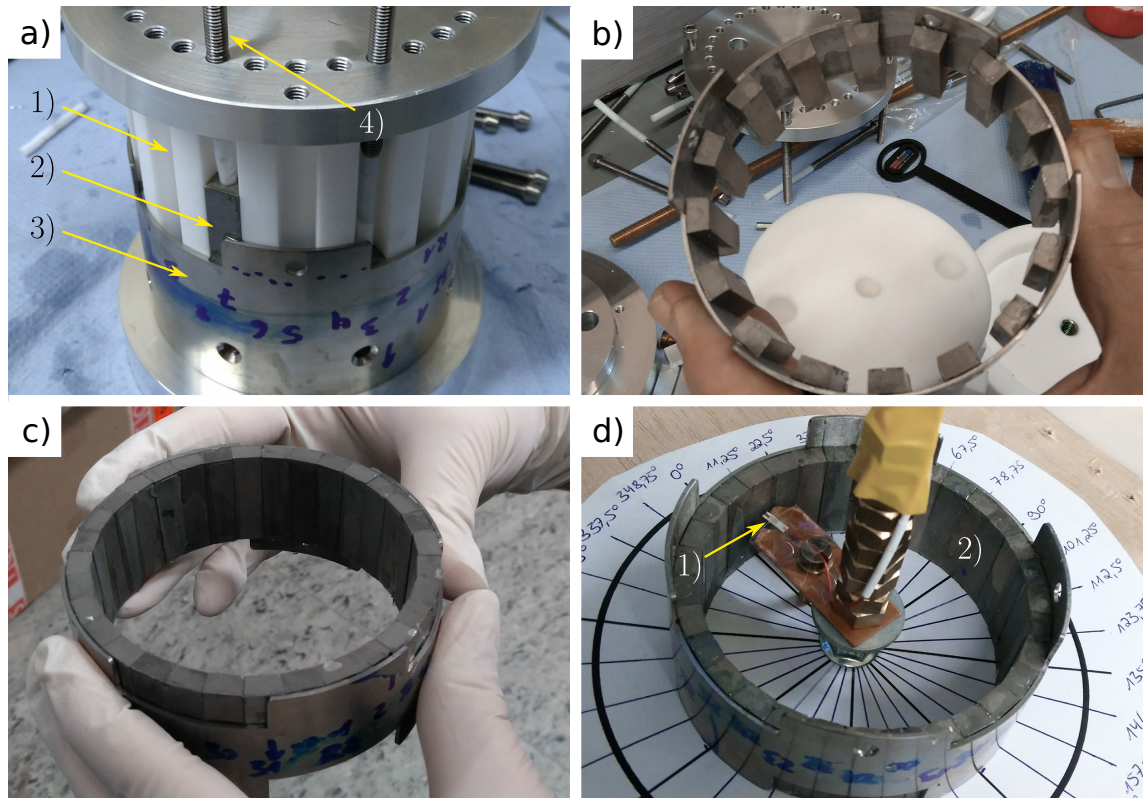


Figure A.4: Construction and measurement setup of the octupole rings. a) Construction setup with segment holder (1), magnetic segment (2), titanium ring (3), and Ti screw with PTFE end cap (4). b) Inner titanium ring with the first 16 magnets in place fixed by glue. c) Finished octupole ring. The top and bottom surfaces were grinded afterwards to avoid slits between the rings. d) Setup for the magnetic field measurement of the octupole rings with a Hall probe on a Cu plate (rotatable) (1) and octupole ring (2). Data points were taken at $r = 39 \pm 1$ mm and $\varphi = 11.25(2.0)^\circ$.

of the glue. This construction aid is shown in Fig. A.4 a). The first half of segments was covered with glue, pushed into place and held there by screws with PTFE end caps. After the glue had cured, the ring was taken out of the construction aid and ready for the second set of segments (Fig. A.4 b)). A second construction aid similar to the first one, but milled in the lower half to fit into the octupole ring, was used to place the remaining segments. The finished ring is shown in Fig. A.4 c). Afterwards, the front surfaces of all rings were ground to reduce slits between adjacent rings.

Finally, the rings were magnetically measured, in order to check, if the segments were placed correctly and the field shows the expected octupole structure. The calibrated 3-axis Hall probe (cf. Ch. 3.2.2.1) was mounted on a rotatable piece of copper pinned to a rod as shown Fig. A.4 d). The octupole rings were placed around the rod concentrically and a measurement was done every $\varphi = 360^\circ/32 = 11.25^\circ$ (in the centre of each segment) on a radius of $r = 39 \pm 1$ mm. The estimated rotation error is $\Delta\varphi = 2^\circ$. Fig. A.5 shows the radial component of the measured magnetic field of all five rings on the left, and the z -component on the right. If the measurement plane were exactly horizontal and in the

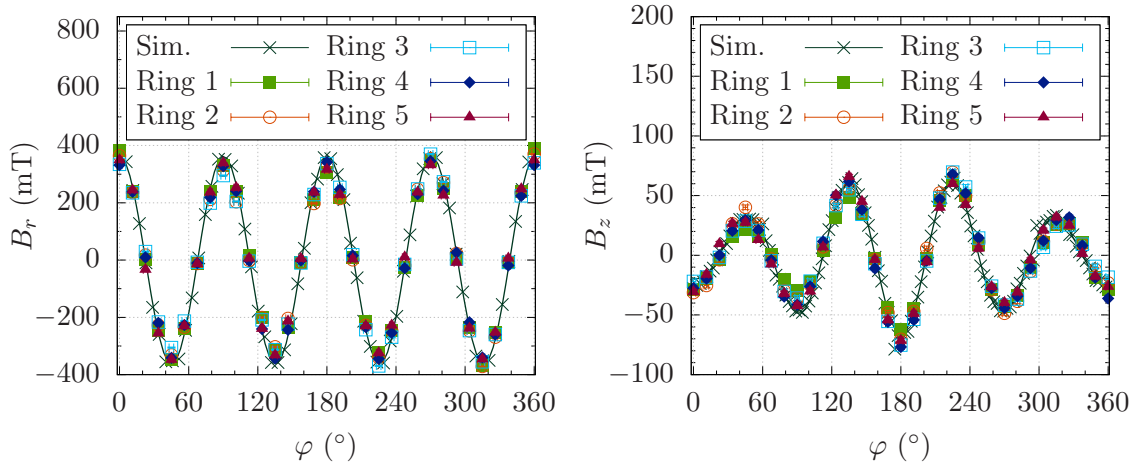


Figure A.5: Radial (left) and longitudinal component (right) of the magnetic field shown for the 5 octupole rings on a measurement radius of $r = 39 \pm 1$ mm. The errors are smaller than the point size. The black crosses show data from a FEM simulation on a plane $\Delta z = 1.6$ mm from the vertical centre of the rings and with a tilt of 1° , the lines are a fits of a sine function to this data.

vertical centre of the ring, B_z would be expected to vanish for symmetry reasons. A FEM simulation using COMSOL Multiphysics[®] showed, however, that the remaining structure in B_z was caused by an offset in the measurement plane by $\Delta z = 1.6$ mm and a tilt by 1° . The agreement between measurement and simulation confirms, that all segments were placed correctly and that the rings are of approximately equal field strength.

Nevertheless, slight inhomogeneities in the magnetic field can create an offset between

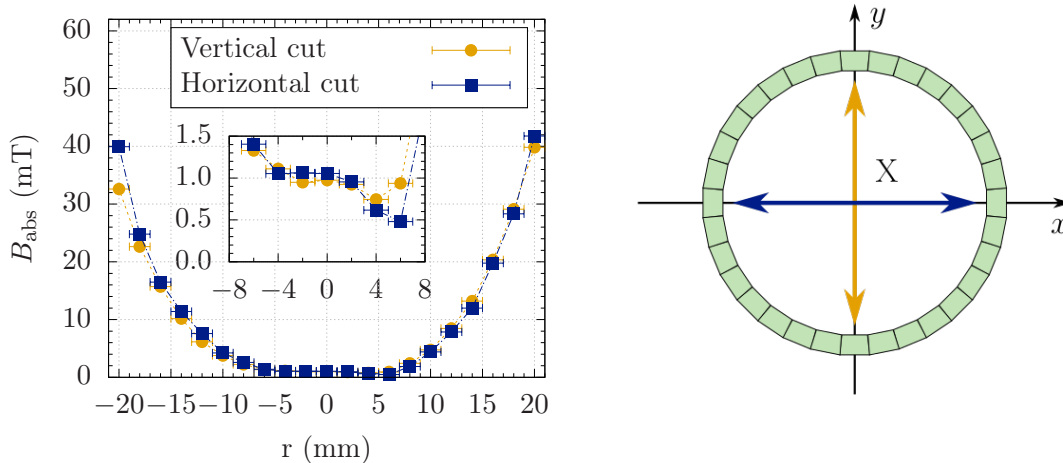


Figure A.6: Left: Measurement of the absolute magnetic field on a vertical (yellow) and horizontal line (blue) through octupole ring No. 1. The inset shows a detailed view around the geometric centre. Right: The measurement lines within the octupole ring. The cross marks the quadrant of the magnetic minimum.

the magnetic minimum and the geometric centre of the octupole rings. Therefore, before the final assembly of the compensation octupole, each ring was measured magnetically on a vertical (0°) and horizontal line (90°) through the geometric centre at $r = 0$ mm as seen from above (cf. Fig. A.6, right). The resulting absolute magnetic field on both lines is shown on the left side of Fig. A.6 for ring No. 1. The inset is a detailed view of the region around the geometric centre. The magnetic minimum is found both vertically and horizontally on the positive axis, which corresponds to the first quadrant in a coordinate system. The octupole rings were oriented relative to each other with their magnetic minima all in the same quadrant in order to avoid additional inhomogeneities of the resulting octupole field.

The total assembly of the compensation octupole finally proved to be challenging, because equal magnetic poles had to be pushed together (requiring force) and the rings were not to lose their orientation (requiring precision). Thus, an assembly aid was built, which is shown in Fig. A.7 (left). The rotation of the rings was prevented by rods being stuck through the supporting holes in each ring and through a slit in the assembly aid. Two metal plates at the top and bottom were connected by threaded rods. By slowly tightening the nuts at the top, the rings were pushed together carefully and the rods were removed as soon as the cutouts of the rings engaged. Finally, the holding cylinder was moved upwards and bolted with the top and bottom end ring. The bolts were additionally fixed with epoxy resin⁴. The finished octupole is shown on the right side of Fig. A.7.

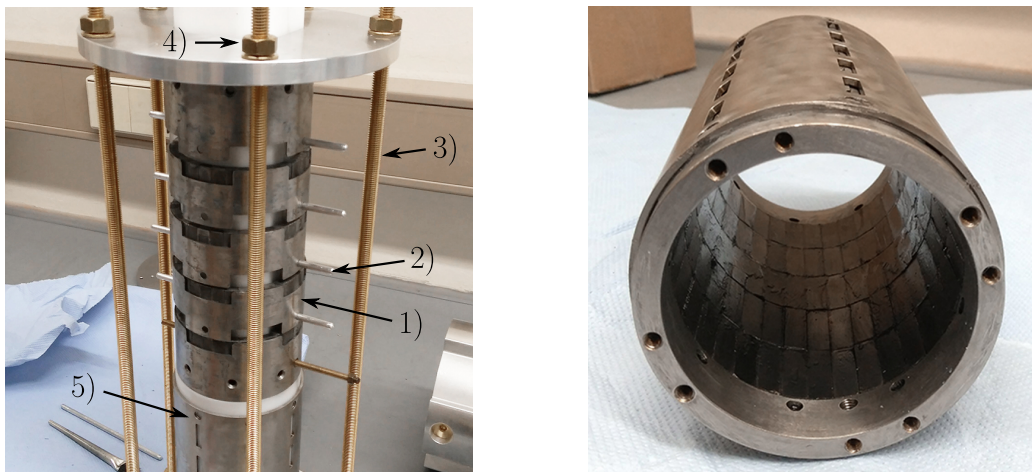


Figure A.7: Final steps of the octupole assembly. Left: Octupole rings (1) stacked on top of each other onto an assembly aid with rods (2) preventing them from rotation. Two metal plates, connected by threaded rods (3) pushed the rings together when the nuts at the top (4) were tightened. As soon as the cutouts of the rings engaged, the rods were removed. Finally, the holding cylinder (5) was pulled upwards and bolted with the end rings. Right: The finished compensation octupole.

⁴Stycast 2762 FT in combination with Catalyst No. 17

A.2.3 Allan deviation of the Hall probe

The magnetic field measurements during the construction and characterisation process of the compensation octupole (cf. Chs. A.2 and 3.2.2.1) were done using a calibrated 3-axis Hall probe. In order to avoid fluctuations, multiple data points were taken for each measurement and the average value was calculated afterwards. With an Allan deviation the temporal stability of a measurement system with respect to noise can be estimated, which in case of the Hall probe is useful in order to find the optimum number of data points n for each measurement⁵. If n is too small, internal fluctuations of the Hall probe increase the error of the average, whereas a large n includes slow drifts of the Hall probe. The optimum is found where the error of the average is minimum.

During the Allan deviation measurement, the Hall probe was fixed on a holder and a continuous measurement was done for 60 s. The probe controller features internal averaging modes over 2^m with $2 \leq m \leq 7$ single measurements for each data point. The Allan deviation was repeated for each of these modes and is shown in Fig. A.8. The calculation was done using the Python3 package *AllanTools*. The procedure is to cut the data of the total measurement time into segments of equal length, which is called the integration time τ (at 60 s, the resulting number of segments is $k = 60\text{ s}/\tau$). The data in each segment is averaged and finally, the standard deviation of all the segments is calculated. The integration time is then varied so that with increasing length, fluctuations cancel out more and more. As soon as the integration time is too large, sensor drifts become dominant.

⁵A detailed introduction into the Allan deviation can be found for example at <http://home.engineering.iastate.edu/shermanp/AERE432/lectures/Rate%20Gyros/Allan%20variance.pdf> (last visited on June 17, 2021).

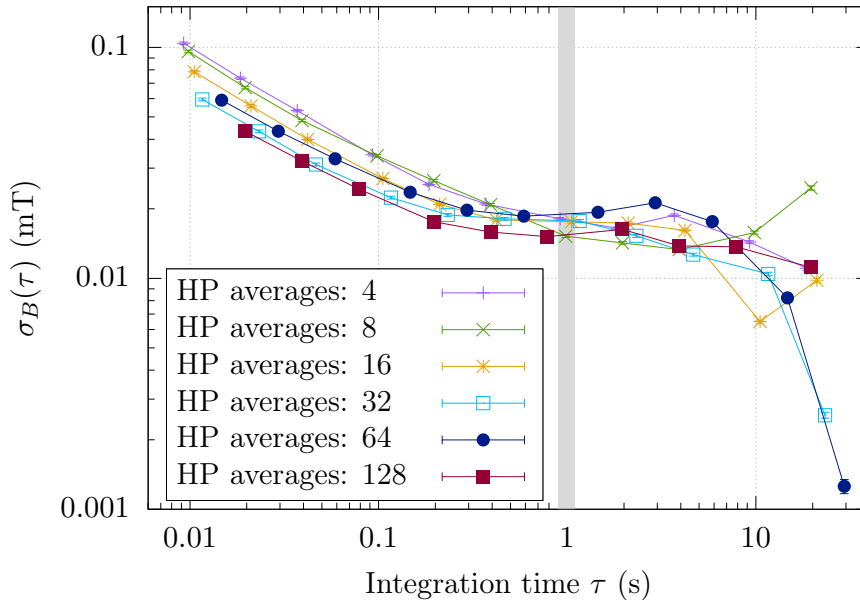


Figure A.8: Allan deviation of the Hall probe for the six internal averaging modes of the probe controller. The optimum at $\tau = 30$ s and 64 averages per data point requires a long measurement time, so that a compromise is found at $\tau = 1$ s with 128 averages.

From Fig. A.8 follows an optimum integration time of 30 s with an internal averaging mode of 64 measurements per data point. However, this would result in a long overall measurement time for the field maps (cf. Ch. 3.2.2.1), so that a compromise was found using $\tau = 1$ s and an averaging mode of 128 measurements per data point.

A.2.4 The orientation of the compensation octupole

The octupole symmetry and the rotational fixation of the compensation octupole by the translation stage show a 90° symmetry (cf. Fig. 3.9), allowing four different orientations of the compensation octupole with respect to the storage octupole. If both octupoles produced a uniform magnetic field without fluctuations, the orientation would not matter. As this is not the case, a combination was to be found, which resulted in the lowest remaining field.

Therefore, all four possible orientations were mounted one by one and a rough field map was measured at $r = 25$ mm: To save time, only every fourth adjustable angle was measured, so that the angle between different measurements was $\Delta\varphi = 22.5^\circ$ instead of the $\Delta\varphi = 5.63^\circ$ steps described in Ch. 3.2.2.1. This results in a total of 16 measurements for either orientation. At each position the absolute magnetic field was measured using the calibrated 3-axis Hall probe. The spring-mounted rolls at the front of the compensation octupole were replaced only in a later iteration (cf. Ch. 5.2.1) so that in the test measurement here the compensation octupole was still aligned at an axial offset by $\delta y = -2.6$ mm (cf. Ch. A.5.1.2).

Fig. A.9 (left) shows the measurement results at all angles depending on the longitudinal

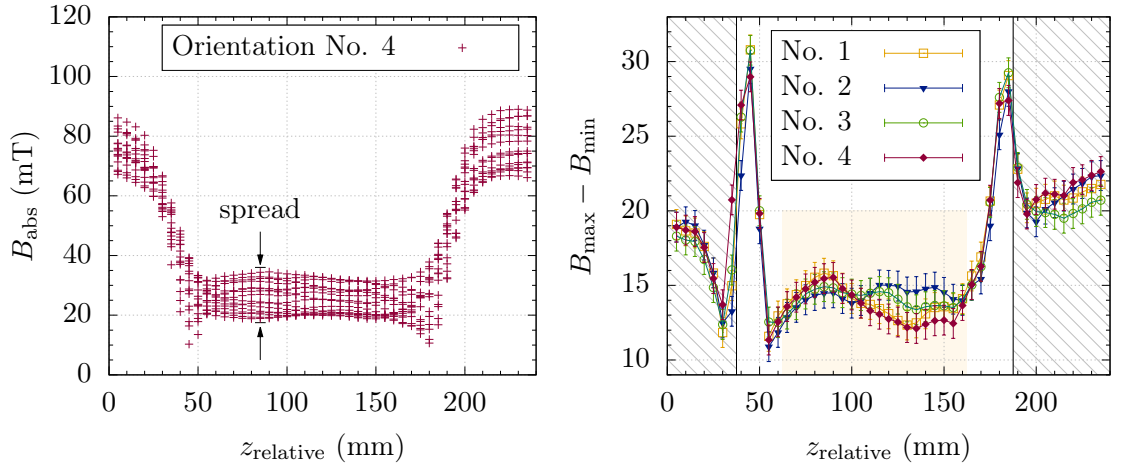


Figure A.9: Orientation optimisation of the compensation octupole. Left: The absolute magnetic field of all measurements along z and in steps of $\Delta\varphi = 22.5^\circ$ at $r = 25$ mm for orientation No. 4. The difference between maximum and minimum field at each z -position is called the spread B_{spread} . Right: The spread at each z -position for all four orientations. Grey shaded: Range outside of the compensation octupole; yellow shaded: Spin flip region within the compensation octupole. The lowest mean spread in this region was found with orientation No. 4.

position exemplary for orientation No. 4. The errors⁶ are not shown here for visibility reasons. The measurements start in front of the compensation octupole and end behind it, therefore the remaining storage octupole field of around $B_{\text{abs}} \approx 80 \text{ mT}$ is visible on the left and right side of the plot. The low field region in the middle corresponds to the compensated field. A measurement on a circle with fixed radius and z -position with two perfectly aligned ideal octupoles should result in the same absolute field amplitude at all measurement angles. Using real octupoles, the amplitude differs with the angle between a maximum and a minimum value; this is even more the case considering the axial misalignment of our two octupoles⁷. The difference between the maximum and minimum field on a given circle is here called the 'spread', $B_{\text{spread}} = B_{\text{abs}}^{\text{max}} - B_{\text{abs}}^{\text{min}}$, and is used to find the optimum orientation of the compensation octupole. B_{spread} was calculated at all measured z -positions of each orientation and is shown on the right side of Fig. A.9. The error is calculated as $\Delta B_{\text{abs}}^{\text{max}} + \Delta B_{\text{abs}}^{\text{min}}$. The lower the spread, the more homogeneous is the magnetic field on the circle at the respective z -position.

The first thing that stands out is the two spikes in the spread at around $z_{\text{relative}} = 45 \text{ mm}$ and 180 mm : These might be caused by a combination of large gradients in the transition region between compensated and uncompensated field and small position errors, which suggest a comparably large spread. Additionally, we find that the spread of the uncompensated field ($z_{\text{relative}} \lesssim 20 \text{ mm}$ and $z_{\text{relative}} \gtrsim 200 \text{ mm}$) is larger than that of the compensated field. In Ch. 3.2.2.1 it was suspected, that the rotation axis of the measurement setup and the axis of the storage octupole were not fully aligned but offset by $\delta y \simeq +0.8 \text{ mm}$, which lead to a weaker field measured at the bottom of the storage octupole than at the top. Such an offset would suggest a spread as well, which is more prominent in the uncompensated field ($B \sim r^3$) than in the compensated field ($B \sim r^2$ due to the hexapole structure of the field resulting from the axial misalignment). This makes a quantification of the optimum orientation of the compensation octupole difficult.

However, as in the compensated field region no orientation stands out as an optimum directly, we can assume that on the whole all orientations are more or less comparable. For the sake of completeness the mean spread was calculated in the spin flip region for all orientations, the lowest result was found with orientation No. 4, which was thus declared as optimum and used as final setup in τ SPECT.

A.3 The spin flipper

A.3.1 The signal phase shift $\Delta\varphi$ for the birdcage resonator

The birdcage resonator was operated in quadrature excitation. Therefore, the signal was split after the amplifier and one of the signals was shifted by 90° by inserting a cable of additional length $\Delta l = 5.1 \text{ m}$ in order to increase the delay line of the signal (cf. Ch. 3.3.2.1). The phase between the shifted and the unshifted signal was afterwards measured using a sine wave of amplitude $U_0 = 2.5 \text{ V}$ and $f = 10.26 \text{ MHz}$. The resulting signal is shown in Fig. A.10 resulting in a phase between the shifted and the unshifted signal of $\Delta\varphi = 90.25^\circ$. However, the shifted signal is reduced in amplitude by around 0.09 V , corresponding to

⁶The errors are $\Delta z = 2 \text{ mm}$ and ΔB_{abs} , calculated from Gaussian error propagation with $\Delta B = 0.5 \text{ mT}$ in each field component (cf. Ch. 3.2.2.1).

⁷The centring of the compensation octupole by the installation of rigid axles of the rolls (cf. Ch. 5.2.1) reduce this problem to a negligible level.

$\sim 3.6\%$. This might be caused by damping effects in the longer cable. In combination with the small deviation from 90° in the phase shift, the generated B_1 field inside the spin flipper was expected to be slightly elliptical.

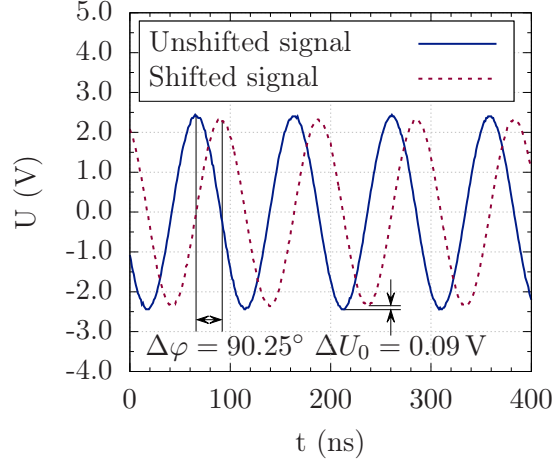


Figure A.10: Phase shift realised for the birdcage resonator. The two outputs of a frequency generator at $U_0 = 2.5\text{ V}$ and $f = 10.26\text{ MHz}$ were monitored on an oscilloscope. The additional cable of length $l = 5.1\text{ m}$ creates a phase shift of $\Delta\varphi = 90.25^\circ$ in the shifted signal (red dashed line) with respect to the unshifted one (blue solid line). The amplitude of the shifted signal is reduced by 3.6% .

A.3.2 Calibration of the pick-up coil for magnetic field measurements

The magnetic field measurement of the birdcage resonator requires a pick-up coil calibrated with a well-known field. The induced voltage in the pick-up coil is deduced beginning with Maxwell-Faraday's induction law and integrating the electric field over the cross sectional area A of the coil. The induced voltage then follows from

$$\vec{\nabla} \times \vec{E} = -\frac{\partial \vec{B}}{\partial t} \quad (\text{A.1})$$

$$U_{ind} = \oint_{\partial A} \vec{E} \cdot d\vec{s} = \int_A -\frac{\partial \vec{B}}{\partial t} \cdot d\vec{A} \quad (\text{A.2})$$

$$-\int U_{ind} dt = \vec{B} \cdot \int_A d\vec{A} = \vec{B} \cdot \vec{A} = B \cdot A_{coil} \cdot \cos(\alpha) \cdot n. \quad (\text{A.3})$$

Here, n is the number of coil windings and α is the angle between the magnetic field vector and the normal vector of the pick-up coil cross section. Assuming $\cos(\alpha) = 1$ and an oscillation frequency ω of the field, solving for the magnetic field B with $U_{ind} = U_0 \cdot \sin(\omega t)$ yields

$$B = -\frac{1}{n \cdot A_{coil}} \cdot \int U_0 \cdot \sin(\omega t) dt, \quad (\text{A.4})$$

which after integration over a half oscillation results in the average magnetic field

$$B = \frac{2 \cdot U_0}{n \cdot A_{\text{coil}} \cdot \omega}. \quad (\text{A.5})$$

With this equation, the magnetic field is calculated by measuring the amplitude of the induced voltage U_0 in the pick-up coil.

The reference field for the calibration is generated by a solenoid with N windings and length l . With a current I flowing through the coil, the resulting magnetic field is given by Ampère's law

$$\oint_s \vec{B} d\vec{s} = \mu_0 \cdot I. \quad (\text{A.6})$$

Considering the cylindrical shape of the solenoid, the calculation of B simplifies to

$$B = \mu_0 \cdot \frac{I \cdot N}{l}. \quad (\text{A.7})$$

Knowing N and the length of the coil, the reference field is deduced from the measurement of the current.

The calibration setup is shown in Fig. A.11 (left). The solenoid⁸ was connected to a frequency generator and produced a vertical, time-varying magnetic field with a frequency

⁸The solenoid was kindly provided by Karl-Heinz Lenk from the electronics workshop at the Institute of Physics.

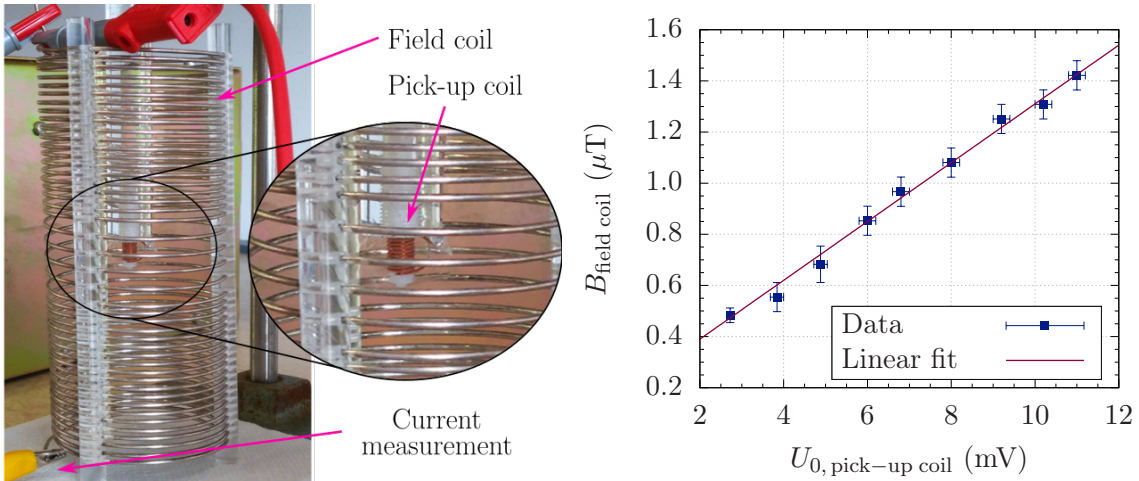


Figure A.11: Calibration of a pick-up coil for the measurement of the magnetic field inside the spin flipper. Left: Calibration setup with the solenoid producing the reference field, and the pick-up coil. The magnetic field is produced by a frequency generator signal connected at the top and bottom of the solenoid. The current required for Eq. A.7 is measured at the marked position. Right: The calculated reference field plotted against the measured pick-up coil voltage (blue squares). The calibration results from the fit function in Eq. A.8, taking into account the pick-up coil parameters and the oscillation frequency.

$f = 10.26$ MHz. It was designed with denser windings at the top and bottom to homogenise the field in the centre. The pick-up coil was positioned upright in the centre in order to fulfill the condition $\cos(\alpha) \approx 1$. The current in the solenoid was measured using a current probe⁹, the induced voltage at the pick-up coil was monitored with an oscilloscope. The results are shown on the right side of Fig. A.11. A fit of the shape

$$B = a \cdot \frac{2 \cdot U_0}{n \cdot A_{\text{coil}} \cdot 2\pi f} + b \quad (\text{A.8})$$

provides the calibration with the fit parameters $a = 1.18(3) \text{ Tm}^2\text{HzV}^{-1}$ and $b = 1.60(19) \times 10^{-7} \text{ T}$, as well as the pick-up coil parameters $n = 10$ and $A_{\text{coil}} = 1.59(14) \cdot 10^{-5} \text{ m}^2$, and $f = 10.26$ MHz.

A.3.3 The theoretical field shape of birdcage and saddle coil

In τ SPECT, two different types of spin flipper have been investigated so far: A birdcage resonator (cf. Ch. 3.3.1) and a double saddle coil (cf. Ch. 5.1). The magnetic fields of both spin flippers were simulated using COMSOL Multiphysics[®], the results are shown in Fig. A.12 (as the two saddle coils generate their fields independently, only one saddle coil was simulated). In both cases the current was scaled up to result in a field at the centre of $B_1 \simeq 0.5 \text{ mT}$, the yellow circles mark the inner diameter of the narrowed neutron guide (cf. Ch. 3.1.2).

It is visible already by eye, that the birdcage resonator generates a more homogeneous field than the saddle coil, nevertheless, as quantification we can use e.g. the non-uniformity criterion in [SVM06]: This criterion calculates the root mean square deviation σ relative to the magnetic field at the centre B_c

$$NU = \frac{\sigma}{B_c} \cdot 100 \quad (\text{A.9})$$

⁹Fluke & Philips PM9355.

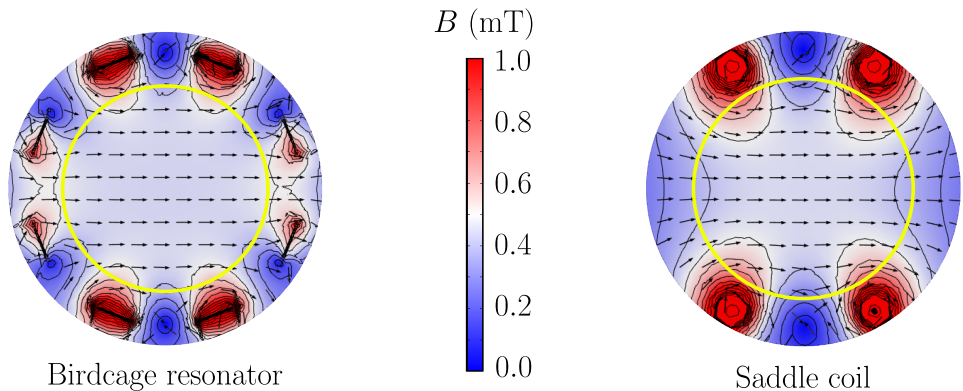


Figure A.12: Magnetic field of a birdcage resonator (left) and a saddle coil (right) from a FEM simulation with COMSOL Multiphysics[®]. The current was adjusted, so that $B_1 \simeq 0.5 \text{ mT}$ in the field centre. The yellow circles correspond to the inner diameter of the neutron guide. The arrows show the direction of the magnetic field at a fixed point of time, the black lines are equipotential lines between 0.1 and 1.5 mT in steps of 0.1 mT.

and results in $NU = 2.1\%$ for the birdcage resonator. In comparison, the saddle coil generates a visibly more inhomogeneous field, especially in the region between the left and right wires. These regions are, however, outside of the neutron guide - within the region accessible by neutrons the non-uniformity still reaches $NU = 5.4\%$. With the saddle coil being the simplest approximation of a cosine-theta coil (zeroth order), a higher field homogeneity could be achieved by building a more complex coil of higher order.

With τ SPECT, saturation of the trap was reached with both spin flippers (cf. Chs. 3.6.3 and 5.1.1.2), which leads to the conclusion, that - despite the lower homogeneity of the saddle coils - both spin flippers were maximally efficient.

A.4 The neutron detector

A.4.1 Neutron event recognition

The detector ADC sends the digitised analog signal to a PC at a transmission rate of 10 MHz, which results in large data files of several gigabyte for each measurement (cf. Ch. 3.4). In order to speed up later analyses concerning the counting of neutron and background events, an intermediate step is necessary, which detects events in the raw data and generates a reduced data file. Any peak in the raw data is called an 'event', only after its identification, it is decided, whether the peak is likely caused by the neutron capture reaction ('neutron event') or something else ('background event').

A.4.1.1 The single-cut threshold

A first attempt for an event recognition was done by averaging the analog signal in the first 100 ms of the measurement, resulting in a mean ADC voltage \bar{U}_{ADC} and the corresponding standard deviation σ_{ADC} . This time window is free of neutrons, since due to the delayed pulse trigger (cf. Ch. 3.5), neutrons are produced only at $t_0 \simeq 1.5\text{s}$ in the detector data. A threshold of $\bar{U}_{\text{ADC}} + 7\sigma_{\text{ADC}}$ was defined and every time the signal exceeded this threshold longer than a predefined time-over-threshold, an event was identified. However, this method contains two problems:

1. As shown in Fig. A.13 (left), 50 Hz noise, which was present in beamtime *Sept2019*, resulted in a comparably high threshold so that smaller signals were lost regardless whether they were neutron events or not.
2. A fixed threshold is not sensitive to slow fluctuations of the average detector voltage, so that event loss can occur for long time periods, if the ADC signal is permanently above or below the threshold (cf. Fig. 6.12 in [Kah20]).

Therefore a new peakfinding algorithm was developed using a dynamic threshold and a more complex identification of neutron events.

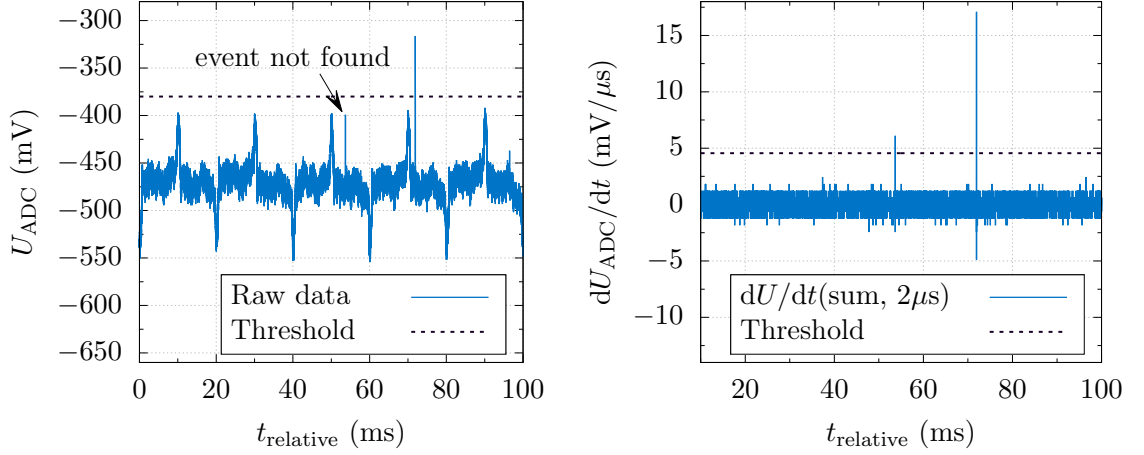


Figure A.13: Influence of single-cut and dynamic threshold on neutron event recognition. Left: Detector raw data with 50 Hz noise (blue) and single-cut threshold at $\bar{U}_{\text{ADC}} + 7\sigma_{\text{ADC}}$ (black dashed line). In case of small events or slow baseline drifts, events may be lost. Right: The same raw data after pre-processing by calculating the signal sum in $2\ \mu\text{s}$ and the time derivative. Events appear as sharp signals (note the time scale of the x -axis in ms), while slow noise and drifts average out. The threshold in this frame is set to $4.6\ \text{mV}/\mu\text{s}$.

A.4.1.2 Neutron identification using a dynamic threshold

Setting the dynamic threshold requires a pre-processing of the raw data, which is shown in Fig. A.14 using a 'zoom' into a single event: The top (a) represents the raw data of a typical event at 100 ns binning with a sharp rising edge and a signal decay of about $20\ \mu\text{s}$. The voltage is calculated from ADC units. The signal is summed in $2\ \mu\text{s}$ intervals (b) to smoothen the data¹⁰. Afterwards, the first time derivative of the summed signal is calculated (c), resulting in a baseline around zero and a sharp peak caused by the rising edge of the event. This peak is used for the dynamic threshold, because it is independent of the ADC baseline voltage and slow noise and drifts are averaged out.

The impact becomes clearly visible in comparison with the single-cut threshold in Fig. A.13: The raw data including the 50 Hz noise on the left is pre-processed as described and shown on the right. The single-cut threshold applied to the raw data would recognise only one of the two events in this time interval, whereas the threshold set in the pre-processed data allows for both events being detected.

In order to distinguish neutron events from electronic noise, dark counts in the MPPC or background radiation, further properties of the specific event are analysed as shown in Fig. A.15. A temporary threshold U_{thr} is set in the raw data as reference. Afterwards, the event is analysed for its peak height U_{max} , the peak rise time Δt_{rise} between U_{thr} and U_{max} , the peak fall time Δt_{fall} between U_{max} and the time when the signal drops below the threshold again, the total event length $\Delta t_{\text{event}} = \Delta t_{\text{rise}} + \Delta t_{\text{fall}}$, as well as the time-normalised integral voltage U_{integral} of the event¹¹.

¹⁰This process is similar to a running average, only that the division by the time interval is omitted in order to avoid floating point numbers.

¹¹The integral is calculated as $U_{\text{integral}} = \frac{1}{\Delta t} \int U_{\text{ADC}} dt$.

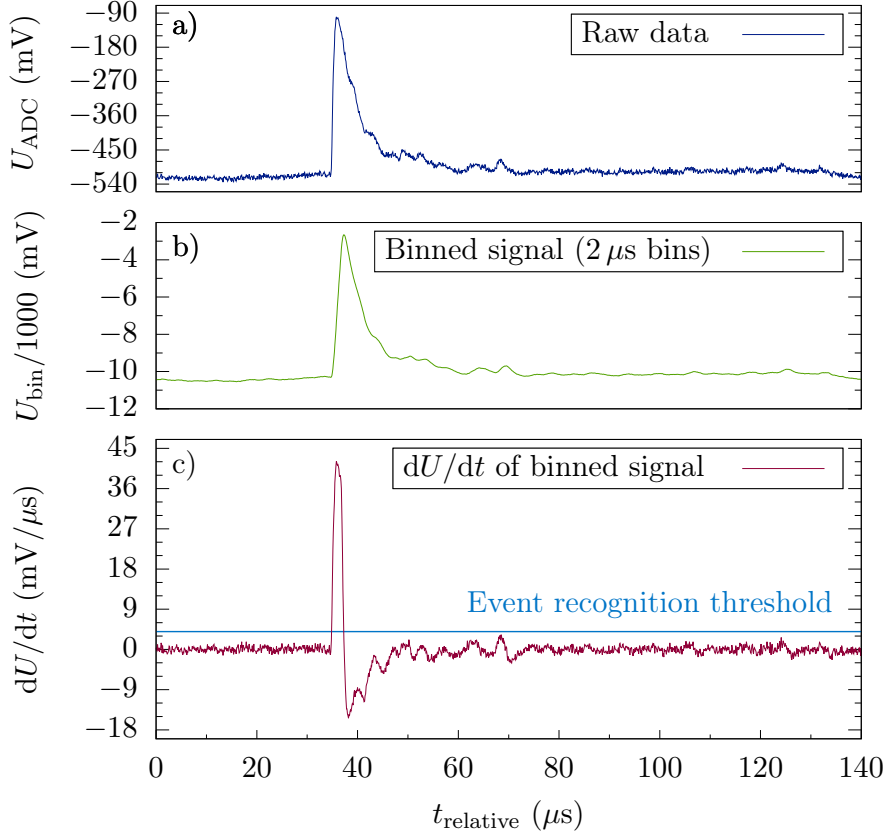


Figure A.14: Signal processing for neutron event recognition. a) The raw data of a typical single event, the voltage is calculated from ADC channels. b) The signal is summed in intervals of $2 \mu\text{s}$ to smoothen small fluctuations $< 2 \mu\text{s}$. c) The first time derivative of the signal sum (red curve) and the dynamic threshold set to $1.1 \text{ mV}/\mu\text{s}$ (blue line).

The properties of events occurring in two 50 s storage measurements - one with and one without neutrons¹² - are compared in order to separate neutron events from background events. An example is shown on the left side in Fig. A.16: For each event, its total length Δt_{event} is plotted depending on its occurrence time relative to the thermal peak (cf. Ch. 3.5). The analysis window here is restricted to the range around the counting interval (cf. Ch. 3.6.2), which in the plot starts at¹³ $t \approx 60 \text{ s}$. Only the measurement with neutrons shows a bunch of data points with $\Delta t_{\text{event}} \gtrsim 5 \mu\text{s}$ within the counting interval. Therefore, a cut is applied at $\Delta t_{\text{event}} = 3 \mu\text{s}$ and all events below this cut are ignored.

This procedure was repeated for different parameters and parameter combinations, such as for example $U_{\text{integral}}/U_{\text{max}}$. As soon as no further cut options could be recognised and changing the cut order lead to no different results, the peakfinding algorithm was finished. In the final version, events must satisfy the following conditions to be identified as neutron

¹²The measurement without neutrons is termed a 'dry run' and was done between two reactor pulses.

¹³This time calculates as the sum of the duration until filling of the trap is finished ($t_{\text{fill}} = 2.0 \text{ s} + \Delta t_{\text{fill}} = 4.0 \text{ s}$), the storage time $t_s = 50 \text{ s}$ and the time until the detector has moved from its storage position to the edge of the trap ($t \approx 4 \text{ s}$), where counting of neutrons begins.

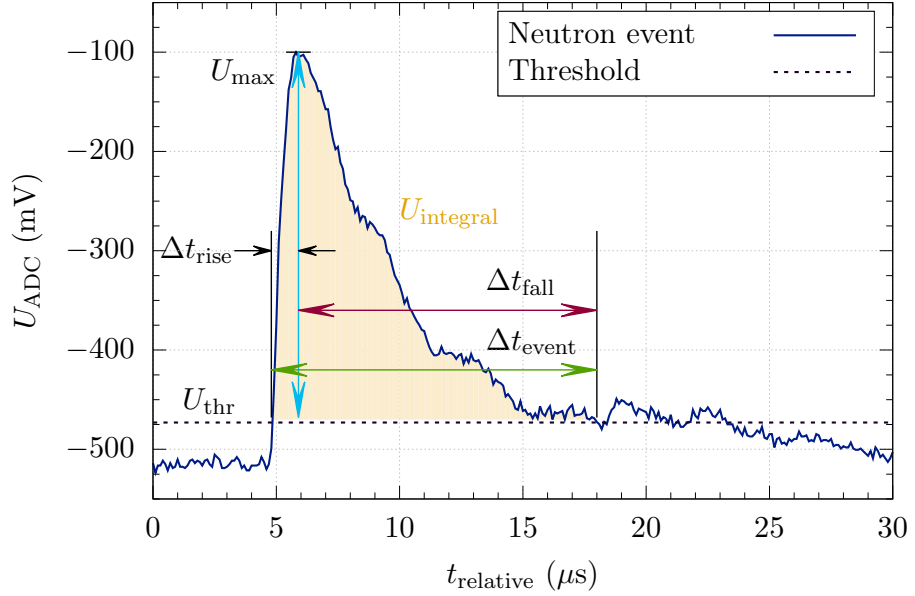


Figure A.15: Event properties used for the peakfinding algorithm. The blue curve shows a typical neutron event, the black dashed line marks the temporary threshold U_{thr} . The event parameters used for the analysis are the maximum voltage U_{max} , the rise time Δt_{rise} between U_{thr} and U_{max} , the fall time Δt_{fall} between U_{max} and the time when the signal falls below threshold again, the total event length $\Delta t_{\text{event}} = \Delta t_{\text{rise}} + \Delta t_{\text{fall}}$, and the integral voltage U_{integral} .

events:

$$\begin{aligned}
 \Delta t_{\text{event}} &\geq 3 \mu\text{s} \\
 \frac{U_{\text{integral}}}{U_{\text{max}}} &\geq 22 \\
 \frac{U_{\text{max}}}{\Delta t_{\text{fall}}} &\geq 3 \text{ mV}/\mu\text{s}
 \end{aligned} \tag{A.10}$$

Analysing the same 50 s storage measurements as before with this algorithm results in the spectra shown in Fig. A.16 on the right. The increased count rate around 60 s corresponds to the neutrons in the counting interval, the background level both with and without neutrons is ~ 1.1 Hz.

A.4.2 Optimisation of the detector overvoltage

The operation voltage of the detector is adjusted by an internal circuit of the signal shaper box, which converts the analog detector signals into a shape understood by the ADC (cf. Ch. 3.4). With the temperature dependent nominal breakdown voltage V_{bd} as the minimum setting, the overvoltage V_{over} is to be raised manually.

In order to find the optimum operating range, 50 s storage measurements were done with τ SPECT¹⁴. The number of stored neutrons N with normalisation to the pulse energy

¹⁴The measurements were done using the birdcage resonator as spin flipper at $z_{\text{SF}} = 879$ mm and

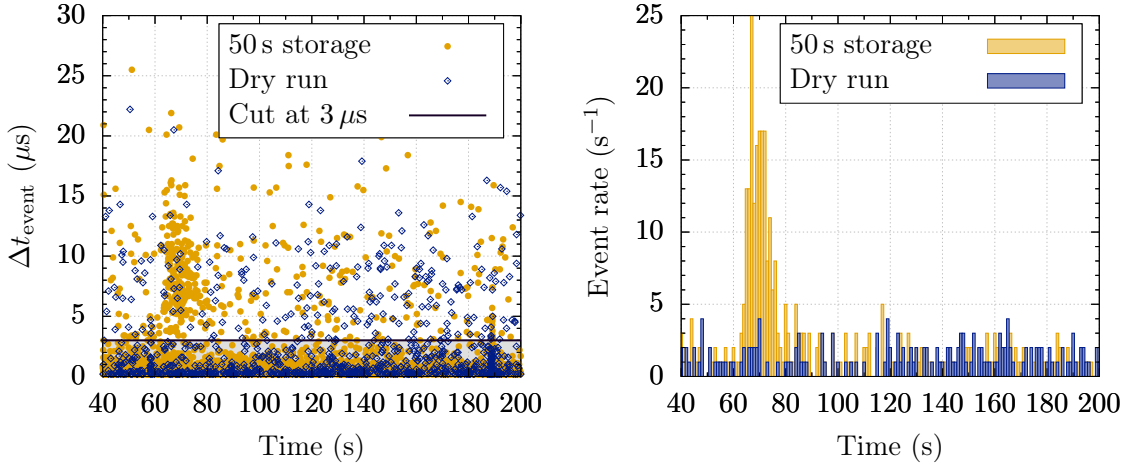


Figure A.16: Neutron recognition process. Left: Length Δt_{event} of signal events measured with (\bullet) and without neutrons (\diamond) after a predefined storage time of 50 s, the x -axis corresponds to the time after the thermal peak. The bunch in the yellow data at around 60 s with $\Delta t_{\text{event}} \gtrsim 5 \mu\text{s}$ is identified as neutron events, the offset of ~ 10 s with respect to the storage time accounting for the duration of the filling process and the time until the detector is moved into the trap. A cut at $\Delta t_{\text{event}} = 3 \mu\text{s}$ (black line) ignores all events shorter than this value. Right: The same measurements analysed with the finished peakfinding algorithm (cf. Eq. A.10), the binning is in 1 s intervals. The high count rate in the measurement with neutrons corresponds to neutron events. The background level in both measurements is ~ 1.1 Hz.

and the background count rate R_{bg} were analysed depending on V_{over} , the result is shown in Fig. A.17 (left). It shows, that a plateau is reached between $V_{\text{over}} = +3.0$ V and $+5.0$ V, lower voltages lead to a reduced detection efficiency, whereas at higher voltages the background increases.

The right side of Fig. A.17 shows the raw data in the first 40 ms of measurements at different overvoltages. As data recording is started before the pulse is executed (the thermal peak in the detector data occurs only at $t_0 \simeq 1.5$ s, cf. Ch. 3.5) this interval does not yet contain neutron events. While the measurements at $V_{\text{over}} = +1.0$ V and $+3.5$ V exhibit a comparable noise level, we find the noise at $V_{\text{over}} = +5.0$ V significantly increased already. The optimum operating range is thus restricted further to $V_{\text{over}} = +3.0$ V to $+4.5$ V.

If not mentioned otherwise, all measurements in this work were done at $V_{\text{over}} = +3.5$ V. Here, the background is at roughly $R_{\text{bg}} \simeq 1.2(2)$ Hz. Even though the interval from which the neutron counts N are inferred is much longer, the largest fraction of neutrons is counted within ~ 20 s, resulting in an average neutron count rate¹⁵ $R_N \simeq 200/20 \text{ s} = 10$ Hz.

¹⁵ $P = 230$ W

¹⁵For statistical reasons, the background count rate and the neutron counts were averaged over the plateau between $V_{\text{over}} = +3.0$ V and $+4.5$ V. The result for the neutron counts $N = 197(18)$ is rounded to $N = 200$ as we are only interested in a rough estimation.

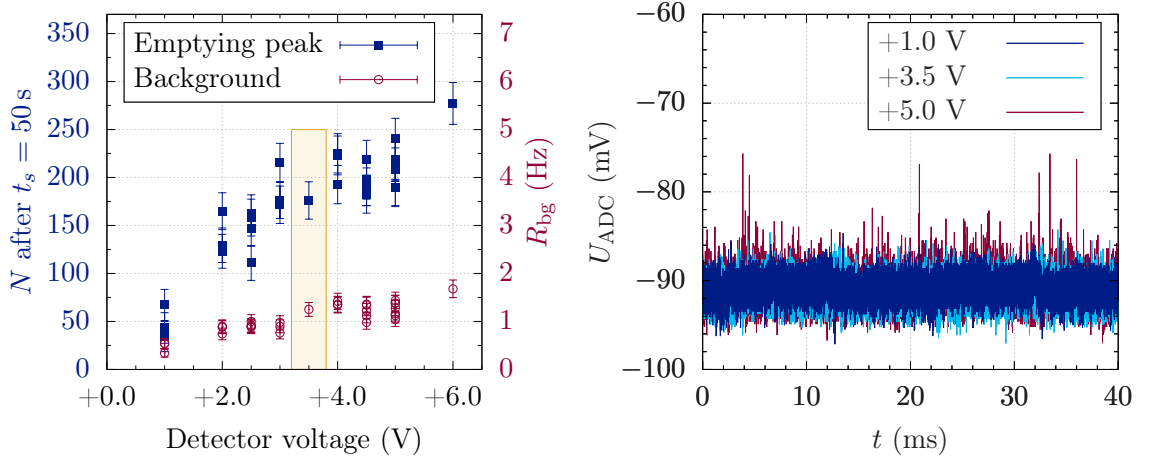


Figure A.17: Optimisation of the detector overvoltage. Left: Neutron counts N after $t_s = 50$ s (blue squares, left axis) and average background count rate R_{bg} (red hollow circles, right axis) measured with $P = 230$ W RF power at $z_{\text{SF}} = 879$ mm using the birdcage resonator as spin flipper. The optimum operating range is found between $V_{\text{over}} = +3.0$ V and 4.5 V, the typical setting in this work is $V_{\text{over}} = +3.5$ V (yellow box). Right: Detector raw data at different overvoltages in the first 40 ms of measurements, i.e. before the pulse was triggered. The noise level at $V_{\text{over}} = +5.0$ V (red) is significantly higher than at $V_{\text{over}} = +3.5$ V (light blue) and +1.0 V (dark blue), so that overvoltages above $V_{\text{over}} \geq 5.0$ V are to be avoided.

A.5 Spin tracking using Monte Carlo simulations

It was discussed in Ch. 4.1.1, that numeric solutions of the Bloch equations are necessary for an estimation of the spin flip efficiency, especially if forces such as gravity and the Stern-Gerlach force are to be taken into account. Therefore, a Monte Carlo simulation is used, in which neutrons fly through the magnetic fields in τ SPECT while their spin movement is tracked. Furthermore, if the simulation extends over the entire region of the first high field peak of B_0 , estimations with respect to the double spin flip technique can be made. In order to simplify the simulation, however, analytic approximations of all magnetic fields was to be found in advance.

A.5.1 Analytic approximation of the magnetic fields in τ SPECT

The magnetic fields in τ SPECT can be divided into static fields, of which some are scalable in magnitude, and dynamic fields. The static B_0 field is scaled by the current running through the field generating coils, whereas the fields of both storage and compensation octupole are fixed. Here, the only free parameters are the position of the compensation octupole in longitudinal direction as well as the rotational and axial offsets $\delta\varphi$ and δy between the two octupoles. The magnetic fields of the two spin flippers SF1 and SF2 (cf. Ch. 6) are dynamic due to their oscillation in the xy -plane with time. They are scalable in the B_1 amplitude, which includes that they can be switched off by setting $B_1 = 0$ mT. Furthermore, their frequencies and polarisations can be adjusted.

Altogether, the simulation is to contain all free parameters, which are available in τ SPECT. In summary these parameters are: The current in the main and the gradient coils I_{main} , I_{C3} and I_{C5} , the B_1 amplitude of both spin flippers, their frequencies f_{SF} and phases $\Delta\varphi$, as well as the spin flip position z_{SF2} , which implies the position of SF1 due to the fixed distance of $\Delta z = 930$ mm.

A.5.1.1 The model for the B_0 -field

The B_0 field is a superposition of a main field $B_{\text{main}}(z)$ and the fields of the two gradient coils $B_{C3}(z)$ and $B_{C5}(z)$ in anti-Helmholtz configuration. As their name suggests, the gradient coils generate the gradient in the high field region required for SF1 (cf. Ch. 6.2.1). The field shapes are found partially experimentally and partially by fits to the simulation data of B_0 from the former a SPECT experiment [Sch20]. They are given in Eqs. A.11 to A.13 with their parameters summarised in Tabs. A.1 and A.2.

$$\begin{aligned}
B_{\text{main}}(z) = & a_1 \left(\frac{2}{\pi} \arctan \left(\exp \left[\frac{\pi a_2}{2} (z + a_3) \right] \right) \right) \\
& - b_1 \left(\frac{2}{\pi} \arctan \left(\exp \left[\frac{\pi b_2}{2} (z + b_3) \right] \right) \right) \\
& - c_1 \left(\frac{2}{\pi} \arctan \left(\exp \left[\frac{\pi c_2}{2} (z + c_3) \right] \right) \right) \\
& + \left[d_1 \left(\frac{2}{\pi} \arctan \left(\exp \left[\frac{\pi d_2}{2} (z + d_3) \right] \right) \right) \right. \\
& \left. - e_1 \left(\frac{2}{\pi} \arctan \left(\exp \left[\frac{\pi e_2}{2} (z + e_3) \right] \right) \right) \right] \\
& \times \left[1 - \left(\frac{2}{\pi} \arctan \left(\exp \left[\frac{\pi}{2} f_2 (z + f_3) \right] \right) \right) \right] \\
& + \frac{g_1 g_2^2}{g_2^2 + (z - g_3)^2} + \frac{2h_1 h_2}{h_2^2 + (z - h_3)^2}
\end{aligned} \tag{A.11}$$

$$B_{C3}(z) = a_{C3,1} \times \exp \left(-\frac{(z + a_{C3,3})^2}{a_{C3,2}} \right) + \frac{b_{C3,1}}{\cosh(b_{C3,2}(z + b_{C3,3}))} \tag{A.12}$$

$$B_{C5}(z) = a_{C5,1} \times \exp \left(-\frac{(z - a_{C5,3})^2}{a_{C5,2}} \right) + \frac{b_{C5,1}}{\cosh(b_{C5,2}(z - b_{C5,3}))} \tag{A.13}$$

Table A.1: Parameters for the longitudinal shape of the B_{main} field according to the function given in Eq. A.11. For simplicity, the parameter units are omitted here.

Index i	a	b	c	d	e	f	g	h
1	0.031	0.0031	0.022	0.0473	0.0397		$-5.28e - 4$	$2.061e - 5$
2	20	17	8.5	4.7999	17.315	70	0.07409	0.0583
3	0.27	-0.23	-0.78	0.3275	0.271	0.19	0.9549	0.8098

Table A.2: Parameters for the longitudinal shape of the B_{C3} and B_{C5} field according to the function given in Eqs. A.12 and A.13. For simplicity parameter units are omitted here.

Index i	a_{C3}	b_{C3}	a_{C5}	b_{C5}
1	1.252e - 5	2.617e - 4	1.348e - 5	2.819e - 4
2	0.2405	13.3617	0.2406	13.3616
3	0.1185	0.1185	0.1185	0.1185

Including the scaling currents I_{main} , I_{C3} and I_{C5} , the total B_0 field results in the superposition

$$\vec{B}_0(z) = [I_{\text{main}}B_{\text{main}}(z) + I_{C3}B_{C3}(z) + I_{C5}B_{C5}(z)] \hat{z}. \quad (\text{A.14})$$

A.5.1.2 The model for the transversal field B_t

The transversal magnetic field is produced by the superposition of storage and compensation octupole, where the compensation octupole is located in the region around the second spin flipper SF2 (centre position at z_{SF2}). Both are separately modelled in xy -direction using the octupole shape¹⁶

$$\vec{B}_{\text{oct}}(x, y) = \begin{pmatrix} B_{\text{oct},x} \\ B_{\text{oct},y} \end{pmatrix} = a_{\text{oct}} \begin{pmatrix} 3yx^2 - y^3 \\ x^3 - 3xy^2 \end{pmatrix}. \quad (\text{A.15})$$

As the fields of both octupoles do not reach over the entire region of the simulation, they have to be restricted to a certain longitudinal range. One way to do this would be multiplying the $\vec{B}_{\text{oct}}(x, y)$ amplitude with a step function, which sets the field to zero outside the defined region. This is shown on the left side of Fig. A.18 in comparison to a measurement of the storage octupole field by J. Haack [Haa16] at the azimuth angle $\phi = 275.4^\circ$, which was scaled down to the radius of the unnarrowed neutron guide $r = 36.5$ mm (cf. Ch. 3.1.2). However, as this is non-physical, rather a smooth transition between the full amplitude of $\vec{B}_{\text{oct}}(x, y)$ and zero field outside of the defined region is required. Therefore $\vec{B}_{\text{oct}}(x, y)$ is multiplied by a 'shaping' function of the form

$$B_{\text{shape},z}(z) = \frac{2}{\pi} \arctan \left(\exp \left[\frac{s\pi}{2} (z - z') \right] \right), \quad (\text{A.16})$$

which was found experimentally and is based on the cumulative distribution function of a normal distribution. The resulting transition is shown on the right side of Fig. A.18. The parameter s adjusts the smoothness and z' the position of half maximum amplitude.

Now we have to find the coefficients a_{oct} of the two octupoles. We take advantage of the fact, that one of the magnetic pole pairs of the field in Eq. A.15 is aligned with the y -axis. With $x = 0$ then follows $y = |\vec{r}|$ and

$$B_{\text{oct},x} = |\vec{B}_{\text{oct}}| = a_{\text{oct}} r^3. \quad (\text{A.17})$$

¹⁶The z -component of the fields is neglected, because even at the edge of the compensation octupole, it is still a factor of $B_0/B_z \approx 200 \text{ mT}/20 \text{ mT} = 10$ smaller than the B_0 field inside the storage volume (cf. Fig. B.2).

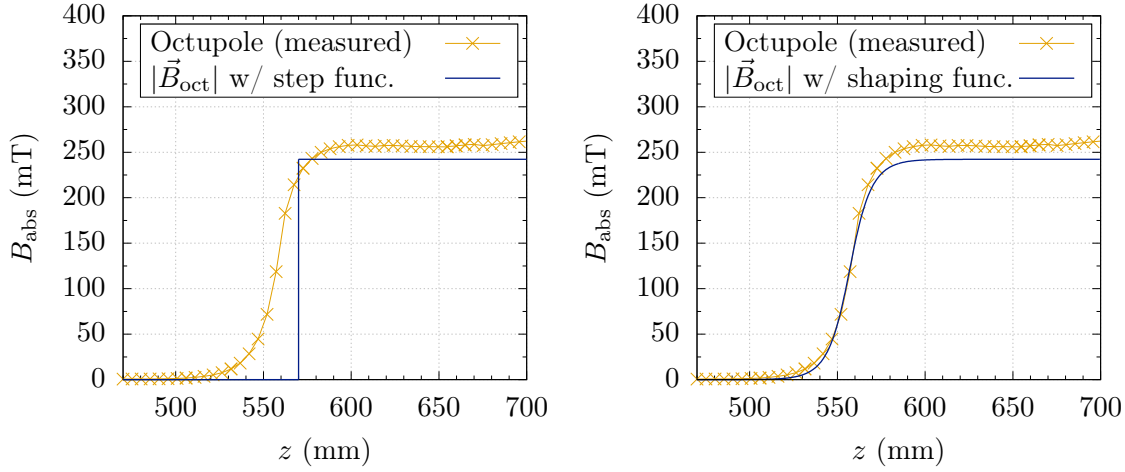


Figure A.18: Octupole field measurement and field approximation in longitudinal direction using a step function (left) and a smooth transition function (right). The field was measured at the azimuth angle $\phi = 275.4^\circ$ (yellow markers, the angle was randomly chosen from the data set) and scaled down to $r = 36.5$ mm. The field approximation yields $|\vec{B}_{\text{oct}}^{\text{SO}}(r = 36.5 \text{ mm})| = 242.2 \text{ mT}$ (cf. Eq. A.17 and Tab. A.3). A sharp restriction of the field to $z_{\text{SO}} \geq 570$ mm using a step function is non-physical, so that instead the ‘shaping’ function in Eq. A.16 is used to create a smooth transition between no field outside and the full field amplitude within the storage octupole region.

The uncompensated magnetic field measurement is used to deduce a_{oct} for the storage octupole: The results from the different measurement radii (cf. Ch. 3.2.2.1) are shown in Fig. A.19 (left). The fit of a cubic function yields $a_{\text{oct}} = 4981.5 \text{ T/m}^3$. The absolute magnetic field of the approximation in Eq. A.15 was calculated as consistency check.

This procedure cannot be repeated for the compensation octupole, as this one was not magnetically measured alone. However, from the magnetic field checks of the individual octupole rings (cf. Fig. A.5) follows an amplitude at $r = 39$ mm of approximately $B = 350 \text{ mT}$. Comparing this result with Eq. A.15 (again with $x = 0$), $a_{\text{oct}} = 5900.3 \text{ T/m}^3$ is deduced.

The compensated field results from a superposition of the two individual octupole fields. From a perfect axial alignment and rotation of exactly $\varphi = 45^\circ$ follows a more or less vanishing residual field. The measurement result of the compensated magnetic field, however, shows a hexapole structure, which is caused by an axial misalignment by δy (cf. Ch. 3.2.2.1). This axial misalignment as well as a rotational offset $\delta\varphi$ are included in the consideration and determined experimentally using Fig. A.19 (right): By variation of δy and $\delta\varphi$, the resulting approximated field is brought as close to the measurement data as possible. The deviation between approximation and measurement is calculated as $B_{\text{approx.}}(\varphi) - B_{\text{meas.}}(\varphi)$. The optimum is found with $\delta y = -2.6 \text{ mm}$ and $\delta\varphi = 0.2^\circ$.

In summary, the fields for storage (SO) and compensation octupole (CO) are given by the following equations:

$$\vec{B}_{\text{SO}}(x, y, z) = \vec{B}_{\text{oct}}(x, y) \cdot B_{\text{shape},z}(z) \quad (\text{A.18a})$$

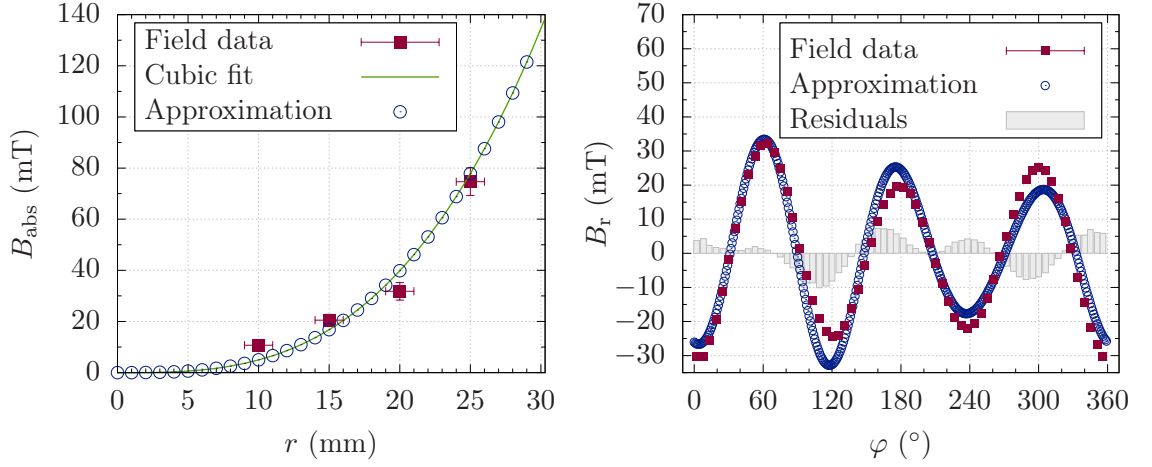


Figure A.19: Process of parameter determination for the storage and compensation octupole analytic fields. Left: Average absolute magnetic field of the storage octupole (red squares, errors in B corresponding to the standard deviation) with fit according to $f(r) = a_{\text{oct}} r^3$ (green line). The blue hollow circles show the resulting analytic approximation given by Eq. A.15. Right: Radial field component of the compensated octupole field measurement at $r = 25$ mm (red squares), the hexapole structure is the result of axial and rotational misalignments of the two octupoles by $\delta y = -2.6$ mm and $\delta\varphi = 0.2^\circ$. The approximation as superposition of Eqs. A.18a and A.18b is shown in blue. The grey boxes mark the residuals $B_{\text{approx.}}(\varphi) - B_{\text{meas.}}(\varphi)$.

$$\vec{B}_{\text{CO}}(x, y, z) = \left[\mathbf{R} \vec{B}_{\text{oct}}(x, y) \right] \cdot B_{\text{shape}, z}(z) \quad (\text{A.18b})$$

with \mathbf{R} a 2×2 rotation matrix with $\varphi = 45^\circ + \delta\varphi$. The field parameters are summarised in Tab. A.3.

Table A.3: Parameters of the analytical storage and compensation octupole fields defined by Eq. A.18a and A.18b. For simplicity parameter units are omitted here. z_{SF2} refers to the longitudinal position of the second spin flipper.

Octupole	a_{oct}	s	z'	δy	$\delta\varphi$
Storage	4981.5	80	0.557	—	—
Compensation	5900.3	150	$z_{\text{SF2}} + 0.08$	-0.0026	0.2°

A.5.1.3 The model for the spin flipper fields

The spin flipper fields B_{SF1} and B_{SF2} each consist of two saddle coils, which are positioned at 90° rotation (cf. Ch. 5.1). Each saddle coil generates an oscillating magnetic field in the xy -plane. The shape of the magnetic fields is approximated using only the straight wires of the coils at $\pm x_0$ and $\pm y_0$. Applying Biot-Savart's law, the field amplitudes of the two saddle coils are given by

$$B_{\text{SF},xy,1} = a_{\text{SF}} \left(\frac{1}{\sqrt{(x-x_{0,1})^2 + (y-y_{0,1})^2}} + \frac{1}{\sqrt{(x-x_{0,1})^2 + (y+y_{0,1})^2}} \right. \\ \left. + \frac{1}{\sqrt{(x+x_{0,1})^2 + (y-y_{0,1})^2}} + \frac{1}{\sqrt{(x+x_{0,1})^2 + (y+y_{0,1})^2}} \right) \quad (\text{A.19a})$$

$$B_{\text{SF},xy,2} = a_{\text{SF}} \left(\frac{1}{\sqrt{(x-x_{0,2})^2 + (y-y_{0,2})^2}} + \frac{1}{\sqrt{(x-x_{0,2})^2 + (y+y_{0,2})^2}} \right. \\ \left. + \frac{1}{\sqrt{(x+x_{0,2})^2 + (y-y_{0,2})^2}} + \frac{1}{\sqrt{(x+x_{0,2})^2 + (y+y_{0,2})^2}} \right). \quad (\text{A.19b})$$

Here, each term is the contribution by a single wire. The factor a_{SF} scales the field shape to be equal to 1 at $x = y = 0$ mm, so that the field is later adjusted by multiplication with the required B_1 amplitude. The longitudinal shape of the field is defined using the 'shaping' functions¹⁷

$$B_{\text{SF},z}(z) = \begin{cases} \frac{2}{\pi} \arctan \left(\exp \left[\frac{s\pi}{2} (z + (z_{\text{SF}} - z')) \right] \right) & \text{for } z \leq z_{\text{SF}} \\ 1 - \frac{2}{\pi} \arctan \left(\exp \left[\frac{s\pi}{2} (z + (z_{\text{SF}} + z')) \right] \right) & \text{for } z > z_{\text{SF}} \end{cases} \quad (\text{A.20})$$

The parameters for the field approximation of SF1 and SF2 are given in Tab. A.4. The amplitude B_1 of the resulting field is left as a free parameter. Furthermore, the oscillation of the fields in x - and y -direction is included with the frequency ω_{SF} and the phase $\Delta\varphi$. The total magnetic field approximation of each spin flipper is thus given by

$$\vec{B}_1(x, y, z, t) = B_1 B_{\text{SF},z}(z) \begin{pmatrix} B_{\text{SF},xy,1}(x, y) \sin(\omega_{\text{SF}}t - \Delta\varphi) \\ B_{\text{SF},xy,2}(x, y) \sin(\omega_{\text{SF}}t) \\ 0 \end{pmatrix}. \quad (\text{A.21})$$

Table A.4: Parameters for the shape of the spin flipper B_1 fields according to the functions given in Eqs. A.19 and A.20. For simplicity parameter units are omitted here.

Spin flipper	a_{SF}	$x_{0,1} = y_{0,2}$	$y_{0,1} = x_{0,2}$	s	z'
1	0.0115	0.023	0.0398	100	0.068
2	0.008	0.01575	0.02728	100	0.0606

¹⁷As in Eq. A.16, the functions and their parameters were found experimentally. With increasing z -positions, the first equation creates a transition from zero to the full field amplitude (corresponding to a multiplication of the field amplitude by 1, cf. Fig. A.18), whereas the second function pushes the field from full amplitude down to zero.

A.5.2 The Monte Carlo simulation

The Monte Carlo simulation is used to estimate the number of storable neutrons depending on parameters related to the filling process. Therefore, the trajectories of neutrons with predefined start parameters (initial energy distribution, start positions in $x - y$ direction, initial flight angles relative to the z -axis and the initial spin direction as HFS or LFS) are simulated from the τ SPECT entrance to the storage volume. On their way, the neutron spin movement is tracked by solving the Bloch equations (cf. Eq. 4.1) using the Python3 numerical integrator `odeint`.

The magnetic fields are implemented according to the analytic approximations in the previous sections. Fig. A.20 shows the amplitudes of the individual fields for illustration purposes as seen by a neutron flying along the z -axis at $r = 20$ mm and ignoring gravity. The B_0 field (cf. Eq. A.14) is generated with the currents $I_{\text{main}} = 33$ A, $I_{C3} = 20$ A and $I_{C5} = -10$ A. In simulations using the single spin flip technique, SF1 is switched off by setting $B_1(\text{SF1}) = 0$ mT, whereas in simulations employing the double spin flip technique SF1 is set to $B_1 = 0.5$ mT. SF2 is in all cases set to $B_1 = 0.5$ mT as well. At the black dashed line, the simulation stops and the outgoing neutron parameters (energy, spin polarisation and positions in the $x - y$ plane) are analysed.

In order to include the correct physical behaviour, gravity and the Stern-Gerlach force

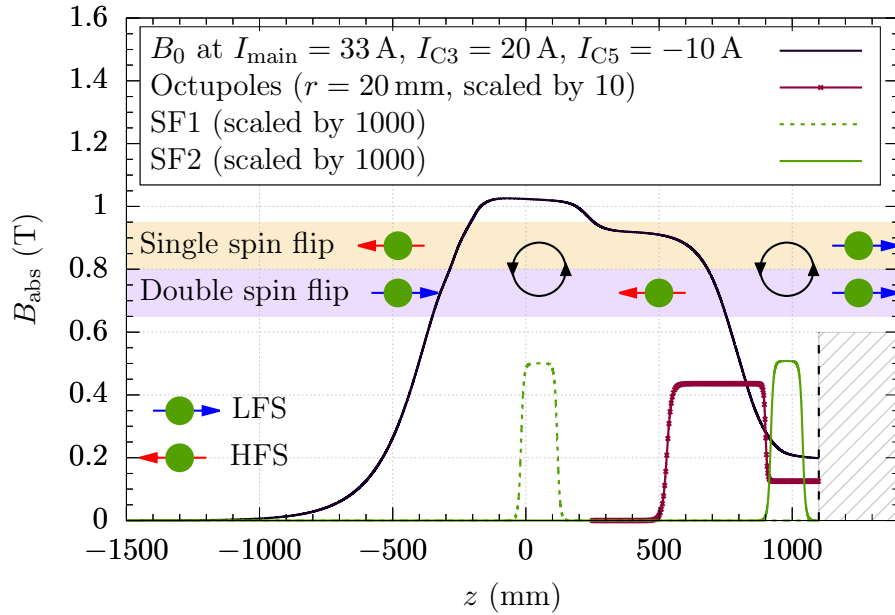


Figure A.20: Absolute magnetic fields used for the Monte Carlo simulation as seen by a neutron flying along z at $r = 20$ mm. Black: B_0 approximated by Eq. A.14; red markers with line: The octupole field with the compensation octupole located around SF2 (Eqs. A.18a and A.18b); and green: B_1 of SF1 (dashed) and SF2 (solid) according to Eq. A.21. At the black dashed line the simulation stops and the neutrons are analysed for storability. The single spin flip technique uses initial HFS and converts them to LFS at SF2 (yellow box) while SF1 is switched off. The double spin flip technique (purple box) transforms initial LFS to HFS, and back, using both spin flippers.

(cf. Chs. 2.1.3 and 2.1.4) are included of which the latter is essential in the double spin flip technique, as it decelerates the initial LFS down to storable energies. Furthermore, the neutron guide including the narrowing section (cf. Ch. 3.1.2) is implemented with a variable Fermi potential, allowing for exchanges of the guide material¹⁸. In this work, only quartz glass with $V_F = 90 \text{ neV}$ is used.

A.5.2.1 Optimisation of the Monte Carlo time step sizes

The Monte Carlo simulation consists of small time steps dt , during which the neutrons travel freely in a direction depending on their current three-dimensional velocity. After each iteration, the velocity and its direction, and the spin state are reanalysed and updated.

However, it could be shown in preliminary studies, that the resulting spin state after the simulation has finished depends significantly on the chosen size of dt : With large values, adiabaticity (cf. Eq. 4.7) is not fulfilled, which is a problem especially in the regions around SF1 and SF2. The B_1 field then changes too fast between each evaluation and the neutron spin does not follow the overall magnetic field, i.e., it is not spin flipped (cf. Ch. 4.1 for an introduction into adiabaticity).

If dt is chosen too small, roundoff errors increase by several orders of magnitude, which is calculated in the following example: We consider a neutron at velocity $v = 3 \text{ m/s}$ on a straight flight path along the z -axis from the beginning of the simulation at $z = -1.5 \text{ m}$ up to SF2 at $z_{\text{SF2}} = 0.98 \text{ m}$ and a time step size of $dt = 1 \text{ ns}$. This would result in a total number of iterations of $m = 2.48 \text{ m} / (3 \text{ m/s} \cdot 1 \text{ ns}) = 827 \times 10^6$. The MC simulation is written in Python3, which uses float precision at $\sim 10^{-13}$. Therefore, the roundoff error has increased to $m \times 10^{-13} \simeq 8 \times 10^{-5}$ until the neutron reaches SF2. Depending on the B_1 amplitude, this is already on the same order of magnitude, so that the neutron spin motion is not simulated correctly anymore. As a result, dt needs to be as large as possible without violating adiabaticity. The time step size was optimised individually in three different regions.

1. Region around SF1: The outgoing spin component S_z of an initial LFS ($S_z = +1$) after passage of SF1 was analysed depending on dt . The result is shown on the left in Fig. A.21, each simulation was done with the same amplitude of $B_1 = 0.5 \text{ mT}$. A successful spin flip yields $S_z = -1$, the incomplete spin flip at smaller dt is caused by roundoff errors and at larger dt by a violation of adiabaticity. The optimum is determined as $dt = 13 \text{ ns}$.
2. Region around SF2: The procedure used for the region around SF1 was repeated for the interval around SF2 (cf. Fig. A.21, right). Also at SF2, the field amplitude was set to $B_1 = 0.5 \text{ mT}$. The smaller RF frequency ($f_{\text{SF2}} \simeq 6 \text{ MHz}$ compared to $f_{\text{SF1}} \simeq 30 \text{ MHz}$) allows for larger time step sizes, so that the optimum is found at $dt = 270 \text{ ns}$, where adiabaticity is still fulfilled.
3. Remaining region: Without a spin flip available for analysis in the remaining region, we take a look at the spin trajectory in the storage octupole fringe field (here, the largest changes in the static field occur, which the neutron spin should fol-

¹⁸The initial tube diameter is $\varnothing = 73 \text{ mm}$, which is reduced to $\varnothing = 50 \text{ mm}$ in front of SF2 (cf. Ch. 3.1.2). The dimensions are taken from [Kah20]. Reflections at the tube walls are purely specular.

low smoothly). Fig. A.22 shows the result¹⁹ for four different time step sizes. It shows, that large fluctuations occur with $dt \geq 200$ ns, whereas a smooth behaviour is achieved with $dt \leq 60$ ns. In order to stay well below the upper limit, $dt = 20$ ns was chosen for the time step sizes outside the spin flipping region.

¹⁹The y -axis shows the deviation from $S_z = +1$ for a HFS, which increases as expected, because the total magnetic field in this region tilts to the transversal plane due to the increasing storage octupole field.

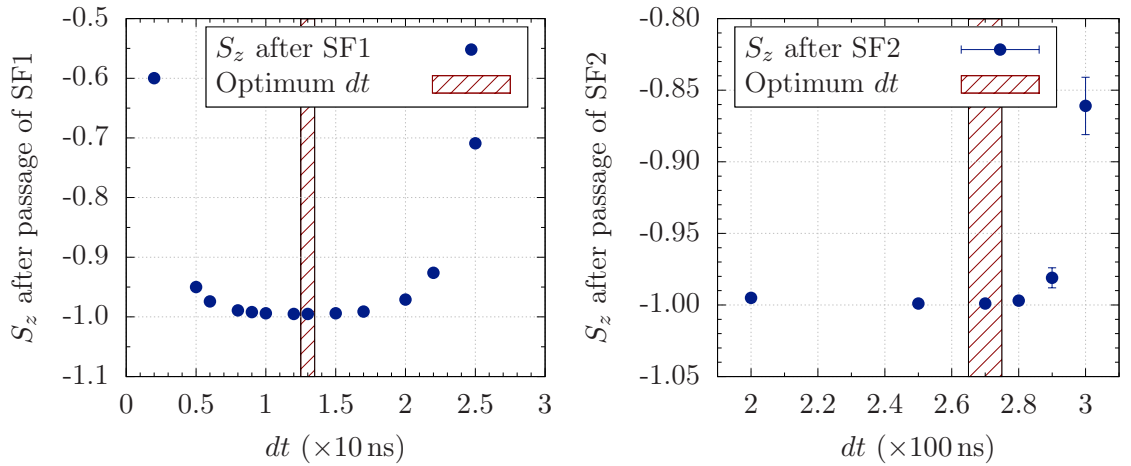


Figure A.21: Optimisation of the Monte Carlo time step size dt in the region around SF1 (left) and SF2 (right). Initial LFS with $S_z = +1$ were transported through the spin flippers, a successful spin flip then results in $S_z = -1$. The settings were in both cases $B_1 = 0.5$ mT at circular polarisation (σ^+ , cf. Ch. 4.1.1.1) and the resonance $2\pi f_{\text{SF}} = \omega_0$ fulfilled at the centre of each spin flipper. At SF1, dt is bounded below by floating point roundoff errors and above by adiabaticity violation. The optimum is found at $dt = 13$ ns (red shaded box). Similar limits are valid for SF2, however, here $f_{\text{SF2}} \simeq 6$ MHz is much smaller than at SF1 ($f_{\text{SF1}} \simeq 30$ MHz), so that adiabaticity is violated at higher values of dt . The optimum is found at $dt = 270$ ns.

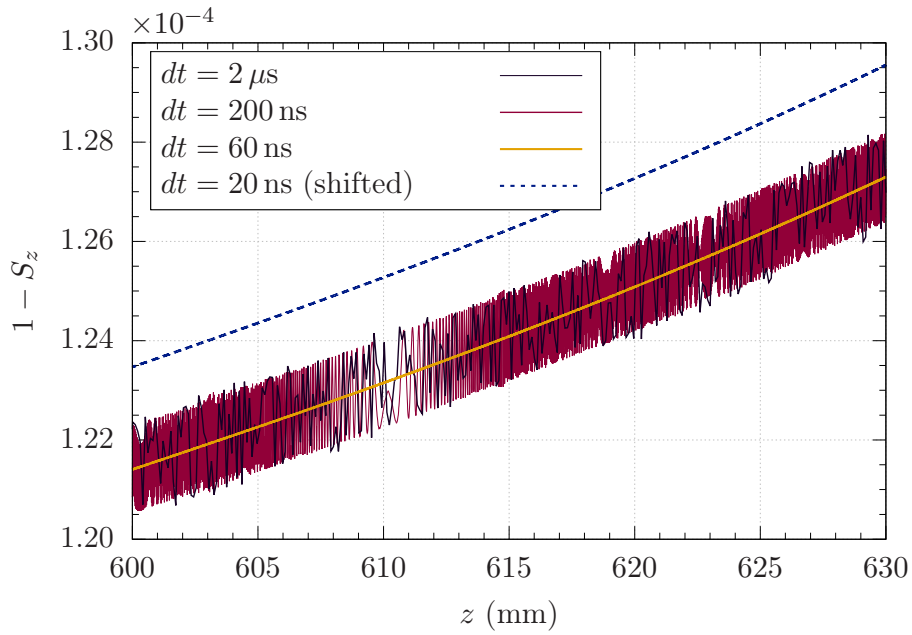


Figure A.22: Optimisation of the Monte Carlo time step size dt in the region outside the spin flippers, here shown for the storage octupole fringe field. The y -axis shows the deviation from $S_z = +1$ as the neutron spin follows the total magnetic field with increasing transversal component. Large time step sizes with $dt \geq 200$ ns show prominent fluctuations (red and black lines). The expected smooth behaviour is achieved with $dt = 60$ ns (yellow) and $dt = 20$ ns (blue, dashed), where the latter is shifted up by 0.1 for better distinguishability. Including a safety margin, $dt = 20$ ns was chosen as the optimum.

A.6 The τ SPECT beamlines

The beamline connects the UCN source of the TRIGA reactor to the shutter of τ SPECT and thus guides the UCN towards the experiment. It consists of several straight and bent tubes with an inner diameter of $d = 66$ mm made from stainless steel ($V_F = 190$ neV) and with a low surface roughness $R_a \leq 0.40$ μm for high UCN transmission²⁰. R_a corresponds to the average profile height deviations from the mean value per evaluated length.

Three different beamlines were used with τ SPECT in this work, which are shown in Fig. A.23 with the measures of each component listed in Tab. A.5. Beamline No. 1 (a) was used for the storage measurements in τ SPECT with the birdcage resonator as spin flipper (cf. Ch. 3.6.3). Its positive aspect is the easily adaptable height by exchange of the vertical tube l_2 . However, [Kah20] shows, that the UCN transmission through bent tubes improves with the bending radius. This is particularly important at the bottom part of the beamline, because with higher radii the impinging angles of the UCN are lower²¹ and the transmission of neutrons with $E \gtrsim V_F$ improves. Consequently, the beamline was exchanged to beamline No. 2 (b) for the saddle coil spin flipper measurements in beamtimes *Feb2020* and *June2020*. In order to investigate the double spin flip technique (cf. Ch. 6.2.2), beamline No. 3 (c) was used in beamtime *Dec2020*: It combines the positive aspect of large radii bent tubes at the bottom while allowing for easy height adaptations by exchanging the vertical straight tube l_2 .

Up to this point, the comparison of the different beamlines refers only to geometrical and practical aspects. Over the year 2020, a general decline in the UCN output of the source was measured, which is to current knowledge related to a HD contamination in the D_2 converter (cf. Ch. A.1). Furthermore, after several hours without heat load from

²⁰The straight tubes are electropolished Neumo Pharmatubes of the hygienic class HE5 ($R_a \leq 0.25$ μm). The bent tubes are of hygienic class H4 with $R_a \leq 0.40$ μm

²¹This is only valid for specular reflection, which is assumed here.

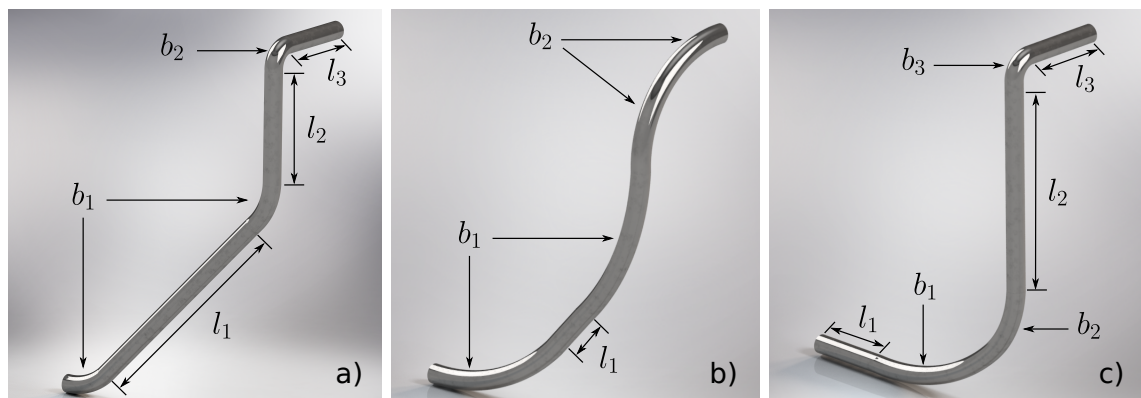


Figure A.23: Beamline configurations used for measurements with τ SPECT in this work. The dimensions of the components are listed in Tab. A.5. Beamline No. 1 (a) was used with the birdcage resonator spin flipper in beamtime *Sept2019*, and beamline No. 2 (b) with the saddle coil spin flipper in beamtimes *Feb2020* and *June2020*. To allow for high flexibility in height adaption and to include large radii bent tubes, beamline No. 3 (c) was used for the double spin flip measurements in beamtime *Dec2020*.

Table A.5: Dimensions of the straight and bent tubes used for beamline Nos. 1 to 3 in Fig. A.23. The first value of the bends b corresponds to the angle coverage and the second value to the radius.

Measure	Beamline 1 (a)	Beamline 2 (b)	Beamline 3 (c)
b_1	45°, 250 mm	45°, 800 mm	45°, 800 mm
b_2	90°, 80 mm	45°, 400 mm	45°, 400 mm
b_3	—	—	90°, 80 mm
l_1	(700 + 280) mm	200 mm	300 mm
l_2	440 mm (adaptable)	—	800 mm (adaptable)
l_3	310 mm	—	310 mm

reactor operation (e.g. on weekends) but without making any changes in the τ SPECT setup, stepwise fluctuations in the UCN output both in positive and negative directions were also observed irregularly, which might be caused by a reformation of the D_2 crystal. This makes a direct comparison regarding UCN transmission difficult.

The problem is discussed further by means of Fig. A.24: The spin flipper power dependency measurement using the saddle coils was done in beamtime *Feb2020*, first using beamline No. 1 and then with beamline No. 2 with a weekend in between. The spin flipper filling position was $z_{\text{SF}} = 900$ mm at $f_{\text{SF}} = 8.021$ MHz in both cases, the neutron counts N after 50 s storage are normalised to the pulse energy. In order to quantify the overall increase in N , the data at each power setting was averaged and individual increasing factors calculated. The weighted average of all factors then results in an improved transmission of 28.94 ± 3.34 % for beamline No. 2. For comparison, the stepwise fluctuations are roughly on the 10 %-level²², so that the measured improvement might as well be a combination of transmission effects and changes in the UCN output. However, this result adds to the argument of improved transmissions through larger radii, so that all measurements in this work were done using beamline No. 2 except for those in beamtime *Dec2020* during the investigation of the double spin flip technique (cf. Ch. 6).

²²To give an example, the average neutron counts measured in a time interval $t = [0, 8]$ s relative to the thermal peak at t_0 (cf. Ch. 3.5) increased from $N = 14611(275)$ to $15690(220)$ over night in the first week of beamtime *June2020*, which gives an increase by 7.4(2.5) %. The data was normalised to the pulse energy.

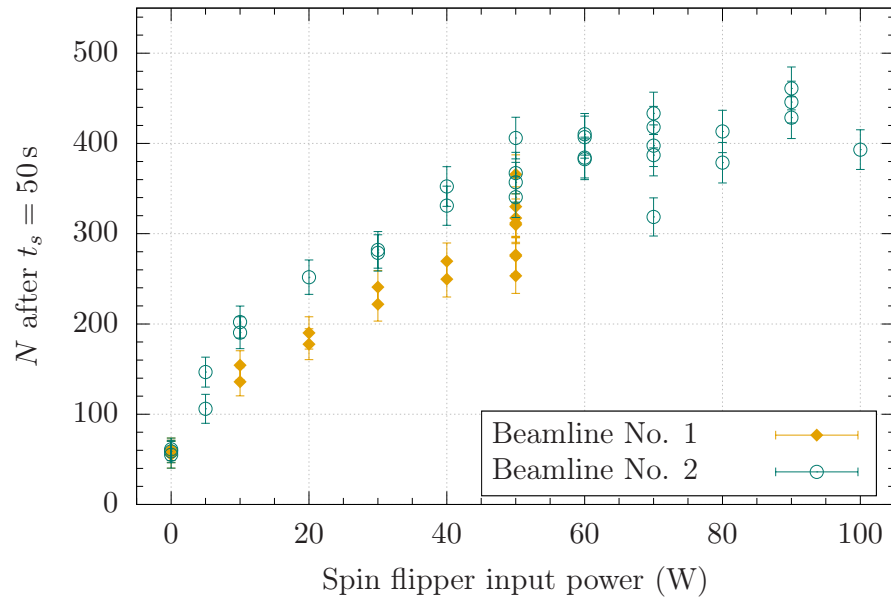


Figure A.24: Comparison between beamline No. 1 (yellow) and beamline No. 2 (turquoise) using the RF power dependency measurement with UCN storage in τ SPECT. The spin flipper position and frequency was equal in both cases ($z_{\text{SF}} = 900$ mm, $f_{\text{SF}} = 8.021$ MHz). After calculating the mean counts at each power setting and the individual increasing factors, a weighted average gain of $28.94 \pm 3.34\%$ is found with beamline No. 2.

A.7 Hardware and electronics

A.7.1 The motor control system of the translation stages

The translation stages are a crucial part of τ SPECT: Without them, the spin flipping unit could not be repositioned and moved out of the storage volume (which is required for the storage of UCN only by magnetic fields), and the detector could not be used for spectrum cleaning inside the trap and counting the surviving neutrons after storage. The mechanical setup is the work of J. Kahlenberg and is described in detail in [Kah20], so that here the focus lies on the electronic part and the remote control.

Both translation stages move their connected components by spindles, which are rotated by stepper motors. The motors in turn are connected each to a controller (an overview over the components is provided in Tab. A.6). The controllers contain several input and output plugs, which need to be configured individually. Furthermore, up to 32 driving profiles, called records, can be saved internally. A specific record is loaded by applying TTL signals to the inputs according to the binary representation of the record number subtracted by 1. An additional start signal executes the record.

Table A.6: Electric components used for the translation stages in τ SPECT.

Component	Translation stage SFU	Translation stage detector
Controller	Nanotec SMCI47-S-2	Nanotec SMCI33-1
Motor	Nanotec ST6018D4508-B	Nanotec ST5909L3008-B
Encoder	Nanotec WEDS5541-A06	Nanotec WEDL5541-A06
Motor voltage	48 V	24 V

For each controller, one input is configured as 'External Reference Switch', which is connected to the two electric end stops of the translation stage. These end stops limit the driving range and if one of them is reached, the motor stops immediately. The outer end stop is furthermore used as reference: After powering up the controller, it has no internal position reference (a so-called 'zero-position'), so that absolute positioning as it is used for τ SPECT is not possible. An internal feedback loop in the controller thus allows only so-called 'reference runs' directly after power up, where the motor drives backwards until the end stop is reached. The position of the end stop is then defined as zero-position.

The translation stage of the spin flipping unit requires two records for every measurement run, one to drive to the filling position and one for the storage position. The detector translation stage requires three records for driving to the storage position, the cleaning position, and the counting position. In principle, the records do not have to be changed anymore in the final τ SPECT measurement configuration. However, as long as e.g. the filling or cleaning process are being optimised, the corresponding positions might change between measurements.

Thus, a remote control including a user friendly graphical user interface (GUI) was implemented (cf. Fig. A.25). It allows on the one hand changing parameters of the spin flipping unit and the detector translation stage without interrupting the measurement sequence, but also enables remote control of the motors without TTL signals. The current status as well as current positions are permanently queried and displayed, so that internal

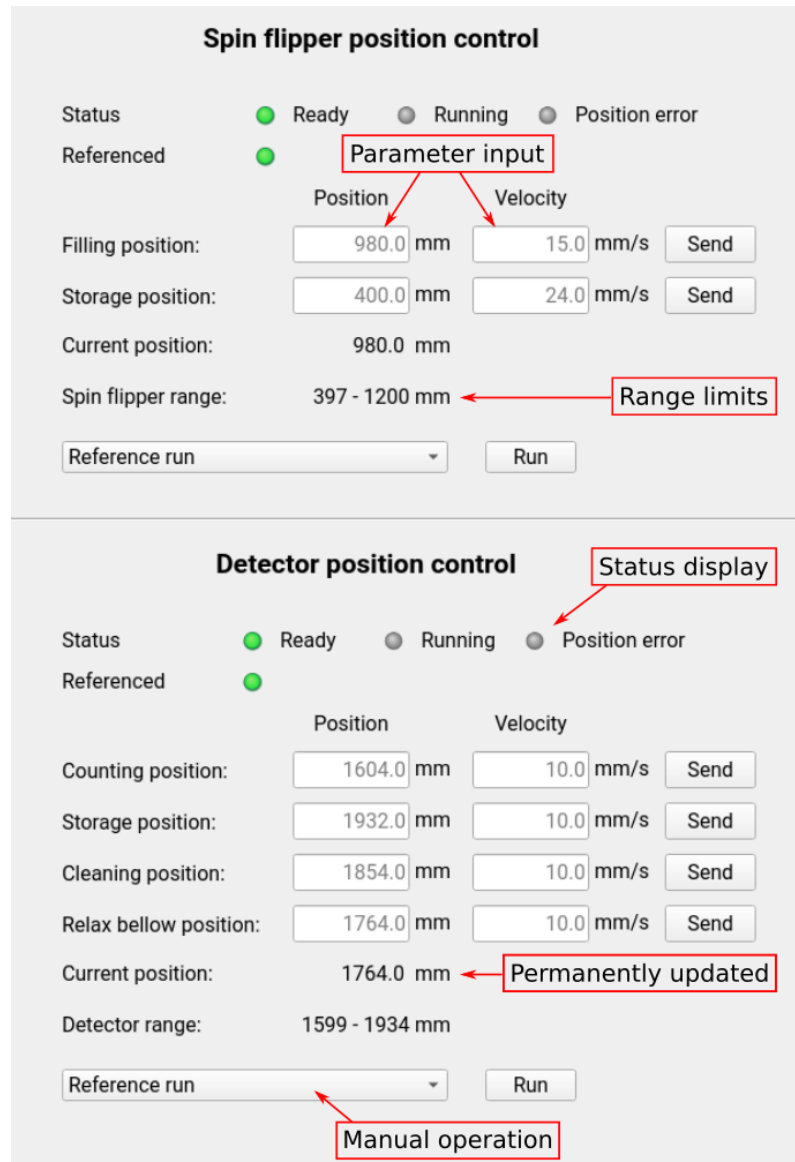


Figure A.25: GUI of the status surveillance program of the translation stage controllers.

errors of the controllers are directly detected. In addition, the program writes log and configuration files for later analyses.

A.7.2 The shutter interlock system

The beamline connects the UCN source exit of the TRIGA reactor to the shutter of τ SPECT. Consequently, the vacuum inside the beamline has to be as good as possible in order not to significantly change the vacuum conditions inside the cryostat ($p \sim 1.3 \times 10^{-7}$ mbar). Furthermore, in case of any leakage in the beamline, the shutter has to close immediately. Therefore, a shutter interlock system was developed, which closes the shutter automatically if the beamline pressure rises over a predefined threshold (currently, the threshold is set to $p = 8.6 \times 10^{-3}$ mbar for no specific reason).

The beamline pressure is monitored using a Pirani sensor connected to a pressure gauge²³. The threshold is configured within the gauge; if the pressure is below this threshold, a relay, which is accessible from the outside, is closed. The shutter is moved with pressurised air and requires a +24 V signal at its control relay to open.

A control circuit is connected between the gauge and the shutter as shown in Fig. A.26: The +24 V signal from an external power supply is looped through the gauge and connected to the control box of the interlock. Here, it passes a two-step switch system, the first switch generally enabling the output of the control box and the second switch changing the mode of the interlock. These modes can be either automatic mode, during which the shutter is open as long as the pressure is below threshold, or TTL driven mode, where the shutter is open only for the duration of an additional TTL signal from the Delay Box. So far, τ SPECT runs in TTL mode. If the pressure rises over the predefined threshold, the +24 V signal is interrupted by the gauge and the shutter closes.

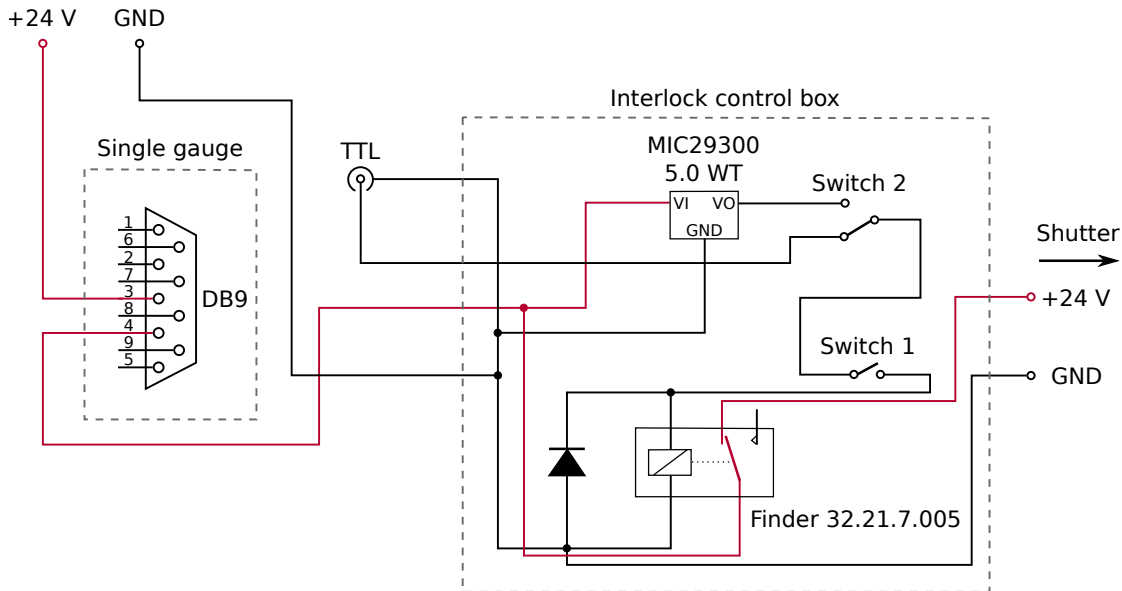


Figure A.26: Electric circuit of the shutter interlock system. A +24 V signal (red lines) is looped through the gauge measuring the beamline pressure. Switch 2 sets the operation mode to automatic or TTL driven mode. By enabling the interlock control box (Switch 1) the shutter opens if the beamline pressure is below the threshold configured in the gauge. If the pressure rises over this threshold, the +24 V signal is interrupted and the shutter closes.

²³Sensor: Pfeiffer Vacuum TPR 280; Gauge: Pfeiffer Vacuum TPG261 (single gauge)

Appendix B

Additional figures and tables

Table B.1: Fermi potential V_F of selected materials commonly associated in connection with UCN.

Material	V_F in neV	Reference
Nickel (^{58}Ni)	335	[GRL91]
Nickel molybdenum ($^{58}\text{NiMo}$, 85%/15%)	311	[KRR ⁺ 17]
Nickel molybdenum (NiMo, 85%/15%)	225	[KRR ⁺ 17]
Stainless steel	190	[ADF ⁺ 08]
Copper (Cu) (natural)	168	[GRL91]
Fomblin [®] oil	106.5	[MAB ⁺ 89]
Solid deuterium ($^2\text{H}_2$)	105	[Ign90]
Quartz glass	90	[ABB ⁺ 09]
Aluminum (Al)	54	[GRL91]
Water (H_2O)	-17.6	[GRL91]
Titanium (Ti)	-48	[GRL91]

Table B.2: Average pulse energies and their standard deviations of the beamtimes discussed in this work. Normalisations are scaled only by the average value.

Beamtime	Average pulse energy
<i>Sept2019</i>	$\bar{E}_{Sept2019} = 9.95(18)$ MWs
<i>Nov2019</i>	$\bar{E}_{Nov2019} = 9.61(24)$ MWs
<i>Feb2020</i>	$\bar{E}_{Feb2020} = 9.42(24)$ MWs
<i>June2020</i>	$\bar{E}_{June2020} = 9.45(18)$ MWs
<i>Aug2020</i>	$\bar{E}_{Aug2020} = 9.30(14)$ MWs
<i>Dec2020</i>	$\bar{E}_{Dec2020} = 9.47(16)$ MWs
<i>June2021</i>	$\bar{E}_{June2021} = 9.76(21)$ MWs

B.1 Magnetic field measurements

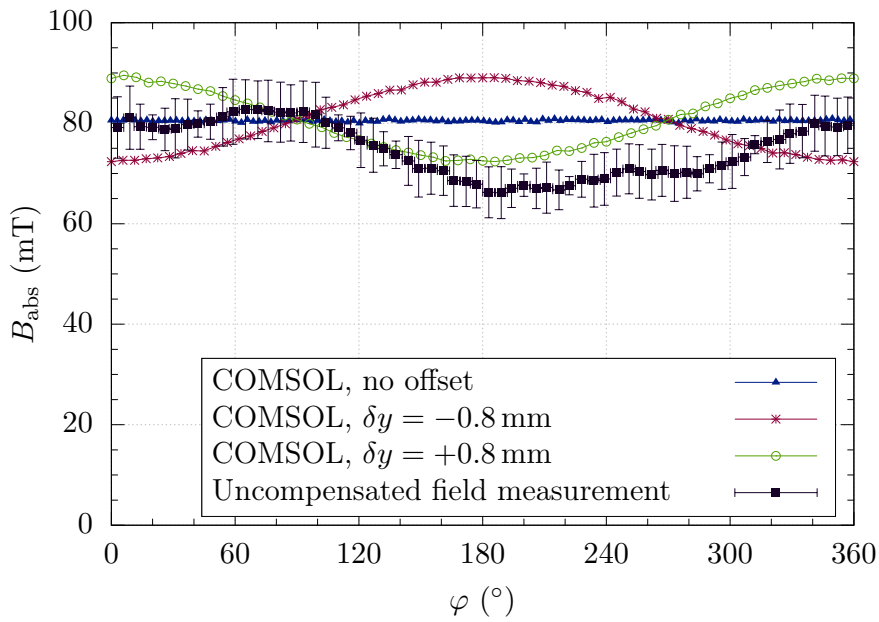


Figure B.1: Uncompensated absolute field of the storage octupole in the $r - \varphi$ plane in comparison with a simulation using COMSOL Multiphysics[®]. The centre of the analysis plane in the simulation is either aligned with the axis of the octupole (blue triangles), or offset in vertical direction by $\delta y = -0.8$ mm (red crosses) or $\delta y = +0.8$ mm (green circles). The measurement results are shown by the black squares, their shape matching the simulation results at $\delta y = +0.8$ mm best. This indicates, that the rotational axis of the measurement setup was not perfectly aligned with the axis of the octupole but at an offset in positive vertical direction.

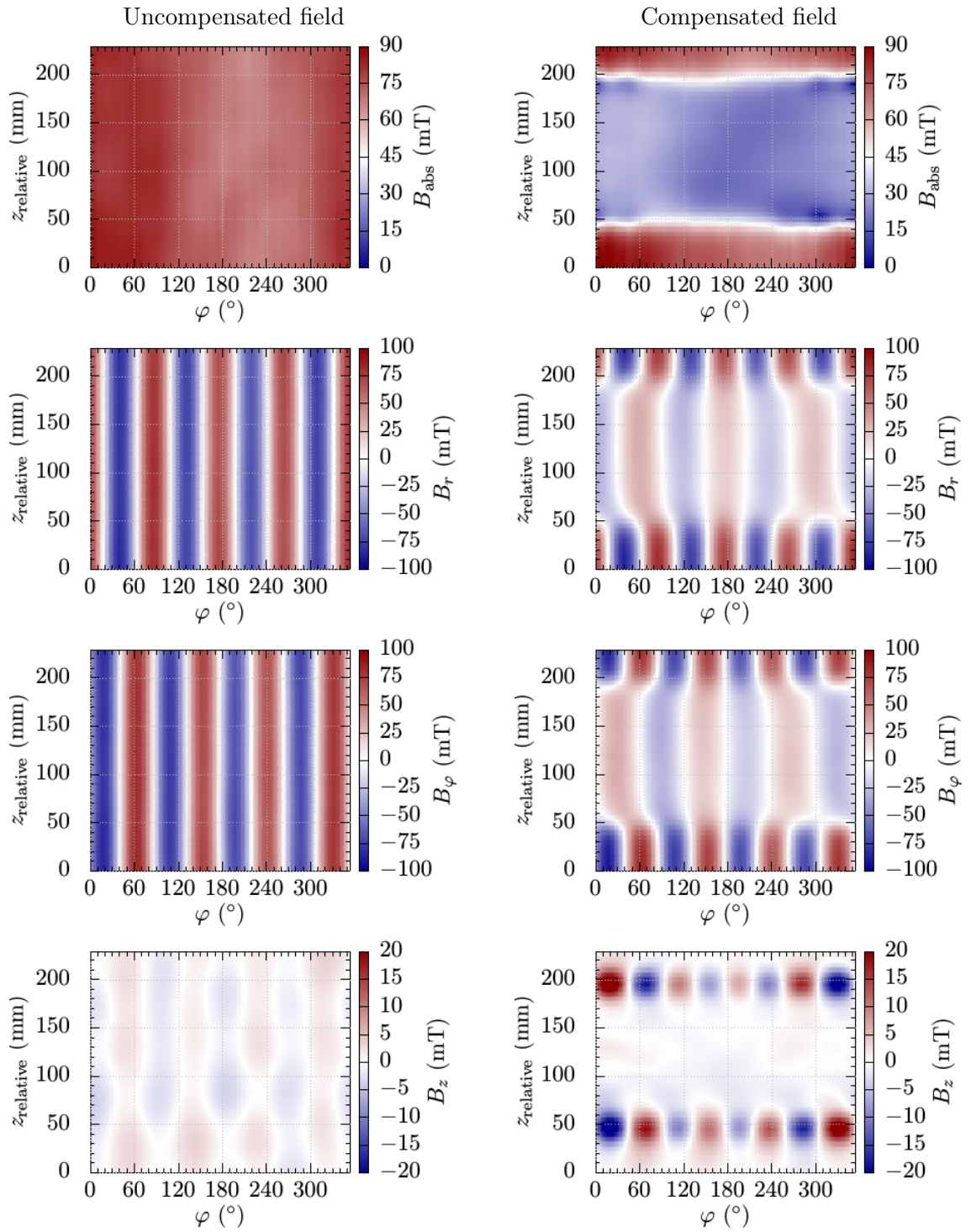


Figure B.2: Depiction of the octupole field maps by components on a measurement radius of $r = 25$ mm. Left column: Uncompensated field; Right column: Compensated field. From top to bottom: 1) Absolute field, 2) Radial field component, 3) Angular field component, and 4) Longitudinal field component. Due to the axial misalignment of the compensation octupole by $\delta y = -2.6$ mm during the measurement, the compensated field shows a hexapole structure.

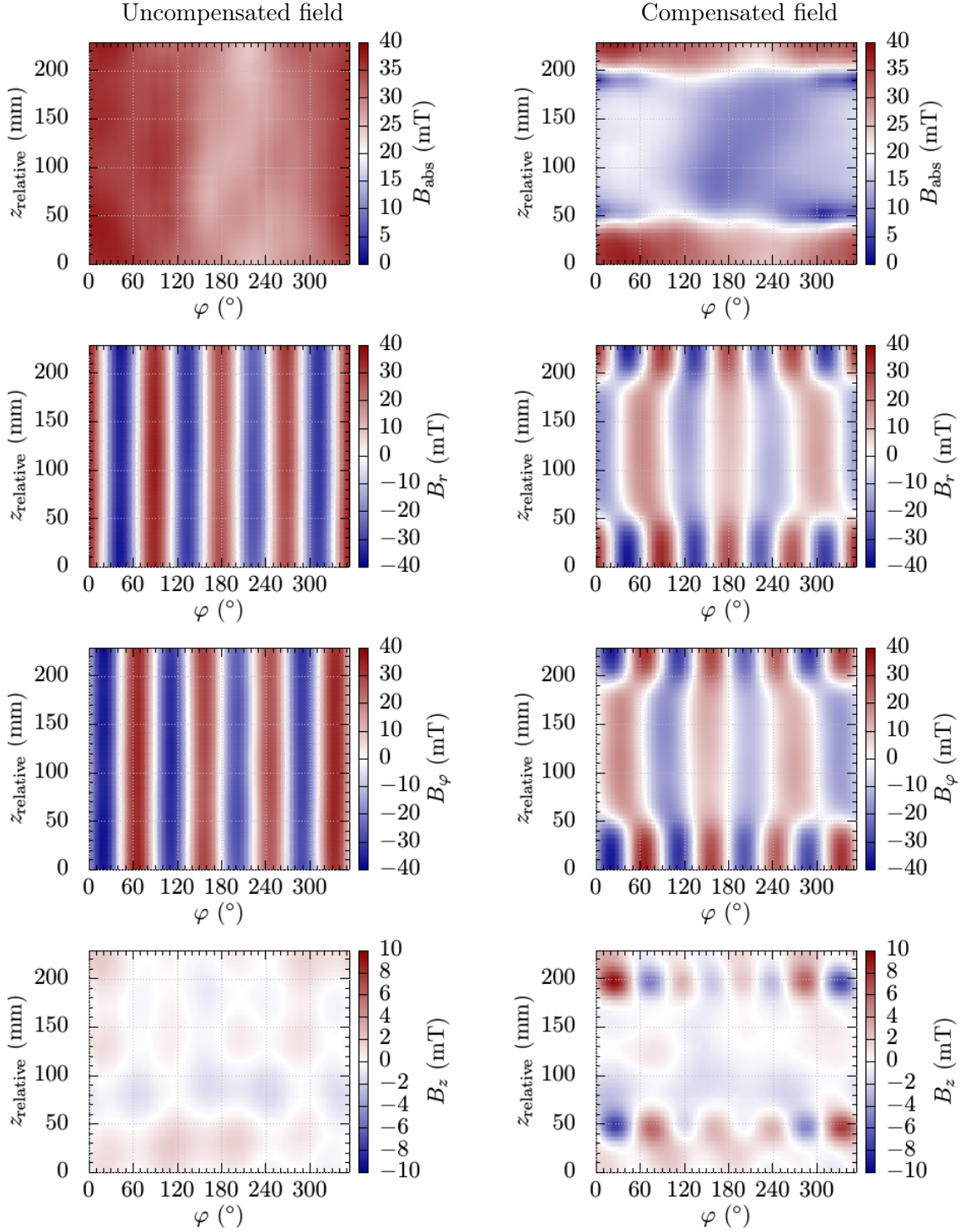


Figure B.3: Depiction of the octupole field maps by components on a measurement radius of $r = 20$ mm. Left column: Uncompensated field; Right column: Compensated field. From top to bottom: 1) Absolute field, 2) Radial field component, 3) Angular field component, and 4) Longitudinal field component. Due to the axial misalignment of the compensation octupole by $\delta y = -2.6$ mm during the measurement, the compensated field shows a hexapole structure.

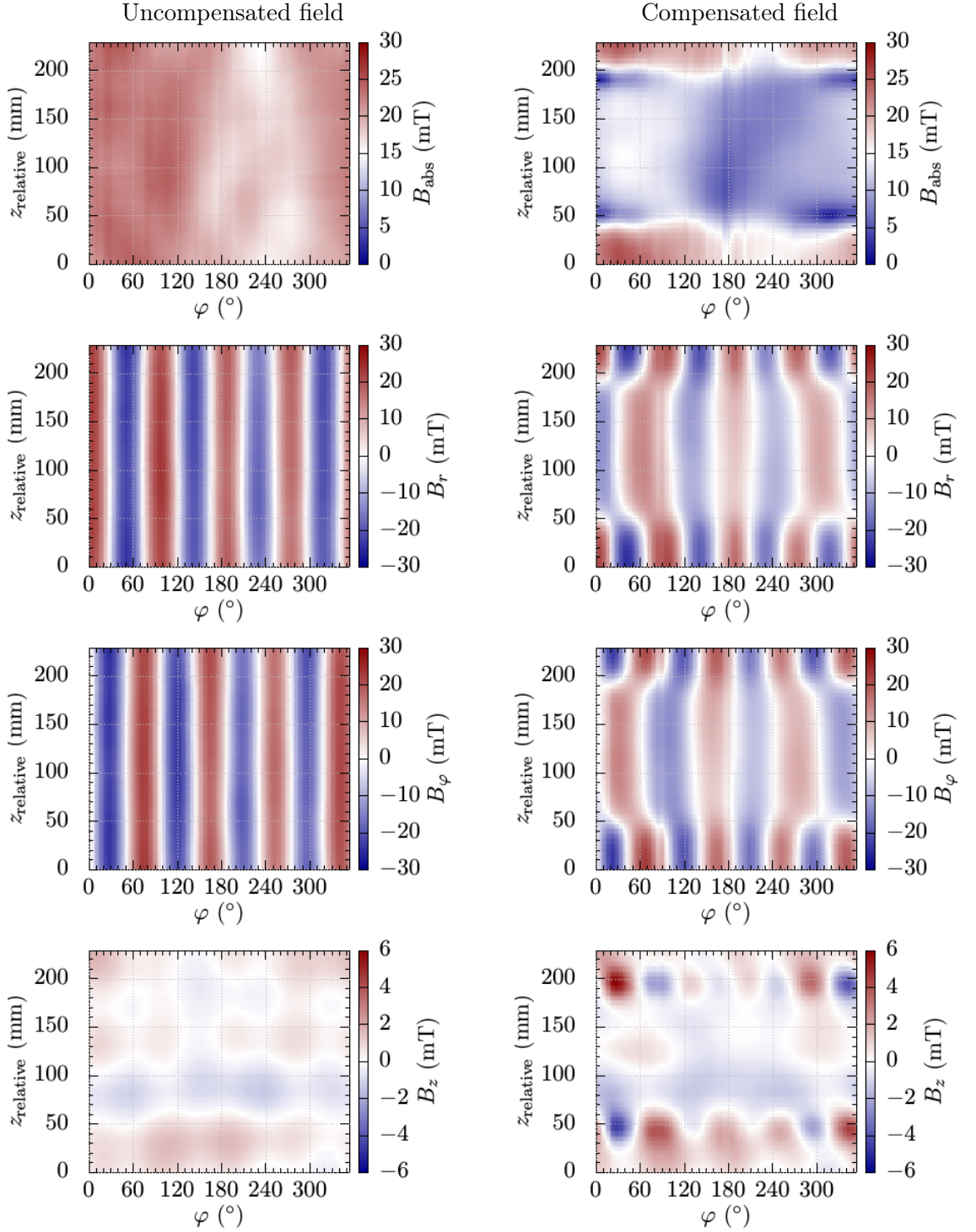


Figure B.4: Depiction of the octupole field maps by components on a measurement radius of $r = 15$ mm. Left column: Uncompensated field; Right column: Compensated field. From top to bottom: 1) Absolute field, 2) Radial field component, 3) Angular field component, and 4) Longitudinal field component. Due to the axial misalignment of the compensation octupole by $\delta y = -2.6$ mm during the measurement, the compensated field shows a hexapole structure.

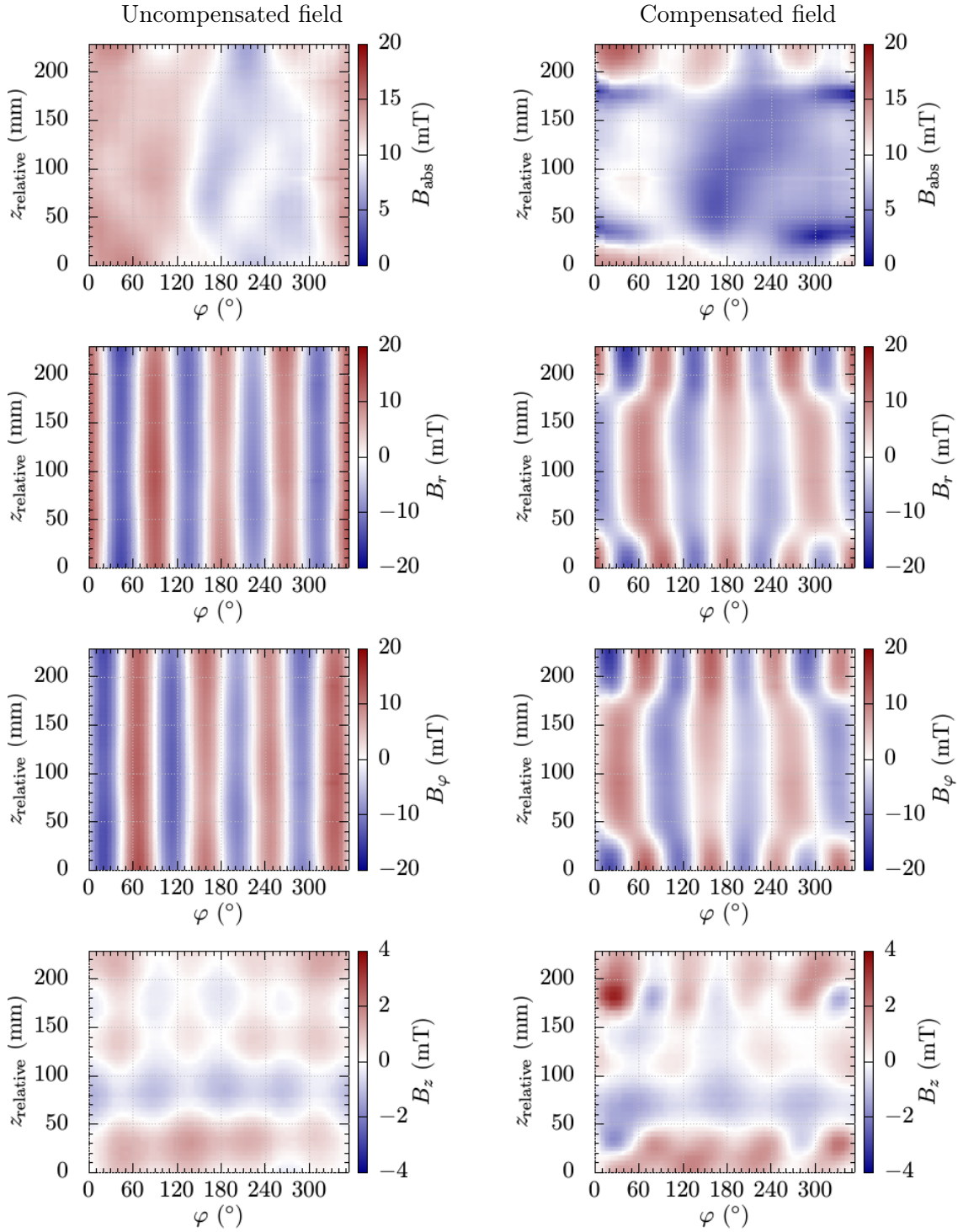


Figure B.5: Depiction of the octupole field maps by components on a measurement radius of $r = 10$ mm. Left column: Uncompensated field; Right column: Compensated field. From top to bottom: 1) Absolute field, 2) Radial field component, 3) Angular field component, and 4) Longitudinal field component. Due to the axial misalignment of the compensation octupole by $\delta y = -2.6$ mm during the measurement, the compensated field shows a hexapole structure.

B.2 Spin flipper parameter optimisation

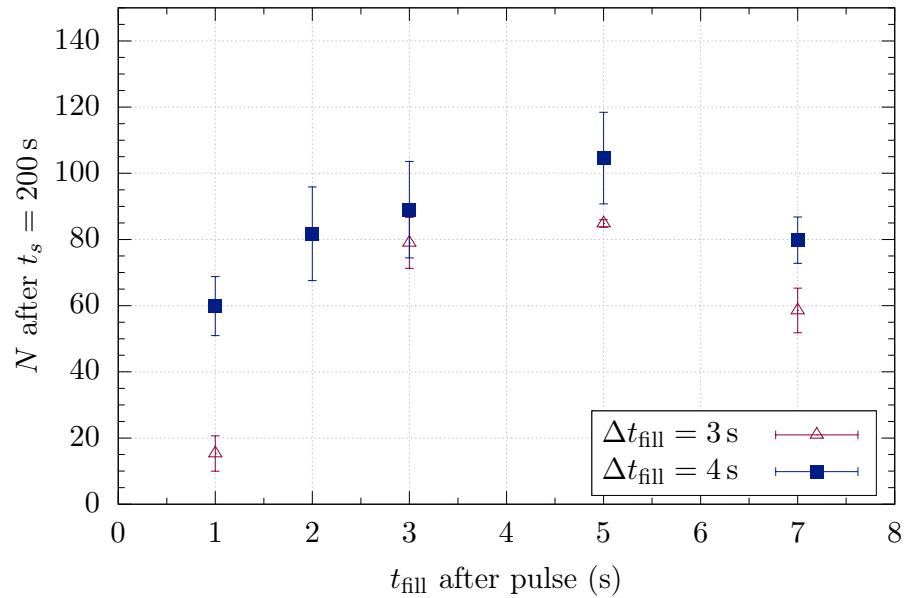


Figure B.6: RF timing optimisation of the birdcage resonator using 200 s storage measurements and a normalisation to the average pulse energy. The filling duration was varied between $\Delta t_{\text{fill}} = 3$ s (red) and 4 s (blue) with the filling start time t_{fill} after the pulse trigger on the x -axis. At each start time, the results were averaged with the error the standard deviation. A plateau-shaped behaviour is visible within errors from $t_{\text{fill}} = 2$ s on for both filling durations, which is caused by continuous arrival of neutrons in the storable energy range at the spin flipper.

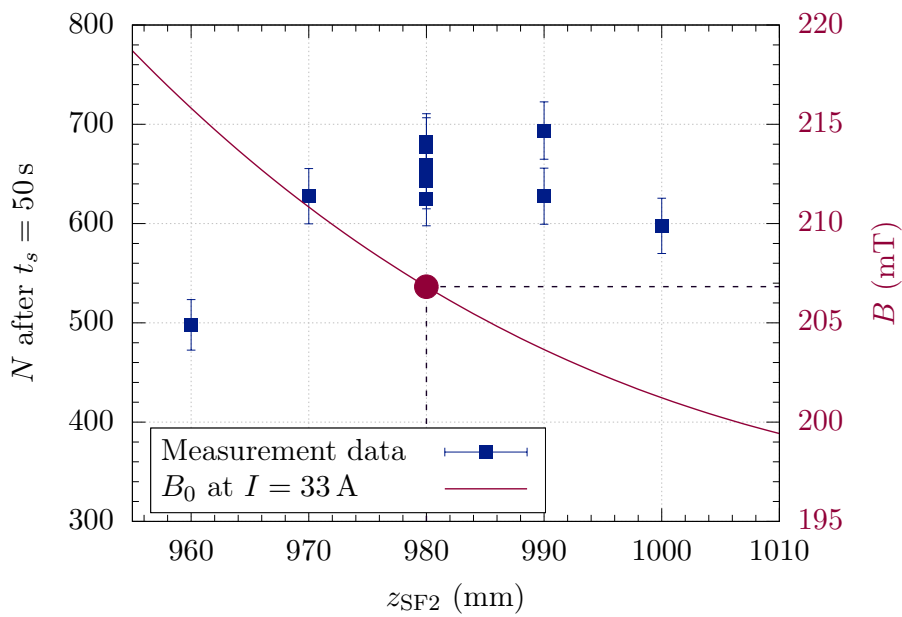


Figure B.7: Spin flip position optimisation around $z_{\text{SF2}} = 980$ mm measured in beamtime *Dec2020* using $t_s = 50$ s storage measurements at $P = 80$ W with a normalisation to the average pulse energy (blue squares, referring to the left axis). The red line corresponds to B_0 at $I_{\text{main}} = 33$ A (right axis), the calculated optimum position is marked by the red circle. The expected plateau-shaped behaviour due to the spin flipper length is confirmed between $z_{\text{SF2}} = 970$ mm and 1000 mm.

B.3 Cleaning

The fits in this section are done using single and double exponential functions

$$\begin{aligned} N_{\text{single}}(t) &= a_1 \exp(-t/\tau_1) \\ N_{\text{double}}(t) &= a_1 \exp(-t/\tau_1) + a_2 \exp(-t/\tau_2). \end{aligned} \quad (\text{B.1})$$

Table B.3: Fit results of single and double exponential functions (cf. Eq. B.1) to the storage curves measured at $\Delta t_{\text{clean}} = 20$ s at the cleaning positions $z_{\text{clean},2} = 1854$ mm and $z_{\text{clean},3} = 1864$ mm. The corresponding measurement data is shown in Fig. B.8 (left).

z_{clean}	a_1	τ_1	a_2	τ_2	χ^2/ndf
1854 mm	502.4(28.2)	631.6(89.9) s			3.04
1854 mm	187.9(2123.0)	180.5(1774.0) s	347.5(2257.0)	1109.8(1.1e4) s	3.96
1864 mm	448.6(11.8)	656.3(44.7) s			0.62
1864 mm	134.4(100.4)	51.3(58.1) s	404.8(41.8)	785.1(148.5) s	0.46

Table B.4: Fit results of a single and a double exponential function (cf. Eq. B.1) to the storage curve measured at $\Delta t_{\text{clean}} = 40$ s at the cleaning position $z_{\text{clean},2} = 1854$ mm. The corresponding measurement data is shown in Fig. B.8 (right).

z_{clean}	a_1	τ_1	a_2	τ_2	χ^2/ndf
1854 mm	450.7(11.1)	683.3(33.2) s			0.70
1854 mm	85.7(113.5)	53.7(89.1) s	425.8(30.0)	730.3(65.2) s	0.70

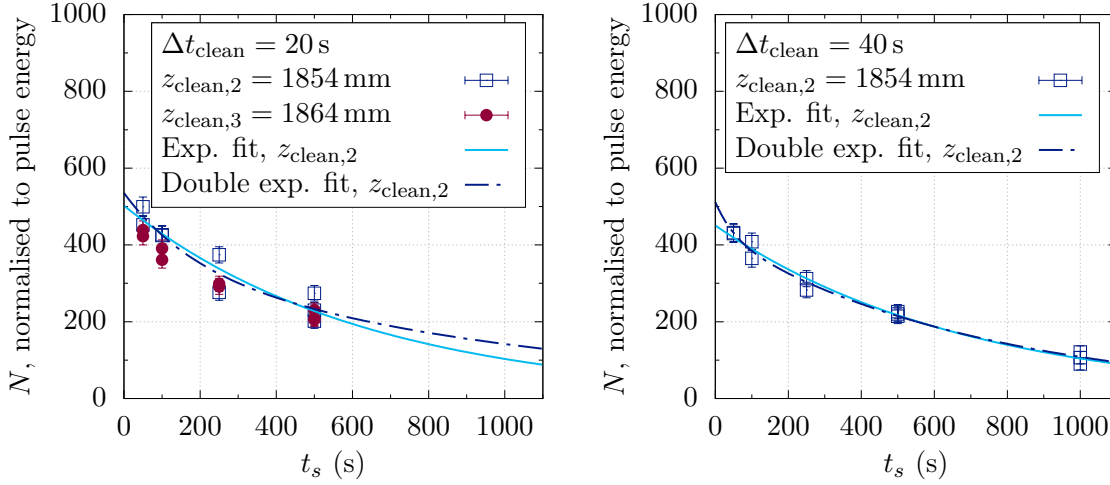


Figure B.8: Storage curves measured with cleaning of durations $\Delta t_{\text{clean}} = 20$ s (left) and $\Delta t_{\text{clean}} = 40$ s (right) at the cleaning positions $z_{\text{clean},2} = 1854$ mm (blue) and $z_{\text{clean},3} = 1864$ mm (red, not measured at $\Delta t_{\text{clean}} = 40$ s). The solid line corresponds to a single exponential fit to the results at $z_{\text{clean},2}$, the dashed line to a double exponential fit to the same data (cf. Eq. B.1). The fit parameters are listed in Tabs. B.3 and B.4.

Table B.5: Multi-dimensional fit results of a single exponential function (cf. Eq. B.1) to the storage curve measured at $\Delta t_{\text{clean}} = 200$ s at the cleaning position $z_{\text{clean},2} = 1854$ mm. The corresponding measurement data is shown in Fig. 7.1.

Measurement day	Parameter	Value
June 28th	a_1^1	476.66(13.03)
June 29th	a_1^2	556.85(10.25)
June 30th	a_1^3	592.23(10.73)
July 01st	a_1^4	573.77(9.95)
July 02nd	a_1^5	604.50(14.77)
July 05th	a_1^6	636.42(9.85)
July 07th	a_1^7	628.36(10.25)
July 08th	a_1^8	645.79(9.94)
July 09th	a_1^9	650.00(12.47)
	τ	858.59(15.52) s
	χ^2/ndf	1.14

List of Figures

1.1	β^- decay of the neutron	3
1.2	Fermi and Gamow-Teller transitions in neutron β decay	4
1.3	Comparison of the V_{ud} uncertainties inferred from $0^+ \rightarrow 0^+$ and neutron β decays	7
1.4	The process of Helium synthesis	9
1.5	Recent results of experimental Y_P determination in comparison to the theoretical prediction	10
2.1	Illustration of the four neutron interaction types	13
2.2	Schematic setup of a beam type neutron lifetime measurement	14
2.3	Schematic setup of a bottle type neutron lifetime experiment	16
2.4	Results of neutron lifetime measurements since the year 2005	18
3.1	Field superposition used for magnetic storage of neutrons	22
3.2	Field shapes of $B_0(z)$ and B_{oct} along the z -axis	23
3.3	Schematic overview of the τ SPECT experimental setup and filling process	24
3.4	Measurement procedure in τ SPECT after the filling process.	25
3.5	Overview of components in the spin flipping unit	26
3.6	Ideal Halbach arrays of linear and cylindrical shape.	27
3.7	Principle of octupole field compensation and resulting fields from a FEM simulation	30
3.8	Finished compensation octupole and front assembly	31
3.9	The gearing principle of the compensation octupole rotation fixation	32
3.10	Setup for the magnetic field measurement with and without compensation octupole	33
3.11	Reproducibility of the magnetic field measurement of the compensation octupole	34
3.12	Measured and simulated radial magnetic field component without and with field compensation at $r = 25$ mm	35
3.13	Uncompensated and compensated octupole field on a measurement radius $r = 25$ mm	35
3.14	Superposition of the compensated octupole field measurement and B_0	37
3.15	Simulation of the total magnetic field in τ SPECT including a 3 mm axial misalignment of the compensation octupole	38

3.16	Schematic depiction of a cosine-theta coil and resulting transversal B_1 field	39
3.17	Birdcage resonator in low-pass design	40
3.18	Finished birdcage resonator and its resonance frequency	41
3.19	Signal scheme of the birdcage resonator	42
3.20	Cool down behaviour of the birdcage resonator	43
3.21	CAD rendering of the magnetic field measurement setup of the birdcage resonator	44
3.22	Magnetic field of the birdcage resonator	45
3.23	UCN detection principle and detector setup	48
3.24	Schematics of TTL pulses and gates for individual components in τ SPECT	51
3.25	Experimental setup of the τ SPECT experiment from the side	52
3.26	Calibration of the translation stage positions of SFU and detector	53
3.27	Neutron arrival spectrum of a typical 50s storage measurement with cleaning	54
3.28	Dependency of B_1 and the number of stored neutrons on the RF power of the birdcage resonator	55
3.29	Spin flipper position optimisation of beamtime <i>Sept2019</i>	56
3.30	The RF timing optimisation of the spin flipper	57
3.31	First purely magnetic storage curve measured in beamtime <i>Sept2019</i>	58
3.32	Simulated statistical sensitivity $\Delta\tau_n$ with respect to the number of beamtimes at the TRIGA reactor for selected initial values of N_0	60
4.1	Longitudinal magnetic field with zoom into the spin flipping region, and the resonance position of the spin flipper in τ SPECT	64
4.2	Vector diagram of the magnetic fields involved in the spin flipping process in the co-rotating frame without transversal fields	65
4.3	Spin motion during adiabatic fast passage	65
4.4	Schematic depiction of circular, elliptic and linear field polarisation	67
4.5	Spin flip efficiency depending on the field characterisation parameter $k(z_{\text{SF}})$ inferred from a Monte Carlo simulation	69
4.6	Resonance bands in the spin flipping region depending on the field parameter $k(z_{\text{SF}})$ at $z_{\text{SF}} = 980$ mm and $z_{\text{SF}} = 1020$ mm	71
4.7	Constraints on the spin flip position by the longitudinal and transversal field gradients	72
4.8	Spin flip efficiency ε_{SF} depending on the B_1 amplitude as inferred from a Monte Carlo simulation	73
4.9	Magnetic potential difference relative to $V_{\text{magn}} = 0$ neV as seen by high- and low-field seeking neutrons at $I_{\text{main}} = 33$ A	74
4.10	Schematics of the spin flipping unit front section for an estimation of the gravitational acceleration of neutrons in the storage octupole	76
4.11	Maximum initial kinetic energy of storable neutrons depending on the spin flip position	77
4.12	Schematics of SFU front section and storable fraction of neutron energy distribution	78
4.13	Required spin flipper frequency depending on the spin flip position in τ SPECT	80

5.1	Schematics of a single saddle coil and the double saddle coil configuration	82
5.2	The finished saddle coil spin flipper and the excitation circuit	83
5.3	Number of stored neutrons depending on the spin flip position	84
5.4	Spin flip position optimisation around $z_{\text{SF}} = 900$ mm	85
5.5	Pick-up coil voltage at the saddle coil spin flipper depending on the input RF power	87
5.6	Number of storable neutrons depending on the irradiated RF power	88
5.7	Number of storable neutrons depending on $\Delta\varphi$ at $P = 20$ W	89
5.8	Number of storable neutrons depending on $\Delta\varphi$ at $P = 80$ W	90
5.9	Centring principle of the compensation octupole and simulation of the effect on the compensated magnetic field	92
5.10	Number of stored neutrons depending on the spin flip position after centring of the octupole field	94
5.11	Influence of a reduction of I_{main} and the experimental result	95
5.12	Magnetic fields around the spin flipper side storage octupole edge	96
5.13	Storage curve measured with optimised parameters of the single spin flip technique in beamtime <i>Feb2020</i>	99
5.14	Field maps of the storage octupole fringe region in τ SPECT	100
5.15	Magnetic field change on a circular orbit and depolarisation time depending on the radius of the closed orbit	101
5.16	Dependency of detected neutrons on the counting position in τ SPECT	103
5.17	Cleaning durations used in the optimisation process with respect to the arrival spectrum of a measurement with and without cleaning	104
5.18	Storage curves measured with cleaning of duration $\Delta t_{\text{clean}} = 30$ s at three different cleaning positions	105
5.19	Comparison of the normalisation of 500 s measurements to pulse energy, higher energy neutrons and cleaned UCN	108
6.1	The potential energy of neutrons in the double spin flip technique at $I_{\text{main}} =$ 33 A	112
6.2	Neutron energy by components with deceleration by the Stern-Gerlach force and the deceleration efficiency $\varepsilon_{\text{decel}}(\theta)$ depending on the beam divergence θ_{max} using the double spin flip technique	114
6.3	Relative number of storable neutrons depending on θ_{max} using the single and the double spin flip technique in a Monte Carlo simulation and the inferred deceleration effect $\varepsilon_{\text{dSF}}(\theta_{\text{max}})$	116
6.4	Position of spin flipper No. 1 and configuration of the gradient	118
6.5	The setup of spin flipper No. 1	119
6.6	Phase optimisation using the double spin flip technique at heights h_1 and h_2	122
6.7	Timing optimisation using the double spin flip technique.	123
6.8	Optimisation of the filling position and the RF power of SF1 using the double spin flip technique	124
6.9	Comparison between the single and the double spin flip technique	126
6.10	Schematics of neutron transmission through a 90° bent tube and using a 45° mirror	128

7.1	Storage curve measured in beamtime <i>June2021</i> with multi-dimensional fit	133
A.1	'Nose' region of UCN source D at the TRIGA reactor	136
A.2	Setup and result of the magnetic segments measurement	137
A.3	Gearing principle of the compensation octupole rings	138
A.4	Construction and magnetic measurement setup for the octupole rings	139
A.5	Radial and longitudinal component of the magnetic field for the 5 octupole rings	140
A.6	Measurement of the absolute magnetic field on a vertical and horizontal line through octupole ring No. 1	140
A.7	Final assembly of the compensation octupole	141
A.8	Allan deviation measurement of the Hall probe	142
A.9	Orientation optimisation of the compensation octupole	143
A.10	Phase shift realised for the birdcage resonator	145
A.11	Calibration of a pick-up coil for the measurement of the magnetic field inside the spin flipper	146
A.12	Magnetic field of a birdcage resonator and a saddle coil as the result of a FEM simulation	147
A.13	Influence of single-cut and dynamic threshold on neutron event recognition	149
A.14	Signal processing for neutron event recognition	150
A.15	Event properties used for the peakfinding algorithm	151
A.16	Neutron recognition process and resulting event spectrum	152
A.17	Optimisation of the detector overvoltage	153
A.18	Octupole field measurement and field approximation in longitudinal direction using a step function and a smooth transition function	156
A.19	Analytic approximation of the octupole fields using magnetic field measurement results	157
A.20	Absolute magnetic fields used for the Monte Carlo simulation	159
A.21	Optimisation of the Monte Carlo time step size dt in the region of the spin flippers	161
A.22	Optimisation of the Monte Carlo time step size dt in the region outside the spin flippers	162
A.23	Beamline configurations used for measurements with τ SPECT in this work	163
A.24	Comparison between beamline Nos. 1 and 2 using the RF power dependency measurement with UCN storage in τ SPECT	165
A.25	GUI of the status surveillance program of the translation stage controllers	167
A.26	Electric circuit of the shutter interlock system	168
B.1	Uncompensated absolute field of the storage octupole in the $r - \varphi$ plane in comparison with a simulation using COMSOL Multiphysics [®] at different axial offsets of the measurement plane	170
B.2	Depiction of the octupole field maps by components at $r = 25$ mm	171
B.3	Depiction of the octupole field maps by components at $r = 20$ mm	172
B.4	Depiction of the octupole field maps by components at $r = 15$ mm	173

B.5	Depiction of the octupole field maps by components at $r = 10$ mm	174
B.6	RF timing optimisation of the birdcage resonator with 200 s storage measurements	175
B.7	Spin flip position optimisation around $z_{\text{SF2}} = 980$ mm	176
B.8	Storage curves measured with cleaning of durations $\Delta t_{\text{clean}} = 20$ s and $\Delta t_{\text{clean}} = 40$ s	178

List of Tables

1.1	Overview of neutron properties	3
3.1	Comparison of the uncompensated and compensated octupole field on a measurement radius $r = 25$ mm	36
3.2	The fit parameters of the storage curve measured in beamtime <i>Sept2019</i>	58
3.3	Sequence optimisation in the determination of τ_n	59
5.1	Fit parameters of Eq. 5.4	88
5.2	Storage octupole field before and after centring	93
5.3	RF frequencies and induced pick-up coil voltages at the spin flip positions used in beamtime <i>Dec2020</i>	93
5.4	Summary of the optimum spin flipper parameters	98
5.5	Fit parameters of the storage curve measured in beamtime <i>Feb2020</i>	99
5.6	Fit results of single and double exponential functions to the storage curves measured at $\Delta t_{\text{clean}} = 30$ s at three different cleaning positions	105
6.1	Spin flipper timing used for the double spin flip technique	123
6.2	Results of the filling technique comparison measurement and their ratios at h_1 and h_2	127
A.1	Parameters for the analytical approximation of B_{main}	154
A.2	Parameters for the analytical B_{C3} and B_{C5} shape in longitudinal direction	155
A.3	Parameters for the analytical octupole fields	157
A.4	Parameters for the analytical B_1 shape of the spin flippers	158
A.5	Dimensions of the components used for the τ SPECT beamlines	164
A.6	Electric components used for the translation stages in τ SPECT	166
B.1	Fermi potentials for selected materials commonly associated with UCN	169
B.2	Average pulse energies of the beamtimes discussed in this work	169
B.3	Fit results of single and double exponential functions to the storage curves measured at $\Delta t_{\text{clean}} = 20$ s at two different cleaning positions	177
B.4	Fit results of a single and a double exponential function to the storage curve measured at $\Delta t_{\text{clean}} = 40$ s	177
B.5	Multi-dimensional fit results of a single exponential function to the storage curve measured at $\Delta t_{\text{clean}} = 200$ s	178

Bibliography

- [AAA⁺20] N. Aghanim, Y. Akrami, M. Ashdown, *et al.*. ‘Planck 2018 results’. *Astron. Astrophys.*, **641**, A6 (2020). URL <http://dx.doi.org/10.1051/0004-6361/201833910>. 9, 10
- [AAB⁺21] C. Abel, N. Ayres, G. Ban, *et al.*. ‘A search for neutron to mirror-neutron oscillations using the nedm apparatus at psi’. *Phys. Lett. B*, **812**, 135993 (2021). URL <http://dx.doi.org/https://doi.org/10.1016/j.physletb.2020.135993>. 19
- [ABB⁺06] B. Aubert, R. Barate, D. Boutigny, *et al.*. ‘Measurement of the inclusive electron spectrum in charmless semileptonic B decays near the kinematic end point and determination of $|V_{ub}|$ ’. *Physical Review D*, **73**(1) (2006). URL <http://dx.doi.org/10.1103/physrevd.73.012006>. 6
- [ABB⁺09] I. Altarev, G. Ban, G. Bison, *et al.*. ‘Towards a new measurement of the neutron electric dipole moment’. *Nucl. Instrum. Meth. A*, **611**, 133 (2009). URL <http://dx.doi.org/10.1016/j.nima.2009.07.046>. 169
- [ABBH⁺17] Y. Amhis, S. Banerjee, E. Ben-Haim, *et al.*. ‘Averages of b -hadron, c -hadron, and τ -lepton properties as of summer 2016’. *Eur. Phys. J. C*, **77**(12), 895 (2017). URL <http://dx.doi.org/10.1140/epjc/s10052-017-5058-4>. 6
- [ABC⁺15] S. Arzumanov, L. Bondarenko, S. Chernyavsky, *et al.*. ‘A measurement of the neutron lifetime using the method of storage of ultracold neutrons and detection of inelastically up-scattered neutrons’. *Phys. Lett. B*, **745**, 79 (2015). URL <http://dx.doi.org/10.1016/j.physletb.2015.04.021>. 16, 18
- [Abe08] H. Abele. ‘The neutron. Its properties and basic interactions’. *Prog. Part. Nucl. Phys.*, **60**(1), 1 (2008). URL <http://dx.doi.org/10.1016/j.pnpnp.2007.05.002>. 6
- [ABG48] R. A. Alpher, H. Bethe, and G. Gamow. ‘The origin of chemical elements’. *Phys. Rev.*, **73**, 803 (1948). URL <http://dx.doi.org/10.1103/PhysRev.73.803>. 7
- [ADF⁺08] Altarev, I., M. Daum, A. Frei, *et al.*. ‘Neutron velocity distribution from a superthermal solid 2H2 ultracold neutron source’. *Eur. Phys. J. A*, **37**(1), 9 (2008). URL <http://dx.doi.org/10.1140/epja/i2008-10604-8>. 169
- [AOS15] E. Aver, K. A. Olive, and E. D. Skillman. ‘The effects of He I $\lambda 10830$ on helium abundance determinations’. *J. Cosmol. Astropart. Phys.*, **2015**(07),

- 011–011 (2015). URL <http://dx.doi.org/10.1088/1475-7516/2015/07/011>. 9, 10
- [BA13] Y. B. Band and Y. Avishai. ‘Quantum mechanics with applications to nanotechnology and information science’. 4-Spin, p. 159 – 192 (Academic Press, 2013). URL <http://dx.doi.org/10.1016/B978-0-444-53786-7.00004-6>. 2
- [BAGB⁺20] M. Beck, F. Ayala Guardia, M. Borg, *et al.*. ‘Improved determination of the β - $\bar{\nu}_e$ angular correlation coefficient a in free neutron decay with the α SPECT spectrometer’. *Phys. Rev. C*, **101**, 055506 (2020). URL <http://dx.doi.org/10.1103/PhysRevC.101.055506>. 5, 21, 118
- [BBD⁺07] G. Ban, K. Bodek, M. Daum, *et al.*. ‘Direct experimental limit on neutron–mirror-neutron oscillations’. *Physical Review Letters*, **99**(16) (2007). URL <http://dx.doi.org/10.1103/physrevlett.99.161603>. 19
- [BBG⁺18] Z. Berezhiani, R. Biondi, P. Geltenbort, *et al.*. ‘New experimental limits on neutron – mirror neutron oscillations in the presence of mirror magnetic field’. *The European Physical Journal C*, **78**(9) (2018). URL <http://dx.doi.org/10.1140/epjc/s10052-018-6189-y>. 19
- [BBGS18] G. Baym, D. H. Beck, P. Geltenbort, *et al.*. ‘Testing dark decays of baryons in neutron stars’. *Phys. Rev. Lett.*, **121**, 061801 (2018). URL <http://dx.doi.org/10.1103/PhysRevLett.121.061801>. 19
- [BD96] J. Byrne and P. Dawber. ‘A Revised Value for the Neutron Lifetime Measured Using a Penning Trap’. *Europhys. Lett.*, **33**, 187 (1996). URL <http://dx.doi.org/10.1209/epl/i1996-00319-x>. 14, 18
- [BDA⁺18] M. A.-P. Brown, E. B. Dees, E. Adamek, *et al.*. ‘New result for the neutron β -asymmetry parameter A_0 from UCNA’. *Phys. Rev. C*, **97**, 035505 (2018). URL <http://dx.doi.org/10.1103/PhysRevC.97.035505>. 5
- [BDS⁺90] J. Byrne, P. G. Dawber, J. A. Spain, *et al.*. ‘Measurement of the neutron lifetime by counting trapped protons’. *Phys. Rev. Lett.*, **65**, 289 (1990). URL <http://dx.doi.org/10.1103/PhysRevLett.65.289>. 14
- [Ber19] Z. Berezhiani. ‘Neutron lifetime puzzle and neutron–mirror neutron oscillation’. *Eur. Phys. J. C*, **79**, 484 (2019). URL <http://dx.doi.org/10.1140/epjc/s10052-019-6995-x>. 19
- [BKP⁺78] L. Bondarenko, V. Kurguzov, Y. Prokofev, *et al.*. ‘Measurement of the Neutron Half Time’. *Pisma Zh. Eksp. Teor. Fiz.*, **28**, 328 (1978). 14
- [Blo46] F. Bloch. ‘Nuclear induction’. *Phys. Rev.*, **70**, 460 (1946). URL <http://dx.doi.org/10.1103/PhysRev.70.460>. 63, 68
- [Blu16] P. Bluemler. ‘Proposal for a permanent magnet system with a constant gradient mechanically adjustable in direction and strength’. *CMRB*, **46**(1) (2016). URL <http://dx.doi.org/10.1002/cmr.b.21320>. 28

- [BNT99] S. Burles, K. M. Nollett, and M. S. Turner. ‘Big-bang nucleosynthesis: Linking inner space and outer space’ (1999). 8
- [BW19] J. Byrne and D. L. Worcester. ‘The neutron lifetime anomaly and charge exchange collisions of trapped protons’. *J. Phys. G Nucl. Part. Phys.*, **46**(8), 085001 (2019). URL <http://dx.doi.org/10.1088/1361-6471/ab256b>. 18
- [Cab63] N. Cabibbo. ‘Unitary symmetry and leptonic decays’. *Phys. Rev. Lett.*, **10**, 531 (1963). URL <http://dx.doi.org/10.1103/PhysRevLett.10.531>. 4
- [CFOY16] R. H. Cyburt, B. D. Fields, K. A. Olive, *et al.*. ‘Big bang nucleosynthesis: Present status’. *Rev. Mod. Phys.*, **88**, 015004 (2016). URL <http://dx.doi.org/10.1103/RevModPhys.88.015004>. 7, 8, 9
- [CG34] J. Chadwick and M. Goldhaber. ‘A nuclear photo-effect: Disintegration of the diplon by γ -rays’. *Nature*, **134**(3381), 237 (1934). URL <http://dx.doi.org/10.1038/134237a0>. 1
- [CG35] J. Chadwick and M. Goldhaber. ‘The nuclear photoelectric effect’. *Proc. R. Soc. A*, **151**(873), 479 (1935). URL <http://dx.doi.org/10.1098/rspa.1935.0162>. 1, 2
- [CGH13] V. Cirigliano, S. Gardner, and B. R. Holstein. ‘Beta decays and non-standard interactions in the lhc era’. *Prog. Part. Nucl. Phys.*, **71**, 93–118 (2013). URL <http://dx.doi.org/10.1016/j.pnpnp.2013.03.005>. 4
- [Cha32] J. Chadwick. ‘The existence of a neutron’. *Proc. R. Soc. A*, **136**(830), 692 (1932). URL <http://dx.doi.org/10.1098/rspa.1932.0112>. 1
- [CHS83] C.-N. Chen, D. I. Houlst, and V. J. Sank. ‘Quadrature detection coils - a further $\sqrt{2}$ improvement in sensitivity’. *J. Magn. Reson.*, **54**(2), 324 (1983). URL [http://dx.doi.org/10.1016/0022-2364\(83\)90057-4](http://dx.doi.org/10.1016/0022-2364(83)90057-4). 40
- [CNB⁺72] C. J. Christensen, A. Nielsen, A. Bahnsen, *et al.*. ‘Free-neutron beta-decay half-life’. *Phys. Rev. D*, **5**, 1628 (1972). URL <http://dx.doi.org/10.1103/PhysRevD.5.1628>. 14
- [cod19] (2019). URL <https://physics.nist.gov/cuu/Constants/index.html>. CODATA recommended values (NIST). xii, 2, 3
- [CSW04] N. Cabibbo, E. C. Swallow, and R. Winston. ‘Semileptonic hyperon decays and CKM unitarity’. *Phys. Rev. Lett.*, **92**, 251803 (2004). URL <http://dx.doi.org/10.1103/PhysRevLett.92.251803>. 6
- [DBD⁺17] G. Darius, W. A. Byron, C. R. DeAngelis, *et al.*. ‘Measurement of the Electron-Antineutrino Angular Correlation in Neutron β Decay’. *Phys. Rev. Lett.*, **119**(4), 042502 (2017). URL <http://dx.doi.org/10.1103/PhysRevLett.119.042502>. 5
- [Dra14] S. Dragisic. Master’s thesis, Johannes Gutenberg University Mainz (2014). 28

- [DS11] D. Dubbers and M. G. Schmidt. ‘The neutron and its role in cosmology and particle physics’. *Rev. Mod. Phys.*, **83**, 1111 (2011). URL <http://dx.doi.org/10.1103/RevModPhys.83.1111>. 5
- [EAB18] V. F. Ezhov, A. Z. Andreev, and G. Ban. ‘Measurement of the Neutron Lifetime with Ultracold Neutrons Stored in a Magneto-Gravitational Trap’. *J. Exp. Theor. Phys. Lett.*, **107**, 671 (2018). URL <http://dx.doi.org/10.1134/S0021364018110024>. 17, 18
- [Ebe21] (2021). Klaus Eberhardt, Department of Chemistry (TRIGA), JGU (private communication). 135
- [EMMP99] S. Esposito, G. Mangano, G. Miele, *et al.*. ‘Precision rates for nucleon weak interactions in primordial nucleosynthesis and 4He abundance’. *Nucl. Phys. B*, **540**(1), 3 (1999). URL [http://dx.doi.org/10.1016/S0550-3213\(98\)00757-3](http://dx.doi.org/10.1016/S0550-3213(98)00757-3). 8
- [FBM00] H. Fujita, W. O. Braum, and M. A. Morich. ‘Novel quadrature birdcage coil for a vertical b_0 field open mri system’. *Magn. Reson. Med.*, **44**(4), 633 (2000). URL [http://dx.doi.org/10.1002/1522-2594\(200010\)44:4<633::AID-MRM18>3.0.CO;2-K](http://dx.doi.org/10.1002/1522-2594(200010)44:4<633::AID-MRM18>3.0.CO;2-K). 39
- [FG18] B. Fornal and B. Grinstein. ‘Dark matter interpretation of the neutron decay anomaly’. *Phys. Rev. Lett.*, **120**, 191801 (2018). URL <http://dx.doi.org/10.1103/PhysRevLett.120.191801>. 19
- [FKL⁺12] M. J. Fromerth, I. Kuznetsova, L. Labun, *et al.*. ‘From Quark-Gluon Universe to Neutrino Decoupling: $200 < T < 2 \text{ MeV}$ ’. *Acta Phys. Pol. B*, **43**(12), 2261 (2012). URL <http://dx.doi.org/0.5506/APhysPolB.43.2261>. 7
- [Fra19] K. Franz. Master’s thesis, Johannes Gutenberg University Mainz (2019). 52
- [FTD⁺18] V. Fernández, E. Terlevich, A. I. Díaz, *et al.*. ‘Primordial helium abundance determination using sulphur as metallicity tracer’. *Monthly Notices of the Royal Astronomical Society*, **478**(4), 5301 (2018). URL <http://dx.doi.org/10.1093/mnras/sty1206>. 9, 10
- [Gam46] G. Gamow. ‘Expanding universe and the origin of elements’. *Phys. Rev.*, **70**, 572 (1946). URL <http://dx.doi.org/10.1103/PhysRev.70.572.2>. 7
- [GFCW⁺21] F. M. Gonzalez, E. M. Fries, C. Cude-Woods, *et al.*. ‘An improved neutron lifetime measurement with UCN τ ’ (2021). 17, 18
- [GH20] S. Gundacker and A. Heering. ‘The silicon photomultiplier: fundamentals and applications of a modern solid-state photon detector’. *Phys. Med. Biol.*, **65**(17), 17TR01 (2020). URL <http://dx.doi.org/10.1088/1361-6560/ab7b2d>. 49
- [GLSP02] G. Giovannetti, L. Landini, M. F. Santarelli, *et al.*. ‘A fast and accurate simulator for the design of birdcage coils in MRI’. *Magma (New York, N.Y.)*, **15**, 36 (2002). URL <http://dx.doi.org/10.1007/BF02693842>. 39

- [GM70] D. M. Ginsberg and M. J. Melchner. ‘Optimum geometry of saddle shaped coils for generating a uniform magnetic field’. *Rev. Sci. Instrum.*, **41**(1), 122 (1970). URL <http://dx.doi.org/10.1063/1.1684235>. 82
- [Gor13] T. Gorringer. ‘MuLan Measurement of the Positive Muon Lifetime and Determination of the Fermi Constant’. In *7th International Workshop on the CKM Unitarity Triangle* (2013). 5
- [GRL91] R. Golub, D. Richardson, and S. Lamoreaux. ‘Ultra-cold neutrons’. CRC Press (1991). URL <https://books.google.de/books?id=OyAuDwAAQBAJ>. 11, 12, 75, 169
- [Haa16] J. Haack. Master’s thesis, Johannes Gutenberg University Mainz (2016). 21, 28, 31, 96, 155
- [Haa21] (2021). Jan Haack (private communication). 96
- [Hal80] K. Halbach. ‘Design of permanent multipole magnets with oriented rare earth cobalt material’. *Nuclear Instruments and Methods*, **169**(1), 1 (1980). URL [http://dx.doi.org/10.1016/0029-554X\(80\)90094-4](http://dx.doi.org/10.1016/0029-554X(80)90094-4). 27
- [HBD12] A. T. Holley, L. J. Broussard, and J. L. Davis. ‘A high-field adiabatic fast passage ultracold neutron spin flipper for the UCNA experiment’. *Rev. Sci. Instrum.*, **83**(7), 073505 (2012). URL <http://dx.doi.org/10.1063/1.4732822>. 39, 40, 66
- [Hei32] W. Heisenberg. ‘Über den Bau der Atomkerne. I’. *Zeitschrift für Physik*, **77**(1), 1 (1932). URL <http://dx.doi.org/10.1007/BF01342433>. 1
- [Hel21] (2021). Mark Heller, Department of Chemistry (TRIGA), JGU (private communication). 107, 135
- [HES85] C. E. Hayes, W. A. Edelstein, and J. F. Schenck. ‘An efficient, highly homogeneous radiofrequency coil for whole-body NMR imaging at 1.5 T’. *J. Magn. Reson.*, **63**, 622 (1985). URL <https://cfmriweb.ucsd.edu/ecwong/birdcage.pdf>. 39, 40
- [HT15] J. C. Hardy and I. S. Towner. ‘Superaligned $0^+ \rightarrow 0^+$ nuclear β decays: 2014 critical survey, with precise results for V_{ud} and ckm unitarity’. *Phys. Rev. C*, **91**, 025501 (2015). URL <http://dx.doi.org/10.1103/PhysRevC.91.025501>. 5, 6
- [HT18] J. Hardy and I. Towner. ‘Nuclear Beta Decays and CKM Unitarity’. In *13th Conference on the Intersections of Particle and Nuclear Physics* (2018). 6
- [Ign90] V. Ignatovich. ‘The physics of ultracold neutrons’. Clarendon Press (1990). 169
- [IPT13] A. N. Ivanov, M. Pitschmann, and N. I. Troitskaya. ‘Neutron β^- decay as a laboratory for testing the standard model’. *Phys. Rev. D*, **88**, 073002 (2013). URL <http://dx.doi.org/10.1103/PhysRevD.88.073002>. 4

- [ITG14] Y. I. Izotov, T. X. Thuan, and N. G. Guseva. ‘A new determination of the primordial He abundance using the He I $\lambda 10830$ Å emission line: cosmological implications’. *Mon. Not. R. Astron. Soc.*, **445**(1), 778–793 (2014). URL <http://dx.doi.org/10.1093/mnras/stu1771>. 9, 10
- [Iwa32] D. Iwanenko. ‘The neutron hypothesis’. *Nature*, **129**(3265), 798 (1932). URL <http://dx.doi.org/10.1038/129798d0>. 1
- [JTW57] J. D. Jackson, S. B. Treiman, and H. W. Wyld. ‘Coulomb corrections in allowed beta transitions’. *Nucl. Phys.*, **4**, 206 (1957). URL [http://dx.doi.org/10.1016/0029-5582\(87\)90019-8](http://dx.doi.org/10.1016/0029-5582(87)90019-8). 5
- [Kah20] J. Kahlenberg. Ph.D. thesis, Johannes Gutenberg University Mainz (2020). URL <http://doi.org/10.25358/openscience-5455>. 21, 24, 26, 29, 31, 32, 47, 48, 49, 51, 106, 107, 117, 128, 148, 160, 163, 166
- [Kar17] J. P. Karch. Ph.D. thesis, Johannes Gutenberg University Mainz (2017). URL <http://doi.org/10.25358/openscience-1364>. 22, 26, 40, 46, 95
- [Kee02] J. Keeler. ‘Understanding nmr spectroscopy’. Wiley (2002). URL <https://doi.org/10.17863/CAM.968>. 64
- [KJM⁺19] M. Klopff, E. Jericha, B. Märkisch, *et al.*. ‘Constraints on the Dark Matter Interpretation $n \rightarrow \chi + e^+e^-$ of the Neutron Decay Anomaly with the PERKEO II Experiment’. *Phys. Rev. Lett.*, **122**, 222503 (2019). URL <http://dx.doi.org/10.1103/PhysRevLett.122.222503>. 19
- [KKMT80] Y. Y. Kosvintsev, Y. A. Kushnir, V. I. Morozov, *et al.*. ‘Use of ultracold neutrons for measurement of the neutron lifetime’. *J. Exp. Theor. Phys. Lett. (USSR)*, **31**(4), 236 (1980). 16
- [KM73] M. Kobayashi and T. Maskawa. ‘CP-Violation in the Renormalizable Theory of Weak Interaction’. *Prog. Theor. Phys.*, **49**(2), 652 (1973). URL <http://dx.doi.org/10.1143/PTP.49.652>. 4
- [KRR⁺17] J. Kahlenberg, D. Ries, K. U. Ross, *et al.*. ‘Upgrade of the ultracold neutron source at the pulsed reactor triga mainz’. *Eur. Phys. J. A*, **53**(11), 226 (2017). URL <http://dx.doi.org/10.1140/epja/i2017-12428-9>. 21, 135, 137, 169
- [KSB⁺14] J. Karch, Y. Sobolev, M. Beck, *et al.*. ‘Performance of the solid deuterium ultra-cold neutron source at the pulsed reactor triga mainz’. *Eur. Phys. J. A*, **50**(4), 78 (2014). URL <http://dx.doi.org/10.1140/epja/i2014-14078-9>. 21, 135, 136, 137
- [LAA⁺05] A. Limosani, K. Abe, K. Abe, *et al.*. ‘Measurement of $|V_{ub}|$ near the endpoint of the electron momentum spectrum from semileptonic B-meson decays’. *Physics Letters B*, **621**(1-2), 28–40 (2005). URL <http://dx.doi.org/10.1016/j.physletb.2005.06.011>. 6
- [Lei97] M. C. Leifer. ‘Resonant modes of the birdcage coil’. *J. Magn. Reson.*, **124**(1), 51 (1997). URL <http://dx.doi.org/10.1006/jmre.1996.7488>. 40

- [LT84] V. I. Luschikov and Y. V. Taran. ‘On the calculation of the neutron adiabatic spin-flipper’. Nucl. Instrum. Methods Phys. Res. A, **228**(1), 159 (1984). URL [http://dx.doi.org/10.1016/0168-9002\(84\)90025-1](http://dx.doi.org/10.1016/0168-9002(84)90025-1). 63, 66
- [LT99] R. E. Lopez and M. S. Turner. ‘Precision prediction for the big-bang abundance of primordial ^4He ’. Phys. Rev. D, **59**, 103502 (1999). URL <http://dx.doi.org/10.1103/PhysRevD.59.103502>. 9
- [MAB⁺89] W. Mampe, P. Ageron, C. Bates, *et al.*. ‘Neutron lifetime measured with stored ultracold neutrons’. Phys. Rev. Lett., **63**, 593 (1989). URL <http://dx.doi.org/10.1103/PhysRevLett.63.593>. 16, 169
- [Mar07] B. R. Martin. ‘Nuclear and particle physics - an introduction’. John Wiley & Sons (2007). 5
- [MBM⁺93] W. Mampe, L. Bondarenko, V. Morozov, *et al.*. ‘Measuring neutron lifetime by storing ultracold neutrons and detecting inelastically scattered neutrons’. J. Exp. Theor. Phys. Lett., **57**, 82 (1993). 16
- [MKS05] G. J. Mathews, T. Kajino, and T. Shima. ‘Big bang nucleosynthesis with a new neutron lifetime’. Phys. Rev. D, **71**, 021302 (2005). URL <http://dx.doi.org/10.1103/PhysRevD.71.021302>. 8
- [MMS⁺19] B. Märkisch, H. Mest, H. Saul, *et al.*. ‘Measurement of the weak axial-vector coupling constant in the decay of free neutrons using a pulsed cold neutron beam’. Phys. Rev. Lett., **122**, 242501 (2019). URL <http://dx.doi.org/10.1103/PhysRevLett.122.242501>. 5, 7
- [Mou17] M. Moulson. ‘Experimental determination of V_{us} from kaon decays’. PoS Proc. Sci., **CKM2016**, 033 (2017). URL <http://dx.doi.org/10.22323/1.291.0033>. 6
- [MS06] W. J. Marciano and A. Sirlin. ‘Improved calculation of electroweak radiative corrections and the value of V_{ud} ’. Phys. Rev. Lett., **96**, 032002 (2006). URL <http://dx.doi.org/10.1103/PhysRevLett.96.032002>. 5
- [Mum18] P. Mumm. ‘Resolving the neutron lifetime puzzle’. Science, **360**(6389), 605 (2018). URL <http://dx.doi.org/10.1126/science.aat7140>. 3
- [NDG⁺05] J. S. Nico, M. S. Dewey, D. M. Gilliam, *et al.*. ‘Measurement of the neutron lifetime by counting trapped protons in a cold neutron beam’. Phys. Rev. C, **71**, 055502 (2005). URL <http://dx.doi.org/10.1103/PhysRevC.71.055502>. 14, 18
- [NHI⁺19] Nagakura, Naoki, Hirota, Katsuya, Ieki, Sei, *et al.*. ‘New project for precise neutron lifetime measurement at j-parc’. EPJ Web Conf., **219**, 03003 (2019). URL <http://dx.doi.org/10.1051/epjconf/201921903003>. 19
- [Pau09] S. Paul. ‘The puzzle of neutron lifetime’. Nucl. Instrum. Methods Phys. Res. A, **611**(2), 157 (2009). URL <http://dx.doi.org/https://doi.org/10.1016/j.nima.2009.07.095>. Particle Physics with Slow Neutrons. 18

- [PCCW⁺18] J. Pattie, R. W., N. B. Callahan, C. Cude-Woods, *et al.*. ‘Measurement of the neutron lifetime using a magneto-gravitational trap and in situ detection’. *Science*, **360**(6389), 627 (2018). URL <http://dx.doi.org/10.1126/science.aan8895>. 18
- [PKQ⁺19] D. Patel, S.-H. Kim, W. Qiu, *et al.*. ‘Niobium-titanium (nb-ti) superconducting joints for persistent-mode operation’. *Sci. Rep.*, **9**, 14287 (2019). URL <http://dx.doi.org/10.1038/s41598-019-50549-7>. 22
- [PPL16] A. Peimbert, M. Peimbert, and V. Luridiana. ‘The primordial helium abundance and the number of neutrino families’. *Rev. Mex. Astron. Astrofis.*, **52**, 419 (2016). URL <https://ui.adsabs.harvard.edu/abs/2016RMxAA..52..419P>. 9, 10
- [PVSG10] A. Pichlmaier, V. Varlamov, K. Schreckenbach, *et al.*. ‘Neutron lifetime measurement with the UCN trap-in-trap MAMBO II’. *Phys. Lett. B*, **693**(3), 221 (2010). URL <http://dx.doi.org/10.1016/j.physletb.2010.08.032>. 16, 18
- [Rob50] J. M. Robson. ‘Radioactive decay of the neutron’. *Phys. Rev.*, **78**, 311 (1950). URL <http://dx.doi.org/10.1103/PhysRev.78.311>. 3
- [Rob51] J. M. Robson. ‘The radioactive decay of the neutron’. *Phys. Rev.*, **83**, 349 (1951). URL <http://dx.doi.org/10.1103/PhysRev.83.349>. 14
- [Rob71] R. T. Robiscoe. ‘A spin flip problem’. *Am. J. Phys.*, **39**(2), 146 (1971). URL <http://dx.doi.org/10.1119/1.1986080>. 66
- [Ros17] K. U. Ross. Master’s thesis, Johannes Gutenberg University Mainz (2017). 29
- [Rut20] E. Rutherford. ‘Bakerian lecture: Nuclear constitution of atoms’. *Proc. R. Soc. A*, **97**(686), 374 (1920). URL <http://dx.doi.org/10.1098/rspa.1920.0040>. 1
- [SAB⁺14] D. J. Salvat, E. R. Adamek, D. Barlow, *et al.*. ‘Storage of ultracold neutrons in the magneto-gravitational trap of the UCN τ experiment’. *Phys. Rev. C*, **89**, 052501 (2014). URL <http://dx.doi.org/10.1103/PhysRevC.89.052501>. 17
- [Sak91] A. Sakharov. ‘Violation of CP Invariance, C asymmetry, and baryon asymmetry of the universe’. *Sov. Phys. Usp.*, **34**(5), 392 (1991). URL <http://dx.doi.org/10.1070/PU1991v034n05ABEH002497>. 6
- [Sau19] A. Saunders. ‘Overview of recent efforts and results of the neutron lifetime measurements’. *Physics of fundamental Symmetries and Interactions* (2019). 19
- [Sch19] C. Schmidt. Ph.D. thesis, Johannes Gutenberg University Mainz (2019). URL <http://nbn-resolving.org/urn:nbn:de:hebis:77-diss-1000029381>. 5
- [Sch20] (2020). Christian Schmidt (private communication). 154

- [SCK⁺21] A. P. Serebrov, M. E. Chaikovskii, G. N. Klyushnikov, *et al.*. ‘Search for explanation of the neutron lifetime anomaly’. *Phys. Rev. D*, **103**, 074010 (2021). URL <http://dx.doi.org/10.1103/PhysRevD.103.074010>. 18
- [sen19] (2019). URL <https://www.senis.ch/>. Senis AG. 32
- [SGP⁺18] C.-Y. Seng, M. Gorchtein, H. H. Patel, *et al.*. ‘Reduced hadronic uncertainty in the determination of V_{ud} ’. *Phys. Rev. Lett.*, **121**, 241804 (2018). URL <http://dx.doi.org/10.1103/PhysRevLett.121.241804>. 5, 6
- [SKF⁺18] A. P. Serebrov, E. A. Kolomensky, A. K. Fomin, *et al.*. ‘Neutron lifetime measurements with a large gravitational trap for ultracold neutrons’. *Phys. Rev. C*, **97**(5) (2018). URL <http://dx.doi.org/10.1103/physrevc.97.055503>. 16, 18, 106
- [SLK⁺17] A. Steyerl, K. K. H. Leung, C. Kaufman, *et al.*. ‘Spin flip loss in magnetic confinement of ultracold neutrons for neutron lifetime experiments’. *Phys. Rev. C*, **95**, 035502 (2017). URL <http://dx.doi.org/10.1103/PhysRevC.95.035502>. 100
- [SPK⁺12] A. Steyerl, J. M. Pendlebury, C. Kaufman, *et al.*. ‘Quasielastic scattering in the interaction of ultracold neutrons with a liquid wall and application in a reanalysis of the Mambo I neutron-lifetime experiment’. *Phys. Rev. C*, **85**, 065503 (2012). URL <http://dx.doi.org/10.1103/PhysRevC.85.065503>. 18
- [SPM50] A. H. Snell, F. Pleasonton, and R. V. McCord. ‘Radioactive decay of the neutron’. *Phys. Rev.*, **78**, 310 (1950). URL <http://dx.doi.org/10.1103/PhysRev.78.310>. 3
- [SU19] A. Saunders and T. T. UCN τ . ‘Tau2: A next generation neutron lifetime experiment based on UCN&tau’ (2019). 19
- [SVK⁺05] A. Serebrov, V. Varlamov, A. Kharitonov, *et al.*. ‘Measurement of the neutron lifetime using a gravitational trap and a low-temperature fomblin coating’. *Phys. Lett. B*, **605**(1-2), 72–78 (2005). URL <http://dx.doi.org/10.1016/j.physletb.2004.11.013>. 16, 18
- [SVMT06] C. E. G. Salmon, E. L. G. Vidoto, M. J. Martins, *et al.*. ‘Optimization of saddle coils for magnetic resonance imaging’. *Braz. J. Phys.*, **36**, 4 (2006). URL http://www.scielo.br/scielo.php?script=sci_arttext&pid=S0103-97332006000100004&nrm=iso. 82, 147
- [TBB⁺18] Z. Tang, M. Blatnik, L. J. Broussard, *et al.*. ‘Search for the neutron decay $n \rightarrow x + \gamma$, where x is a dark matter particle’. *Phys. Rev. Lett.*, **121**, 022505 (2018). URL <http://dx.doi.org/10.1103/PhysRevLett.121.022505>. 19
- [TCC⁺19] Z. Tang, C. Cude-Woods, S. Clayton, *et al.*. ‘Ultra-Cold Neutron measurement of Proton branching ratio in neutron Beta decay (UCNProBe)’. In *APS April Meeting Abstracts*, volume 2019 of *APS Meeting Abstracts*, H14.005 (2019). 19

- [THH⁺18] M. Tanabashi, K. Hagiwara, K. Hikasa, *et al.*. ‘Review of particle physics’. *Phys. Rev. D*, **98**, 030001 (2018). URL <http://dx.doi.org/10.1103/PhysRevD.98.030001>. 9
- [UTM⁺05] M. Utsuro, M. Tanaka, K. Mishima, *et al.*. ‘Ucn production with a single crystal of ortho-deuterium’. *Journal of Research of the National Institute of Standards and Technology*, **110**(3), 273 (2005). URL <http://dx.doi.org/10.6028/jres.110.038>. International Conference on Precision Measurements with Slow Neutrons, Natl Inst Stand & Technol, Gaithersburg, MD, APR 05-07, 2004. 136
- [VPPS19] M. Valerdi, A. Peimbert, M. Peimbert, *et al.*. ‘Determination of the Primordial Helium Abundance Based on NGC 346, an H ii Region of the Small Magellanic Cloud’. *Astrophys. J.*, **876**(2), 98 (2019). URL <http://dx.doi.org/10.3847/1538-4357/ab14e4>. 9, 10
- [WFG⁺16] F. E. Wietfeldt, N. Fomin, G. L. Greene, *et al.*. ‘BL3: A Next Generation Beam Neutron Lifetime Experiment’. In *APS Division of Nuclear Physics Meeting Abstracts*, volume 2016 of *APS Meeting Abstracts*, KG.006 (2016). 19
- [WG11] F. E. Wietfeldt and G. L. Greene. ‘Colloquium: The neutron lifetime’. *Rev. Mod. Phys.*, **83**, 1173 (2011). URL <http://dx.doi.org/10.1103/RevModPhys.83.1173>. 14, 15, 19
- [Wie18] F. Wietfeldt. ‘Measurements of the Neutron Lifetime’. *Atoms*, **6**(4), 70 (2018). URL <http://dx.doi.org/10.3390/atoms6040070>. 15
- [Wor18] (2018). Mechanical workshop, Institute of Physics, JGU (private communication). 31
- [WTP⁺11] D. M. Webber, V. Tishchenko, Q. Peng, *et al.*. ‘Measurement of the positive muon lifetime and determination of the fermi constant to part-per-million precision’. *Phys. Rev. Lett.*, **106**, 041803 (2011). URL <http://dx.doi.org/10.1103/PhysRevLett.106.041803>. 5
- [YCF⁺14] A. R. Young, S. Clayton, B. W. Filippone, *et al.*. ‘Beta decay measurements with ultracold neutrons: a review of recent measurements and the research program at los alamos national laboratory’. *J. Phys. G*, **41**(11), 114007 (2014). URL <http://dx.doi.org/10.1088/0954-3899/41/11/114007>. 2
- [YDG⁺13] A. T. Yue, M. S. Dewey, D. M. Gilliam, *et al.*. ‘Improved determination of the neutron lifetime’. *Phys. Rev. Lett.*, **111**(22) (2013). URL <http://dx.doi.org/10.1103/physrevlett.111.222501>. 14, 18, 19
- [ZBB⁺20] P. A. Zyla, R. M. Barnett, J. Beringer, *et al.*. ‘Review of Particle Physics’. *Prog. Theor. Exp. Phys.*, **2020**(8) (2020). URL <http://dx.doi.org/10.1093/ptep/ptaa104>. 083C01. 2, 3, 5, 6, 7, 8, 18

Declaration

I hereby declare that this thesis titled 'Towards a high precision measurement of the free neutron lifetime with τ SPECT' represents my own work. The information derived from the literature has been duly acknowledged in the text and a list of references provided. No part of this dissertation was previously presented for another degree or diploma at this or any other institution.

July 21st 2021

Date



Kim Ulrike Roß

Curriculum Vitae

Kim Ulrike Roß

Curriculum Vitae

Bodenheimer Straße 10
55129 Mainz

Nationality: German

Born on 12/10/1991 in Heppenheim

Education

- Since 10/2017 **Doctoral studies**, *Johannes Gutenberg University*, Mainz, Institute of Physics.
Title: 'Towards a high precision measurement of the free neutron lifetime with τ SPECT'
(Supervisor: Prof. Dr. Werner Heil)
- 04/2015 – 06/2017 **Master of Science (Physics)**, *Johannes Gutenberg University*, Mainz, (Final grade: 1.5).
Title: 'Transport und Speicherung von ultrakalten Neutronen im Lebensdauerexperiment τ SPECT' (Supervisor: Prof. Dr. Werner Heil)
- 04/2012 – 06/2015 **Bachelor of Science (Physics)**, *Johannes Gutenberg University*, Mainz, (Final grade: 2.4).
Title: 'Inbetriebnahme und Test des Protonendetektors bei τ SPECT' (Supervisor: Prof. Dr. Werner Heil)
- 10/2011 – 04/2012 **Preclinical studies of dental medicine**, *Johannes Gutenberg University*, Mainz.
- 05/2011 **Abitur**, *Altes Kurfürstliches Gymnasium*, Bensheim, Final grade: 1.6.

Publications

- 06/2021 **The design of the n2EDM experiment**, N. J. Ayres, G. Ban, L. Bienstman *et. al.*, *Eur. Phys. J. C* **81**, 512 (2021).
- 06/2021 **Johnson-Nyquist noise effects in neutron electric-dipole-moment experiments**, N. J. Ayres, G. Ban, G. Bison *et. al.*, *Phys. Rev. A* **103**, 062801 (2021).
- 11/2017 **Upgrade of the ultracold neutron source at the pulsed reactor TRIGA Mainz**, J. Kahlenberg, D. Ries, K. U. Ross *et. al.*, *Eur. Phys. J. A* **53**, 226 (2017).

Scientific contributions

- 06/2021 **The Filling Process in the Neutron Lifetime Experiment τ SPECT**, Talk (online), Group seminar, NC State University, North Carolina, USA.
- 03/2021 **Status of the Neutron Lifetime Experiment τ SPECT**, Talk (online), AstroNews Colloquium (ETAP), Johannes Gutenberg University, Mainz, Germany.
- 10/2019 **Spin manipulation and detection of UCN in the neutron lifetime experiment τ SPECT**, Poster, PSI2019 conference, Villigen, Switzerland.

- 06/2018 **Measuring the free neutron lifetime with magnetic storage**, Poster, SSP2018 conference, Aachen, Germany.
- 03/2018 **Compensation of a magnetic octupole field for the lifetime experiment τ SPECT**, Talk, DPG conference, Bonn, Germany.

Teaching

Experimentalphysik 4 (Winter semester 2017/2018)
Experimentalphysik 2 (Summer semester 2018)
Experimentalphysik 1 (Summer semester 2019)

Qualifications

Languages	German (mother tongue), English (excellent command), Italian (good command), French (basic communication skills)
Skills	Automation, data science, engineering, sensor technology, high frequency technology, CAD, vacuum technology, cryogenics
Programming	Python, basic knowledge in JAVA, C/C++, Git und SQL
Simulation	Monte Carlo methods, FEM simulation (COMSOL Multiphysics [®])
Environments	Windows, Linux, Raspberry Pi, Arduino
Office	Microsoft Office, OpenOffice, LaTeX
Visualisation	Gnuplot, Inkscape, Gimp, Photoshop

Additional training

Fernuniversität Hagen *'Einführung in die Wirtschaftswissenschaft'* (course attendance)

